

## Hybridization of Localized States in Semiconducting and Superconducting Circuits

Prosko, C.G.

**DOI**

[10.4233/uuid:612b784f-8a1e-4500-bc99-68c7fe2382e0](https://doi.org/10.4233/uuid:612b784f-8a1e-4500-bc99-68c7fe2382e0)

**Publication date**

2024

**Document Version**

Final published version

**Citation (APA)**

Prosko, C. G. (2024). *Hybridization of Localized States in Semiconducting and Superconducting Circuits*. [Dissertation (TU Delft), Delft University of Technology]. <https://doi.org/10.4233/uuid:612b784f-8a1e-4500-bc99-68c7fe2382e0>

**Important note**

To cite this publication, please use the final published version (if applicable). Please check the document version above.

**Copyright**

Other than for strictly personal use, it is not permitted to download, forward or distribute the text or part of it, without the consent of the author(s) and/or copyright holder(s), unless the work is under an open content license such as Creative Commons.

**Takedown policy**

Please contact us and provide details if you believe this document breaches copyrights. We will remove access to the work immediately and investigate your claim.

# Hybridization of Localized States in Semiconducting and Superconducting Circuits

Hybridization of Localized States in Semiconducting and Superconducting Circuits

Christian Glenn Prosko



Christian Glenn Prosko

**HYBRIDIZATION OF LOCALIZED STATES IN  
SEMICONDUCTING AND SUPERCONDUCTING  
CIRCUITS**



# **HYBRIDIZATION OF LOCALIZED STATES IN SEMICONDUCTING AND SUPERCONDUCTING CIRCUITS**

## **Dissertation**

for the purpose of obtaining the degree of doctor  
at Delft University of Technology,  
by the authority of the Rector Magnificus, prof. dr. ir. T.H.J.J. van der Hagen,  
chair of the Board for Doctorates,  
to be defended publicly on Thursday 27 June at 10:00 o'clock

by

**Christian Glenn PROSKO**

Master of Science in Applied Physics  
Delft University of Technology, Netherlands  
born in Edmonton, Alberta, Canada

This dissertation has been approved by the promotor.

Composition of the doctoral committee:

Rector Magnificus	chairperson
Prof. dr. ir. L. P. Kouwenhoven	Delft University of Technology, promotor
Dr. S. Goswami	Delft University of Technology, copromotor

*Independent members:*

Prof. dr. J. Levy	University of Pittsburgh, USA
Prof. dr. C. Schönenberger	University of Basel, Switzerland
Prof. dr. G. A. Steele	Delft University of Technology
Dr. ir. T. van der Sar	Delft University of Technology
Prof. dr. ir. L. M. K. Vandersypen	Delft University of Technology, reserve member



QuTech



*Cover:* Illustration of the capacitance associated with the hybridization of an electron between doubly-connected quantum dots threaded by magnetic flux, by Hélène Spring.

*Printed by:* [www.printenbind.nl](http://www.printenbind.nl)

Copyright © 2024 by Christian Glenn Prosko

ISBN 978-94-6384-602-8

An electronic version of this dissertation is available at  
<http://repository.tudelft.nl/>.

# CONTENTS

<b>Summary</b>	<b>ix</b>
<b>Samenvatting</b>	<b>xi</b>
<b>Frequently Used Acronyms</b>	<b>xiii</b>
<b>1 Introduction</b>	<b>1</b>
1.1 Thesis Outline . . . . .	2
<b>2 Theory</b>	<b>5</b>
2.1 Confined Systems of Quasiparticles or Charge . . . . .	5
2.1.1 Classical Charge Islands and Quantum Dots . . . . .	5
2.1.2 Confinement by Superconductivity: Andreev Bound States . . . . .	11
2.1.3 Superconducting Islands. . . . .	14
2.1.4 Electrically Floating Dot Systems . . . . .	16
2.1.5 Second-Order Tunneling Processes . . . . .	19
2.2 Probing Quantum Circuits with Microwave Resonators. . . . .	22
2.2.1 Resonators in the Quantum and Semiclassical Limits . . . . .	25
2.2.2 Impedance of Quantum Charge Systems. . . . .	28
2.2.3 Driving due to Landau-Zener Transitions . . . . .	34
2.2.4 Optimizing Resonator Design for Measurements . . . . .	35
<b>3 Rapid microwave-only characterization and readout of quantum dots using multiplexed gigahertz-frequency resonators</b>	<b>41</b>
3.1 Introduction . . . . .	42
3.2 Experimental setup . . . . .	42
3.3 High-frequency conductance measurements . . . . .	43
3.4 Rapid multiplexed reflectometry . . . . .	46
3.5 Signal to noise . . . . .	47
3.6 Conclusions. . . . .	49
3.7 Supplemental material . . . . .	49
3.7.1 Correspondence between $Y$ and resonator response. . . . .	49
3.7.2 Derivation of $G_{\text{RF}}$ . . . . .	51
3.7.3 Determination of $\gamma\ell$ and $Z_{\text{nw}}$ from experimental data. . . . .	52
3.7.4 Comparison of $G_{\text{DC}}$ and $G_{\text{RF}}$ for all pinchoff curves . . . . .	52
3.7.5 SNR measurement . . . . .	54
3.7.6 Relation between SNR and amplifier noise temperature . . . . .	55

<b>4</b>	<b>Controllable single Cooper pair splitting in hybrid quantum dot systems</b>	<b>57</b>
4.1	Introduction	57
4.2	Experimental Design & Setup	58
4.3	Triple dot charge stability diagram	59
4.4	Gate-induced Single Cooper Pair Splitting	60
4.5	Parity sensing in a quadruple quantum dot	62
4.6	Conclusions & Outlook	64
4.7	Supplemental Information	65
4.7.1	Projection and Normalization of Resonator Data	65
4.7.2	Device Properties	65
4.7.3	Simulation of Charge Stability Diagrams	65
4.7.4	Model and Fits of the Cooper Pair Splitting Transition	70
<b>5</b>	<b>Flux-Tunable Hybridization in a Double Quantum Dot Interferometer</b>	<b>77</b>
5.1	Introduction	77
5.2	Device Overview	79
5.3	Phase-coherent Loop and Quantum Ring	81
5.4	Flux-Tunable interdot Coupling	83
5.5	Limits of Flux-tuned Tunnel Coupling Readout	85
5.6	Conclusions & Outlook	88
5.7	Supplemental Information	89
5.7.1	Calculating RF Signal Deviation from Coulomb Blockade	89
5.7.2	Tuning Symmetric Parallel Tunnel Barriers	90
5.7.3	Coulomb Diamonds	90
5.7.4	Fitting Procedure for Tunnel Coupling Extraction	91
5.7.5	Field-Dependence of Peak Heights in Different Coupling Regimes	93
<b>6</b>	<b>Flux-tunable Josephson Effect in a Four-Terminal Junction</b>	<b>95</b>
6.1	Introduction	95
6.2	Device Design & Characterization	96
6.3	Flux-Tunable Nonlocal Josephson Effect	99
6.4	Multiterminal Junctions as Two-Terminal Junction Arrays	101
6.5	Conclusions & Outlook	104
6.6	Supplemental Information	105
6.6.1	Gate Performance	105
6.6.2	Field Direction Calibration	105
6.6.3	Current-Phase Relations of Four-Terminal Junctions embedded in Asymmetric SQUIDs	106
6.6.4	Nonlocal Flux Dependence in SQUID R	107
6.6.5	Supporting data on a Second Device	109
6.6.6	Two-terminal Array Models of Multiterminal Junctions	110
<b>7</b>	<b>Conclusion &amp; Outlook</b>	<b>113</b>
7.1	Conclusions	113
7.2	Nonlocal RF Measurements of Hybrid Devices	114
7.3	Quasiparticle Poisoning of Parity Qubits	117
7.4	Floating Kitaev Chains & Hybrid Qubits	120

---

<b>A</b>	<b>Fabrication details</b>	<b>125</b>
A.1	RF-Compatible Devices in Two-Dimensional Electron Gases . . . . .	125
A.2	Fabrication Procedure . . . . .	126
<b>B</b>	<b>Measurement Setups</b>	<b>135</b>
B.1	Microwave Transmission Measurement Setup . . . . .	136
B.2	Sub-GHz Reflectometry Measurement Setup . . . . .	137
B.3	Wideband Reflectometry Setup . . . . .	138
B.4	DC Setup with High-Current Lines . . . . .	139
<b>C</b>	<b>Resonator Response Fitting</b>	<b>141</b>
<b>D</b>	<b>Quantum Capacitance Formula including Mutual Capacitances</b>	<b>145</b>
<b>E</b>	<b>Capacitance of a Dot with Normal and Superconducting Leads</b>	<b>147</b>
<b>F</b>	<b>Fermionic Simulation of a Floating Hybrid Triple Quantum Dot</b>	<b>153</b>
	<b>Acknowledgements</b>	<b>185</b>
	<b>Curriculum Vitae</b>	<b>187</b>
	<b>List of Publications</b>	<b>189</b>



## SUMMARY

Hybrid semiconducting-superconducting mesoscopic circuits are the basis of topological and parity quantum bits or ‘qubits’. Both qubits are expected to be intrinsically protected from decoherence, making them promising candidates for fault-tolerant quantum computation. As topological phases effectively manifest exotic nonabelian particles which might not exist in nature, these systems are also of fundamental interest. This thesis primarily employs radio-frequency (RF) reflectometry, an important measurement tool for qubit readout, in order to study localized states in hybrid circuits. Since the hybridization of localized quantum dot and Andreev bound states is foundational to the aforementioned qubit implementations, our focus is on using RF tools to characterize such hybridization. We therefore begin by outlining background theory of these states and of RF reflectometry accompanied by simulations. Subsequently, we describe the results of four distinct experiments.

First, in a system comprised of multiple quantum dots, we demonstrate a signal-to-noise ratio of 15 in  $1\ \mu\text{s}$  for resolving interdot electron tunneling with RF reflectometry of the dot gate electrodes, a proxy for the readout of numerous types of qubits including spin and topological qubits. Additionally, we show RF reflectometry of the device leads is mappable to DC conductance a priori, implying it can completely replace DC measurement techniques for the characterization of semiconducting quantum circuits.

In the next experiment, we probe a superconducting island surrounded on either side by a semiconducting quantum dot with RF gate reflectometry. Therein, we electrically isolate the system from its leads, fixing the system’s total charge. Afterwards, we correlate electron tunneling events between dots using frequency multiplexing of different gate resonators, culminating in the controllable splitting of a single Cooper pair into its constituent electrons. We also demonstrate a form of parity sensing using a strongly coupled double quantum dot and gate reflectometry.

Continuing, we present a study of an irregularly shaped double quantum dot arranged in a loop and threaded by a magnetic flux. Employing gate reflectometry to measure the interdot hybridization, we observe that it oscillates as a function of flux with a period of one flux quantum but with unpredictably varying amplitude and contrast. This result is a prerequisite for the readout and manipulation of measurement-based topological qubits and hybrid parity qubits.

As a final experiment, we investigate markers of the hybridization between Andreev bound states in a multiterminal Josephson junction, itself a potential platform for simulating topological Weyl systems. There, we characterize the current-flux relation of a four-terminal junction using two coupled DC superconducting quantum interference loops, observing a ‘nonlocal’ Josephson effect tuned by the magnetic fluxes through both loops. With a minimal theoretical model, we show that this behavior can be fully described by an array of two-terminal Josephson junctions and is not a unique signature of the hybridization of Andreev bound states in the junction.

To conclude, we summarize our experimental results and discuss potential future work. Namely, we emphasize the importance of understanding quasiparticle poisoning for the performance of topological and parity qubits, and consider further applications of RF measurement tools in studying hybrid systems. The results of this dissertation establish RF sensing as a complete characterization tool for hybrid quantum circuits, display its utility in studying floating systems to probe the movement of single electrons and Cooper pairs, and demonstrate the flux-control of interdot tunnel couplings required for hybrid parity qubits. Lastly, we highlight the indistinguishability of hybridized Andreev states from trivial multiterminal Josephson effects in a multiterminal junction's current-phase relation.

# SAMENVATTING

Hybride halfgeleider-supergeleider mesoscopische circuits vormen de basis van topologische en pariteit qubits of 'qubits'. Van beide qubits wordt verwacht dat ze intrinsiek beschermd zijn tegen decoherentie, waardoor ze veelbelovende kandidaten zijn voor fouttolerante quantumcomputatie. Aangezien topologische fasen effectief exotische niet-abeliaanse deeltjes manifesteren die mogelijk niet in de natuur voorkomen, zijn deze systemen ook van fundamenteel belang. Dit proefschrift maakt voornamelijk gebruik van radiofrequentie (RF) reflectometrie, een belangrijk meetinstrument voor qubit uitlezing, om gelokaliseerde toestanden in hybride circuits te bestuderen. Aangezien de hybridisatie van gelokaliseerde quantum dots en Andreev bound states de basis vormt voor de eerder genoemde qubit-implementaties, richten wij ons op het gebruik van RF-instrumenten om dergelijke hybridisatie te karakteriseren. We beginnen daarom met het schetsen van de theoretische achtergrond van deze toestanden en van RF reflectometrie, vergezeld met simulaties. Vervolgens beschrijven we de resultaten van vier verschillende experimenten.

Ten eerste, in een systeem bestaande uit meerdere quantum dots, demonstreren we een signaal-ruisverhouding van 15 in 1  $\mu\text{s}$  voor het blootleggen van elektrontunneling tussen dots met RF reflectometrie van de dot gate elektroden, een proxy voor de uitlezing van talrijke soorten qubits, waaronder spin- en topologische qubits. Daarnaast tonen we aan dat RF reflectometrie van de apparaatleidingen a priori kan worden vertaald naar DC-geleiding, wat impliceert dat het DC-meettechnieken volledig kan vervangen voor de karakterisering van halfgeleider quantum circuits.

In het volgende experiment onderzoeken we een supergeleidend eiland omgeven aan beide zijden door een halfgeleidende quantum dot met RF gate reflectometrie. Daarin isoleren we het systeem elektrisch van zijn leidingen, waardoor de totale lading van het systeem wordt vastgezet. Vervolgens correleren we elektrontunneling gebeurtenissen tussen dots met behulp van frequentiemultiplexing van verschillende gate resonatoren, wat resulteert in het controleerbaar splitsen van een enkel Cooper paar in zijn samenstellende elektronen. We demonstreren ook een vorm van pariteitsdetectie met behulp van een sterk gekoppelde dubbele quantum dot en gate reflectometrie.

Vervolgens presenteren we een studie van een onregelmatig gevormde dubbele quantum dot opgesteld in een lus en doorboord door een magnetische flux. Door gate reflectometrie te gebruiken om de interdot hybridisatie te meten, observeren we dat deze oscilleert als een functie van flux met een periode van één flux quantum, maar met onvoorspelbaar variërende amplitude en contrast. Dit resultaat is een vereiste voor de uitlezing en manipulatie van op metingen gebaseerde topologische qubits en hybride pariteit qubits.

Als laatste experiment onderzoeken we de signaturen van de hybridisatie tussen Andreev bound states in een multiterminal Josephson junction, welke zelf een potentieel platform vormen voor het simuleren van topologische Weyl systemen. Daar karaktere-

riseren we de stroom-flux relatie van een vier-terminal junction met behulp van twee gekoppelde DC supergeleidende kwantum interferentie lussen, waarbij we een 'niet-lokaal' Josephson effect waarnemen dat wordt afgestemd door de magnetische fluxen door beide lussen. Met een minimaal theoretisch model tonen we aan dat dit gedrag volledig kan worden beschreven door een array van twee-terminal Josephson junctions en geen unieke signatuur is van de hybridisatie van Andreev gebonden toestanden in het knooppunt.

Tot slot vatten we onze experimentele resultaten samen en bespreken we potentieel toekomstig werk. We benadrukken het belang van het begrijpen van quasiparticle poisoning voor de prestaties van topologische en pariteit qubits, en overwegen verdere toepassingen van RF meetinstrumenten bij het bestuderen van hybride systemen. De resultaten van dit proefschrift vestigen RF-sensing als een compleet karakterisatie-instrument voor hybride quantum circuits, tonen het nut ervan aan bij het bestuderen van zwevende systemen om de beweging van enkele elektronen en Cooper paren te onderzoeken, en demonstreren de flux-controle van interdot tunnelkoppelingen die nodig zijn voor hybride pariteit qubits. Tot slot benadrukken we de ononderscheidbaarheid van gehybridiseerde Andreev toestanden van triviale multiterminal Josephson effecten in de stroom-fase relatie van een multiterminal junction.

## FREQUENTLY USED ACRONYMS

<b>Acronym</b>	<b>Meaning</b>	<b>Explanation</b>
QD	quantum dot	A confined quantum system of electrons where Coulomb repulsion effects are significant
DQD	double quantum dot	Two QDs coupled capacitively or through tunneling
SCI	superconducting island	A QD made superconducting, either by forming the entire island out of superconducting material or by adding a floating piece of superconductor to a semiconducting QD
DGS	dispersive gate sensing	Reflectometry measurement technique where a resonator is coupled to the gate of a quantum device, operated at frequencies far detuned from the device's energy scales
SNR	signal-to-noise ratio	The ratio of the distance between two signals of interest to some measure of the noise in this signal
ABS	Andreev bound state	Subgap state formed in a normal conducting material when it is confined by a boundary which is superconducting
CSD	charge stability diagram	Map of a multi-QD system's ground state charge distribution
JJ	Josephson junction	Weak link between two superconducting leads, formed by a narrow constriction, insulating region, or normal/semiconducting region
SQUID	superconducting quantum interference device	A circuit of a single JJ (RF SQUID) or two JJs (DC SQUID) in a superconducting loop threaded by a magnetic flux
CPR	current-phase relation	The supercurrent through a JJ as a function of the phase difference of the superconducting pairing potentials on either lead
CFR	current-flux relation	The supercurrent through a SQUID circuit as a function of the magnetic flux threading the SQUID



# 1

## INTRODUCTION

*We shouldn't fear a world that is more interacted.*

George W. Bush

Advancements in technology often arise when scientists come to appreciate the applicability of ideas from seemingly disparate research areas to their own. For example, nuclear magnetic resonance imaging was employed to characterize organic molecules for decades before it was considered as one of the earliest avenues to create a quantum computer [1]. Likewise, one of the currently most promising types of quantum bits or 'qubits' proposed to construct a quantum computer are superconducting qubits, which use circuit quantum electrodynamics (cQED) as a foundation for their operation [2, 3]. This arose from the realization that principles of cavity quantum electrodynamics, where light is made to coherently interact with atoms, could similarly be applied in superconducting circuits containing 'artificial atoms' in the form of qubits [4, 5].

In the world of mesoscopic physics where small electrical circuits are described by quantum mechanics [6], the search for a scalable quantum computer has seen great advancements as different technologies meet, not the least of which is the advent of cQED mentioned above. More pertinently to this thesis however, a flurry of research commenced after the technique of combining properties of superconductors with those of semiconductors through the proximity effect was shown to enable the formation of topologically protected phases of matter [7, 8]. These include Majorana 'quasi'-particles, an *effective* realization of the hypothetical particle which is its own antiparticle proposed by Ettore Majorana in 1937 [9]. Majorana quasiparticles, if conclusively observed, could form the basis of topologically protected quantum computers [10, 11], the principal motivation for the experiments of this thesis.

In parallel, microwave reflectometry techniques have been employed since the advent of radar technology, but only in the past couple decades have they proven indispensable for the investigation of mesoscopic quantum systems [12]. Not only are these

techniques now the basis for readout of semiconducting qubits [13], they are also crucial for the readout and control of topological qubits [11] and useful for the investigation of topological phases [14]. They provide fast access to many physical properties of mesoscopic systems including and beyond those retrievable from direct-current measurements, an idea which we try to further cement herein.

This thesis discusses experiments which aimed to exploit these combined technologies just a little bit further. We emphasize through these experiments that microwave techniques are powerful tools for characterizing and understanding all semiconducting and superconducting hybrid devices. In particular, we focus on studying one of the most fundamental characteristics of mesoscopic quantum devices: the quantum hybridization of localized states. These states could be electron levels in a semiconducting quantum dot, Andreev bound states in a superconducting Josephson junction, or a hybrid middleground in superconducting islands—all three of which are potential building blocks of future topologically protected qubits, and all three of which are investigated in the coming chapters.

## 1.1. THESIS OUTLINE

This thesis begins in **Chapter 2** with an outline of the theoretical concepts in mesoscopic physics and microwave measurement techniques employed in the subsequent chapters. Namely, we discuss how electrons and quasiparticles form localized states in semiconductors and superconductors, then discuss how these states can be probed with microwave reflectometry techniques, accompanied by example simulations. These techniques form the basis of most of this thesis' experiments.

As a fundamental illustration of the utility of microwave measurements for investigating and characterizing semiconducting and hybrid systems, in **Chapter 3** we present experiments probing a nanowire multi-quantum-dot device with GHz-frequency resonators. We show that these techniques can effectively replace DC measurements for characterization of semiconducting quantum devices. With an extremely high signal-to-noise ratio we also demonstrate the rapid measurement of electron hybridization between two quantum dots, relevant for spin and topological qubits [11, 13].

Next, in **Chapter 4** we use the same resonators to probe a more advanced device consisting of quantum dots separated by a superconducting island. This system is probed while completely isolated from Ohmic contacts, and we locally resolve interdot tunneling processes by frequency-multiplexing resonators coupled to each dot or island in the system. With this approach, we manage to split individual Cooper pairs from the superconducting island and retain them on the quantum dots, and also demonstrate a technique using a strongly hybridized double quantum dot for measuring parity in such systems.

**Chapter 5** revisits the hybridization of electron levels in quantum dots with a twist: with two elongated dots connected at two points to form a loop, a magnetic flux was passed through to magnetically tune the hybridization. We successfully measure a hybridization controlled by this flux, demonstrating the principle of quantum interference in an irreducibly simple system of two hybridized states. We also quantify the limitations of this tunability, since it is necessary for measurement-based topological qubits and unavoidably present in two-dimensional quantum dot arrays used in quantum computing.

The experiment of **Chapter 6** aimed to study hybridization of a different type of localized state: Andreev bound states in Josephson junctions, as the bound state spectrum of multiterminal junctions may host topological phases [15]. We do so by studying the current-phase relation of a four-terminal Josephson junction, finding that it has a highly nontrivial dependence on the superconducting phase differences across its terminals, even appearing as a Josephson junction with a tunable superconducting phase offset. It is tempting to view these measurements as arising due to the hybridization of different bound states localized between different junction terminals, however we find that these results and the results of related experimental works can be modeled simply by considering a network of two-terminal Josephson junctions.

Finally, in **Chapter 7** we summarize the experimental results of this thesis, and describe potential experiments in which the advantages of microwave measurement techniques could further be put to good use in hybrid semiconducting-superconducting experiments.

Separate data repositories for each subsequent chapter of this thesis are available on Zenodo and referred to within each chapter, except for Chapters 2 and 7 which have a combined repository available in Ref. [16]. Every repository contains code necessary to generate all figures and fits from raw experimental and simulation data, as well as the code necessary to run any simulations (the only exception being the charge stability simulations of Chapter 4 which are described in that chapter's supplemental sections).



# 2

## THEORY

*I'm going to try to see if I can remember as much to make it sound like I'm smart on the subject.*

George W. Bush

### 2.1. CONFINED SYSTEMS OF QUASIPARTICLES OR CHARGE

The field of mesoscopic physics primarily explores the quantum nature of electrons and photons in solid materials<sup>1</sup>, achievable by lowering the system's temperature  $T$  such that  $k_B T$  is much less than the characteristic energy scales of the quantum electronic system, where  $k_B$  is Boltzmann's constant. Such discrete electronic states and bands can be formed through electrostatic confinement of electrons, by condensing them into a superfluid through superconductivity [19], or by the application of strong magnetic fields to reach the quantum Hall regime [6]. This section discusses the first two mechanisms, which in this thesis enable us to study the hybridization of individual fermionic states, aided by radio-frequency reflectometry and DC transport measurements.

#### 2.1.1. CLASSICAL CHARGE ISLANDS AND QUANTUM DOTS

##### CLASSICAL ISLANDS

To begin, we describe the technique by which we can control and study individual electrons in mesoscopic circuits: electrostatic confinement<sup>2</sup>. Any piece of conducting material or 'island' has some self-capacitance  $C_{\text{self}}$  arising from Coulomb repulsion of charges inside the finitely-sized material, and some capacitance  $C_e$  to the environment, leading to a total capacitance  $C_{\Sigma} = C_{\text{self}} + C_e$ . A circuit with such a charge island is depicted in

---

<sup>1</sup>Researchers also actively explore the quantum mechanics of phonons – quantized vibrations of the crystal lattice – through studies of nanomechanical resonators [17] and quantum thermodynamics [18].

<sup>2</sup>Reviews of the physics discussed in the next two sections can be found in Refs. [6, 20–23]

Fig. 2.1(a) connected via tunnel barriers to two leads. Placing  $N$  electrons on this island then has an energy cost of  $U_{\text{el}}(N) = e^2 N^2 / 2C_{\Sigma}$ , corresponding to the energy stored in the capacitor  $C_{\Sigma}$ . To add an electron, there is a chemical potential cost of

$$\mu(N) \equiv U_{\text{el}}(N) - U_{\text{el}}(N-1) = e^2(1-2N)/2C_{\Sigma} \quad (2.1)$$

to accommodate for Coulomb repulsion [6]. A charge reservoir at Fermi level<sup>3</sup>  $\mu_{\text{F}}$  can only add another electron on the island after the energy has been shifted so  $\mu(N) < \mu_{\text{F}}$ , at which point the ground state charge increases from  $N-1$  to  $N$ . The fixed distance between these successive transitions motivates defining the *charging energy*  $E_{\text{C}} \equiv e^2/(2C_{\Sigma})$ . This is half the spacing between consecutive charge resonances<sup>4</sup>  $\Delta\mu(N) \equiv \mu(N) - \mu(N-1)$ , which itself is more generally called the *addition energy*.

Remarkably, we have found discrete energies separate charge states in small capacitors. As a consequence, we can add or remove individual electrons by controlling the Fermi level of a coupled reservoir or through electrostatic gating, as we describe below. So far, we have also treated the capacitances coupled to this island as grounded, but if a ‘gate’ electrode at voltage  $V_{\text{g}}$  capacitively couples to the island with  $C_{\text{g}}$ , it induces an opposing charge  $C_{\text{g}}V_{\text{g}}$  on the island’s side of the capacitor, so the island energy becomes

$$U_{\text{el}}(N) = E_{\text{C}}(N - n_{\text{g}})^2, \quad (2.2)$$

where  $n_{\text{g}} \equiv C_{\text{g}}V_{\text{g}}/|e|$  is the *reduced gate voltage*. These energies are plotted in black in Fig. 2.1(b). In this way, we can tune the chemical potential  $\mu(N) = E_{\text{C}}(N - n_{\text{g}} - 1/2)$  to change the ground charge state of the island. As illustrated with the chemical potential diagrams of Fig. 2.1(c), the island can support a current when  $\mu(N)$  is within the chemical potential ‘bias window’ due to an applied voltage  $V_{\text{bias}}$  across the island near the Fermi level. In fact, the most common characterization tool for islands is to measure *Coulomb diamonds*—a map of DC conductance<sup>5</sup> as a function of  $V_{\text{g}}$  and  $V_{\text{bias}}$  [21]. A schematic of such a measurement is shown in Fig. 2.1(d). Due to the aforementioned condition of  $\mu$  residing within the bias window for current to flow, the island forms diamond-shaped regions where its charge is stably fixed. This state of fixed charge is known as *Coulomb blockade*. Outside these diamonds, current may flow across the island (shown as gray). The slopes of the diamond edges are determined by capacitances  $C_{\text{s}}$  and  $C_{\text{d}}$  to the source and drain contacts, as well as whether  $V_{\text{bias}}$  is applied symmetrically about the charge island or with the drain grounded [23]. In Fig. 2.1(d), the case of  $C_{\text{s}} = C_{\text{d}} = 0$  and a grounded drain is plotted. From the expression for  $\mu(N)$  we see that the degree to which  $V_{\text{g}}$  tunes the chemical potential is quantified by the *lever arm*  $\alpha \equiv C_{\text{g}}/C_{\Sigma}$ , which can be extracted from Coulomb diamond measurements as the ratio of the full width of a diamond in  $V_{\text{g}}$  to its half height in  $V_{\text{bias}}$ .

Interestingly, nothing about the above reasoning has invoked quantum mechanics. Indeed, charge islands can be completely classical: while the energy separation in the

<sup>3</sup>As a reference point, we hereon take  $\mu_{\text{F}} = 0$  since all microscopic models considered in this thesis are only valid near the Fermi energy.

<sup>4</sup>Note that by convention,  $E_{\text{C}}$  is often defined as  $e^2/C_{\Sigma}$  instead [20–23], but examples of the  $e^2/(2C_{\Sigma})$  definition’s usage are similarly common (see Refs. [11, 24, 25] among many other examples).

<sup>5</sup>RF conductance or RF gate sensing measurements can also probe Coulomb diamonds, as will be introduced later in this thesis and measured in Chapters 3 and 5 respectively.

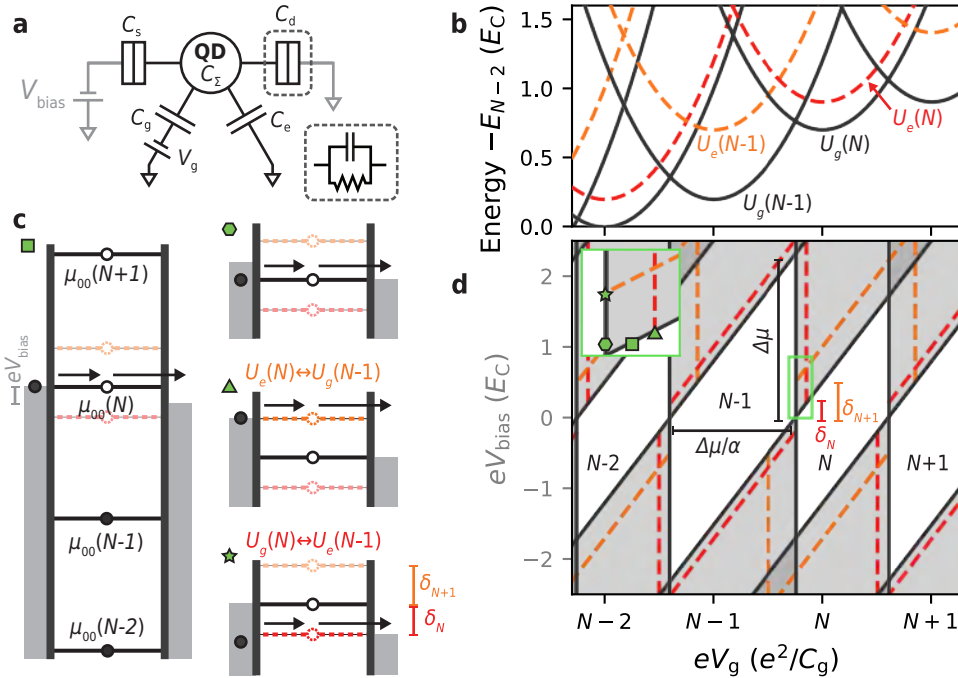


Figure 2.1: **(a)** Circuit model of a charge island or QD. The inset defines a commonly used symbol for tunnel barriers modeled by a parallel  $RC$  circuit [22]. **(b)** Energy spectrum of a QD. Here, we chose  $\delta_n$  alternating between  $\delta_a = 0.2E_C$  (red excitations) and  $\delta_b = 0.5E_C$  (orange excitations) and only show the first excited state for each charge state. **(c)** Chemical potential diagram of the QD at different conductance resonances. Conductance is only possible when  $\mu_{00}(N)$  is within the bias window formed by  $V_{\text{bias}}$  across the source and drain. Excited states introduce an additional conducting path when they enter the bias window, provided the ground state transition  $\mu_{00}(N)$  is also in the bias window [23]. **(d)** ‘Coulomb diamond’ stability diagram of charge and tunneling processes a finite  $V_{\text{bias}}$ , assuming  $C_s = C_d = 0$ . Blockaded regions with a stable QD charge are white and form diamond shapes, while conducting regions are shown in gray. The onset of resonant tunneling processes between charge ground states (dark gray) appear in measurements as a spike in conductance. From these diagrams,  $\alpha$  can be extracted as the ratio of a diamond’s half height in  $V_{\text{bias}}$  to its full width in  $V_g$ , while excitation energies can be read from the  $V_{\text{bias}}$  value at which excited state transitions appear (dashed lines). *Inset*: Zoomed plot at the window indicated by the green rectangle. Green markers correspond to the resonances indicated in **(c)**.

Fock space between states involving a different charge on the island is of the order  $E_C$ , the Hilbert space of states for fixed  $N \gg 1$  may be an arbitrarily large and completely incoherent system. This is the case for an island made out of a small piece of metal, for example [26]. Such classical charge islands are often called Single-Electron Transistors or SETs [12, 27].

### QUANTUM DOTS

Let us now consider the quantum limit of the charge island: *quantum dots* (QDs). For mesoscopic islands at cryogenic temperatures in general,  $\mu(N) = U_{\text{el}}(N) - U_{\text{el}}(N-1) + E_N - E_{N-1}$  where  $E_N$  is the ground state energy of the Hilbert space with  $N$  charges on the island in excess of  $U_{\text{el}}$ . When  $E_N - E_{N-1}$  is large compared to  $k_B T$ , the island be-

comes a quantum mechanical system or QD with a clear ground state  $|N\rangle$  for each dot charge. In this case we refer to the resulting spacing between charge-state transitions as the addition energy, since it contains both  $E_C$  and  $E_N$  terms. We then treat the dot as having the low-energy Hamiltonian  $\hat{H} = E_C (\hat{N} - n_g)^2 + \sum_n E_n |n\rangle \langle n|$ , where the total charge  $\hat{N} = \sum_n n |n\rangle \langle n|$  is now an operator. Even now, however, because the energy scale  $E_C$  associated with electron-electron interactions is typically much larger than the excitation energy  $E_N - E_{N-1}$  arising from quantum confinement of the system's electrons, it is feasible that the energy spectrum of the  $N$ -electron Hilbert space is completely uncorrelated with the  $(N \pm 1)$ -electron spectra [28]. Nonetheless, it is very often the case that the QD spectrum behaves as though each added electron sequentially fills independent single-electron states [29–32], as we will observe in the measurements of Fig. 5.4.

When this behavior is observed, we may describe the dot with fermionic creation operators  $\hat{c}_{j,\sigma}^\dagger$  indexed by quantum number  $j$  and spin  $\sigma \in \{\downarrow, \uparrow\}$ . Though not obviously true, one can accurately assume Coulomb repulsion forms a separate term in the Hamiltonian from some single-particle energies  $\delta_{j,\sigma}$  [33], giving

$$\hat{H} = E_C (\hat{N} - n_g)^2 + \sum_{j,\sigma} \delta_{j,\sigma} \hat{c}_{j,\sigma}^\dagger \hat{c}_{j,\sigma}, \quad (2.3)$$

with eigenenergies  $U = U_{\text{el}}(N)$  plus  $N$  energies  $\delta_{j,\sigma}$  for the occupied levels. By these assumptions we have that  $\hat{N} = \sum_{j,\sigma} \hat{c}_{j,\sigma}^\dagger \hat{c}_{j,\sigma}$  and  $E_N$  is the sum over the  $N$  smallest  $\delta_{j,\sigma}$  values. Because  $E_C$  is typically the largest energy scale compared to all  $\delta_{j,\sigma}$ , charge is still a good quantum number. In other words, only the  $\hat{c}_{j,\sigma}$  with  $\delta_{j,\sigma}$  very close to the  $N$ 'th lowest energy  $\delta_{j,\sigma}$  for a QD of charge  $N$  need to be considered at low energies. Consequently, QDs form mesoscopic systems where individual fermionic states can be studied, as is the focus of Chapter 5.

For semiconductor QDs with many electrons, the situation can be somewhere in between this noninteracting fermion case and one where individual  $\hat{c}_{j,\sigma}$  levels are not possible to define [32]. Ranges of Coulomb transitions may show correlated addition energies and others could show lesser correlation or none at all. For the large ring-shaped QD measured in Fig. 5.2 for example, we observe a consistently finite excitation energy in the QD but only partial correlation between successive Coulomb resonance positions. Importantly, neither observing a finite excitation energy nor a Zeeman splitting of energies with applied magnetic field in a QD definitively proves the system states are well-described by spinful single-particle states, though it strongly suggests this is the case.

Aside from granting the system a well-defined quantum ground state, the above-mentioned fermionic levels have measurable signatures at higher energies. The lowest two energies are given by  $U_g(N) \equiv U_{\text{el}}(N) + \sum_{j=0}^N \delta_N$  and  $U_e(N) \equiv U_g(N) + \delta_{N+1}$  if we suppress the spin index and assume all fermionic levels are nondegenerate. In this case, for the ground state we have  $\Delta\mu(N) = U_{\text{el}}(N) - U_{\text{el}}(N-1) + \delta_N$ . The excitation energy  $U_e(N) - U_g(N)$  is measurable as alternations in Coulomb diamond sizes in experiment (see Fig. 2.1(d)). Additionally, many tunneling pathways produce additional conductance resonance lines at finite bias (orange and red lines in Fig. 2.1) [23, 34]. Chemical potential diagrams for the transitions  $U_e(N) \leftrightarrow U_g(N-1)$  and  $U_g(N) \leftrightarrow U_e(N-1)$  are shown in Fig. 2.1(c) to illustrate this process, but care must be taken: Even if the excited process' chemical potential  $U_e(N) - U_g(N-1)$  or  $U_g(N) - U_e(N-1)$  is within the bias

window, transport via this pathway cannot occur if the bias window doesn't include the  $U_g(N) \leftrightarrow U_g(N-1)$  transition as well. Some excited state transitions may be less prominent if the lead reservoirs cannot directly inject electrons into the excited state [23, 34]. If any discrete states exist in the contacts near the QD, for example in the gap in a nanowire QD between the QD and deposited metal contacts, these states can also appear in diamond measurements and are easily mistaken for excited states of the QD [35, 36]. A clue that resonant lines correspond to lead states, however, is that they have a different slope than the Coulomb diamond resonances, indicating that  $V_g$  has a different capacitance to those states.

### MULTI-DOT SYSTEMS

Since QDs can be viewed as artificial atoms with discrete fermionic 'orbitals' [21], multiple QDs connected together hold interest as artificial molecules [22], particularly as a platform where quantum hybridization between discrete states can be controlled and studied. In a system with multiple charge islands, we must also consider Coulomb repulsion of charges on different islands. We consider  $M$  islands with cross-capacitances  $c_{ij} = c_{ji}$  for  $i \neq j$  and total capacitances  $C_{\Sigma i}$  summed over all  $c_{ij}$ , the gate capacitance  $C_{gi}$  of the island, and its remaining stray capacitance to the environment  $C_{ei}$ . A circuit diagram for the case of a double quantum dot (DQD) in series with two leads is shown in Fig. 2.2(a). The electrostatic charging energy of this system in the charge state  $\vec{N} = (N_1, N_2, \dots, N_M)$  and with reduced gate voltages  $\vec{n}_g = (n_{g1}, n_{g1}, \dots, n_{gM})$  is

$$U_{\text{el}}(\vec{N}) = \frac{e^2}{2} (\vec{N} - \vec{n}_g) \cdot [\mathbf{C}^{-1}(\vec{N} - \vec{n}_g)] \quad (2.4)$$

where  $\mathbf{C}$  is the capacitance matrix of the system<sup>6</sup>. It has off-diagonal elements  $C_{ij} = -c_{ij}$  and diagonal elements  $C_{ii} = C_{\Sigma i}$ . This energy still contains the single-dot energies  $\propto (N_i - n_{gi})^2$ , but now also contains 'mutual' charging terms, resulting from the Coulomb repulsion of electrons across different QDs. These terms are characterized by a mutual charging energy  $E_{mij} = e^2 c_{ij}^{-1} (C_{\Sigma i} C_{\Sigma j} / c_{ij}^2 - 1)^{-1}$  and contribute  $E_{mij} (N_i - n_{gi})(N_j - n_{gj})$  to the energy [22]. Importantly, there are now different chemical potentials for each QD. Considering a DQD for example, one has  $\mu_1(N_1, N_2) \equiv U(N_1, N_2) - U(N_1 - 1, N_2)$  and  $\mu_2(N_1, N_2) \equiv U(N_1, N_2) - U(N_1, N_2 - 1)$  where  $U$  includes  $U_{\text{el}}$  and the individual QD level spacings.

By measuring zero-bias conductance through the multi-dot system or reflectometry from the dots' gates (discussed in Sec. 2.2) as a function of different gate voltages, we can measure the resulting charge stability diagram (CSD) of stable charge ground states. As an example, we show the CSD for a DQD in Fig. 2.2(b). Stable charge states are separated by gray lines when a charge must be exchanged with an external lead, while blue lines show interdot transitions where a charge is exchanged between the QDs. If the lever arms  $\alpha_i \equiv C_{gi} / C_{\Sigma i}$  of the gates are known, the system's charging energies and other energy scales such as tunnel couplings can be inferred from CSD measurements, as labeled in the figure. Lever arms can be extracted from Coulomb diamond measurements as de-

<sup>6</sup>Despite appearing to be a natural extension of the single-dot formula in eq. 2.2, the derivation of this expression is nontrivial. It is given in Ref. [22] and more rigorously in Ref. [37].

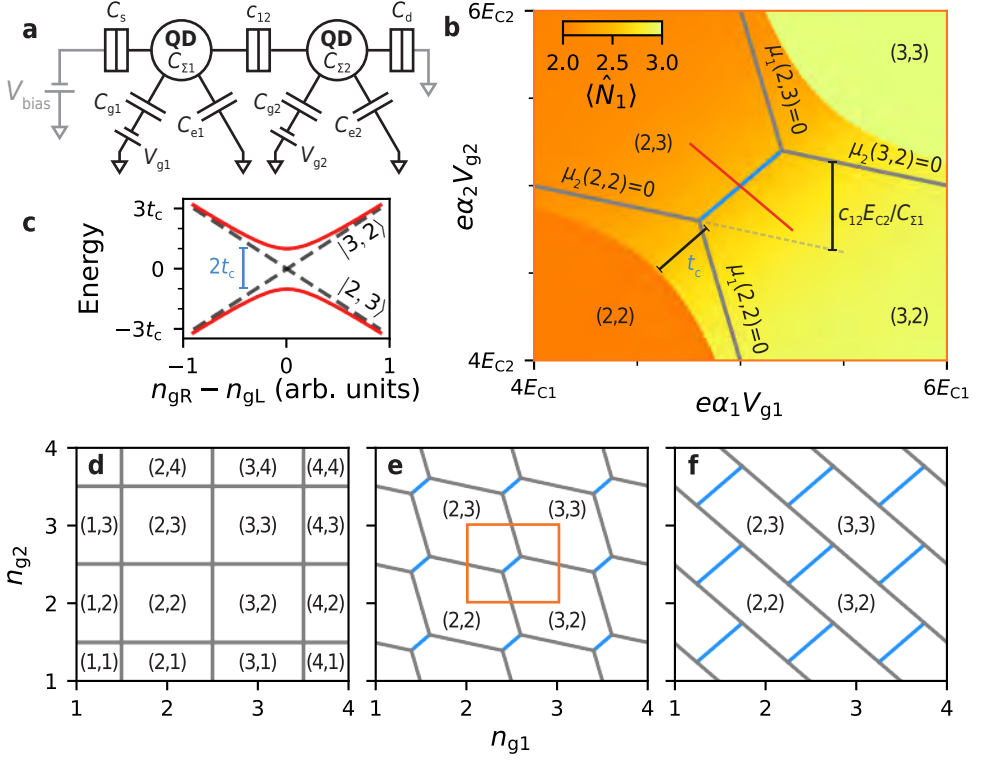


Figure 2.2: Double quantum dots. **(a)** Circuit model of a DQD with charging energies  $E_{Cj} = e^2/(2C_{\Sigma j})$  for  $j \in \{1,2\}$ . **(b)** CSD showing the ground charge state in the absence of tunnel couplings (solid lines) near an interdot charge transition (blue line) with  $E_{m12} = 0.5E_{C1} = 0.5E_{C2}$ . The expectation value of charge on the left QD is also plotted for an interdot tunnel amplitude  $t_c = 0.3E_{C1}$ . **(c)** Energy spectrum of a DQD near the interdot charge transition along the red line in **(b)**. **(d-f)** Zoomed out CSDs in the absence of interdot coupling for  $E_{m12} = 0$  **(d)**,  $0.5E_{C1}$  **(e)**, and  $2E_{C1}$  **(f)**. The system continuously evolves from two independent QDs **(d)** to a strongly capacitively coupled DQD **(f)** described by a single charging energy with its chemical potential tuned by both QD gates. All CSDs are labeled with the charge ground states  $(N_1, N_2)$  in each Coulomb blocked region up to some arbitrary offset. Figure is based on Refs. [22, 38].

scribed in Sec. 2.1.1, but  $c_{ij}$  will change as the system is tuned from a single dot into a multidot system, affecting  $\alpha_i$ .

Given  $\alpha_1$  and  $\alpha_2$ , we now discuss how the system energy scales manifest in the CSD. In the absence of tunnel coupling, interdot transitions only have a finite length (labeled in Fig. 2.2(b)) in the CSD when  $c_{12} \neq 0$ . In Figs. 2.2(d-f), we illustrate this by plotting CSDs for  $c_{12}$  values ranging from 0 to encompassing the entire dot capacitances  $C_{\Sigma, j}$ . The intersections between the interdot and lead transitions are known as triple points because each nearest dot level is resonant with each other and the lead reservoirs, enabling zero-bias conductance [22]. We see that the size of interdot charge transitions increases with increasing  $c_{12}$ , and grants the stable charge regions a hexagonal shape for modest  $c_{12}$  values indicative of DQD behavior. For very large  $c_{12}$ , the lead transitions of the two dots appear as though they are a single QD sharing one charging energy, even if

the two QDs cannot actually directly exchange charge with each other but only with the lead reservoirs [39].

Now if we include a quantum tunnel coupling  $t_c$  hybridizing, for example, the ground states  $|2,3\rangle$  and  $|3,2\rangle$  of each charge configuration, the interdot transition broadens in a hyperbolic shape, shown by a plot of the expectation value of charge on dot 1 in Fig. 2.2 (b). From the distance between the hyperbolic lead transitions and the triple points,  $t_c$  can be extracted as illustrated in the figure [22]. Near the interdot transition, the DQD forms bonding and antibonding states separated by an energy gap  $2t_c$  [40] which enable its usage as a semiconducting charge qubit [41–43], albeit with coherence times severely limited by charge noise. The corresponding energy spectrum is shown in Fig. 2.2(c).

Outside of this DQD example, we remark that CSDs of systems with more than two dots quickly become complicated to interpret in any two-dimensional measurement [44]. Nonetheless, floating triple and quadruple QD systems isolated from lead reservoirs are investigated in Chapter 4 of this thesis.

### 2.1.2. CONFINEMENT BY SUPERCONDUCTIVITY: ANDREEV BOUND STATES

We move on to consider what happens if we construct charge islands out of superconducting materials, or strongly couple semiconducting regions to a superconductor. We will find that localized states can appear bound not by electrostatic confinement, but also by boundaries with a superconductor. Further, we will see that properties of superconductors – such as their excitations being superpositions of electrons and holes – directly compete with the Coulomb repulsion in charge islands, since the latter distinguishes between positive and negative charge.

Superconductivity is an electronic phase characterized by a vanishing electrical resistance and an expulsion of all magnetic fields from the material in the form of the Meissner effect [19]. Many conventional superconductors such as Al or NbTiN are well described by Bardeen-Cooper-Schrieffer (BCS) theory, wherein electrons form bound pairs of opposite spin and momenta known as *Cooper pairs* due to an effective attraction between them mediated by electron-phonon interactions [45]. Considering  $\hat{c}_{\mathbf{k},\sigma}^\dagger$  as the creation operator for an electron of wave vector  $\mathbf{k}$  and spin  $\sigma \in \{\downarrow, \uparrow\}$ , this interaction leads to terms in the Hamiltonian of the form  $\hat{c}_{\mathbf{k},\uparrow}^\dagger \hat{c}_{-\mathbf{k},\downarrow}^\dagger \hat{c}_{\mathbf{k}',\uparrow} \hat{c}_{-\mathbf{k}',\downarrow}$ , making it difficult to diagonalize exactly. In the mean field approximation where fluctuations of Cooper pair occupations  $\hat{c}_{\mathbf{k},\uparrow} \hat{c}_{-\mathbf{k},\downarrow}$  about the mean value  $\langle \hat{c}_{\mathbf{k},\uparrow}^\dagger \hat{c}_{-\mathbf{k},\downarrow}^\dagger \rangle$  are small, the system can be solved. This is at the expense of removing the Hamiltonian's charge conservation, however, as the approximate Hamiltonian then contains terms of the form  $\Delta \hat{c}_{\mathbf{k},\uparrow}^\dagger \hat{c}_{-\mathbf{k},\downarrow}^\dagger$ . The parameter  $\Delta$  is known as the superconducting pairing potential.

The system's ground state  $|g\rangle$  under this approximation is a condensate of Cooper pairs: The pairing potential makes it more favorable for electrons to exist in Cooper pairs than on their own, opening an energetic gap to any single particle excitations. Injecting an electron or hole into the system requires an energy of at least  $|\Delta|$  to reach the possible excitation energies  $E_{\mathbf{k}} = \sqrt{\varepsilon_{\mathbf{k}}^2 + |\Delta|^2}$ , so  $|\Delta|$  is referred to as the *superconducting gap*. The density of states in this system is

$$v_{\text{SC}}(E) = \frac{|E|}{\sqrt{E^2 - |\Delta|^2}} v_{\text{N}} \quad (2.5)$$

where  $\nu_N$  is the system's density of states in the absence of superconductivity, which we plot in Fig. 2.3(a). The added electron or hole brings the system to a state  $\hat{\gamma}_{\mathbf{k},\sigma}^\dagger |g\rangle$  at energy  $E_{\mathbf{k}}$  above the ground state  $|g\rangle$  where  $\{\hat{\gamma}_{\mathbf{k},\sigma}\}$  are fermionic operators given by

$$\hat{\gamma}_{\mathbf{k},\sigma} = u_{\mathbf{k}} \hat{c}_{\mathbf{k},\sigma} - \sigma v_{\mathbf{k}} \hat{d}_{-\mathbf{k},\bar{\sigma}}^\dagger e^{-i\hat{\phi}} \quad (2.6)$$

with electron- and hole-like *coherence factors* satisfying

$$|u_{\mathbf{k}}|^2 = \frac{1}{2} - \frac{\epsilon_{\mathbf{k}}}{2\sqrt{\epsilon_{\mathbf{k}}^2 + |\Delta|^2}}, \quad |v_{\mathbf{k}}|^2 = \frac{1}{2} + \frac{\epsilon_{\mathbf{k}}}{2\sqrt{\epsilon_{\mathbf{k}}^2 + |\Delta|^2}}, \quad u_{\mathbf{k}}^* v_{\mathbf{k}} = -\frac{\Delta}{2\sqrt{\epsilon_{\mathbf{k}}^2 + |\Delta|^2}}. \quad (2.7)$$

Above,  $\sigma = +1$  for  $\sigma = \uparrow$  and  $-1$  for  $\sigma = \downarrow$ , while  $e^{-i\hat{\phi}}$  removes a Cooper pair from the superconducting condensate. These  $\hat{\gamma}_{\mathbf{k},\sigma}$  excitations obey fermionic anticommutation rules and in that sense are like particles. Because they are described as a superposition of an electron and a hole added to the condensate rather than a single real particle, however, they are referred to as *quasiparticles*, in this case *Bogoliubons* specifically.

In the spectrum of Fig. 2.3(a) where all states below the Fermi level are filled, a natural question arises: Where are the Cooper pairs in this picture? In terms of the electron vacuum state  $|0\rangle$ , the superconducting ground state is equal to  $|g\rangle = \prod_{\mathbf{k}} (u_{\mathbf{k}} + v_{\mathbf{k}} \hat{c}_{\mathbf{k}\uparrow}^\dagger \hat{c}_{-\mathbf{k}\downarrow}^\dagger) |0\rangle$ . This is a superposition of the presence or absence of Cooper pairs—the Cooper pair condensate described above. It turns out, however, that  $|g\rangle = \prod_{\mathbf{k}} \hat{\gamma}_{\mathbf{k}\downarrow}^\dagger |0_\gamma\rangle$  where we identify the negative-energy ‘excitation’ operator  $\hat{\gamma}_{\mathbf{k}\downarrow}^\dagger \equiv \hat{\gamma}_{\mathbf{k}\uparrow}$  and  $|0_\gamma\rangle$  is the vacuum state of the Bogoliubons in the  $\{\hat{\gamma}_{\mathbf{k}\uparrow}, \hat{\gamma}_{\mathbf{k}\downarrow}\}$  quasiparticle basis [46]. The state  $|0_\gamma\rangle$  has an energy  $\sum_{\mathbf{k}} E_{\mathbf{k}}$  above the ground state energy. In this sense, we can view  $|g\rangle$  equivalently as the Bogoliubon vacuum with all negative energy excitations filled. This picture shows that the superconducting condensate is described by the single-particle excitation spectrum rather than being something independent. Relative to  $|g\rangle$ , on the other hand, applying any of the original Bogoliubon operators  $\hat{\gamma}_{\mathbf{k}\sigma}^\dagger$  raises the system's energy by  $E_{\mathbf{k}}$ . Thusly we can view an excitation of the condensate as adding a positive-energy electron above the gap or removing a negative energy electron below the gap: in either case breaking the corresponding  $\mathbf{k}$ -vector's Cooper pair.

Finally, we are prepared to discuss how superconductivity can lead to bound quasiparticle states. Consider an interface between a normal conducting material and a superconducting one. Electrons and holes impinging on the superconductor at energies below  $|\Delta|$  and above  $-|\Delta|$  respectively cannot enter ordinarily due to the excitation gap. If an electron enters the superconductor at positive energy  $E$  while a hole leaves the superconductor at energy  $-E$ , however, energy is conserved and the superconductor can remain in its ground state while gaining a Cooper pair. This process is called *Andreev reflection*. Of course the reverse process can occur for current to flow in the opposite direction.

It is interesting to take this principle a step further and consider a normal conducting region confined either electrostatically or by a superconductor on all sides. Introducing superconductivity into a system, we find it is not only simple electrostatic fields that can confine charge into bound states. Boundaries between normal conducting and superconducting regions can form potential barriers in the form of the superconducting pairing potential  $\Delta(\mathbf{x})$ , which switches from  $\Delta(\mathbf{x}) = 0$  inside the normal region to  $\Delta(\mathbf{x}) = \Delta$  for

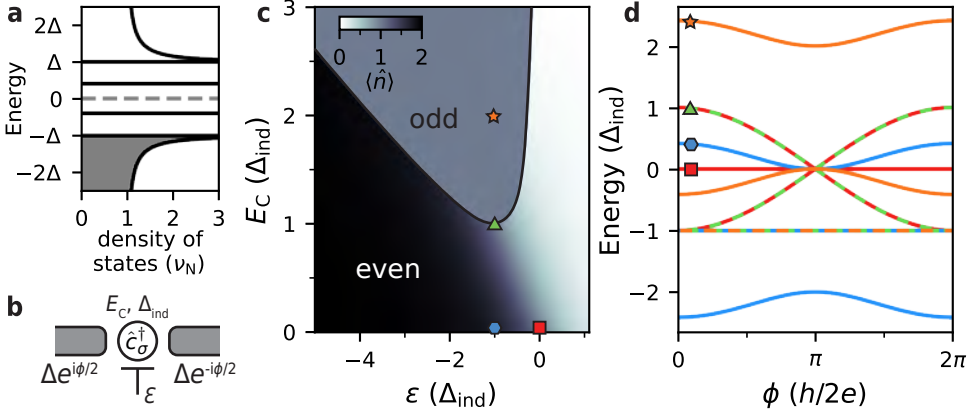


Figure 2.3: Superconductivity, and the connection between Yu-Shiba-Rusinov and Andreev bound superconducting states. **(a)** Density of states in a bulk superconductor according to eq. 2.5 along with a discrete subgap state. **(b)** Schematic of a single electron level  $\hat{c}_\sigma^\dagger$  coupled to superconducting leads with a superconducting phase difference of  $\phi$  applied across them. The electron level has chemical potential  $\varepsilon$ , may have charging energy  $E_C$ , and has a superconducting pairing potential  $\Delta_{\text{ind}}$  induced by the leads. **(c)** Phase diagram of the system. For  $E_C < \Delta_{\text{ind}}$ , the ground state has even parity—consisting of a varying superposition of the level containing zero electrons or a pair. At higher  $E_C$ , a region of fixed odd parity forms (outlined by a black line). **(d)** Energy spectra of the system at the markers indicated in **(c)** as a function of  $\phi$ .

$\mathbf{x}$  in the superconductor. Outside the normal region, the system has a superconducting gap, and ordinary electrons and holes with energies below  $\Delta$  cannot enter except by Andreev reflection. Particles also reflect ordinarily from any electrostatic confining boundary, so overall a bound state is expected to form. Because the resulting state consists of superpositions of reflected holes and electrons, it has a superconducting character and is referred to as an *Andreev bound state* (ABS) [46, 47]. In particular, the bound state has an energy gapped above the Fermi level but below  $\Delta$  by an amount depending on the microscopic characteristics of the system.

To illustrate this and investigate superconducting pairing's competition with electrostatic confinement, we consider a single electronic level  $\hat{c}_\sigma^\dagger$  where  $\sigma \in \{\uparrow, \downarrow\}$  with some coupling to two superconducting terminals. We plot a schematic of the system in Fig. 2.3 **(b)**. These terminals have a phase difference of  $\phi$  in their superconducting wave functions, applied for example by forming them into a loop and threading a magnetic flux [19]. The dot itself may have charging energy  $E_C \geq 0$  and level energy  $\varepsilon_\sigma$ . In the 'atomic limit' where the leads' superconducting gap is taken  $|\Delta| \rightarrow \infty$ , the leads induce an effective pairing term  $\hat{H}_p \equiv -\Delta_{\text{ind}} \cos(\phi/2) e^{i\phi/2} \hat{c}_1^\dagger \hat{c}_1^\dagger + \text{h.c.}$  for some induced gap  $\Delta_{\text{ind}}$  [48].  $\Delta_{\text{ind}}$  is a function of the tunnel coupling between the level and leads. At zero magnetic field,  $\varepsilon_\sigma = \varepsilon$  and the dot may be described by the Hamiltonian  $\hat{H} = \hat{H}_p + \varepsilon \sum_\sigma \hat{n}_\sigma + 2E_C \hat{n}_\uparrow \hat{n}_\downarrow$ . Note the latter two terms are equivalent to eq. 2.3 up to a constant offset. Diagonalizing the system, we plot the expected charge  $\langle \hat{n} \rangle$  of the electron level in Fig. 2.3 **(c)**. For  $E_C < \Delta_{\text{ind}}$ , the system ground state has fixed even parity and consists of a superposition of zero charge on the level and two charges. The state in this region is localized on the dot solely by superconductivity (though admittedly that was done *a priori* in this exam-

ple by assuming the existence of  $\hat{c}_\sigma^\dagger$ ) and so is referred to as an ABS. On the other hand, when  $E_C > \Delta$  a region in parameter space with an odd-parity ground state forms, but this region is narrower as a function of  $\epsilon$  than if there were no superconducting pairing. From the example energy spectra plotted in Fig. 2.3(d), we see that the odd-parity ground states are unaffected by  $\phi$ . In this latter case, excitation energies may be thought of as a spinful electron in the level being screened by a quasiparticle in the superconductors, accordingly lowering the excitation energy [49]. Usually, the excitations in this case are referred to as *Yu-Shiba-Rusinov* (YSR) states for historic reasons relating to models of impurities embedded in superconductors [49–52]. As the superconducting states are traced out by taking the  $|\Delta| \rightarrow \infty$  limit, this spin-screening effect is not captured in our model, though it does reveal the competition between superconducting pairing and charging energy, which defines the boundary between the YSR and ABS scenarios.

In this thesis, subgap excitations in superconductors are formed by coating a semi-conducting region epitaxially with a superconducting shell, such as in excitations of the superconducting island of Chapter 4 or the ABSs mediating supercurrent in Chapter 6. Due to varying degrees of electrostatic confinement and coupling to the superconductor which is not necessarily fully transparent, the resulting subgap excitations in the *hybrid* semi- and superconducting system are always determined by a combination of charging and pairing effects. The former effect is what leads to gate-voltage-dependent subgap state spectra in hybrid systems [53], but in literature these states are broadly referred to as ABSs [54, 55].

### 2.1.3. SUPERCONDUCTING ISLANDS

A superconducting island (SCI) is simply a charge island made up of a piece of superconducting material either on its own, or collectively forming a hybrid island with a small semiconducting region strongly coupled to the superconductor, see Fig. 2.4(a). The result is a charge island modified by an energy cost associated with containing an odd number of charges due to the superconducting excitation gap. The former case is the basis of many early experiments on SCIs [56–58] and superconducting qubits like superconducting charge qubits and transmons, where a piece of superconductor is connected to reservoirs by a Josephson junction and has a weak charging energy shunted by a capacitance to ground [5, 24]. Meanwhile, the latter hybrid situation has also been widely explored [59–72], principally with the motivation of seeking Majorana bound states [10, 11, 73–78] or for engineering hybrid qubits based on ABSs [25, 79]. By coupling a semiconducting material to a superconductor, the material properties of the semiconductor (such as spin-orbit coupling, large  $g$ -factors, and gate tunability) are combined with superconducting pairing via the proximity effect [47, 80–83]. It has been shown that in such a system formed in a one-dimensional nanowire with extremely low disorder, topologically-protected Majorana bound states can appear at the ends of the wire since it effectively forms a Kitaev chain [7, 8, 84]. Moreover, prominent qubit proposals exploiting these protected states form a Coulomb-blockaded island out of the system [10, 11], granting it protection from quasiparticle poisoning [85]. Additionally, hybrid SCIs can be chained together as a metamaterial to effectively form a Kitaev chain [86–88]. These and other applications have driven the wealth of research into SCIs over the last two decades, and motivated the experiments of this thesis.

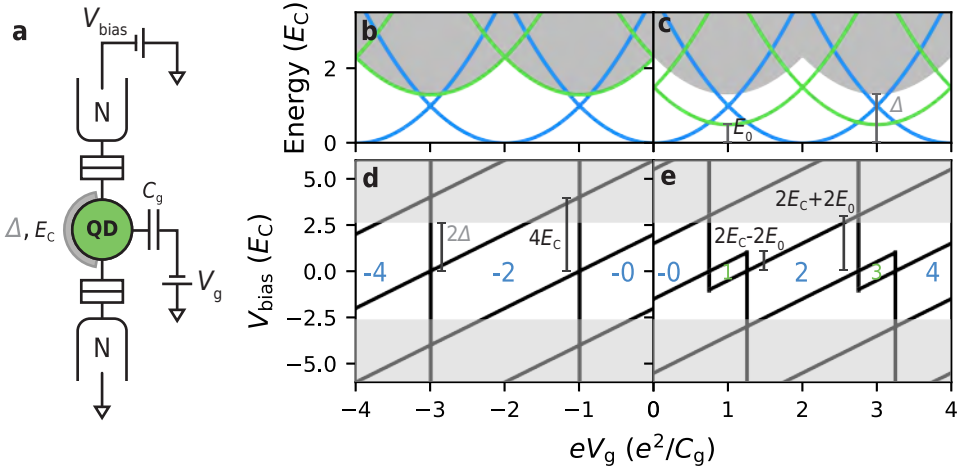


Figure 2.4: Characterization of superconducting islands. **(a)** Schematic of a hybrid SCI of charging energy  $E_C$  connected via tunnel barriers to lead reservoirs. A floating superconducting material (gray) of gap  $\Delta = 1.3E_C$  proximitizes a semiconducting QD (green), potentially inducing subgap states at energies below  $\Delta$ . In this case, we consider a single subgap state at energy  $E_0$ . **(b-c)** Energy spectrum for different charge states in the island with  $E_0 = \Delta$  **(b)** and  $E_0 = 0.5E_C$  **(c)**. Even-parity ground states are shown in blue while odd-parity ground states are in green. Notably, odd-parity charge states have a minimum energy  $E_0$  higher than any even-parity state. **(d-e)** Coulomb diamond schematics for the  $E_0$  values in **(b-c)**, with only ground-state Coulomb resonances depicted, and with source and drain capacitances neglected. For biases larger than  $2\Delta$  (grayed regions), cotunneling via the superconducting shell's quasiparticle states may occur, enabling non-zero conductance even in Coulomb blockade [89].

Unfortunately, modeling SCIs presents an obvious difficulty: the BCS Hamiltonian describing a superconductor under mean-field theory does not conserve particle number [19], while a charging energy on the superconductor pressures particle number into being a good quantum number. Solving a superconductor's Hamiltonian without applying the mean-field approximation is difficult, but can be done for example with numerical renormalization group methods [90]. Thankfully, to understand the behavior of SCIs, in many cases it is sufficient to simply ignore this contradiction. Small-size effects are not expected to appear in SCIs until their size decreases enough such that the single-particle level spacing exceeds the superconducting gap [91] — a limit which is not easily reached [92] — so projecting the system onto states where quasiparticle parity matches the charge parity is often sufficient [73, 74] (see also Appendix F).

If a SCI is weakly coupled to other QDs or leads and we are indifferent to spin effects, we can then simulate the charge stability of the system using the ground state energies

$$U_{\text{SCI}}(N) = U_{\text{el}}(N) + E_0 \frac{1 + (-1)^N}{2}, \quad (2.8)$$

simply imposing a free energy cost  $E_0$  of the superconducting gap on states with an odd number of charges [57, 76, 89]. Here,  $E_0$  is the lowest energy quasiparticle excitation energy, and could be less than  $\Delta$  if subgap states are present. Aside from spin-splitting effects on the island's quasiparticle states and effects of the superconductor proximitizing

neighboring QDs, this toy model is sufficient to calculate the CSD of a system consisting of normal and superconducting QDs. More generally, one can model a SCI by adding the charging energy term to the Hamiltonian for the superconductor. Most notably, nonzero  $E_0$  results in two distinct regimes of behavior of a SCI: that for charging energy  $E_C < E_0$  and that for  $E_C > E_0$ , see Fig. 2.4(b),(c).

In the former case, single-electron or ‘1e’ transport is suppressed in favor of Cooper pairs tunneling on and off the island (notable exceptions include floating systems, see Sec. 2.1.4). The relevant chemical potential determining the locations of transitions is thus  $U_{\text{SCI}}(N) - U_{\text{SCI}}(N-2)$ , adding two electrons to the system. As the chemical potential in the source contact  $eV_{\text{bias}}$  is the energy available to supply a *single* electron, the condition for conductance resonance with the source is now  $2eV_{\text{bias}} = U_{\text{SCI}}(N) - U_{\text{SCI}}(N-2)$ . Hence, the height of Coulomb diamonds can be found to be  $4E_C$ , in contradiction with Refs. [62, 93] which claim it is  $8E_C$ . As we will see from the case  $E_0 < E_C$ , the latter would lead to an unphysical discontinuous jump in the diamond size as  $E_0$  is lowered. The resulting expected Coulomb diamonds are plotted in Fig. 2.4(d). The fact that  $E_0 > E_C$  can be inferred by observing a splitting of Coulomb resonances as the gap is suppressed below  $E_C$ , or a transition from  $2e$ - to  $1e$ -periodic Coulomb resonances as a bias voltage across the island  $|eV_{\text{bias}}|$  is increased above  $2E_0$  [58]. In the figure, we only show the positions of ground state Coulomb resonances in black and mark the region of  $|eV_{\text{bias}}| > 2\Delta$  in gray rather than showing the precise location of excited-state Coulomb oscillations. What can be said with certainty, however, is that above biases of  $2E_0$  the lead reservoirs may supply quasiparticles to maintain the island in a state consistently ‘poisoned’ with quasiparticles. For  $|eV_{\text{bias}}| > 2E_0$  the Coulomb oscillations therefore must be  $1e$ -periodic outside of the Coulomb diamonds. This allows one to read off  $E_0$  from such measurements, in fact. Inference of  $\Delta$  itself is made possible by noting that above  $\Delta$ , many states become available for second-order tunneling processes across the island (see Sec. 2.1.5), greatly increasing the amplitude of cotunneling currents [94]. Often then,  $2\Delta$  can be identified as the  $eV_{\text{bias}}$  at the onset of horizontal cotunneling lines in the Coulomb diamonds [60, 62, 69, 89].

In the second case where  $E_C > E_0$  on the other hand, single-electron tunneling occurs at Coulomb resonances. Notably though, because of the  $E_0$  cost of having odd numbers of electrons, the regions in parameter space consisting of a stable odd charge are smaller than those with an even charge. This is evident from the chemical potential differences  $\mu(N) - \mu(N-1) = 2E_C - 2E_0$  and  $\mu(N+1) - \mu(N) = 2E_C + 2E_0$  for even  $N$ . Hence, both  $E_0$  and  $E_C$  can be read out from Coulomb diamond measurements in this regime, as is illustrated in Fig. 2.4(e). Finally, note that as  $E_0 \rightarrow 0$ , we recover the conventional  $1e$ -periodic Coulomb oscillations of a metallic charge island or QD.

#### 2.1.4. ELECTRICALLY FLOATING DOT SYSTEMS

In discussions of QD systems up to this point, we have assumed that the system’s total charge can freely vary. In this case, given that the dots’ charging energies are large energy scales compared to  $k_B T$ , the system always resides in states near in energy to its ground charge state. Isolating or *floating* a multi-QD system from all leads fixes its total charge, on the other hand, forcing it to remain in an excited subspace of charge states satisfying charge conservation. Without leads, one must resort to RF measurement methods (see

Sec. 2.2) or charge sensing techniques to probe the system, so why impose this additional constraint?

For one, broadened lead transitions in CSDs can overlap with and conceal details of more interesting charge-conserving tunneling processes within the multidot system. Additionally, interdot transitions in floating systems are not interrupted by lead transitions and therefore occupy larger regions in gate space, facilitating their investigation. For example, one can measure successive interdot transitions in a floating double QD or SCI system (schematized in Fig. 2.5(a)) by simply sweeping one of the QD's gate voltages instead of measuring a two-dimensional CSD [64, 67, 95]. There, we consider an island with charging energy  $E_{C2}$  smaller than its lowest subgap excitation  $E_0$ , and a QD of charging energy  $E_{C1} > E_0$ . The general principle behind this is that without lead reservoirs, there is no chemical potential serving as a reference for the QD energies, removing one charge degree of freedom. Hence, for an  $N$ -dot floating system, only  $N - 1$  gates need be swept to navigate the full space of allowed charge states. This is evident in the CSD shown for a floating QD-island system in Fig. 2.5(d), which only contains diagonal lines. To visualize how a nonfloating QD-island evolves into this picture, one must imagine that all transitions disappear from the CSD except for the interdot transitions conserving the now-fixed total charge. These transitions extend across gate space since there are no others to interrupt them. As another example, the CSD of a floating triple QD (depicted in Fig. 2.5(b)) is shown in Fig. 2.5(c). There, we see that interdot transitions between any pair of dots can be reached by tuning only two of the three QDs' gate voltages. From both of these CSD examples, we also observe that increasing a reduced gate voltage  $C_{gi} V_{gi} / |e|$  by one no longer necessarily increases a semiconducting QD's charge by one. This is because without lead reservoirs, adding charges to a QD requires adding the energy required to increase its charge *and* the energy required to remove charge from another QD.

A second interesting property of floating hybrid systems is that fixing their charge can reveal tunneling processes which were not energetically accessible in equilibrium otherwise. Returning to the example of a QD-island: at zero bias voltage and weak tunnel couplings the SCI with charging energy  $E_{C2} < E_0$  exchanges charges two at a time as Cooper pairs with any other dots or leads. Meanwhile, if we remove the leads from this system and keep only the island tunnel coupled to the QD of substantial charging energy  $E_{C1} > E_0$ , *only* interdot charge transitions can occur. In this case, the energy cost of two electrons tunneling is always at least  $2E_{C1} + 2E_{C2} - 2E_0$  as both dots' charging energies must be paid for a charge transition to occur. We show the CSD and energy spectrum of such a system in Figs. 2.5(d) and 2.5(e) respectively. The latter illustrates how higher and higher energy charge states become the system's ground state as gate voltages deviate from the analogous nonfloating system's ground state. By making the system floating, we may therefore probe quasiparticle states and single-electron tunneling at equilibrium even in a SCI with a vanishing charging energy [64, 67]. Though not featured in this thesis, we thusly tuned multidot systems into floating QD-QD or QD-island systems as a technique for characterizing the devices pertaining to the projects of Chapters 3 and 4 [37, 38].

As a final example, we consider the case of Cooper pair splitters: devices which use charging energies of separated QDs to force a Cooper pair's constituent electrons to

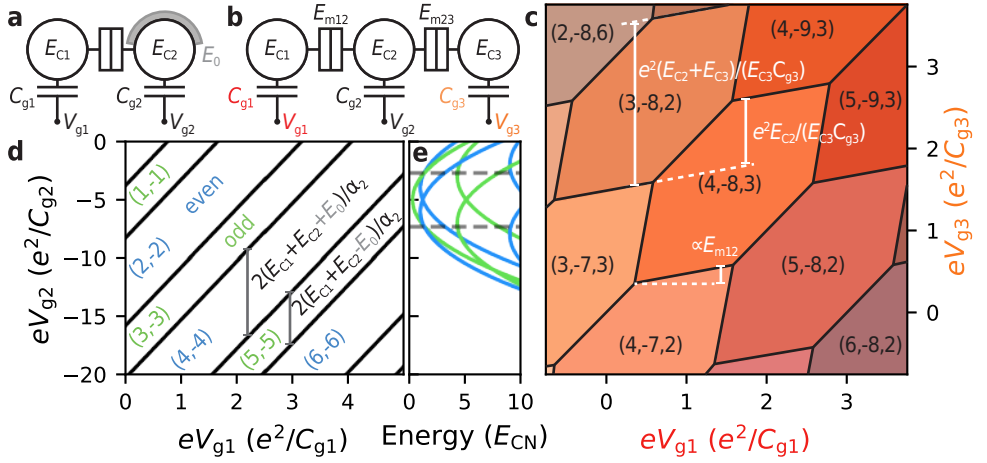


Figure 2.5: Floating systems of quantum dots. **(a)** Schematic of a floating system consisting of a semiconducting QD of charging energy  $E_{C1}$  coupled to a SCI with lowest subgap excitation energy  $E_0$  and charging energy  $E_{C2}$ . **(b)** Schematic of a floating triple QD. **(c)** CSD of the floating triple QD system depicted in **(b)**, with  $E_{C1} = E_{C2} = E_{C3}$  and  $E_{m12} = E_{m23} = 0.3E_{C1}$  and with tunnel couplings and quantum level spacings neglected. Charge states are labeled as  $(N_1, N_2, N_3)$  up to some arbitrary charge offset. **(d)** CSD of the floating QD-island system depicted in **(a)**, using  $E_{C2} = 0.2E_{C1}$ ,  $E_0 = 0.3E_{C1}$ , and neglecting mutual capacitances. Charge states are labeled as  $(N_1, N_2)$  up to an arbitrary even offset with  $N_2 = 0$  corresponding to some even charge on the island. Regions of odd parity are narrower in gate space due to their additional minimum energy cost of  $E_0$ . **(e)** State energies for the QD-island system depicted in **(a)** with  $C_{g1} V_{g1} / |e| = 5$ . Energies increase rapidly as gate voltages deviate from the values at which their charge state in a nonfloating system would equal the floating system's total charge. The system exhibits  $1e$  charge transitions even though  $E_{C2} < E_0$  because the energy of transferring an electron is at least  $2(E_{C1} + E_{C2})$  in a floating DQD.

'split' into separate locations [96], see Chapter 4 for further discussion. Fixing the QD chemical potentials at the Fermi level of their metallic leads, only single electrons can flow from the superconducting lead unless it is biased by at least its superconducting gap  $\Delta$ . This is because the QD charging energies  $E_C$  imply there is a cost of at least  $E_C$  for two excess electrons to enter this QD simultaneously, inhibiting entire Cooper pairs from tunneling. If the two QDs are placed within the superconducting coherence length of each other, there is a possibility for *crossed Andreev reflection* (CAR) to occur, however. In this process, the spin-entangled electrons from a Cooper pair coherently split and tunnel into separate QDs [96]. As long as the QDs have the same chemical potential and are within the bias window, this can occur at any finite bias voltage of the superconducting lead. In this manner Cooper pair splitting has been demonstrated in numerous material systems, including InAs nanowires [97–101], carbon nanotubes [102–104], graphene [105–107], two-dimensional electron gases [108], and others [109]. A disadvantage of this approach is that individual Cooper pairs are not retained on the QDs but quickly tunnel into the metallic drain reservoirs, making tests of their coherence or entanglement difficult. But what happens if we remove the metallic leads, essentially rendering the system 'half-floating'? In this case electrons cannot escape from the QDs upon entry, and tuning the superconductor's chemical potential between  $\mu > 0$  and  $\mu < 0$  tunes the system between a Cooper pair being split onto the dots or recombined into the superconduc-

tor, respectively. The Cooper pair's electrons now stably reside on the QDs and could be tested for spin entanglement by checking for violations of the Bell inequality, as has been done in spin qubit platforms [110]. In Chapter 4, we similarly split Cooper pairs in the case where the system is fully floating with the superconducting lead replaced by a SCI. We also consider the applicability of such a floating hybrid triple QD as a basis for forming dot-based Kitaev chains in Chapter 7. More generally, half-floating a system by pinching off all leads except for one makes the remaining lead's bias voltage behave as a gate voltage for all dots with a lever arm of one. Accordingly, lever arms of QDs can be extracted from the slope of measurements of bias against QD gate voltages in such systems.

### 2.1.5. SECOND-ORDER TUNNELING PROCESSES

Second-order tunneling processes occur when two quantum states that do not have a wave function overlap are indirectly coupled via some intermediate states. As a generic example, consider arbitrary states  $|a\rangle$  and  $|b\rangle$  coupled to a central mediating manifold of  $N \geq 1$  states detuned in energy, say  $|v_j\rangle$  with quantum number  $j \in \{0, 1, \dots, N-1\}$ . The system may then tunnel from  $|a\rangle$  to  $|b\rangle$  via the states' mutual wave function overlaps with  $|v_j\rangle$ , schematically depicted in Fig. 2.6(a). Second-order tunneling or *cotunneling* processes are fundamental to the functionality of hybrid quantum technologies, and unavoidable in any system using more than two QDs [111]. In hybrid systems, CAR is essential to the formation of Majorana bound states in QD-based Kitaev chains [86–88]. It is a cotunneling process where a superconductor having an excess Cooper pair or two normal regions around it containing a pair of excess electrons take the place of  $|a\rangle$  and  $|b\rangle$ , while states with a quasiparticle in the superconductor take the place of  $|v_j\rangle$ . We observe coherent CAR and compare it to the cotunneling formalism described below in Sec. 4.7.4. As another example, charging-energy-protected Majorana qubits can measure the qubit state from the effective tunneling amplitude between two QDs, constituted partially from cotunneling via the fermionic mode formed by two Majorana states as  $|v_j\rangle$  [10, 11]. Given the importance of second-order tunneling processes, we discuss more precisely how they arise in this subsection.

To be concrete, let us consider the generic Hamiltonian

$$\hat{H} = \underbrace{\frac{\varepsilon}{2} (|a\rangle\langle a| - |b\rangle\langle b|)}_{\equiv \hat{H}_0} + \underbrace{\sum_j E_j |v_j\rangle\langle v_j| + \sum_{j,\alpha} (t_{\alpha j} |v_j\rangle\langle \alpha| + \text{h.c.})}_{\equiv \hat{V}}, \quad (2.9)$$

where  $\varepsilon$  is a small detuning between  $|a\rangle$  and  $|b\rangle$ ,  $t_{\alpha j}$  for  $\alpha \in \{a, b\}$  are weak tunnel couplings to the virtual states which need not be the same, and the mediating state energies  $E_j > E_0$  for some  $E_0 \gg \varepsilon, t_{\alpha j}$ . Essentially, the states  $|v_j\rangle$  are energetically inaccessible, but are still relevant as the only states coupled to the more energetically favorable states  $|a\rangle$  and  $|b\rangle$ .

Under these assumptions, we aim to project the system onto its low energy subspace, which will consist of the states  $|a\rangle$  and  $|b\rangle$  'dressed' by some occupation of  $|v_j\rangle$  states and with an effective cotunneling amplitude between them. To do so, we apply a unitary Schrieffer-Wolff transformation  $e^{\hat{S}} \hat{H} e^{-\hat{S}}$  to the Hamiltonian [112], using the transforma-

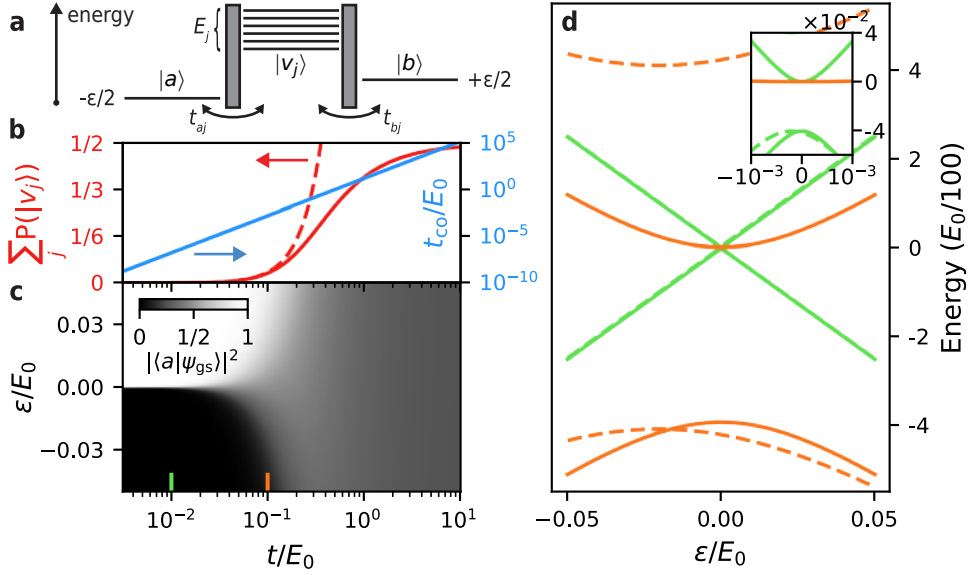


Figure 2.6: Limits of the cotunneling approximation's validity. **(a)** Schematic of the generic system: states  $|a\rangle$  and  $|b\rangle$  detuned by  $\varepsilon$  are coupled indirectly via states  $\{|v_j\rangle\}_j$  at energies  $E_j \gg |\varepsilon|$  with tunnel couplings  $t_{\alpha j}$  for  $\alpha \in \{a, b\}$  such that  $|t_{\alpha j}| \ll E_j \forall j, k$ . **(b-d)** Simulations of this system for  $N = 2 |v_j\rangle$  states of equal energy  $E_0$ , with all tunnel couplings set equal to  $t$ . **(b)** Total wave function overlap of the ground state  $|\psi_{\text{gs}}\rangle$  with the mediating states  $|v_j\rangle$  in the full Hamiltonian (solid red) and the low-energy Hamiltonian of eq. 2.16 (dashed). For comparison, the effective coupling between  $|a\rangle$  and  $|b\rangle$  is plotted in blue. **(c)** Wave function overlap of  $|\psi_{\text{gs}}\rangle$  with  $|a\rangle$  as a function of  $\varepsilon$  and  $t$ , showing how the transition broadens due to hybridization between  $|a\rangle$  and  $\{|v_j\rangle\}_j$  with increasing coupling. **(d)** Low-energy spectra of the system at the two linecuts indicated in **(c)** in the full Hamiltonian (solid lines) and in the low-energy Hamiltonian of eq. 2.16 (dashed lines). *Inset:* Zoomed view of the center of the plot. The low-energy Hamiltonian drastically diverges from the true spectrum even for  $t = 0.1E_0$  (orange).

tion matrix  $\hat{S}$  defined as

$$\hat{S} = \sum_{j,\alpha} \left( \frac{t_{\alpha j}^*}{E_j} |\alpha\rangle \langle v_j| - \frac{t_{\alpha j}}{E_j} |v_j\rangle \langle \alpha| \right). \quad (2.10)$$

Note the property  $\hat{S}^\dagger = -\hat{S}$  ensures  $e^{\hat{S}}$  is unitary. To calculate the transformed Hamiltonian, we make use of the Baker-Campbell-Hausdorff formula to expand the exponential and find

$$e^{\hat{S}} \hat{H} e^{-\hat{S}} = \hat{H} + [\hat{S}, \hat{H}] + \frac{1}{2} [\hat{S}, [\hat{S}, \hat{H}]] + \mathcal{O} \left( t_{\alpha j}^3 / E_j^3 + \varepsilon^3 / E_j^3 \right). \quad (2.11)$$

With this relation, the purpose of our choice of  $\hat{S}$  becomes clear. It satisfies  $[\hat{S}, \hat{H}_0] = -\hat{V} + \mathcal{O}(\varepsilon t_{\alpha j} / E_j^2)$ , such that

$$e^{\hat{S}} \hat{H} e^{-\hat{S}} = \hat{H}_0 + \frac{1}{2} [\hat{S}, \hat{V}] + \mathcal{O} \left( t_{\alpha j}^3 / E_j^3 + \varepsilon t_{\alpha j} / E_j^2 \right). \quad (2.12)$$

To second order in the small energy parameters we may calculate the commutator and

explicitly write the Hamiltonian as

$$e^{\hat{S}} \hat{H} e^{-\hat{S}} \sim \frac{\varepsilon'}{2} (|a'\rangle \langle a'| - |b'\rangle \langle b'|) + t_{\text{co}} |b'\rangle \langle a'| + t_{\text{co}}^* |a'\rangle \langle b'| \\ + \sum_j E_j' |v_j'\rangle \langle v_j'| + \sum_{j \neq k, \alpha} t_{\alpha j} t_{\alpha k}^* \left( \frac{1}{E_j} + \frac{1}{E_k} \right) |v_j'\rangle \langle v_k'| + \text{h.c.} \quad (2.13)$$

up to a constant offset, where  $\varepsilon' \equiv \varepsilon + \sum_{\alpha, j} |t_{\alpha j}|^2 / (2E_j)$ ,  $E_j' \equiv E_j + (|t_{\alpha j}|^2 + |t_{b_j}^2) / E_j + \sum_{k, \alpha} |t_{\alpha k}^2 / (2E_k)$ , and

$$t_{\text{co}} \equiv - \sum_j \frac{2t_{\alpha j} t_{b_j}^*}{E_j} \quad (2.14)$$

Crucially, the Hamiltonian is now in a transformed basis given by

$$|\alpha'\rangle \equiv e^{\hat{S}} |\alpha\rangle = \left( 1 - \sum_j \frac{|t_{\alpha j}|^2}{2E_j^2} \right) |\alpha\rangle - \sum_j \frac{t_{\alpha j}}{E_j} |v_j\rangle - \sum_j \frac{t_{\bar{\alpha} j} t_{\alpha j}^*}{2E_j^2} |\bar{\alpha}\rangle + \mathcal{O}(t_{\alpha j}^3 / E_j^3) \\ |v_j'\rangle \equiv e^{\hat{S}} |v_j\rangle = \left( 1 - \frac{|t_{\alpha j}|^2 + |t_{b_j}|^2}{2E_j^2} \right) |v_j\rangle + \sum_{\alpha} \frac{t_{\alpha j}^*}{E_j} |\alpha\rangle - \sum_{k \neq j, \alpha} \left( \frac{t_{\alpha j} t_{\alpha k}^*}{2E_j E_k} \right) |v_k\rangle + \mathcal{O}(t_{\alpha j}^3 / E_j^3), \quad (2.15)$$

calculated from the series expression for  $e^{\hat{S}}$ . As written above, the states are orthogonal to second order in  $t_{\alpha j}$  and  $\varepsilon$ .

The Hamiltonian is now also in two decoupled blocks, one for the  $\{|a'\rangle, |b'\rangle\}$  states and one for the  $\{|v_j'\rangle\}_j$  states. At low energies, we then only need to consider the Hamiltonian block of the  $|a'\rangle$  and  $|b'\rangle$  states, since the eigenvalues of the  $|v_j'\rangle$  block are of the same order of magnitude as  $E_j$ , while those of the  $\{|a'\rangle, |b'\rangle\}$  block are of the order  $\varepsilon' \ll E_j$ . We therefore have

$$e^{\hat{S}} \hat{H} e^{-\hat{S}} \sim \frac{\varepsilon'}{2} (|a'\rangle \langle a'| - |b'\rangle \langle b'|) + t_{\text{co}} |b'\rangle \langle a'| + t_{\text{co}}^* |a'\rangle \langle b'|. \quad (\text{low energies}) \quad (2.16)$$

Hence, for weak tunnel couplings the system is naturally described in the basis of our original states  $|a\rangle, |b\rangle \rightarrow |a'\rangle, |b'\rangle$  dressed by some occupation of the mediating states, and effectively coupled to each other via  $t_{\text{co}}$ . In practice, eq. 2.16 is implicitly applied in dot-based Kitaev chain models to describe both elastic electron cotunneling (ECT) and CAR [87], is used to describe ECT in semiconducting QD systems [111], and we consider the applicability of this formalism to a floating hybrid triple QD in Sec. 4.7.4.

We assess the range of validity of the low-energy model of eq. 2.16 in Fig. 2.6. Considering the case of  $N = 2$  with  $E_1 = E_0$  and setting all  $t_{\alpha j} = t$  for some coupling  $t$ , we plot the wave function overlap of the system ground state with the mediating states  $|v_j\rangle$  (red lines) as well as the effective cotunneling amplitude between  $|a\rangle$  and  $|b\rangle$  in Fig. 2.6(b) (blue line)<sup>7</sup>. As is evident from eqs. 2.15 and 2.16, both  $t_{\text{co}}$  and the wave function overlap with  $\{v_j\}_j$  increase quadratically with  $t$ .

<sup>7</sup>The case  $N = 2$  is often the minimum number of states involved in cotunneling, since electron tunneling processes via a middle Bogoliubon or QD usually have at least one nearby electron-like or hole-like tunneling path [111].

With this in mind, we emphasize the main point of this section: it is at best misleading and at worst incorrect to refer to  $|v_j\rangle$  as a ‘virtual’ state mediating cotunneling as is done pervasively in literature [6, 93, 111, 113, 114]. The effective coupling  $t_{\text{co}}$  is only nonzero insofar as the system’s low energy states involve wave function overlap with the ‘virtual’ states, which is of the order of  $|t_{\text{co}}|/E_j$ . Additionally, we remark that by the point where  $t_{\text{co}}$  (plotted in blue) is a few percent of the mediating state energy  $E_j$ , the cotunneling approximation already significantly diverges from the full Hamiltonian’s solution. In Figs. 2.6(c) and 2.6(d) we emphasize this further, by showing the broadening of the  $|a\rangle \rightarrow |b\rangle$  transition (see Fig. 2.6(c)) and the low-energy spectrum for two small values of tunnel couplings in Fig. 2.6(d). Even for tunnel couplings 10% as large as the  $E_j$  energies,  $t_{\text{co}}$  is an ill-defined measure of the effective coupling between  $|a\rangle$  and  $|b\rangle$ . Since the true eigenstates involve substantial wave function overlap with the  $|v_j\rangle$  states, there is no obvious way to define a single energy scale describing an effective hybridization between  $|a\rangle$  and  $|b\rangle$  for such  $t_{aj}$  values. It may seem apt to refer to cotunneling as occurring via ‘virtual’ states since these states are classically inaccessible in energy, but it is crucial to remember that higher-order tunneling processes may only occur so long as there is a real wave function overlap of the eigenstates with these mediating states [115].

## 2.2. PROBING QUANTUM CIRCUITS WITH MICROWAVE RESONATORS

To measure properties of quantum systems as fast as possible and avoid  $1/f$  noise ubiquitous in quantum circuits, it is desirable to probe quantum systems at high frequencies  $f$  in the microwave range<sup>8</sup> [12]. When doing so, one typically scatters a microwave tone from the device of interest (*e.g.* from a gate or lead), measuring its complex reflection coefficient  $\Gamma$  with a vector network analyzer or other readout electronics<sup>9</sup>, defined as the ratio of reflected to incident voltage. Portions of the signal reflected in-phase or out-of-phase with the incident photons form the real and complex parts of  $\Gamma$  [116]. Unfortunately, stray capacitances shunt the microwave signal to ground, meaning conventional DC measurement lines are impractical for this purpose. By using a transmission line such as a coaxial cable where inductances and capacitances are tuned to form a waveguide for microwave photons, however, this obstacle can be overcome. The characteristic impedance of most coaxial lines is a standard  $Z_0 = 50\Omega$ , making  $\Gamma = (Z - Z_0)/(Z + Z_0)$  for a device impedance of  $Z$  [116], with example circuits depicted in Figs. 2.7(a,c). Here we encounter another issue however: semiconducting quantum devices are typically characterized by large resistances and small capacitances [13], making  $|Z| \gg Z_0$ . In this limit  $|\Gamma| \rightarrow 1$  becomes insensitive to changes in  $Z$ , making the measurement useless. We show

<sup>8</sup>For too large of a frequency, the resulting energy scale  $hf$  approaches the energy scales of the system, making driving effects and circuit quantum electrodynamics (cQED) important [5]. We avoid this regime as much as possible throughout this dissertation, though we encounter it in Ch. 4.

<sup>9</sup>Other devices capable of measuring high frequency complex scattering parameters include ultra or super high frequency lockin amplifiers or electronics tailor-made for measuring qubits such as the Qblox QRM module, Quantum Machines OPX, Zurich Instruments UHFQA, and Intermodulation Products Presto. All of these devices boil down to a combination of digital-to-analog converters generating the RF signals, mixers used to reach desired frequencies, filters, and analog-to-digital converters to read the returning signals, which can be built out of individual components by the experimenter as well. Note that *scalar* network analyzers are phase-insensitive and can only measure  $|\Gamma|$ .

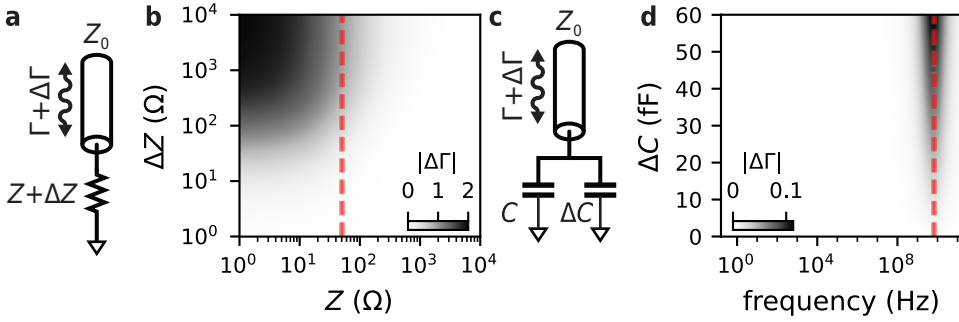


Figure 2.7: Impedance matching reflectometry circuits. **(a)** A minimal circuit measuring the reflected RF signal  $\Gamma(Z)$  from a resistive impedance  $Z$  into a transmission line of characteristic impedance  $Z_0 = 50\Omega$ , shifted by a change in impedance  $\Delta Z$ . **(b)** Absolute difference in RF signal change  $\Delta\Gamma \equiv \Gamma(Z + \Delta Z) - \Gamma(Z)$  for different bare impedances  $Z$  and impedance shifts  $\Delta Z$ .  $Z_0$  is plotted as a dashed red line. When  $Z \lesssim Z_0$ , a change in impedance can be resolved in  $|\Delta\Gamma|$ , while for  $Z \gg Z_0$ , the reflected signal is insensitive to  $\Delta Z$ . **(c)** A minimal circuit measuring the reflected signal from a bare capacitance  $C$  shifted by a change in capacitance  $\Delta C$ . **(d)** Absolute change in  $\Gamma$  for the circuit in **(c)** with or without  $\Delta C$ , using a bare capacitance  $C = 0.5$  pF. The measurement frequency  $f$  at which  $|1/(2\pi i f C)| = Z_0$  is shown as a red dashed line. This frequency aligns with the maximal possible signal, indicating the importance of impedance matching. The range of  $\Delta C$  shown corresponds to charge islands of charging energies ranging from  $e^2/(2\Delta C) \approx 1$   $\mu$ eV upwards.

the expected reflected signal change from a real impedance  $Z$  changing by  $\Delta Z > 0$  in Fig. 2.7(b). Similarly, coupling a coaxial line via bonding wires to a device chip where one expects to measure a capacitance (see Fig. 2.7(c)), there is generally an unavoidable parasitic capacitance of at least  $C = 0.1$  pF to ground [13]. Measuring a superimposed change of capacitance  $\Delta C$ , we plot the absolute change in  $\Gamma$  expected for the impedance  $1/(2\pi i f(C + \Delta C))$  for different probe frequencies  $f$  in Fig. 2.7(d). Choosing  $f$  to create a capacitive impedance matching  $Z_0$  maximizes the signal, but one is restricted to measure near this frequency, and even in this case the optimal signal is nowhere near the maximum possible  $|\Delta\Gamma| = 2$ . Due to this requirement of  $Z \lesssim Z_0$  in both cases, we say that it is desirable to *match the impedance* of  $Z$  to the readout circuit.

Here is where resonators come in. A circuit resonates at frequencies where all of its reactive components – capacitors and inductors that is – have an impedance which cancels out to zero. At angular frequency  $\omega = 2\pi f$ , the impedance of a capacitance  $C$  is  $-i/\omega C$  and that of an inductance  $L$  is  $i\omega L$ . A system of an inductor and capacitor forms a simple harmonic oscillator, with the charged capacitor plate forcing current to increase or decrease, resisted by the inductor. Since the former impedance has a negative imaginary part and diverges at small  $\omega$  while the latter's imaginary part diverges to  $+\infty$  as  $\omega \rightarrow \infty$ , these resonances will always exist if the circuit isn't damped by excessive dissipation [116]. Due to their impedance's high sensitivity to  $L$  and  $C$  near a resonance, they form a simple impedance transformer.

By embedding our device of impedance  $Z$  in such an  $LC$  circuit, the impedance of the entire circuit becomes strongly sensitive to changes in  $Z$  near resonance frequencies. For the circuit depicted in Fig. 2.8(a) with internal losses modeled by a resistance  $R$  (not

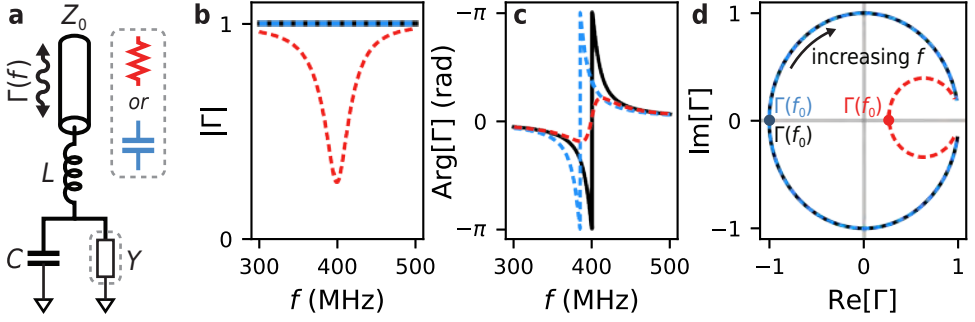


Figure 2.8: Reflectometry response of a loaded resonator circuit. **(a)** A minimal reflectometry circuit formed by an inductance  $L$  in series with a parallel capacitance  $C$  and admittance  $Y$ , which in this example is either a resistance or capacitance. **(b-d)** The resonator response near its bare resonance frequency  $f_0 \approx 400$  MHz given parameters  $L = 420$  nH and  $C = 0.377$  pF chosen based on Chapter 5. The response of the resonator is shown for  $Y = 0$  (black),  $Y = 2e^2/h$  (one conductance quantum, red), and  $Y = 2\pi i f \Delta C$  (blue) where  $\Delta C = 30$  fF is chosen very large compared to typical experimental values in order to exaggerate the resonance frequency shift it imparts on the resonator. We plot the reflected signal's amplitude **(b)**, phase **(c)**, and full complex response **(d)**.

pictured), the input impedance is

$$Z_{\text{res}} = i\omega L + R + \frac{1}{i\omega C + Y} \quad (2.17)$$

where  $Y \equiv 1/Z$  is the complex *admittance* of the device. For  $Y = 0$ , this circuit resonates at frequency  $f_0 = \omega_0/2\pi = 1/(2\pi\sqrt{LC})$ , and near resonance we have [116]

$$Z_{\text{res}} \sim R + 2iRQ \frac{\omega - \omega_0}{\omega_0} \quad |\omega - \omega_0| \ll \omega_0 \quad (\text{series circuit}) \quad (2.18)$$

which holds over all frequencies of interest, since the bandwidth in frequency space where the resonator responds is typically much narrower than its resonance frequency. Here,  $Q \equiv \omega_0 RC$  is the *quality factor* of the resonator circuit, roughly representing the number of cycles the resonator can oscillate over before a photon leaves or is dissipated from the circuit.

Now, suppose  $Y$  can be modeled as  $Y = G + i\omega\Delta C$ , that is, a resistor and capacitor in parallel. When  $GZ_0$  is very small, as is often the case for reflectometry across semi-conducting QDs and their gates, we can Taylor expand eq. 2.17 to find that eq. 2.18 holds with  $\omega_0 \rightarrow 1/\sqrt{L(C + \Delta C)}$  and  $Q \rightarrow \omega_0(R(C + \Delta C) + LG)$  to lowest order in  $G$ . By fitting a resonator's response to extract  $Q$  and  $\omega_0$  (see Appendix C), one can thus measure the impedance of a quantum circuit, a possibility we pursue further in Chapter 3. Resonators may also be formed from distributed elements like coplanar waveguides, but in Sec. 3.7.1 we show that a similar result holds for such resonators. To illustrate the effect of  $Y$  on the resonator response, we plot the reflected signal from a resonator for capacitive and dissipative  $Y$  and  $R = 0$  in Figs. 2.8(b-d). With no internal losses, the resonator forms a circle of unit radius in the complex  $\Gamma$  plane (see Fig. 2.8(d)), and a capacitive shift moves the resonance frequency without changing the resonator lineshape. As a result, the capacitive shift is only resolvable in  $\text{Arg}[\Gamma]$ , shown in Fig. 2.8(c). Real resonators with some

internal losses shrink the circle towards  $\Gamma = 1$ , giving it a characteristic dip in amplitude near the resonance. This effect, pictured in the red curve of Fig. 2.8(b), enables resolving changes in device conductance. A capacitive shift in the presence of internal losses is then also resolvable as a shift in this dip as well as a change in its depth, since  $Q$  depends on  $\omega_0$  when  $R \neq 0$ . To ensure no information is lost, it is best to consider the full complex  $\Gamma$  data when looking for a signal.

Notably, the lineshape of the resonator response can be alternatively viewed by comparing the loss rate of photons from the  $LC$  circuit into the readout line characterized by an *external* or *coupling* quality factor  $Q_c$ , to the loss rate of photons to the environment characterized by the *internal* quality factor  $Q_i$ . Expressions for these quantities depend on the specific resonator circuit [13, 116]. In this case, the total  $Q = 1/(Q_c^{-1} + Q_i^{-1})$ . In these terms, the resonator has a unit-radius lineshape in the complex plane when  $Q_i \gg Q_c$ . Conversely, when  $Q_c \gg Q_i$ , the resonator response shrinks to a point either due to excessive losses (low  $Q_i$ ) or from not enough photons being exchanged with the readout line (high  $Q_c$ ). For this reason we therefore call the resonator *undercoupled* or *overcoupled* when  $Q_i < Q_c$  or  $Q_i > Q_c$  respectively. When  $Q_i = Q_c$  the resonator amplitude dips precisely to 0 on resonance, and the resonator is *critically coupled*. For measuring small resistive or capacitive signals, the maximal signal often occurs for critically coupled resonators [13, 117], depending on the circuit.

These principles form the basis of radio frequency reflectometry techniques routinely applied in semiconducting quantum devices [13]. As described below, resonators are quantum harmonic oscillators whose excitations are photons, but for this dissertation's purposes we do not exploit this fact. Resonators serve only as tools for probing quantum circuits here. This begs the question: when can we safely neglect the quantum mechanical nature of our resonator and treat its electromagnetic fields classically, focusing on the device of interest?

### 2.2.1. RESONATORS IN THE QUANTUM AND SEMICLASSICAL LIMITS

Practical resonator circuits may consist of numerous capacitors and inductors, and may not even be lumped-element circuits. The speed of light in a medium can be a fraction of that in vacuum<sup>10</sup>, so for millimeter-scale resonator circuits operating at few-GHz frequencies the light wavelength can be comparable to the circuit size. As a result, the circuit elements are 'distributed' and the spatial dependence of voltages and currents must be considered. Nonetheless, for a given frequency (*e.g.* near a resonance) any circuit with only linear components can be written as an equivalent circuit with a single inductor  $L$ , capacitor  $C$ , and resistor  $R_r$  via Norton's and Thévenin's theorems [118]. Whether the resulting  $RLC$  circuit is in parallel or series configuration, its classical Hamiltonian is  $H_r = Q^2/2C + \Phi^2/2L$  where  $Q$  is the capacitor charge and  $\Phi = \int_{-\infty}^t V(t') dt'$  is the integral of the voltage across the inductor. In a superconducting circuit these variables can be promoted to canonical quantum variables  $\hat{Q}$  and  $\hat{\Phi}$  obeying the commutation relation  $[\hat{\Phi}, \hat{Q}] = i\hbar$  so that  $H_r \rightarrow \hat{H}_r$  becomes a quantum Hamiltonian [2]. As this Hamiltonian is of the form of a quantum harmonic oscillator, we can solve it by introducing the bosonic ladder operator  $\hat{a} \equiv i\hat{Q}/\sqrt{2C\hbar\omega_0} + \hat{\Phi}/\sqrt{2L\hbar\omega_0}$  with  $[\hat{a}^\dagger, \hat{a}] = 1$  and  $\omega_0 = 1/\sqrt{LC}$ . In terms of  $\hat{a}$  the Hamiltonian becomes  $\hat{H}_r = \hbar\omega_0(\hat{a}^\dagger \hat{a} + 1/2)$ . In other words, the  $RLC$  circuit hosts

<sup>10</sup>The speed of light in a typical coaxial cable is roughly  $2c/3$ , for example.

a single photonic mode with annihilation operator  $\hat{a}$  of energy  $\omega_0$ . Meanwhile, the resistor can be viewed as a coupling between the cavity photons and a thermal bosonic bath, inducing dissipation [119, 120].

2

This quantization of superconducting circuits is the basis for circuit quantum electrodynamics (cQED): the coupling of photons to quantum circuits. Aside from introducing microwave-frequency methods like two-tone spectroscopy for probing the energy spectrum and state of quantum circuits [121], this field is crucial for the formation and coupling of superconducting qubits [4, 5], and even semiconducting qubits [122]. Modeling resonators as quantum mechanical systems as in cQED is the approach usually taken when resonator frequencies approach the energy scales of the system – typically in the range of a few-GHz<sup>11</sup>.

Nonetheless, in this dissertation we mainly use microwave resonators as a probe for the quantum device of interest, and not for its own quantum behavior. Hence, it is relevant to consider when we can treat the resonator as a classical system of oscillating voltages and currents, instead of a photonic cavity. Following Ref. [123], we describe an expression for the response of the resonator including both parametric contributions and quantum interactions between the resonator and probed device. Counter to intuition, we find that these two contributions are additive, and both can simultaneously be relevant. As an example, we apply the theory to a charge qubit where an electron is tunnel-coupled between the states of two QDs.

Broadly, the argument is as follows: The Hamiltonian of the system is  $\hat{H} = \hat{H}_r + \hat{H}_d(x)$  where  $\hat{H}_d$  is the device's Hamiltonian with bare eigenstates  $\{|\psi_i\rangle\}_i$  at energies  $E_i$ . It is a function of some charge or flux variable  $x$ . The resonator couples to the device through quantum variations of  $x \rightarrow x_0 + \hat{x}_r$  related to photons in the resonator. For a resonator capacitively coupled to a device by capacitance  $C_g$ , we have  $\hat{x}_r = (C_g/C)\hat{Q}/e = i\lambda(\hat{a}^\dagger - \hat{a})$  where  $\lambda \equiv 2(C_g/C)\sqrt{\hbar/(2e^2\sqrt{L/C})}$ . Essentially,  $\hat{x}_r$  is the charge induced on the device-resonator capacitor by resonator photons in units of  $e$  while  $x_0$  is a DC charge offset [2, 123]. Galvanic coupling of the resonator to a semiconducting device inevitably involves incoherent tunneling into the device's leads and is ill-suited for this purely quantum description. Instead, the approaches of Section 2.2.2 should be employed. For capacitances between a gate electrode and a submicron-scale QD, we typically have  $C_g \ll C$  such that  $\lambda \ll 1$ . Accordingly, one may Taylor expand the Hamiltonian to second order in  $\lambda$ . The  $\hat{x}_r$ -dependent part of the Hamiltonian is the resonator-device coupling Hamiltonian, while the  $x_0$ -dependent part describes the bare device Hamiltonian. Additionally, we assume the resonator is in the *dispersive regime* where  $\hbar\omega_0 - |E_i - E_j|$  for any  $i, j$  is much larger than the energy scales of the coupling Hamiltonian  $\propto \lambda$ . In this way, we can neglect resonant excitations in the device induced by the resonator. Considering the resonator as containing  $n$  photons, from the second-order energy corrections in  $\lambda$  proportional to  $n$  we may finally read out the resonator frequency shift. When the device is

<sup>11</sup>The reason for this is one of convenience: It happens that many semiconducting and superconducting qubits are easily tuned such that their transition frequencies are in the range of a few to tens of GHz. On the other hand, it is convenient that standard SMA cables operate from DC to 18 GHz, as do a great deal of other useful microwave components such as amplifiers, circulators, and measurement electronics.

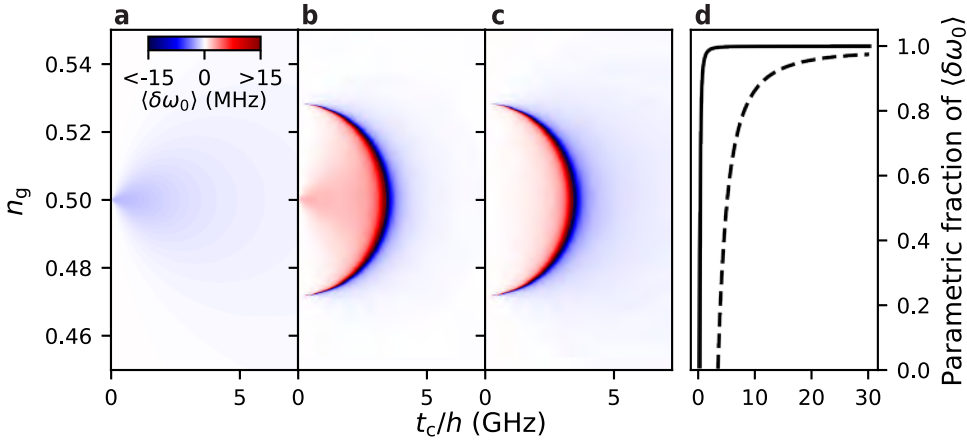


Figure 2.9: Parametric and dispersive response of a resonator to a DQD charge transition when the resonator is coupled to one of the dot's gates. (a–c) Thermally averaged expected resonance frequency shift  $\langle \delta\omega_0 \rangle$  of a resonator with equivalent parallel  $L = 1.28$  nH and  $C = 0.427$  pF (such that  $\omega_0/2\pi = 6.81$  GHz) for different  $t_c$  including only the parametric shift (a), the dispersive shift (b), and both contributions (c). (d) The fraction of  $\langle \delta\omega_0 \rangle$  given by the parametric contribution at  $n_g = 0.5$  for the 6.81 GHz resonator (dashed) and for a lower frequency resonator with  $L = 420$  nH,  $C = 0.377$  pF, and  $\omega_0/2\pi = 400$  MHz as was measured in Chapter 5 (solid). For all plots, a QD charging energy  $E_C = 500$   $\mu$ eV, temperature  $T = 71$  mK (based on the results of Chapter 5), and lever arm of 0.1 are used.

in state  $|\psi_i\rangle$ , it is

$$\delta\omega_{0,i} = \frac{\lambda^2}{\hbar} \frac{\partial^2 E_i}{\partial x^2} + \frac{1}{\hbar} \sum_{j \neq i} g_{ij}^2 \left( \frac{2}{E_i - E_j} - \frac{1}{E_i - E_j - \hbar\omega_0} - \frac{1}{E_i - E_j + \hbar\omega_0} \right) \quad (2.19)$$

where  $g_{ij} = \left| \langle \psi_i | \frac{\partial \hat{H}_d}{\partial x}(x_0) | \psi_j \rangle \right|$  is the resonator coupling strength to the transition  $|\psi_i\rangle \leftrightarrow |\psi_j\rangle$ . The first term is a parametric shift of the resonator frequency due to the device occupying state  $|\psi_i\rangle$ : this may be viewed as arising due to the *quantum capacitance*  $C_q = 4e^2 (\partial^2 E_i / \partial x^2)^{-1}$  of the device. Meanwhile, the second term is the dispersive shift resulting from virtual second-order photon transitions between the device and resonator.

Often, only the former is considered at low frequencies while only the latter is considered at higher frequencies, but both terms are distinct and additive [123]. At very low frequencies where  $\hbar\omega_0 \ll |E_i - E_j|$  it is valid to consider only the parametric contribution, but it is less obvious when the parametric contribution could be neglected. The second derivative of  $E_i$  in the device ground state could be very small away from anticrossings or at anticrossings arising from a very strong hybridization between states.

To investigate the crossover between these two regimes, we consider the case of a DQD near an interdot charge transition, as is probed with resonators in Chapters 3 and 5. This example is mathematically equivalent to the Cooper pair box example considered in Ref. [123] with the Josephson energy replaced by interdot tunneling and with a single charge tunneling instead of a Cooper pair. We consider both QDs as having charging energy  $E_C$ , with one dot coupled to a resonator via  $C_g$  leading to a reduced gate voltage  $n_g = -x$  and the other dot's reduced gate voltage fixed at  $1/2$ . Considering a single charge

shared between the dots, the Hamiltonian up to a constant offset is

$$\hat{H}_{\text{DQD}} = \begin{pmatrix} E_C n_g^2 & t_c \\ t_c^* & E_C(1 - n_g)^2 \end{pmatrix} \quad (2.20)$$

where  $t_c$  is the interdot tunnel coupling. Including a mutual charging energy between the dots only serves to shift the center of the interdot transition as a function of  $n_g$ , so we neglect it here. The energy eigenvalues are

$$E_{\pm} = E_C(n_g^2 - n_g + 0.5) \pm 0.5\sqrt{E_C^2(2n_g - 1)^2 + 4|t_c|^2} \quad (2.21)$$

which has a minimum excitation energy of  $2t_c$  at  $n_g = 0.5$ . Also,  $\partial\hat{H}_{\text{DQD}}/\partial n_g$  is readily calculable, so we plot the thermally averaged frequency shift  $\langle\delta\omega_0\rangle$  in Fig. 2.9 for a 6.81 GHz resonator. We consider parametric and dispersive terms from eq. 2.19, and find that both substantially contribute to the full frequency shift when  $2t_c \lesssim \omega_0/2\pi$ . When  $2t_c$  is relatively close but not equal to  $\omega_0/2\pi$ , the dispersive terms dominate. Many experiments in circuit quantum electrodynamics consider only these terms [123], as do we in Chapters 3 and 4. Finally, when  $\omega_0$  is much smaller than any excitation energy, the parametric shift dominates the resonator response. We plot the fraction of the total frequency shift given by the parametric shift in Fig. 2.9(d) for the 6.81 GHz resonator (dashed line) and a 400 MHz resonator (as measured in Chapter 5, solid), confirming this expectation. This justifies considering only the parametric impedance of a system when measuring at very low frequencies, but as excitation energies approach the resonator frequency, virtual photon transitions with the resonator must also be considered.

### 2.2.2. IMPEDANCE OF QUANTUM CHARGE SYSTEMS

Since our focus is on using resonators as a noninvasive probe of quantum systems, we hereon focus on the classical regime where the resonance frequency  $\omega_0$  is small, and its detuning from the excitation frequencies  $(E_i - E_j)/\hbar$  of the system under investigation is much larger than the resonator's characteristic coupling strengths  $g_{ij}$  to this system. In terms of the quantum mechanical theory of Sec. 2.2.1, this corresponds to  $\omega_0 \ll \omega_{ij}$  and  $|\omega_0 - \omega_{ij}| \ll g_{ij}$  for all  $i$  and  $j$ . The latter condition is that for being in the *dispersive regime* where the resonator state is altered due to photon-induced virtual transitions in the quantum system, dressing the resonator state without introducing driven transitions in the quantum system. Meanwhile, the condition  $\omega_0 \ll \omega_{ij}$  suppresses even these virtual conditions, meaning that the only effect of the quantum system on the resonator is its effective impedance associated with the quantum or thermal state of the system. In this case, the resonator can be treated in terms of how its electromagnetic field couples into the quantum system. Conversely, the quantum system can be treated as a parametric impedance perturbing the circuit parameters of the resonator. This is the approach we will take to discuss the modeling of potentially-open quantum systems of charge in the 'weak-signal' regime, where the resonator does not cause driving effects in the system. We focus on the case of the resonator being capacitively coupled to the device, but also briefly discuss the expected signal for Ohmic coupling to a device lead.

### GATE REFLECTOMETRY

For completeness we begin as generally as possible<sup>12</sup>: Consider a quantum charge system with Hilbert space  $\mathcal{H}$  described by a density matrix  $\hat{\rho}$  related to the system's Hamiltonian  $\hat{H}$ . Let  $\hat{H}$  have eigenstates  $|\psi_\alpha\rangle$  indexed by quantum number  $\alpha$ . The system may in general be in a mixed state due to incoherent coupling to thermal reservoirs (phonons) or charge reservoirs (leads). A small oscillating resonator voltage  $V_g(t) = V_g^0 + \delta V_g \sin(\omega t)$  weakly capacitively couples via gates with lever arms  $\alpha_i = C_{gi}/C_i$  to a set of QDs with charge operators  $\{\hat{Q}_i\}_i$ , where  $C_{gi}$  is the gate's capacitance and  $C_i$  is the total capacitance of the QD. The charge  $\langle Q_i \rangle$  is the charge induced on the capacitor  $C_{gi}$  including the QD charge  $-e\langle \hat{n}_i \rangle$ . The resonator then becomes sensitive to the system's effective impedance, which we will infer from the total gate currents  $I_g = \sum_i d\langle \hat{Q}_i \rangle / dt$  [125]. Here, 'weak' coupling means that the resonator's energy per photon  $\hbar\omega_0$  and the amplitude of its oscillations to the Hamiltonian  $\hat{H}$  parameters are small compared to other energy scales of the system. In this case, we may treat the resonator as a classical oscillating electromagnetic field parametrically affecting  $\hat{H}$  and its tunnel rates to external reservoirs. In terms of  $\hat{\rho}$ , the effective current seen by the resonator reads  $I_g = \sum_i \frac{d}{dt} \text{trace} [\hat{\rho} \hat{Q}_i]$ .

To continue, we assume that the charge system is weakly coupled to any charge reservoirs and photon or phonon baths. In this case the quantum details of reservoirs and baths can be traced out, such that their only effect on  $\mathcal{H}$  is to incoherently couple charge states of the system via a Markovian master equation. Namely, the dynamics of the system are described by a master equation in the Lindblad form which can be solved for  $\hat{\rho}$  [126]. In addition to dynamics described by the von Neumann equation for the reduced system  $d\hat{\rho}/dt = -(i/\hbar)[\hat{H}, \hat{\rho}]$ , the Lindblad equation adds 'jump' operators to the right hand side, coupling different states of the system with certain characteristic rates. This approach is taken in Ref. [124], but solving a Lindblad equation is complex, so we consider a simpler limit of this formalism: that where the jump operators couple one system eigenstate directly to another. In other words, if the jump operators describe thermal excitations, they cause excitation between eigenstates of the system. Meanwhile, if they describe tunneling between the QDs and leads, then this approximation is only valid if eigenstates of the QD system are charge states. Finally, because  $\{|\psi_\alpha\rangle\}_\alpha$  is an orthonormal eigenbasis of  $\mathcal{H}$  we may write  $\hat{\rho} = \sum_\alpha P_\alpha |\psi_\alpha\rangle \langle \psi_\alpha|$  where  $P_\alpha$  is the probability of occupying state  $|\psi_\alpha\rangle$ .

Under these conditions, we may calculate  $\sum_i \langle Q_i \rangle = C_{\text{geom}} V_g + \sum_i \alpha_{\text{eff},i} |e| \langle \hat{n}_i \rangle$  where  $\alpha_{\text{eff},i} \neq \alpha_i$  is an effective lever arm depending on all QD capacitances and  $C_{\text{geom}}$  is a classical 'geometrical' contribution to the QD capacitance unrelated to quantum effects, see Appendix D for details. Then because the only time dependence of expectation values is contained within  $V_g(t)$ , we may write

$$I_g = C_{\text{geom}} \frac{dV_g}{dt} + \sum_i \alpha_{\text{eff},i} |e| \sum_\alpha \left( \langle \psi_\alpha | \hat{n}_i | \psi_\alpha \rangle \frac{dP_\alpha}{dt} + P_\alpha \frac{\partial \langle \psi_\alpha | \hat{n}_i | \psi_\alpha \rangle}{\partial V_g} \frac{dV_g}{dt} \right). \quad (2.22)$$

By our above assumptions,  $P_\alpha$  can be solved with classical master equations of the form

<sup>12</sup>A more detailed formulation of the impedance of charge systems can be found in Ref. [124], which also includes driving effects.

[127]

$$\frac{dP_\alpha}{dt} = \sum_{\beta \neq \alpha} (\Gamma_{\beta \rightarrow \alpha} P_\beta - \Gamma_{\alpha \rightarrow \beta} P_\alpha), \quad (2.23)$$

where  $\Gamma_{\alpha \rightarrow \beta}$  is an incoherent tunneling rate between  $|\psi_\alpha\rangle$  and  $|\psi_\beta\rangle$  [13, 125, 128–130]. These rates could represent tunneling of charge into lead reservoirs. For a system without charge reservoirs, though,  $\Gamma_{\alpha \rightarrow \beta}$  may also represent phonon absorption or emission from a thermal bath to excite or relax the system [13, 125, 130]. Now we may illustrate why our above approximation was needed: given a hybridized DQD for example, the eigenstates may consist of superpositions of charge states. Meanwhile, it could be the case that incoherent tunneling occurs with lead reservoirs, but these couple one charge state to another, not different eigenstates. In that case, the aforementioned Lindblad formalism [124] or other quantum model of open systems must be used [131].

The impedance described in eq. 2.22 can be understood by noticing three types of terms in the expression. First, there is  $C_{\text{geom}} dV_g/dt$  — the equation for current through a capacitor  $C_{\text{geom}}$ . Second, there is the term  $C_q dV_g/dt$ , where

$$C_q \equiv \sum_i \alpha_{\text{eff},i} |e| \sum_\alpha P_\alpha \frac{\partial \langle \psi_\alpha | \hat{n}_i | \psi_\alpha \rangle}{\partial V_g} \quad (2.24)$$

is the *quantum capacitance*, which we take the time-averaged value of over one resonator cycle. For each quantum state occupied with probability  $P_\alpha$ , this capacitance quantifies the smooth change in charge expectation values in that state as a function of  $V_g$ . Notably, these changes are zero if the quantum state is a simple charge state, and non-zero whenever the state is composed of multiple charge states hybridized together. It is only present when charge states are coherently hybridized, hence the name. Quantum capacitance can be equivalently formulated in terms of the second derivative of energy with respect to voltage as in Sec. 2.2.1, since the energy stored on a capacitor  $C$  is  $CV_g^2/2$  [132]. This manifestation of quantum capacitance has been frequently measured in experiment, from early experiments on Cooper pair boxes [132, 133] to many experiments on DQDs (See Refs. [117, 134–141] for example).

The third type of terms in eq. 2.22 are those proportional to  $dP_\alpha/dt$ . Evidently, these terms relate to changes in the statistical distribution of the system between states in time. Assuming the only time-dependence in our system arises due to  $\delta V_g \sin(\omega t)$ , the solution of eq. 2.23 may include terms proportional only to  $\sin(\omega t)$  or  $\cos(\omega t)$  — that is, proportional to  $V_g$  or  $dV_g/dt$ . From Ohm's law for a resistor, we see that the former terms contribute dissipation to the circuit while the latter contribute an additional capacitance. The potential resistive contribution is referred to as *Sisyphus admittance* [13, 125, 130, 142] because the resonator voltage 'pushes' the system higher in energy only for incoherent relaxation events to dissipate this energy outside the system, depicted in Fig. 2.10(b) in orange. Meanwhile, the capacitive contribution is called *tunneling capacitance* (denoted  $C_t$ ) because it quantifies how the statistical distribution of charge changes as the resonator voltage swings due to the  $V_g$  dependence of tunneling rates  $\Gamma_{\alpha \rightarrow \beta}$ . These two contributions go hand in hand, as the Sisyphus admittance is typically proportional to  $C_t$  [125] (see also Appendix E). Together, we refer to the sum of  $C_t$  and  $C_q$  as  $C_p$ , the *parametric capacitance* [130], since it varies with the applied DC voltage  $V_g^0$  and other parameters of the quantum system.

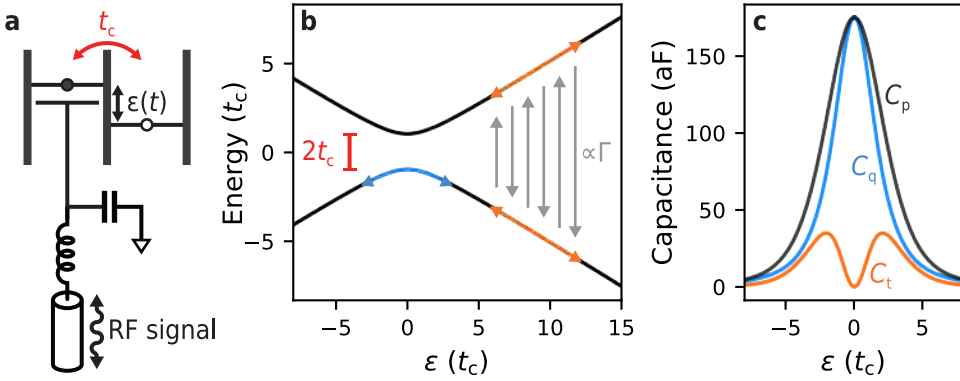


Figure 2.10: Parametric capacitance of interdot tunneling in a DQD. **(a)** Schematic of a DQD tuned close to an interdot charge transition hybridized with strength  $t_c$ , with a gate resonator applying an oscillating detuning between the charge states and sensing the system's parametric capacitance  $C_p$  through reflectometry. **(b)** Energy spectrum of the DQD. A curved anticrossing at charge resonance of width  $2t_c$  is present. Quantum capacitance results from the smooth variation of charge (blue arrow) as the resonator voltage swings back and forth. Meanwhile, tunneling capacitance in this case results from the changing statistical charge distribution due to thermal excitations as the voltage swings (orange arrows). **(c)** Tunneling (orange), quantum (blue), and total parametric capacitance (black) near the interdot charge transition, using  $\alpha_{\text{eff}} = 0.18$ ,  $T = 71$  mK, and  $t_c = 5 \mu\text{eV}$ . The former two parameters are chosen from fit results of Chapter 5. We take the limit of maximal  $C_t$  where  $\Gamma/\omega \rightarrow \infty$  and the  $\Gamma$  and  $\omega$  dependence of  $C_t$  disappears.

To exemplify parametric capacitance, we first summarize a minimal example: that of a DQD with a resonator capacitively coupled to one of the dots' gates, schematized in Fig. 2.10(a). This has been calculated in numerous references [13, 125, 130, 134], so we only restate the result. Given a single electron shared by two QDs 1 and 2 tunnel coupled with strength  $t_c$  with their levels detuned by  $\varepsilon = e\alpha_{\text{eff}}V_g$  where  $\alpha_{\text{eff}} = \alpha_{\text{eff},1} - \alpha_{\text{eff},2}$ , the parametric capacitance is

$$C_p = \underbrace{\frac{(\alpha_{\text{eff}}e)^2}{4k_B T} \left(\frac{\varepsilon}{\Delta E}\right)^2 \frac{\Gamma^2}{\omega^2 + \Gamma^2} \cosh^{-2}\left(\frac{\Delta E}{2k_B T}\right)}_{C_t} + \underbrace{\frac{2(\alpha_{\text{eff}}e)^2 |t_c|^2}{(\Delta E)^3} \tanh\left(\frac{\Delta E}{2k_B T}\right)}_{C_q}. \quad (2.25)$$

Above,  $\Delta E = \sqrt{\varepsilon^2 + 4|t_c|^2}$  is the gap between the ground and excited states, and  $\Gamma$  is a rate characterizing phonon emission and absorption from the DQD causing it to relax or become excited. We plot the energy spectrum of this system in Fig. 2.10(b). The first term  $C_t$  above represents the tunneling capacitance related to changes of state occupation probabilities as a function of voltage due to these thermal processes, and is present even when  $t_c = 0$ . This process is pictured with orange and gray lines in Fig. 2.10(b). The second term is the quantum capacitance  $C_q$  related to the hybridization of energy levels as appeared in Sec. 2.2.1, depicted with a blue line. We plot both contributions to  $C_p$  for a small  $t_c = 5 \mu\text{eV}$  in Fig. 2.10(c), where we see the result is a peak at the interdot charge transition. In particular, at  $\varepsilon = 0$  and  $T = 0$  we have  $C_p = (\alpha_{\text{eff}}e)^2/4t_c$ . This simple case illustrates how gate reflectometry can quantifiably measure resonant tunneling: the maximum parametric capacitance at zero temperature is inversely proportional to the hybridization strength, and therefore so is the maximum measurable frequency shift of

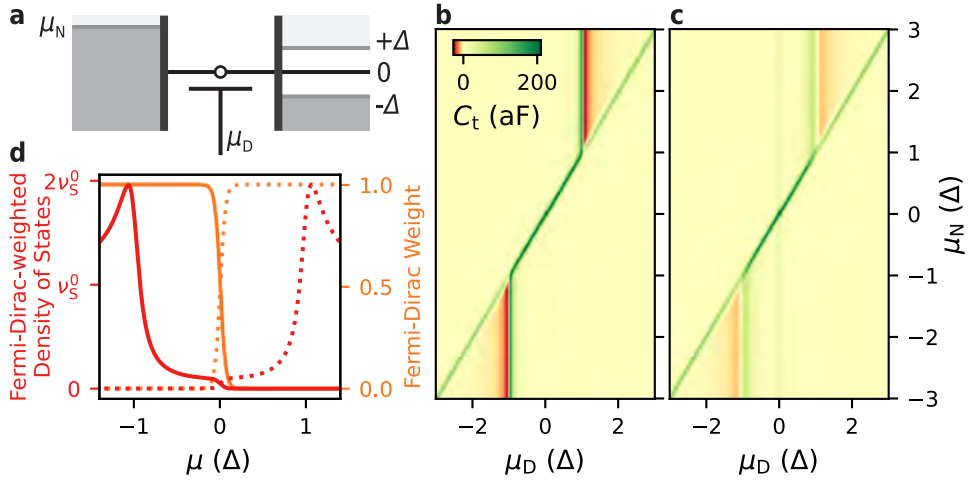


Figure 2.11: Gate reflectometry tunneling capacitance of a quantum dot with one normal and one superconducting lead. **(a)** Schematic of the system, with a QD at chemical potential  $\mu_D$  coupled to a normal lead biased by chemical potential  $\mu_N$  and a grounded superconductor with gap  $\Delta$ . The superconductor's density of states is broadened by a Dynes parameter  $\gamma$  [145]. **(b),(c)** Tunneling capacitance of the QD as seen from its gate with  $\gamma = 0.03\Delta$  **(b)** and  $0.1\Delta$  **(c)**. We take the limit of very large bare coupling strength  $\Gamma_0$  (see Appendix E) such that it and the probe frequency  $\omega$  are irrelevant to  $C_t$ . For other parameters, we take  $\Delta = 200\mu\text{eV}$ ,  $\alpha = 0.18$  as the resonator lever arm,  $T = 71$  mK (based on results of Chapter 5), and take the normal-state density of states in the superconducting lead  $v_S^0$  to be equal to that in the normal lead. **(d)** Dynes-broadened density of states in the superconducting lead (red) multiplied by  $f(\mu)$  (dotted) or  $1 - f(\mu)$  where  $f(\mu)$  is the Fermi-Dirac distribution. The tunneling capacitance contains contributions proportional to this quantity and its derivative. We also plot  $f(\mu)$  (dotted) and  $1 - f(\mu)$  (solid) in orange. For these plots we use the same parameters as **(c)**.

a gate resonator. Notably,  $C_t$  is only noticeable in the figure due to the relatively small  $t_c$  value, and for more substantial  $t_c$  it becomes negligible compared to  $C_q$ . We also remark that at higher temperatures  $C_q$  becomes suppressed since the ground and excited states become equally occupied and contribute opposite capacitances.

Next, we consider two further examples of parametric capacitance in order to illustrate its deviations from the simple result of eq. 2.25. First, we consider a single QD coupled to one normal and one superconducting lead reservoir, then we consider the quantum capacitance of a two-site Kitaev chain device [87, 143, 144]. The former illustrates how incoherent tunneling with *leads* and not just phonon exchange leads to a tunneling capacitance, while the latter shows how higher-order tunneling processes such as elastic cotunneling and CAR also contribute to quantum capacitance.

Beginning with the QD coupled to a normal and superconducting lead shown in Fig. 2.11(a), we suppose the QD is coupled to a gate resonator of lever arm  $\alpha$  with chemical potential  $\mu_D$ , and connected via tunnel barriers to a normal lead and a superconducting lead of gap  $\Delta$ . The superconductor has a finite subgap density of states quantified by a Cooper pair breaking energy scale  $\gamma$  such that  $\gamma = 0$  corresponds to a hard gap [145]. Tunneling rates and the resulting  $C_t$  are calculated with the two reservoirs using Fermi's golden rule, see Appendix E for an analytic calculation of  $C_t$ . We plot  $C_t$  for a nearly hard superconducting gap and a soft gap in Figs. 2.11(b) and (c) respectively. Importantly,

$C_t$  contains terms proportional to the density of states in the leads or their derivatives, multiplied by factors of  $f(\mu)$ ,  $\partial f/\partial\mu$ , or  $1 - f(\mu)$  where  $f(\mu)$  is the Fermi-Dirac distribution function. This is clearly visible in the simulations, as a tunneling capacitance peak appears when the QD level is resonant with the normal lead chemical potential. At this point, the Fermi distribution in this lead transitions from zero to one. Furthermore, as  $\mu_D$  is swept past  $\pm\Delta$  for biases above  $\pm\Delta$ , a sharp positive peak in  $C_t$  followed by a tail dipping below zero is visible. This arises from the sharp peak in the density of states of the superconducting lead, where a negative tunneling capacitance is made possible by the sharply negative slope in this density of states just past the peak. Lastly, we note that a faint peak is visible when the QD level is resonant with the Fermi level of the superconducting lead if it has a softer gap, as in Fig. 2.11(c). This again arises due to the gradual step in the Fermi distribution, but is made faint since it is multiplied by the small in-gap density of states of the superconductor, illustrated in Fig. 2.11(d). These results show that gate sensing of a QD not only reveals characteristics of the dot, but also probes the density of states of any coupled leads.

As a final example, we simulate the quantum capacitance observable in gate reflectometry of a QD forming one site in a two-site Kitaev chain or Cooper-pair-splitting device [87, 143, 144]. This device consists of two spin-polarized QDs (QD 1 and QD 2) separated by a grounded superconducting lead hosting a single discrete subgap state at energy  $E_0$ , depicted in Fig. 2.12(a). Here, we conduct a full fermionic simulation of the system using the model of Appendix F. The resulting charge expectation values  $\langle\hat{N}_1\rangle$  on QD 1 in the ground state are plotted in Fig. 2.12(b). In the lower left and upper right, we see that elastic cotunneling across the superconducting subgap state hybridizes states involving an electron tunneling between the dots. Meanwhile, in the top left and bottom right, we see that CAR couples states involving one electron from each dot resonantly tunneling into the superconductor. As is visible in Fig. 2.12(c), both second-order tunneling processes are measurable in quantum capacitance of QD 1. Charge transitions changing the overall parity of the system appear as sharp lines because tunneling with any normal-metal lead reservoirs is not included in this model. Despite this, we see that even away from CAR and cotunneling transitions,  $C_{q1}$  is nonzero near the sharp lead transitions. This arises due to the QD level hybridizing with the superconductor's ABS. We also note that reflectometry of the superconducting lead would be sensitive to CAR but not cotunneling across the dots, since the latter process doesn't involve any charge exchange with the superconductor when the tunnel barriers are symmetric. This property could prove useful for parity readout of two-site Kitaev chains [14].

### LEAD REFLECTOMETRY

As discussed near the beginning of this section, lead reflectometry where a resonator is galvanically connected to a lead of the device is useful for fast measurements of conductance. Additionally, though, lead reflectometry senses dissipative and capacitive effects even when the device has no DC conductance (such as for a device with one lead). Accordingly, we summarize here a few key features of lead reflectometry signals.

For tunneling between a QD and the lead, the lead reflectometry signal is similar to that which would be measured with gate sensing for a lever arm of one. This is because the chemical potential difference between the dot and lead is directly modulated

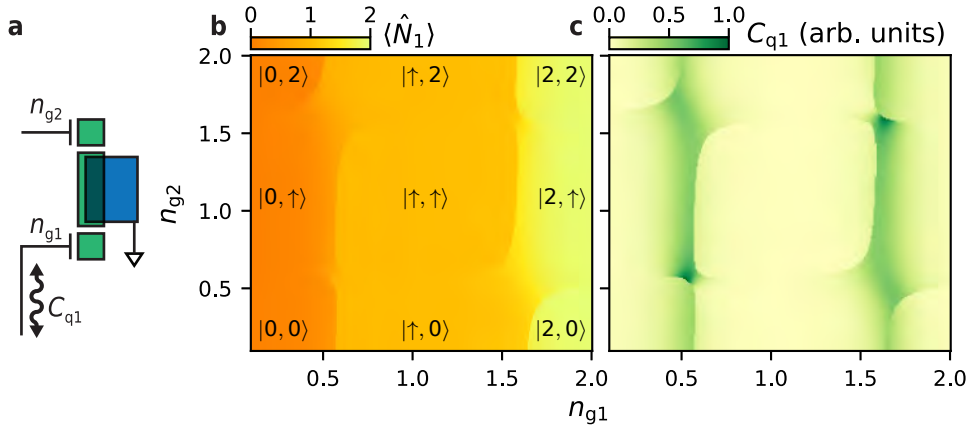


Figure 2.12: Gate reflectometry quantum capacitance of a two-site Kitaev chain device. **(a)** Schematic of the device: two spin-polarized QDs separated by a grounded central superconductor hosting a discrete subgap state at energy  $E_0$  with electron- and hole-like coherence factors  $u$  and  $v$ . **(b)** Expected charge occupation in the ground state of QD 1. Simulated using the fermionic model of Appendix F for a nonfloating system by solving the even- and odd-parity subspaces, and selecting at each point in parameter space the solution which minimizes the energy. For other parameters, we set both QD charging energies to  $5E_0$ , we choose symmetric spin-conserving tunneling strengths equal to  $E_0$ , and use spin-flipping tunneling strengths of  $0.3E_0$ . Finally, we apply a Zeeman splitting of  $1.5E_0$  to both QDs and neglect it for the subgap state. In Coulomb-blockaded regions, the ground state is labeled with the occupation of each dot: ‘0’ charge, a single spinful electron ‘ $\uparrow$ ’, or a singlet of charge ‘2’. **(c)** Thermally averaged (with temperature  $E_0/40$ ) quantum capacitance as seen by a resonator connected to the QD 1 gate. Transitions not conserving total charge show up as sharp boundaries because tunneling with lead reservoirs is not included in our model.

by the resonator voltage. Namely, lead reflectometry is sensitive to tunneling capacitance and Sisyphus resistance. For a superconducting lead, it can even be directly sensitive to quantum capacitance [133] [146]. Additionally, tunnel barriers separating the leads from QDs have a capacitance through which a lead resonator is sensitive to a ‘gate reflectometry’-like signal even when no tunneling is possible between the lead and QD [134, 147].

In general, any lead or gate reflectometry measurement measures tunneling in two-level systems or other charge pockets that it has some stray capacitance to [148]. The fact that all of these signals are superimposed in the measurement can complicate the interpretation of signals. Finally, we note that resonators may be inductively coupled to quantum systems as well, such as in the case of radio-frequency superconducting quantum interference devices (RF SQUIDS) [149]. In this case a different approach using flux instead of charge variables could be taken for calculating the impedance [123].

### 2.2.3. DRIVING DUE TO LANDAU-ZENER TRANSITIONS

As the RF power applied to a quantum system is increased, or as the transition energies of the quantum system decrease, we eventually expect the resonator to drive transitions in the system, altering or suppressing the reflectometry signal. Understanding this limit is clearly important, since for example eq. 2.25 leads to a  $C_q$  which diverges as  $1/k_B T$  at  $\varepsilon = 0$  and  $t_c = 0$ , but of course in this limit our measurements would yield exactly zero

signal, not a divergently large one.

The answer to this contradiction comes by including driving effects induced by the resonator. If the resonator sweeps the detuning across an anticrossing at a fast enough rate and with a large amplitude, it will cause the system to jump into the excited state through a Landau-Zener transition (LZT). Indeed, LZTs make all of the parametric capacitance models we've considered inapplicable for small values of  $|t_c| \lesssim \sqrt{\hbar\alpha\delta V_g f_0}$ , where  $\delta V_g$  is the resonator's oscillating voltage amplitude,  $\alpha$  is its lever arm to the QD, and  $f_0$  is the resonator frequency [150]. There LZTs become frequent, biasing the system towards equal occupation of the excited and ground charge states where quantum capacitance is zero [138]. For a DQD with a short decoherence time, and at zero detuning from the charge transition, the probability of a LZT occurring twice in a resonator cycle is  $e^{-2|t_c|^2/\hbar\alpha\delta V_g f_0}$  [150, 151]. Due to the sinusoidal nature of the oscillating voltage, a LZT occurring twice in a cycle means that the tunneling electron spends an equal amount of time in the excited DQD state as in the ground state. In other words, the population of the excited state is equal to the population of the ground state when this probability is one. Hence, we expect quantum capacitance to be eventually suppressed for small enough tunnel couplings, since LZTs become more probable as tunnel couplings become smaller for fixed  $\delta V_g$ , and the quantum capacitance of ground and excited states in a DQD cancel each other out. Thermal redistribution then serves to further suppress the frequency shift for smaller tunnel couplings [125, 130].

#### 2.2.4. OPTIMIZING RESONATOR DESIGN FOR MEASUREMENTS

The response of a resonator probing a small capacitive response of a quantum device is highly sensitive to the resonator parameters because it is difficult to controllably tune the quantum device to optimal impedance matching conditions<sup>13</sup> [13]. When measuring a charge sensor with reflectometry techniques, the resonator parameters are less important because the resistance of the sensor can be tuned until the resonator circuit has impedance matched with the readout line at  $Z_0 = 50\Omega$ . Hence, even though resonators used in this thesis were not designed specifically for these experiments, we discuss resonator optimization here to illustrate where improvements could be made in future experiments.

Unless measurements are so fast that the time for a readout resonator to reach its steady-state after an RF pulse is applied becomes a significant portion of the measurement time [152], the problem of optimizing readout resonators amounts to maximizing the change in the reflection coefficient  $\Gamma$  for the expected changes in device parameters. Explicitly, this means maximizing  $|\Delta\Gamma| \equiv |\Gamma(Z_1) - \Gamma(Z_2)|$  for device impedances  $Z_1$  and  $Z_2$  corresponding to the two extremes of signals one wants to distinguish [13]. For low-frequency resonators sensing a capacitive signal  $\Delta C$ , the resonator line width is often much larger than the perturbative shift in its frequency due to  $\Delta C$ . In that case, this becomes a problem of maximizing the derivative  $|d\Gamma(C)/dC|$  [117].

Of course, other factors outside of the resonator design affect the *signal-to-noise ratio* (SNR) of an experiment: most notably the noise temperature of the circuit. The SNR is

<sup>13</sup>Note that measuring small inductances is even more difficult with off-chip resonators: the small device inductance forms a low impedance path to ground in parallel with the parasitic capacitance, destroying the resonance.

given by

$$\text{SNR} = \frac{\text{signal}}{\text{noise}} = \left| \frac{(\Delta\Gamma) V_{\text{rf}}}{V_{\text{noise}}} \right| \quad (2.26)$$

where  $V_{\text{rf}}$  is the signal voltage incident on the resonator circuit such that  $\Gamma V_{\text{rf}}$  is the reflected voltage, and  $V_{\text{noise}}$  is the voltage scale associated with noise. The latter is an increasing function of the noise temperature of the system, determined primarily by the noise temperature of the earliest amplification stage [116]. In Chapter 3, we demonstrate an SNR of 15 in  $1\ \mu\text{s}$  measurement time for distinguishing tunneling in a DQD from Coulomb blockade, due in large part to the presence of a parametric amplifier located at the mixing chamber plate of the fridge [153]. This amplifier was also present for the experiment of Chapter 4. Again, noise temperatures are limited to around the temperature of the first amplification stage, which without a parametric amplifier is usually a high-electron-mobility transistor amplifier operating at the 4 K stage. This is the case for the measurements of Chapter 5, but such amplifiers at 4 K were also used in other chapters in addition to the parametric amplifier.

For lower frequency reflectometry measurements well outside of the quantum limit of Sec. 2.2.1, the most typical resonator consists of an off-chip inductor bonded to the device in question [13], as we use in Chapter 5 [154]. The GHz-frequency coplanar waveguide resonators used in Chapters 3 and 4 were designed by Daan Waardenburg [155] based on the work of Ref. [156]. Distributed-element resonators are fabricated on the same chip as the measured quantum device and have more tunable design parameters by definition [157], though they can be modeled as equivalent *RLC* circuits for a given design [158]. We therefore focus on discussing off-chip lumped-element resonators as a simpler example, also because they can be readily applied in any quantum device regardless of the material platform.

In this case, the capacitance  $C$  of the resonator is formed by a parasitic capacitance of the inductor, device leads, and bond wires to ground: surprisingly consistently in the range of 0.1 to 1 pF across different experiments and resonator designs [13, 117, 128, 134, 135, 138, 154, 159, 160]. One facet of optimizing the resonator's performance involves minimizing this capacitance, since higher resonator frequencies can only be achieved by lowering  $L$  or  $C$ , and  $Q_i$  increases with decreasing  $C$  up to an optimum for resonator circuits with  $C$  in parallel with losses [116]. As evidenced by the extensive experimental references above, it is difficult to reduce the parasitic capacitance below 0.1 pF. With just an inductor and capacitor (and some intrinsic losses  $R$ ), there are not many tunable parameters for maximizing  $|\Delta\Gamma|$ .

To tune the coupling of the resonator to the reflectometry circuit ( $Q_c$ ) or to include multiple resonators on the same reflectometry line, the inductor is thus often fabricated in series with a coupling capacitor  $C_c$ . Since the inductor is typically made of a superconducting material like Nb [154], NbN [160] or NbTiN<sup>14</sup>, losses in the resonator mainly come from capacitive coupling to lossy dielectrics and other lossy conductors, so we model the resonator losses by an admittance  $Y$  in parallel with  $C$ . The device impedance  $Z$  is also in parallel with  $Y$  and  $C$ , pictured in Fig. 2.13(a). When measuring parametric capacitance of a QD device such that  $Z = 1/i\omega\Delta C$ , capacitances are typically limited to less than a femtofarad. We will find that the maximum measured quantum capacitance

<sup>14</sup>Used in resonators designed by Yining Zhang and Ivan Kulesh, but not employed in this thesis.

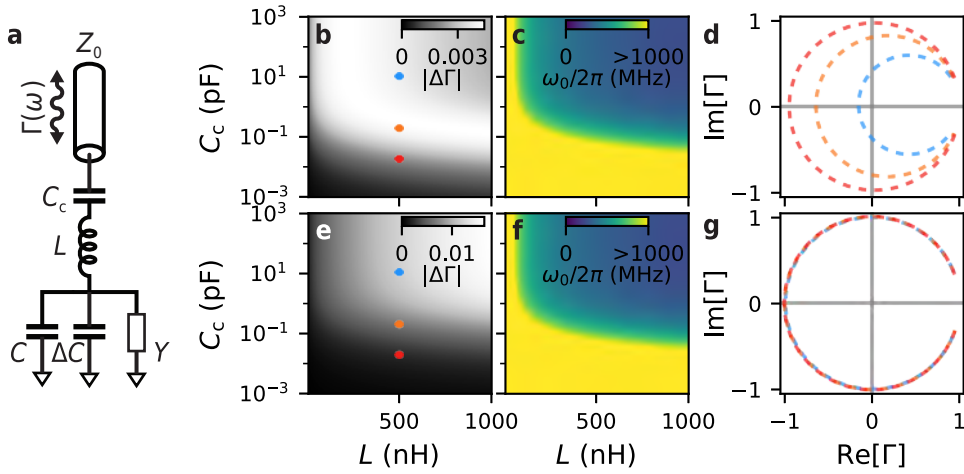


Figure 2.13: Optimization of a series  $LC$  resonator for measuring a small capacitive response. **(a)** Resonator reflectometry measurement circuit, with the resonator coupled to the readout line by coupling capacitance  $C_c$ , and its resonance given by inductance  $L$ , a typical parasitic capacitance  $C = 0.5$  pF to ground, and intrinsic losses  $Y$ . A small capacitive shift  $\Delta C = 150$  aF (calculated from the maximum observed  $\approx 80$  kHz frequency shift in Fig. 5.3(d)) perturbs this resonance. **(b-g)** Response of the resonator to  $\Delta C$  for  $Y = e^2/h$  **(b-d)** and  $0.1e^2/h$  **(e-g)** for different  $C_c$  and  $L$ . **(b,e)** Absolute change in  $\Gamma$  at the bare resonance frequency (numerically calculated as the frequency at which the resonator circuit impedance has no imaginary component) as  $\Delta C$  goes from 0 to 150 aF. **(c,f)** Resonator resonance frequency. **(d,g)** Complex  $\Gamma$  response at the points indicated in **(b)** and **(e)**. For low internal losses,  $C_c$  mostly only affects  $Q_c$  in the same way it affects  $Q_i$ , indicated by the resonator response remaining strongly overcoupled ( $Q_i \gg Q_c$ ).

in Chapter 5 is about  $\Delta C \approx 150$  aF, for example. Since quantum capacitance increases for smaller tunnel couplings until thermal excitations, Landau-Zener transitions, or other incoherent processes set in, these factors determine the maximum  $\Delta C$ . Given typical parasitic capacitances of at least 0.1 pF, this places us solidly in the small-signal regime. As we saw in the previous section, quantum capacitance also scales with the square lever arm of the resonator to the QD being measured. Naturally, a stronger capacitive coupling of the gate to the QD leads to a larger signal, but a weaker lever arm can be overcome by simply increasing the input RF power. If the lever arm is too weak, one does run the risk of the resonator having substantial unintended couplings (such as to a neighboring dot) or for driving and heating effects to occur at the RF powers needed to achieve a good signal.

We begin by considering a series  $LC$  circuit, where the inductor is connected directly to the device, such that the device and parasitic capacitance to ground form in series with  $L$ . In Fig. 2.13(b) and (e), we accordingly plot the achievable signals  $|\Delta\Gamma| \equiv |\Gamma(\Delta C) - \Gamma(0)|$  for  $\Delta C = 150$  aF when measured at the resonance frequency  $\omega_0$  for high  $Y = e^2/h$  and low  $Y = 0.01e^2/h$ , respectively. The higher  $Y$  value here is reasonable for superconducting off-chip resonators (e.g. given the low resonator  $Q$  factors observed in Chapter 5). For higher losses, we see that tuning  $C_c$  leads to a signal maximum, but the signal is not much smaller even when  $C_c \gg C$ . For lower losses this maximum isn't in the observed parameter range at all, and the maximal signal comes from simply maximizing

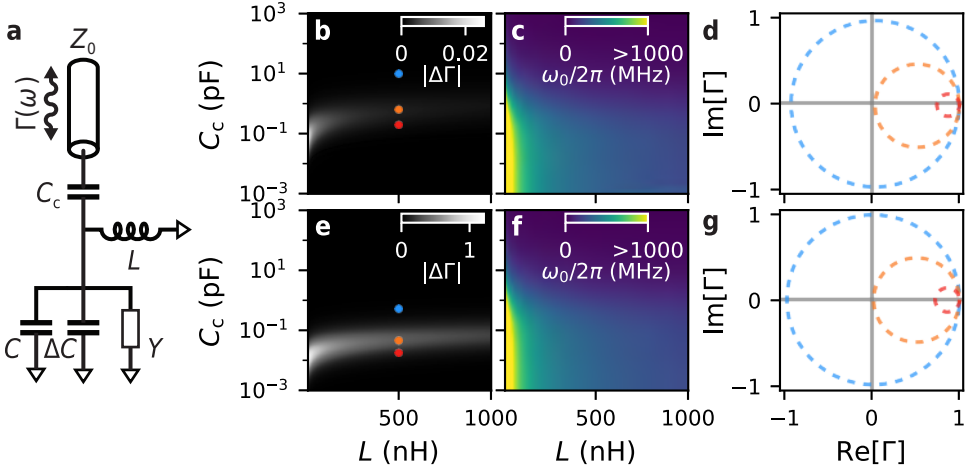


Figure 2.14: Optimization of a parallel  $LC$  resonator for measuring a small capacitive response, similar to Fig. 2.13. (a) The resonator circuit, differing from that of Fig. 2.13 in that the inductor is connected directly to ground, in parallel with a connection to the device capacitance  $\Delta C$ . (b-g) As in Fig. 2.13: resonator response to a small capacitance  $\Delta C = 150$  aF for different  $L$  and  $C_c$  for  $Y = e^2/h$  (b-d) and  $Y = 0.1e^2/h$  (e-g). Unlike in Fig. 2.13, the labeled  $(L, C_c)$  points in (b) and (e) for which the resonator responses are shown in (d) and (g) are different between the low and high  $Y$  cases. This is in order to emphasize that by tuning  $C_c$  across a  $Y$ -dependent optimal value, the resonator can be tuned continuously from being overcoupled to undercoupled.

$C_c$ . Note that in this limit the circuit becomes equivalent to the case without the coupling capacitor. Furthermore, from Figs. 2.13(c) and (f) we see that  $C_c$  strongly affects the resonance frequency, since when  $Y = 0$  the device is simply a series  $LC$  circuit with effective capacitance  $1/(1/C + 1/C_c)$ . As such, the ability of  $C_c$  to tune  $Q_c$  is only present insofar as  $Y > 0$ , so that  $C_c$  can be differentiated from  $C$  in the circuit. This is clear from the resonator responses plotted in Figs. 2.13(d) and (g). Counterintuitively, from Fig. 2.13 (d) we see that  $Q_c/Q_i$  increases with increasing  $C_c$ , because for  $C_c < C$ , the resonance frequency is largely determined by  $C_c$ . As  $C_c$  decreases further below  $C$ ,  $C$  begins to behave as a low-impedance shunt to ground at the resonance frequency  $\omega_0 \approx 1/\sqrt{LC_c}$ , bypassing the dissipation  $Y$  and increasing  $Q_i$ . The reason to add  $C_c$  to the circuit in this case is mostly just to allow multiple resonators to be connected to the same feedline with separate bias tees (since  $C_c$  prevents them from being shorted).

Though not employed in this thesis, we note that additional tunability of  $Q_c$  is possible when the inductor is bonded to ground in parallel with the bond to the device impedance [117], pictured in Fig. 2.14(a). This is in part because  $C_c$  affects the circuit impedance in a nontrivial way compared to  $C$  regardless of the value of  $Y$ . We plot analogous simulations of the resonator response to the series resonator case for this circuit in Fig. 2.14. In this configuration, we observe that generally larger  $|\Delta\Gamma|$  are achievable than for the series case provided  $C_c$  can be accurately engineered to a  $Y$ -dependent range. Particularly, from the resonator responses plotted in Figs. 2.14(d) and (g) for different  $(L, C_c)$  values we see that tuning  $C_c$  allows one to tune continuously from the resonator being very undercoupled to being very overcoupled even for substantial internal losses. We also note that the circuit resonance frequencies are relatively weakly dependent on

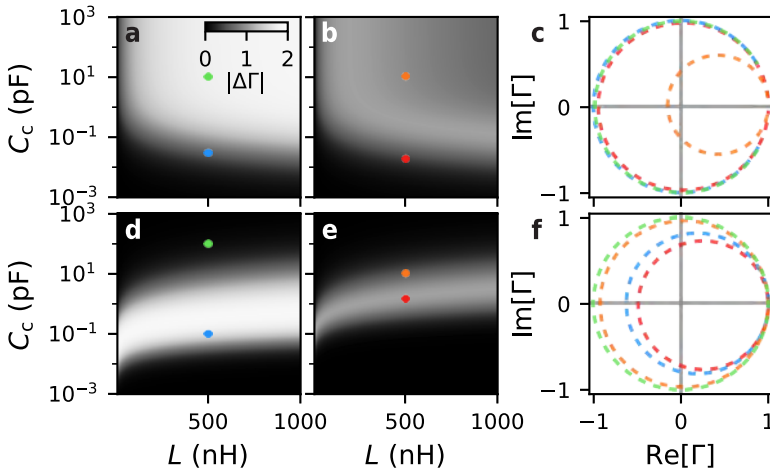


Figure 2.15: Optimization of a parallel and series  $LC$  resonator for measuring a large resistive response. (a-c) and (d-f) show results for the series and parallel  $LC$  resonators discussed above, respectively. (a), (d) Absolute change in signal for device admittance changing from  $\Delta Y = 0$  to  $\Delta Y = 10e^2/h$  with internal resonator losses  $Y = 0.1e^2/h$ , and for  $Y = e^2/h$  in (b), (e). (c), (f) Resonator responses plotted for the  $(L, C_c)$  values indicated in (a), (b), (d), (e).

$C_c$ , making it simpler to independently engineer  $Q_c$  and  $\omega_0$ . A minor downside of this approach is that inserting a bias tee between the coupling capacitor and inductor requires that a large capacitor be placed between  $L$  and ground to avoid a short.

Finally, we consider the case of measuring a resistive response of a quantum device. One may want to connect a resonator to a lead of a device to measure RF conductance more efficiently than one can measure DC conductance. This goal is one of the motivations of the experiments of Chapter 3. Due to the low carrier density of semiconductors and high resistances of tunnel barriers, conductance across semiconductor quantum devices typically ranges from 0 to several conductance quanta  $e^2/h$ , corresponding to a few k $\Omega$ . Assuming resonator losses on the order of  $e^2/h$  or smaller, this range of device conductances corresponds to a large signal. Simply minimizing the resonator's internal losses, one finds the resonator response goes from strongly overcoupled to strongly undercoupled for  $1/Z \equiv \Delta Y$  ranging between 0 and, say, several times  $e^2/h$ . For very small changes in device resistance on the other hand, the optimal resonator response occurs near critical coupling [13]. The problem of resonator optimization for resistive readout is very simple for a series resonator then: Simply choose  $L$  to pick the desired measurement frequency, choose  $C_c \gtrsim C$  to ensure the resonator frequency is determined mostly by  $C$ , and minimize internal losses  $Y$  as much as possible. For both parallel and series resonators, we plot the signal change  $|\Delta\Gamma|$  for a change in device admittance from  $\Delta Y = 0$  and  $\Delta Y = 10e^2/h$  in Fig. 2.15, with  $\Delta Y$  taking the place of the device capacitance in Figs. 2.13 and 2.14. When  $Y$  is small, it is possible to achieve responses around the maximum possible  $|\Delta\Gamma|$  of 2 (recall the resonator response is at largest a unit circle in the complex  $\Gamma$  plane). As  $Y$  becomes comparable to the admittances to be measured, the maximum achievable signal quickly diminishes. Additionally, we note that again the

signal is comparable to its maximum for a series resonator so long as  $C_c \gtrsim C$ , while for parallel resonators,  $C_c$  must be designed to a  $Y$ -dependent range. In the resonator responses plotted in Figs. 2.15(c) and (f), we observe that the optimal signal occurs for resonators between critical coupling and overcoupling. On the other hand, we see that strongly overcoupled resonators have a suppressed signal again, because  $\Delta Y$  can not introduce enough dissipation to take the resonator out of the  $Q_c \ll Q_i$  limit.

In summary, we found that off-chip resonators with the inductor bonded in parallel with a quantum device offer greater tunability of  $Q_c$  than when bonded in series (as was done for the measurements of Chapter 5). This leads to substantially greater achievable signals for the parallel case when the resonator measures a small capacitive response. For readout of typical semiconductor device resistances a few times  $e^2/h$  or smaller, either resonator configuration can achieve a large signal provided internal losses are small compared to the maximum device admittance. For both capacitive and resistive readout, a series-bonded inductor circuit has the advantage that the signal is fairly insensitive to the precise value of  $C_c$  provided  $C_c \gtrsim C$ . In all cases, the signal improves as one minimizes internal losses. Additionally, the optimal signal generally occurs when the device is overcoupled or critically coupled, and undercoupled resonators have poor responses. Finally, we note nanosecond-scale charge sensing experiments have been conducted using resonators inductively coupled to a feedline, in place of  $C_c$  [160].

# 3

## RAPID MICROWAVE-ONLY CHARACTERIZATION AND READOUT OF QUANTUM DOTS USING MULTIPLEXED GIGAHERTZ-FREQUENCY RESONATORS

*D. de Jong, C. G. Prosko, D. M. A. Waardenburg, L. Han, F. K. Malinowski, P. Krogstrup, L. P. Kouwenhoven, J. V. Koski, W. Pfaff*

On-chip superconducting resonators enable fast characterization and readout of mesoscopic quantum devices. Finding ways to perform measurements of interest on such devices using exclusively resonators is therefore of great practical relevance. We report the experimental investigation of an InAs nanowire multi-quantum-dot device by probing GHz-frequency resonators connected to the device. First, we demonstrate accurate extraction of the DC conductance from measurements of the high-frequency admittance. Because our technique does not rely on DC calibration, it can potentially obviate the need for DC measurements in semiconductor qubit devices. Second, we demonstrate multiplexed gate sensing and the detection of charge tunneling on microsecond time scales. The microwave detection of dispersive resonator shifts allows rapid acquisition of charge-stability diagrams, as well as resolving charge tunneling in the device with a signal-to-noise ratio of up to 15 in one microsecond. Our measurements show that GHz-frequency resonators may serve as a universal tool for fast tune-up and high-fidelity readout of semiconductor qubits.

---

The work in this chapter has been published in *Physical Review Applied* **16**, 014007 (2021). arXiv:2103.03659

### 3.1. INTRODUCTION

Microwave resonators in the few-gigahertz range are well known as a powerful means to increase the speed with which properties of mesoscopic quantum devices can be read out [12, 13]. In the field of quantum information, resonators in this so-called ‘Super High Frequency’ (SHF) band have thus enabled the fast and high-fidelity nondemolition readout of quantum bits (qubits) [4, 161–163], as well as mediating interactions between qubits [146, 164–166]. SHF resonators are also an attractive tool for the fast characterization of quantum devices, because the required tuneup routines are generally time-consuming. Additionally, frequency multiplexing using many high-quality-factor resonators has been established for hardware-efficient mass-characterization of devices [167, 168].

Efficient characterization is particularly relevant for semiconductor quantum devices where many gate electrodes result in a large parameter space. In recent years there have been numerous efforts to utilize SHF resonators for this purpose [169–173] as well as reading out qubit degrees of freedom [141, 169, 174–182]. Despite these successes, however, experiments are still often supplemented with DC or low-frequency measurements to quantitatively extract the DC conductance [183]. As larger-scale devices are developed [184, 185], it is interesting to direct focus to readout and tuneup schemes utilizing SHF resonators only, thus allowing a single framework for all measurements performed on a device.

Here, we present experiments using multiplexed resonators in the range 3–7 GHz coupled to a multiple quantum dot (multi-QD) system. Using the resonator response only, we are able to infer quantitatively the DC conductance of the system, and detect single-electron tunneling with high signal-to-noise ratio (SNR) on submicrosecond timescales. The remainder of this paper is organized as follows. In Sec. 3.3 we determine the DC (i.e. zero-frequency) conductance from SHF measurements without any DC calibration data and find agreement with conductance obtained from a DC transport control measurement. In Sec. 3.4, we demonstrate fast multiplexed dispersive gate sensing (DGS) at gigahertz frequencies in a double quantum dot (DQD). This local measurement of charge transitions facilitates fast tuneup of multi-QD systems [185]. Finally, in Sec. 3.5, we attain high SNRs in the detection of charge tunneling in the DQD. State-dependent charge tunneling is a key mechanism for qubit readout in semiconductor and topological qubits [10, 11, 186]. Our optimized resonator design [117], combined with the use of a near-quantum-limited amplifier [153], results in a maximum SNR of 15 in an integration time of 1  $\mu$ s.

### 3.2. EXPERIMENTAL SETUP

The device comprises an InAs nanowire with a few-gigahertz coplanar waveguide resonator [156] coupled to every QD to sense the electronic compressibility of each individual dot. An additional resonator that is galvanically connected to the source of the nanowire is used to probe the admittance of the nanowire. Figures 3.1(a) and 3.1(b) show images of the resonators and the multi-QD device, respectively. An approximate lumped-element schematic of the device is shown in Fig. 3.1(c). Each resonator is coupled to a central feedline in a hanger geometry and is individually addressable us-

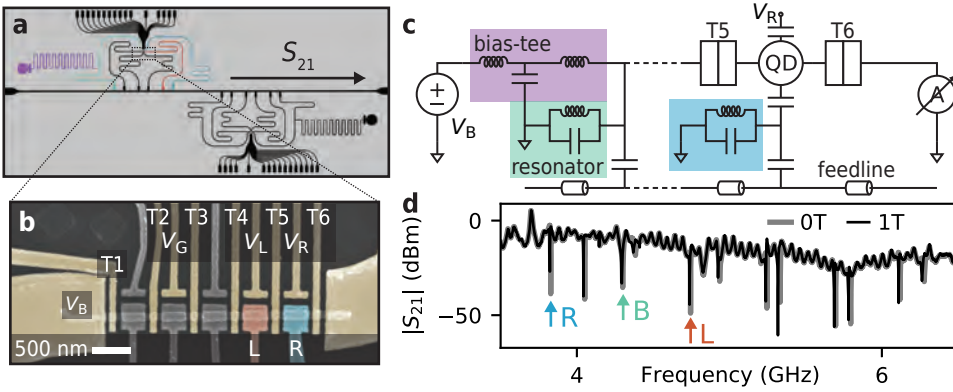


Figure 3.1: Experimental setup and resonator response. (a) Schematic of the device layout and (b) False-colored electron micrograph of the nanowire and the surrounding gates. (c) The RF equivalent circuit diagram of the device. The five top gates are coupled to resonators as is the source electrode of the nanowire that can be DC-biased by  $V_B$  with a bias-tee. The top gates are separated by six tunnel gates such that the nanowire can be pinched off at various positions and quantum dots can be defined. The charge on the quantum dots can be controlled by the side gates. (d) Transmission through the feedline without magnetic field and at 1 T applied parallel to the plane of the resonators. The arrows L (left), R (right), and B (bias) mark the resonators used here.

ing frequency multiplexing (Fig. 3.1(d)). The complex transmission  $S_{21}$  of microwaves through the feedline contains information about the reflection coefficient of each resonator [187]. The obtained SNR is set by the high resonator bandwidth, optimized resonator coupling quality factors, and a traveling-wave parametric amplifier (TWPA) [153] at the base temperature stage of 20 mK of our dilution refrigerator. For further details, see Appendix B.1.

### 3.3. HIGH-FREQUENCY CONDUCTANCE MEASUREMENTS

We begin by investigating the SHF response of the resonator coupled to the lead in response to changing nanowire conductance [170, 171, 183, 188, 189]. For all RF measurements, we denote the transmitted amplitude of resonator  $j \in \{L, R, B\}$  by  $V_{RF}^j$  and the input amplitude by  $V_0$ . By tuning the gate voltage T2 and keeping the other gates at 0 V we alter the nanowire conductance. This modulates the resonator response, shown in Figures 3.2(a) and 3.2(b), through changes in its load admittance. The DC conductance can be extracted from the load admittance either by building up a calibration map of load admittance and DC conductance, or by quantitatively modeling the resonator circuit [183]. We take the latter approach to maintain independence from DC calibration measurements. To quantify the modulation of the resonator response, we fit the response to a hanger input-output model [158, 187, 190]. The relevant parameters for extracting load admittance are the change in the resonance frequency  $\Delta\omega_0$  and the additional photon decay rate  $\Delta\kappa_d$  with respect to the pinched-off regime, which is reached by decreasing the gate voltages until  $\kappa_d$  saturates. Representative fits are plotted in Fig. 3.2(a) and the extracted  $\kappa_d$  and  $\Delta\omega_0$  are shown in Fig. 3.2(c). The load admittance,  $Y$ , is derived in

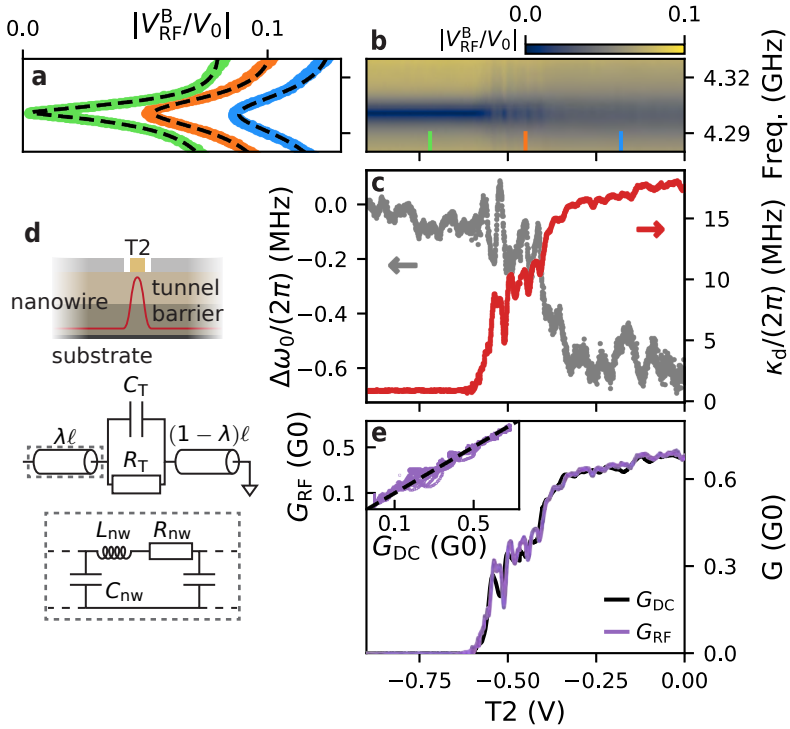


Figure 3.2: Pinchoff measurements. **(a)**, **(b)** Response of the conductance resonator to the tunnel gate voltage T2 and linecuts at the indicated gate voltages in **(b)** offset for clarity. **(c)** Frequency shift  $\Delta\omega_0$  and internal resonator decay  $\kappa_d$  extracted from individual resonator line traces of **(b)**. **(d)** Schematic of the nanowire for the experiment in **(b)** with the corresponding lumped-element model used to convert between resonator admittance and conductance  $G_{RF}$ . **(e)** Conductance  $G_{DC}$ , measured with standard voltage-biased current measurements, together with the conductance  $G_{RF}$  extracted from **(c)**. The inset shows the conductance  $G_{RF}$ , as a function of conductance  $G_{DC}$ , for the gate response of all tunnel gate voltages T1 through T6. The dashed line indicates  $G_{DC} = G_{RF}$ . The individual traces are included in Sec. 3.7.4. All measurements in this figure are taken at  $V_B = 10\text{mV}$  while unused gates are included in 0V such that only the active tunnel gate can deplete the nanowire.

Sec. 3.7.1 to be

$$Y = \frac{\pi}{Z_0\omega_0} \left( \frac{1}{2} \Delta\kappa_d - i\Delta\omega_0 \right), \quad (3.1)$$

which holds for a transmission line resonator of characteristic impedance  $Z_0$  coupled to a high impedance load  $1/|Y| \gg Z_0$ . We estimate  $Z_0 = 116\Omega$  from the resonator design. See Appendix C for more details of the resonator fitting procedure.

Importantly, the load admittance at finite frequency does not directly translate to the DC conductance of the coupled device (i.e. the nanowire). The nanowire itself has an inductive component and the gates surrounding the nanowire add additional shunting capacitive paths to ground, contributing to the load admittance especially for higher frequencies. Our device design using high-capacitance gates necessitates compensating for these contributions explicitly, in contrast to the experiments in Refs. [170, 171,

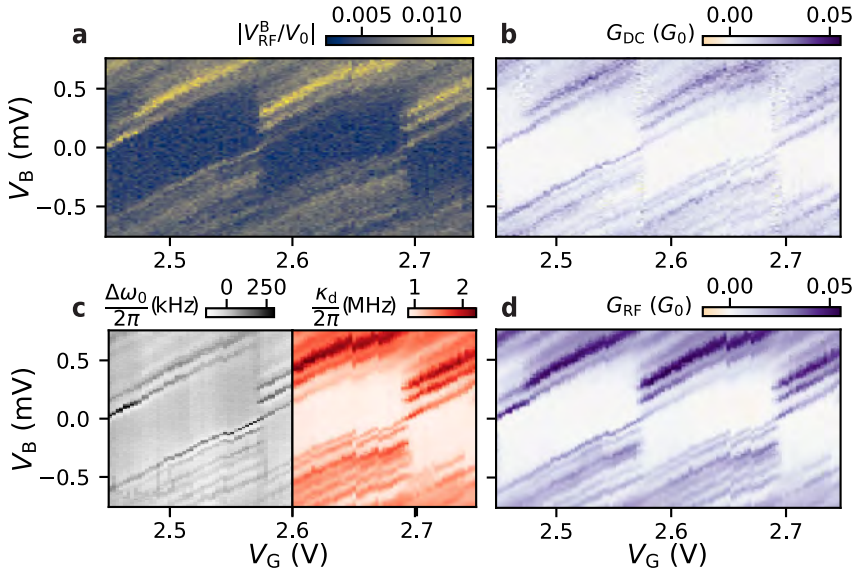


Figure 3.3: Coulomb blockade diamonds measured in a single quantum dot. (a) Single-frequency response near the  $\approx 4.3$  GHz resonance of the resonator. (b)  $G_{DC}$  measurements obtained with standard lock-in measurements at 37 Hz. (c) Frequency shift  $\Delta\omega_0$  and resonator decay rate  $\kappa_d$  extracted from frequency traces. (d) Conductance  $G_{RF}$  extracted from the resonator data in (c).

183]. To account for these effects, we model the load admittance  $Y$  as in Fig. 3.2(d), describing an effective transmission line formed by the nanowire split by a tunnel junction. We denote the series resistance, inductance and parallel capacitance per unit length of this transmission line by  $R_{nw}$ ,  $L_{nw}$  and  $C_{nw}$  and introduce  $Z_{nw} = \ell(R_{nw} + i\omega L_{nw})$  with  $\ell$  the nanowire length. The DC conductance of the nanowire can be calculated from its intrinsic impedance  $Z_{nw}$  and the impedance of the tunnel junction  $Z_T$ .

The relation between  $Z_T$  and  $Y$  depends on the fractional position of the tunnel junction along the nanowire, which we parameterize by  $\lambda \in [0, 1]$ . Explicitly, the relation is given by

$$Z_T = \frac{\frac{Z_{nw}}{\gamma\ell}}{\cosh((1-\lambda)\gamma\ell)} \frac{\frac{YZ_{nw}}{\gamma\ell} \sinh(\gamma\ell) - \cosh(\gamma\ell)}{\sinh(\lambda\gamma\ell) - \frac{YZ_{nw}}{\gamma\ell} \cosh(\lambda\gamma\ell)}, \quad (3.2)$$

where  $\gamma \equiv \sqrt{(R_{nw} + i\omega L_{nw})i\omega C_{nw}}$  denotes the complex propagation constant.

The constants  $Z_{nw}$  and  $\gamma\ell$  are determined from two SHF calibration measurements. For the first calibration measurement, the load impedance  $Y_0$  is measured when all gates are open at 0V, corresponding to the limit that  $Z_T = 0$ . For the second calibration measurement, the load impedance  $Y_p$  as  $|Z_T| \rightarrow \infty$  and  $\lambda = 1$  is measured by tuning the rightmost gate voltage T6 into pinchoff. Solving the resulting two equations for  $\gamma\ell$  and  $Z_{nw}$  yields

$$\gamma\ell = \operatorname{arctanh}\left(\sqrt{\frac{Y_p}{Y_0}}\right) \text{ and } Z_{nw} = \frac{\gamma\ell}{\sqrt{Y_p Y_0}}. \quad (3.3)$$

Using Eq. (3.2) and Eq. (3.3), we then extract  $Z_T$  from the admittance  $Y$ . We model the junction as a resistor  $R_T$  and capacitor  $C_T$  in parallel such that  $Z_T^{-1} \equiv 1/R_T + i\omega C_T$  [191], and then determine the DC-equivalent conductance as

$$G_{\text{RF}}^{-1} = \text{Re}(Z_{\text{nw}}) + 1/\text{Re}(Z_T^{-1}). \quad (3.4)$$

See Sections 3.7.2 and 3.7.3 for the derivation of eqs.3.2-3.4 and for details of measuring  $Y_{p/o}$ , respectively. To validate our method of inferring the conductance, we compare it with the conductance obtained from a control experiment using conventional DC-current detection. Fig. 3.2(e) shows the conductance extracted from DC measurements  $G_{\text{DC}}$  and the DC conductance extracted from the resonator response  $G_{\text{RF}}$ . Excellent agreement is observed between  $G_{\text{RF}}$  and  $G_{\text{DC}}$  for data from pinchoff traces of T1 through T6, changing  $\lambda$  according to the position of the gate, shown in the inset of Fig. 3.2 (e).

Applications of RF conductance are not limited to measuring the impedance of tunnel gates [173, 192–194]. As an example, we probe a quantum dot by tuning T2 and T3 into a tunneling regime and modulating the gate voltage  $V_G$ , leaving the other gates at 0V. We show the amplitude response of the lead resonator on resonance in Fig. 3.3(a) as a function of bias voltage  $V_B$  and gate voltage  $V_G$ . Even though the amplitude response is not translated into DC conductance here, it shows all the qualitative features present in the control data measured by DC lock-in conductance (Fig. 3.3(b)), including the excited states of the quantum dot. The amplitude response of Fig. 3.3(a) is part of a full frequency trace, measured to also allow for a quantitative comparison between the DC results and the resonator response. From these traces, the frequency shift  $\Delta\omega_0$  and photon decay  $\Delta\kappa_d$  are extracted and shown in Fig. 3.3(c). We use the model defined by Eqs. (3.1 - 3.4) to obtain  $G_{\text{RF}}$ , shown in Fig. 3.3(d). This is the same model used for the tunnel junction scans of Fig. 3.2. Note that we neglect here the finite width occupied by the quantum dot and its internal structure; nevertheless we observe reasonable agreement between  $G_{\text{RF}}$  and  $G_{\text{DC}}$ .

### 3.4. RAPID MULTIPLEXED REFLECTOMETRY

We now move on to the capacitively coupled gate resonators and investigate DGS in the DQD regime [95, 134, 135, 137–141, 159, 174, 195, 196]. To tune the system into a DQD, the gate voltages T4, T5, and T6 are each decreased into a tunneling regime. Accordingly, two quantum dots are formed under the rightmost two top gates in the nanowire [191].

A resonator is coupled to both dots to sense the electronic compressibility of the individual dots [123, 125]. In Fig. 3.4 we show a charge stability diagram (CSD) using  $V_L$  and  $V_R$  to change the electron occupation of the DQD. We perform pulsed readout with an integration time of 3  $\mu\text{s}$  per point, constituting a total data acquisition time of 30 ms for the entire CSD [172, 197]. The data acquisition is frequency-multiplexed for both resonators such that the data in Figures 3.4(a) and 3.4(b) are measured simultaneously [154, 185]. Multiplexing not only reduces the measurement time, but also guarantees that the measurements in Figures 3.4(a) and 3.4(b) correspond to the exact same physical regime, regardless of charge jumps and gate hysteresis. To emphasize the correspondence between Figures. 3.4(a) and 3.4(b), the same guides to the eye outlining stable charge configurations are drawn in both panels.

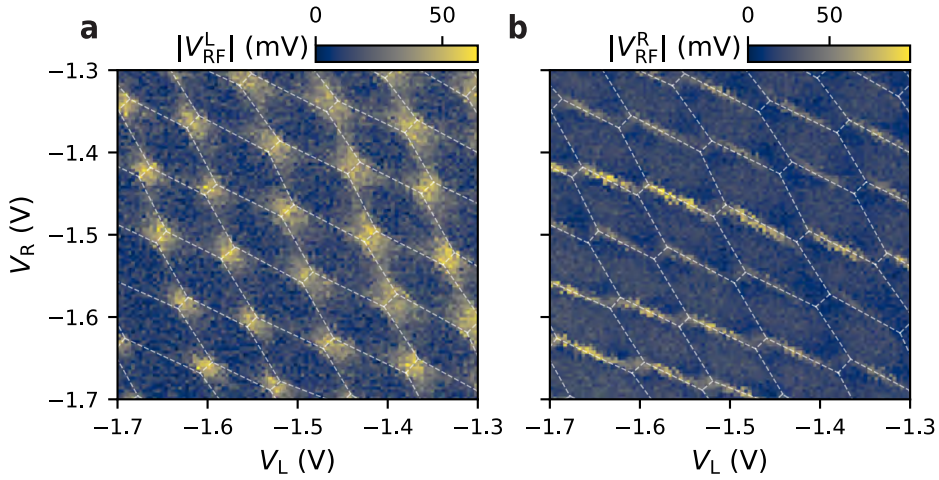


Figure 3.4: Charge stability diagram measured using multiplexed gate-based readout in the double dot regime. (a), (b) Amplitude response of the resonators coupled to the two rightmost quantum dots. Readout power in the feedline is  $-105$  dBm per multiplexed resonator with an integration time of  $3\mu\text{s}$ . The dimensions of this dataset are  $101 \times 101$  points yielding a total integration time of 30 ms excluding overhead from gate settling time, set by low-pass filters on the gate wiring. The dashed lines are guides to the eye delineating the different charge configurations of the double dot and are identical in (a) and (b).

Resonators are only sensitive to charge transitions involving the quantum dots to which they are coupled. Therefore, both resonators detect the interdot transitions; however, transitions from the right dot to the right electrode are detected only by the resonator connected to the right dot. Here, the resonator connected to the left dot does not respond to transitions between the left dot and the left electrode. We attribute this to a mismatched left dot - left electrode tunnel coupling. Hence, multiplexing also enables spatial correlation of electron tunneling by comparing the DGS signal from each gate's resonator, effectively 'tracking' the electron through the device.

### 3.5. SIGNAL TO NOISE

Finally, we investigate the attainable SNR for resolving charge tunneling with DGS by changing detuning from charge degeneracy in the DQD. This procedure serves as a proxy for different qubit states in schemes where readout is based on state-dependent tunneling [10, 11, 138, 141, 189, 198]. Because actual qubit systems have limitations on the readout power [186], we investigate the SNR both at a fixed 'low' excitation voltage in the resonator,  $V_e = 5\mu\text{V}$ , as well as at an optimized excitation voltage,  $V_e = 0.16\text{mV}$ . These excitation voltages are calculated from the signal generator output power and line attenuation in addition to the resonator frequency and coupling capacitance to the feedline.

We fix the total charge in the system by pinching off gates on either side of the DQD. The only remaining transitions are interdot transitions occurring through a tunnel coupling denoted by  $t_C$ . The resonator response as a function of the energy detuning  $\delta$  from the interdot transition is shown in Fig. 3.5(a). We determine  $t_C$  by fitting the resonator response to an input-output model [175], see Sec. 3.7.5. Linecuts of the fit results and

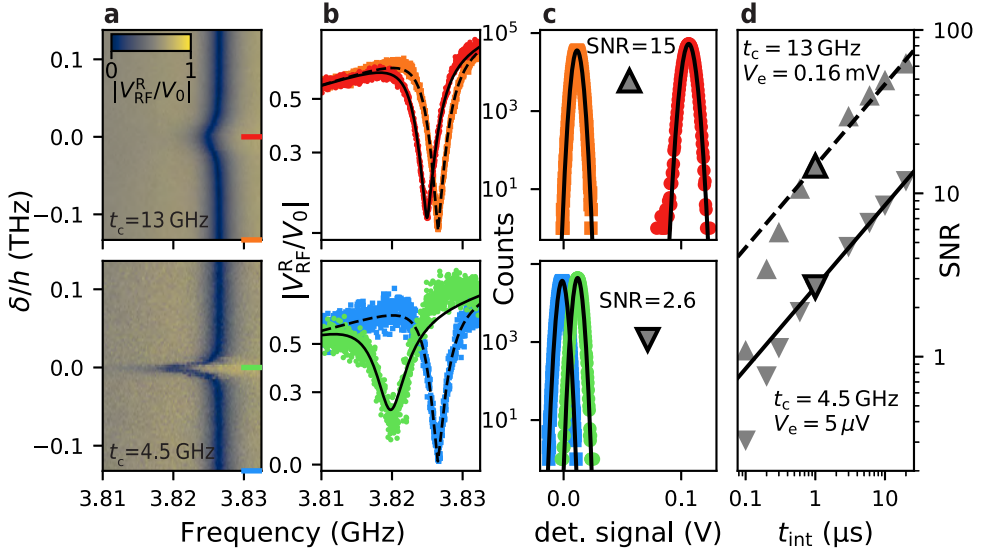


Figure 3.5: Readout SNR. **(a)** Amplitude response as a function of detuning  $\delta$  of the resonator coupled to the right dot for the two different tunnel coupling regimes. **(b)** Linecuts for Coulomb blockade and on resonance ( $\delta = 0$ ) together with fits to the theoretical model. **(c)** Histograms of the resonator responses in Coulomb blockade and charge degeneracy, with pulse length of  $1 \mu\text{s}$ . Responses are acquired with a probe frequency tuned to resonance for the Coulomb blockade case, at approximately 3.826 GHz. **(d)** Attained SNR on the right dot's resonator, defined as  $\Delta/(2\sigma)$ , as a function of measurement pulse length, optimized with excitation voltage as a free parameter (upward triangles) and optimized at fixed excitation voltage of  $5 \mu\text{V}$  (downward triangles). The expected square-root dependence for longer  $t_{\text{int}}$  is shown with dashed and solid lines.

measurement data are shown in Fig. 3.5(b).

We define SNR as the change in signal between charge degeneracy and Coulomb blockade divided by the noise. To measure it, we perform a series of pulsed measurements of complex-valued  $V_{\text{RF}}^{\text{R}}$  with a pulse time of  $t_{\text{int}}$  at both Coulomb blockade and charge degeneracy, and show the obtained histograms for an integration time of  $t_{\text{int}} = 1 \mu\text{s}$  in Fig. 3.5(c). These histograms are fit with a Gaussian to extract the separation between the Gaussian peaks  $\Delta$  in the complex  $V_{\text{RF}}^{\text{R}}$  plane as well as their average standard deviation  $\sigma$  representing the width. The SNR is given by  $\Delta/(2\sigma)$ . More details are given in Sec. 3.7.5.

In Fig. 3.5(d) we plot the dependence of SNR on  $t_{\text{int}}$ , which approaches a square-root dependence (dashed and solid lines) for longer times. We attribute the discrepancy between attained SNR and a square-root dependence for pulse times shorter than  $1 \mu\text{s}$  to the finite bandwidth of the resonators. For these pulse lengths, the resonator cannot reach a steady-state photon population within the integration time, limiting the signal available for readout.

Next, we compare the observed SNR with expected theoretical limits. The change in signal at the feedline level  $\Delta_{\text{f}} = \Delta/G_{\text{sys}}$ , with  $G_{\text{sys}}$  the gain of the amplification chain in the system, can never exceed the total voltage swing in the feedline  $V_{\text{f}}$ . The fit to the data in Fig. 3.5(a), used to extract  $t_{\text{c}}$ , also provides a direct measurement of the ra-

tio  $\Delta_f/V_f = 0.89$ , close to the absolute maximum. In other words, the resonator is coupled near optimally for this tunnel coupling, such that its external coupling rate is nearly equal to the dispersive shift. The achievable SNR is then set by  $\Delta_f$  together with noise temperature,  $T_N$ , and readout time,  $t_{\text{int}}$ , as

$$\text{SNR} = \frac{\Delta_f \sqrt{t_{\text{int}}}}{2\sqrt{Z k_B T_N}}, \quad (3.5)$$

where  $Z = 50\Omega$  is the impedance of the feedline [116], see Sec. 3.7.6. The  $\text{SNR} \approx 2.6$  found in Fig. 3.5(c) together with the readout time  $t_{\text{int}} = 1\mu\text{s}$  and the deduced approximate voltage swing in the feedline,  $V_f = 0.15\mu\text{V}$  corresponds to a noise temperature estimate of  $T_N = 1\text{K}$ . Without the use of a TWPA, we expect that the noise temperature would increase to  $T_N \approx 4\text{K}$ . To improve the SNR, one can increase either the readout time or readout power in accordance with Eq. (3.5), as shown in Fig. 3.5(d). Practically, limits to these two parameters will be determined by the specific qubit implementation. In this case, by optimizing the excitation voltage and tunnel coupling together, a SNR of 15 is achieved at  $V_e = 0.16\text{mV}$ .

## 3.6. CONCLUSIONS

We show the characterization of an InAs nanowire multi-QD system using gigahertz-frequency sensing. Probing the finite frequency admittance of the nanowire allows us to infer the low-frequency conductance with good accuracy, even without calibration from DC measurements. Further, we show high-SNR dispersive sensing on timescales near the bandwidth limit set by the quality factor of the resonators. Besides the use for qubit devices, we envision that fast multiplexed readout of quantum devices may be used for more complex sensing schemes. In particular, conducting multiple rapid local measurements simultaneously could facilitate unique quantum transport experiments because they provide spatial information about tunneling processes. For example, by probing two quantum dots at either end of a central charge island, tunneling events into the outer dots may be correlated [105, 199]. We conclude that multiplexed SHF resonators may serve as a complete toolset for characterization and readout of semiconductor quantum devices, and present intriguing opportunities for developing high-speed quantum transport measurement schemes.

Raw data, analysis code, and scripts for plotting the figures in this chapter are available via the online data repository [200]. We thank D. Bouman and J.D. Mensingh for nanowire deposition and A. Bargerbos for valuable comments on the manuscript. We further thank N.P. Alberts, O.W.B. Benningshof, R.N. Schouten, M.J. Tiggelman, and R.F.L. Vermeulen for valuable technical assistance. This work is supported by the Netherlands Organization for Scientific Research (NWO) and Microsoft.

## 3.7. SUPPLEMENTAL MATERIAL

### 3.7.1. CORRESPONDENCE BETWEEN $Y$ AND RESONATOR RESPONSE

Here we relate the nanowire load admittance to the quality factor and resonance frequency of a resonator connected to its lead. Throughout the following derivations, we assume that within the small window of frequencies used to fit our resonator's resonance

frequency and quality factor, the sample load admittance  $Y$  is constant. The resonator is modeled as a transmission line capacitively coupled to a central feedline and terminated by a load impedance  $Y^{-1}$  determined by the nanowire. Assuming the feedline coupler to behave as a lumped element capacitance  $C_c$ , the input impedance  $Z_{\text{in}}$  of the terminated resonator and coupler is [116]:

$$Z_{\text{in}} = \frac{1}{i\omega C_c} + Z_0 \frac{1 + Z_0 Y \tanh(\gamma_r \ell_r)}{Z_0 Y + \tanh(\gamma_r \ell_r)}, \quad (3.6)$$

where  $Z_0$  is the line's characteristic impedance,  $\gamma_r \equiv \alpha_r + i\beta_r$  is the complex propagation constant, and  $\ell_r$  is the length of the resonator. Note that  $\beta_r = \omega/v_p$  where  $v_p$  is the phase velocity in the transmission line, while  $\alpha_r$  quantifies internal losses. To simplify the above expression, we first note the trigonometric relation

$$\begin{aligned} \tanh(\alpha_r \ell_r + i\beta_r \ell_r) &= \frac{\sinh(\alpha_r \ell_r) \cos(\beta_r \ell_r) + i \cosh(\alpha_r \ell_r) \sin(\beta_r \ell_r)}{\cosh(\alpha_r \ell_r) \cos(\beta_r \ell_r) + i \sinh(\alpha_r \ell_r) \sin(\beta_r \ell_r)} \\ &\sim \frac{\alpha_r \ell_r \cos(\beta_r \ell_r) + i \sin(\beta_r \ell_r)}{\cos(\beta_r \ell_r) + i \alpha_r \ell_r \sin(\beta_r \ell_r)} \end{aligned} \quad (3.7)$$

where we have assumed small internal losses in the resonator,  $\alpha_r \ell_r \ll 1$ . Since the load admittance is assumed to be small, our resonator nearly has an open at one end. Consequently, the effect of  $Y$  should be that of a perturbed  $\lambda/2$  resonator. In this case, for small detuning  $\delta\omega$  from the resonance frequency  $\omega_0$ ,  $\beta_r \ell_r \sim \pi + \pi\delta\omega/\omega_0$  [116]. Since  $Y$  is a small perturbation of the load admittance away from zero, it will shift the resonance frequency only slightly, in which case it is still true that  $\beta_r \ell_r \sim \pi + x$  where  $x$  is a small number. Applying this approximation to Eq. 3.7, we find  $\tanh(\gamma_r \ell_r) \sim \alpha_r \ell_r + i \tan(\beta_r \ell_r)$ . Finally, we assume  $\omega$  is near resonance such that we may apply the limit  $\tan(\beta_r \ell_r) \ll 1$  by the above argument, which in combination with our assumption of small load admittance  $Y \ll Z_0^{-1}$  and losses  $\alpha_r \ell_r \ll 1$  simplifies Eq. 3.6 to:

$$Z_{\text{in}} \sim \frac{1}{i\omega C_c} + \frac{Z_0}{Z_0 Y + \alpha_r \ell_r + i \tan(\beta_r \ell_r)} = \frac{1}{i\omega C_c} + \frac{Z_0}{\alpha_{\text{eff}} \ell_r + i [\tan(\beta_r \ell_r) + Z_0 \text{Im}(Y)]} \quad (3.8)$$

to first order in these small parameters. Above, we defined the effective dissipation constant  $\alpha_{\text{eff}} \ell_r \equiv \alpha_r \ell_r + Z_0 \text{Re}(Y)$ .

Next, we determine the relation between  $\text{Im}(Y)$  and the resonance frequency  $\omega_0$ . At resonance, the imaginary part of  $Z_{\text{in}}$  disappears, so we solve this condition for  $\omega_0$ :

$$0 = \text{Im}(Z_{\text{in}}) = -\frac{1}{\omega_0 C_c} - Z_0 \frac{\tan(\omega_0 \ell_r / v_p) + Z_0 \text{Im}(Y)}{(\alpha_{\text{eff}} \ell_r)^2 + (\tan(\omega_0 \ell_r / v_p) + Z_0 \text{Im}(Y))^2}. \quad (3.9)$$

With the foresight that internal quality factors of our resonators will be related to  $\alpha_{\text{eff}} \ell_r$  through  $\alpha_{\text{eff}} \ell_r = \pi/(2Q_i)$ , from resonator fits we may estimate that  $\alpha_{\text{eff}} \ell_r < 0.002$  even when the nanowire is completely open. In our resonator chip, coupling capacitances are on the order of 40 fF, so that at few-GHz frequencies and when  $Z_0 = 116\Omega$ ,  $\omega_0 C_c Z_0 \approx 0.03$  to 0.1 is a small parameter, but still much larger than  $\alpha_{\text{eff}} \ell_r$ . Rearranging and neglecting terms above first order in  $\alpha_{\text{eff}} \ell_r / (Z_0 \omega C_c)$ , we obtain the implicit solution:

$$\frac{\omega_0 \ell_r}{v_p} = n\pi - \arctan(Z_0 \text{Im}(Y) + \omega_0 C_c Z_0), \quad n \in \mathbb{Z} \quad (3.10)$$

The smallest substantial resonance frequency occurs for  $n = 1$ , constituting the GHz-range resonances of interest. Taylor expanding in the small parameters  $Z_0 \text{Im}(Y)$  and  $\omega_0 C_c Z_0$ , we see then that the coupling capacitance serves only to impose a constant perturbation to the bare resonance frequency, defined as  $\omega_0^* \equiv \omega_0|_{\text{Im}(Y)=0} = \pi(\ell_r/\nu_p + C_c Z_0)^{-1}$ :

$$\omega_0 = \omega_0^* \left( 1 - \frac{Z_0 \text{Im}(Y)}{\pi} \right). \quad (3.11)$$

At frequencies near resonance such that  $\omega = \omega_0 + \delta\omega$  with  $\delta\omega \ll \omega_0$ , Eq. 3.8 is asymptotic to:

$$Z_{\text{in}} \sim \frac{1}{i\omega C_c} + \frac{Z_0}{\alpha_{\text{eff}}\ell_r + i\pi\delta\omega/\omega_0}, \quad \delta\omega \ll \omega_0, \alpha_{\text{eff}}\ell_r \ll Z_0\omega_0 C_c \ll 1, \quad (3.12)$$

which is the input impedance of a capacitively coupled parallel  $LRC$  resonator circuit near resonance of internal quality factor  $Q_i = \pi/(2\alpha_{\text{eff}}\ell_r)$  [116]. The internal quality factor is related to the photon decay rate by  $\kappa_d \equiv \omega_0/Q_i = 2\omega_0\alpha_{\text{eff}}\ell_r/\pi$ . From the definitions of  $\alpha_{\text{eff}}\ell_r$  and  $\omega_0$ , we can thus relate the device admittance to resonator parameters through:

$$Y = \frac{1}{Z_0} \left( \alpha_{\text{eff}}\ell_r - \alpha_r\ell_r \right) - i \frac{\pi}{Z_0\omega_0} \left( \omega_0 - \omega_0^* \right) \equiv \frac{\pi}{Z_0\omega_0} \left( \frac{1}{2}\Delta\kappa_d - i\Delta\omega \right), \quad (3.13)$$

valid to first order in  $\Delta\omega/\omega_0$ , where  $\Delta\omega \equiv \omega_0 - \omega_0^*$  and  $\Delta\kappa_d \equiv \kappa_d - 2\omega_0\alpha_r\ell_r/\pi$ . In other words, load conductance is proportional to shifts in the resonator's internal decay factor, while its susceptance is proportional to shifts in the resonance frequency.

### 3.7.2. DERIVATION OF $G_{\text{RF}}$

Since the nanowire device is covered at most points by a capacitively coupled gate layer of uniform thickness (excluding the small gaps between gates), we model the nanowire as a highly resistive transmission line, and aim to solve for its admittance  $Y$ . As per the lumped element model of Fig. 3.2(d), we parameterize this with a resistance, inductance, and capacitance per unit length of  $R_{\text{nw}}$ ,  $L_{\text{nw}}$ , and  $C_{\text{nw}}$ , respectively. At a fraction  $\lambda$  along the wire's length  $\ell$ , we include a lumped element impedance  $Z_T$ , modeling a cutter gate or quantum dot.

As a transmission line, on either side of  $Z_T$  the nanowire obeys the telegrapher equations [116]:

$$\frac{dV(x)}{dx} = -Z_{\text{nw}}I(x)/\ell \quad \text{and} \quad \frac{dI(x)}{dx} = -i\omega C_{\text{nw}}V(x), \quad (3.14)$$

at every point  $x$  along the wire's length, with  $x = 0$  denoting the source lead. Above, we have assumed phasor solutions of the voltage  $v$  with respect to ground and current  $i$  through the wire so that  $v(x, t) = V(x)e^{i\omega t}$  and  $i(x, t) = I(x)e^{i\omega t}$ . On either side of the impedance  $Z_T$ , these coupled differential equations have the solution:

$$V(x) = \begin{cases} V_s^+ e^{-\gamma x} + V_s^- e^{\gamma x} & x < \lambda\ell \\ V_d^+ e^{-\gamma x} + V_d^- e^{\gamma x} & x > \lambda\ell \end{cases}, \quad I(x) = \begin{cases} \frac{\gamma\ell}{Z_{\text{nw}}} (V_s^+ e^{-\gamma x} - V_s^- e^{\gamma x}) & x < \lambda\ell \\ \frac{\gamma\ell}{Z_{\text{nw}}} (V_d^+ e^{-\gamma x} - V_d^- e^{\gamma x}) & x > \lambda\ell \end{cases} \quad (3.15)$$

The nanowire's input admittance is  $Y = I(0)/V(0)$  and is fully determined by the boundary condition of a grounded wire  $V(\ell) = 0$ , current continuity just before and after  $Z_T$ ,

and Ohm's law across  $Z_T$ . Combined, these three conditions allow us to solve for all constants  $V_s^-$ ,  $V_d^-$ , and  $V_d^+$  in terms of  $V_s^+$ . In particular:

$$V_s^- = V_s^+ \left[ \frac{\frac{Z_T \gamma \ell}{Z_{nw}} (e^{-2\gamma \lambda \ell} + e^{-2\gamma \ell}) - 2e^{-2\gamma \ell}}{\frac{Z_T \gamma \ell}{Z_{nw}} (1 + e^{-2\gamma(1-\lambda)\ell}) + 2} \right] \quad (3.16)$$

After substituting Eq. 3.15 into the definition of  $Y$ , we arrive at the expression

$$Y = \frac{\gamma \ell}{Z_{nw}} \left( \frac{V_s^+ - V_s^-}{V_s^+ + V_s^-} \right) = \frac{\gamma \ell}{Z_{nw}} \left[ \frac{\cosh(\gamma \ell) + \frac{Z_T \gamma \ell}{Z_{nw}} \sinh(\gamma \lambda \ell) \cosh(\gamma(1-\lambda)\ell)}{\sinh(\gamma \ell) + \frac{Z_T \gamma \ell}{Z_{nw}} \cosh(\gamma \lambda \ell) \cosh(\gamma(1-\lambda)\ell)} \right]. \quad (3.17)$$

Finally, this expression may be rearranged to yield Eq. 3.2. Together, Eq. 3.2 and Eq. 3.4 yield an explicit formula for  $G_{RF}$ . Substituting the  $Z_T$  result into Eq. 3.4 we obtain:

$$G_{RF} = \frac{|z_\lambda| \cos(\arg[z_\lambda] - \arg[z_1])}{\text{Re}(Z_{nw})|z_\lambda| \cos(\arg[z_\lambda] - \arg[z_1]) + |z_1|}. \quad (3.18)$$

Above, the parameters

$$z_1 \equiv \sinh(\gamma \ell) Y - (\gamma \ell / Z_{nw}) \cosh(\gamma \ell), \quad (3.19)$$

and

$$z_\lambda \equiv (\gamma \ell / Z_{nw}) \cosh(\gamma(1-\lambda)\ell) [(\gamma \ell / Z_{nw}) \sinh(\gamma \lambda \ell) - \cosh(\gamma \lambda \ell) Y] \quad (3.20)$$

represent singularities of  $Z_T^{-1}$  and  $Z_T$  respectively.

### 3.7.3. DETERMINATION OF $\gamma \ell$ AND $Z_{nw}$ FROM EXPERIMENTAL DATA

As described in Sec. 3.3, the determination of  $\gamma \ell$  and  $Z_{nw}$  requires a measurement of the admittance in both the conducting and pinched-off regime. Since there are many measurements of the admittance in both regimes, we here describe the procedure to fix  $Y_p$  and  $Y_o$ . To approach the open and pinched-off regimes as precisely as possible, the approach is to take the admittances that are furthest removed from the pinched-off and open regime respectively. In practice, before we determine the admittance in the pinched-off regime of T6,  $Y_p$ , we first select any admittance data point where all gates are open  $\tilde{Y}_o$ . We then find  $Y_p$  as the point in the T6 pinchoff measurement that is furthest removed from  $\tilde{Y}_o$ . Subsequently, we determine  $Y_o$  by finding the admittance furthest removed from  $Y_p$  in the aggregated data for all tunnel gates. The aggregate data is shown in Fig. 3.6(b), with the datasets from the T6 pinchoff measurement highlighted in blue. The obtained points  $\tilde{Y}_o$ ,  $Y_p$  and  $Y_o$  are also identified in the figure. We obtain  $\gamma \ell = 0.6 + 0.3i$  and  $Z_{nw} = (16.7 + 3.6i) \text{ k}\Omega$ .

### 3.7.4. COMPARISON OF $G_{DC}$ AND $G_{RF}$ FOR ALL PINCHOFF CURVES

Here, we provide a more detailed overview of all admittance data obtained and used for the inset in Fig. 3.2(e) and for Fig. 3.2(c). The calibration frequency trace used for the data in Fig. 3.2 is shown in Fig. 3.6(a) together with a fit to Eq. (C.1). We find  $\omega_0/2\pi = 4.3 \text{ GHz}$ ,  $\kappa_{\text{ext}}/2\pi = (18.6 - 3.4i) \text{ MHz}$  and  $\kappa_d/2\pi = 0.9 \text{ MHz}$ . The calibration measurement defines

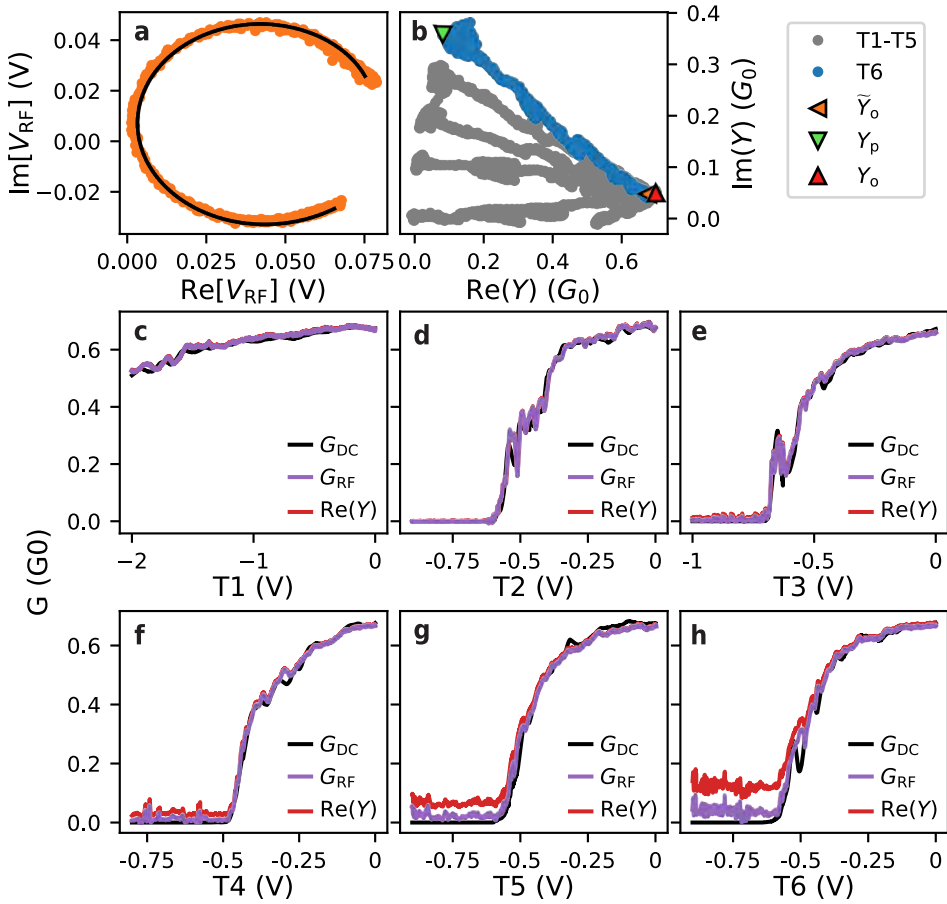


Figure 3.6: Supplemental data for pinch-off measurements. (a) Resonator response in the complex plane together with a fit with Eq. (C.1). The phase delay of the line corresponding to  $e^{i(\theta_0+\theta_1\omega)}$  in Eq. (C.1) is removed from both the data and the fit. (b) Admittance data for all pinch-off measurements. The data obtained for T6 is highlighted in blue. (c) to (h) Conductance measured with DC techniques together with the conductance  $G_{\text{RF}}$  extracted from the admittance in (b). To show the importance of correcting for the finite frequency effects in the nanowire, the real part of the admittance is also shown.

the zero-point of  $\Delta\omega_0$  and  $\Delta\kappa_i$ . We also use the calibration to hold all parameters except for  $\omega_0$  and  $\kappa_i$  fixed when fitting the frequency traces for obtaining the pinch-off data, such as in Fig. 3.2(b). The Root-mean-square error is used to identify points where the fitting algorithm fails to identify the correct resonator line shape. Using this method, we have identified and excluded 7 outliers from subsequent analysis and plotting compared to the 15006 fits used for Fig. 3.2.

Similar to Fig. 3.2(e), we plot a comparison between  $G_{\text{DC}}$  and  $G_{\text{RF}}$  for all tunnel gates in Fig. 3.6c-h. Additionally, we therein show the real part of the admittance, equivalent by definition to the finite frequency conductance. All traces are taken at  $V_{\text{B}} = 10$  mV and every gate that is not being swept is kept at 0V. This ensures the nanowire can only be

depleted close to the swept tunnel gate. The further the tunnel gate is from the source of the nanowire, the more important the correction for finite frequency effects is to obtain the correct  $G_{\text{RF}}$ . This is expected since a larger portion of the shunting capacitance is available as an alternative path to ground which becomes more dominant the closer the nanowire is to pinch-off.

### 3.7.5. SNR MEASUREMENT

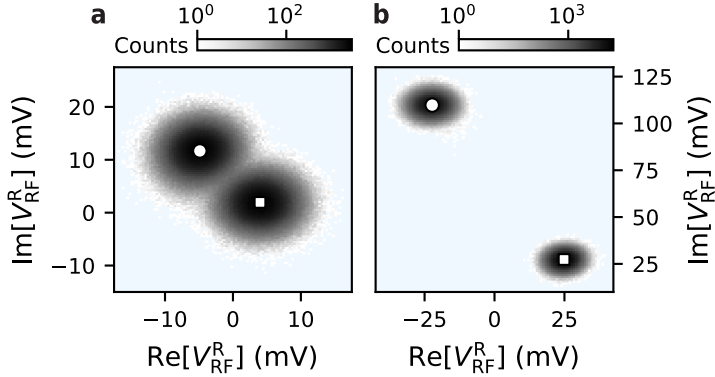


Figure 3.7: Supplemental data for SNR measurements. Histograms of the resonator response in the complex plane with a pulse length of  $t_{\text{int}} = 1 \mu\text{s}$ , corresponding to the two regimes in Fig. 3.5. Both histograms contain measurements for Coulomb blockade (square marker) and on charge degeneracy (circle marker). (a) Histogram for  $t_C = 4.5 \text{ GHz}$  and  $V_e = 5 \mu\text{V}$ . (b) Histogram for  $t_C = 13 \text{ GHz}$  and  $V_e = 0.16 \text{ mV}$ .

Herein we describe how SNR and tunnel coupling was extracted from the data of Fig. 3.5. For fitting the dispersive shift as a function of detuning  $\delta$ , we add the contribution of the DQD to Eq. (C.1). This contribution is accounted for by substituting  $\kappa_d \rightarrow \kappa_d - 2ig\chi$  in Eq. (C.1) caused by coupling to the susceptibility of the DQD [175] with

$$g\chi = \frac{4g_0^2 t_C^2 / \Omega^2}{\omega_0 - \Omega + i\gamma/2}, \quad (3.21)$$

where  $g$  is the effective coupling strength and  $\chi$  the susceptibility of the DQD. Furthermore,  $g_0$  is the Jaynes-Cummings coupling,  $\Omega = \sqrt{4t_C^2 + \delta^2}$  is the DQD energy splitting,  $t_C$  is the tunnel coupling between the dots and  $\gamma$  is the decoherence rate.

The SNR is measured by acquiring a histogram of resonator responses with pulse length  $t_{\text{int}}$  in both Coulomb blockade and on charge degeneracy. The resulting histograms in the complex plane are shown in Fig. 3.7. We denote the average response in Coulomb blockade and charge degeneracy by  $\mu_b$  and  $\mu_r$  respectively. To calculate the SNR from the histogram, the data is rotated in the complex plane by an angle  $\text{Arg}(\mu_r - \mu_b)$ . After the rotation, there is no relevant information in the complex part of the data. Therefore we project to data onto the real axis, the result of which is shown in Fig. 3.5(c). We fit a Gaussian to the projected data for Coulomb blockade and charge degeneracy separately yielding the standard deviation  $\sigma_b$  and  $\sigma_r$  respectively. Finally, the SNR is given

by

$$\text{SNR} = \frac{|\mu_b - \mu_r|}{\sigma_b + \sigma_r}. \quad (3.22)$$

### 3.7.6. RELATION BETWEEN SNR AND AMPLIFIER NOISE TEMPERATURE

To calculate the relation between SNR and the equivalent noise temperature of the amplifier, we assume that the noise level of the input signal is negligible. The equivalent noise temperature  $T_N$  is defined as

$$T_N = \frac{N_{\text{in}}}{k_B B}, \quad (3.23)$$

where  $B$  denotes the measurement bandwidth and  $N_{\text{in}}$  the equivalent noise input power to the amplifier [116]. Since the integration time,  $t_{\text{int}}$  is longer than any other timescale in the system, the bandwidth is given by  $B = 1/t_{\text{int}}$ .

The voltage fluctuations corresponding to this noise power are  $v = \sqrt{N_{\text{in}} Z}$ , where  $Z$  is the characteristic impedance of the feedline. Using  $G_{\text{sys}}$  to denote the gain of the amplification in the system, the SNR is defined as the ratio between signal  $\Delta = G_{\text{sys}} \Delta_f$  and the noise  $2G_{\text{sys}} v$ . As such, we find the following equation for the SNR

$$\text{SNR} = \frac{G_{\text{sys}} \Delta_f}{2G_{\text{sys}} v} = \frac{\Delta_f \sqrt{t_{\text{int}}}}{2\sqrt{Z k_B T_N}}, \quad (3.24)$$

assuming the SNR is limited by the noise introduced by the finite noise temperature of the amplifiers in the system.



# 4

## CONTROLLABLE SINGLE COOPER PAIR SPLITTING IN HYBRID QUANTUM DOT SYSTEMS

*D. de Jong<sup>†</sup>, C. G. Prosko<sup>†</sup>, L. Han, F. K. Malinowski, Y. Liu, L. P. Kouwenhoven, W. Pfaff*

Cooper pair splitters hold utility as a platform for investigating the entanglement of electrons in Cooper pairs, but probing splitters with voltage-biased Ohmic contacts prevents the retention of electrons from split pairs since they can escape to the drain reservoirs. We report the ability to controllably split and retain single Cooper pairs in a multi-quantum-dot device isolated from lead reservoirs, and separately demonstrate a technique for detecting the electrons emerging from a split pair. First, we identify a coherent Cooper pair splitting charge transition using dispersive gate sensing at GHz frequencies. Second, we utilize a double quantum dot as an electron parity sensor to detect parity changes resulting from electrons emerging from a superconducting island.

### 4.1. INTRODUCTION

Cooper pairs—bound electron pairs of correlated spin and momentum—are foundational to superconductivity. Interestingly, coherently splitting a Cooper pair produces two entangled electrons forming a Bell state [201]. It is possible to force a pair to split using Coulomb repulsion in a pair of quantum dots (QDs) [96]. Accordingly, Cooper pair splitting (CPS) has been demonstrated in various material systems [97–99, 101–107, 109], and the resulting electrons' spin was probed through current correlation measurements exploiting spin-polarized QDs [100, 101]. In order to confirm and utilize entanglement of the electrons from a split pair however, it is important to retain them, for example by removing drain contacts from the QDs. In this manner, retention of electrons from split

---

The work in this chapter has been published in Physical Review Letters **131**, 157001 (2023). arXiv:2208.05154

<sup>†</sup>These authors contributed equally.

Cooper pairs was observed using charge sensing of metallic islands [202], though splitting occurred stochastically at sub-Hz rates. Dispersive gate sensing (DGS) provides distinct information from charge sensing, since it is sensitive to the hybridization between charge states [134, 135, 137–141, 159, 160, 174, 195, 196, 203–205], including between states with a split or recombined Cooper pair.

Probed with DGS, we present the coherent splitting of a single Cooper pair by varying voltages on a device's gate electrodes. Separately, we demonstrate the detection of an unpaired electron emerging from a superconducting island (SCI). This is accomplished within a hybrid system comprising a SCI with normal QDs on either side, decoupled from leads. Multiplexed DGS of resonators coupled to the device's gate electrodes allows us to distinguish charge transitions in the system, and thus label relative charge states. Strikingly, one transition corresponds to two charges from the SCI being loaded into neighboring QDs, imparting a 1 MHz frequency shift on the probed few-GHz frequency resonator. This transition likely corresponds to CPS arising due to crossed Andreev reflection (CAR), supported by fitting the DGS signal across the transition to an input-output theory model for an effective low-energy Hamiltonian. Next, we show how DGS detects changes in the charge parity of a double quantum dot (DQD) system. Consequently, DGS can replace charge sensing in our CPS scheme while retaining electrons tunneling to the DQD, since no external charge reservoirs couple to the system. Combined with spin manipulation and readout techniques [23, 206], these demonstrated capabilities could be used to perform a Bell test on electrons constituting Cooper pairs [207–210].

## 4.2. EXPERIMENTAL DESIGN & SETUP

The devices measured (labeled A and B), shown in Figs. 4.1(a) and 4.1(b), consist of an InAs nanowire with an epitaxial Al shell. For both devices, lithographically patterned gates define five QDs in the wire, though the Al covers only the centermost QD (labeled  $M$ ) such that only this QD has a superconducting pairing interaction. The semiconducting QDs (labeled  $L$ ,  $R$ , and  $P$ ) have a length of  $0.44\ \mu\text{m}$  in both devices, while island  $M$  has a length of  $1.2$  and  $0.44\ \mu\text{m}$  in devices A and B, respectively. Every QD is capacitively coupled via top gates to a coplanar waveguide resonator with a common feedline for multiplexed DGS of each QD [154, 156, 185, 204], depicted in Fig. 4.1(c). Separate gates control the QDs' chemical potentials and tunnel barriers. For additional fabrication details, see Ref. [204]. We infer the charging energy of the semiconducting QDs from Coulomb diamond measurements to be  $E_C^N \approx 250\ \mu\text{eV}$  (Supplemental Sec. 4.7.2). From the charge stability diagrams (CSDs) shown in Fig. 4.1(f), we extract the charging energy of the SCI for device A  $E_C^S \approx 100\ \mu\text{eV}$  and its lowest-energy odd-parity state at zero magnetic field  $E_0 \approx 130\ \mu\text{eV}$ . Similarly, for device B, we obtain  $E_C^S \approx 350$  and  $E_0 \approx 50\ \mu\text{eV}$ . The differing values of  $E_0$  signify the presence of distinct subgap states, and are generally dependent on gate voltages. With devices A and B we thus compare the regimes of  $E_C^S < E_0$  and  $E_C^S > E_0$  respectively, verified by a doubling of charge transitions in device A as magnetic field is increased (Supplemental Fig. 4.9). The former case exhibits a transition corresponding to splitting a Cooper pair, while in the latter it is suppressed in favor of single-electron tunneling.

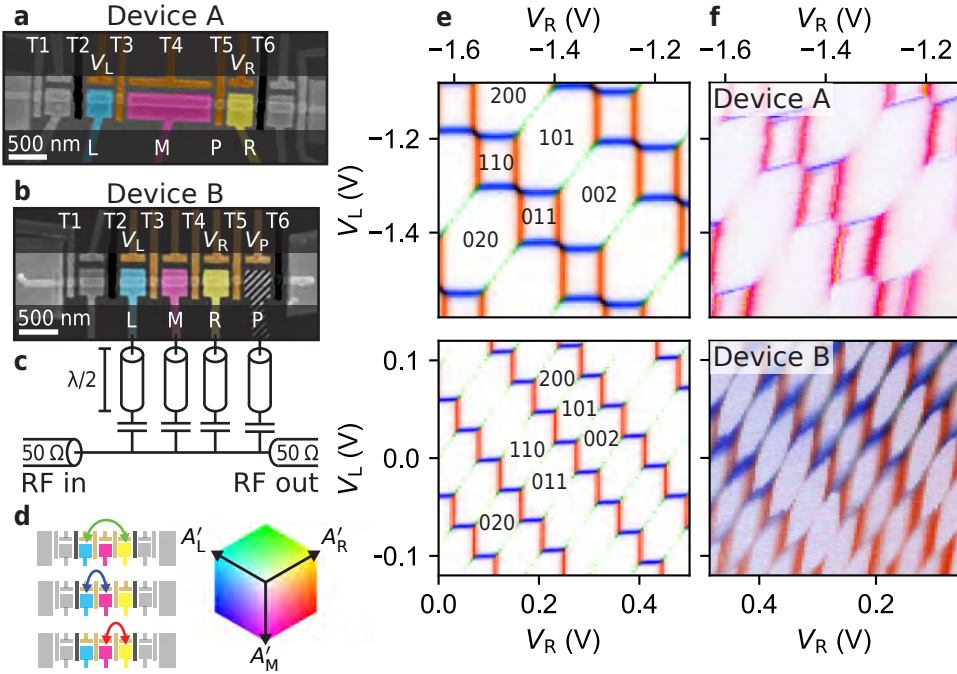


Figure 4.1: Experimental setup and CSDs in the floating TQD regime. **(a),(b)** False-colored SEM images of devices nominally identical to those measured. Device A and B are highlighted in the floating triple and quadruple QD regimes, respectively. Gates are shaded with the assigned colors of their coupled resonators. **(c)** Schematic of the on-chip resonators. We measure transmission through a feedline capacitively coupled to  $\lambda/2$  resonators connected to device gates. **(d)** Shell of the cubic color map for the resonator responses in **(e)**. For each pair of responding resonators, the corresponding tunneling process is depicted. **(e)** Simulated resonator responses using energies given in the main text. **(f)** Measured CSDs of the floating TQD systems. Individual resonator measurements are shown in Supplemental Fig. 4.5. States are labeled with the relative number of electrons in dots L, M, and R, respectively, with 0 charge on island M corresponding to an even charge.

Measurements are conducted in a dilution refrigerator at a base temperature of approximately 20 mK. Low-power signals are amplified by a traveling-wave parametric amplifier [153] and a high-electron-mobility transistor. See Appendix B.1 for more details of the measurement circuit.

### 4.3. TRIPLE DOT CHARGE STABILITY DIAGRAM

We begin by investigating a floating triple quantum dot (TQD) configuration. By measuring a CSD, we obtain the island parity and relative charge occupation for different gate voltages, and thereby infer which charge states hybridize. Both devices are tuned into a TQD by lowering barrier voltages T3 and T4 into weak tunneling regimes. Subsequently, barriers T2 and T5 are set to strongly negative voltages to prevent electrons from tunneling to the leads. In this “floating” regime total charge is conserved, leaving only two charge degrees of freedom. It is therefore sufficient to vary two gate voltages (e.g.,  $V_L$

and  $V_R$ ) to reach any available charge state or transition.

To probe the system's charge stability we employ DGS, measuring complex transmission responses  $A_i$  for  $i \in \{L, M, R\}$  of each of the corresponding top gates' resonators simultaneously with frequency multiplexing. The responses are projected and normalized to produce real-valued quantities  $A'_i$  (Supplemental Sec. 4.7.1), then superimposed in a single CSD to emphasize correlations. The resulting three-dimensional color map and CSDs are shown in Fig. 4.1(d) and Fig. 4.1(f). We observe white Coulomb-blockaded regions separated by charge transitions where electrons hybridize between QDs. As DGS reflects resonant tunneling, the resonators connected to all involved QDs show a response. For the transition between island  $M$  and QDL for example, a response is expected in  $A'_M$  and  $A'_L$ , appearing blue in the CSD. Similarly, the transition between island  $M$  and QDR appears red. These transitions are most prominent since they are first-order tunneling processes. Meanwhile, an electron tunneling from QDL to QDR corresponds to a cotunneling transition via island  $M$  [111, 211]. These transitions appear green, but are much weaker than the first-order transitions in this configuration.

Comparing the CSDs of Fig. 4.1(f), there is a stark difference between device A and B: the former exhibits rectangular regions of stable charge when the SCI has odd parity, while the latter shows only hexagonal Coulomb-blockaded regions. To understand this difference, we compare with charge-state simulations of the QD system combined with an input-output theory calculation of a representative resonator response, shown in Fig. 4.1(e) [119, 182, 204, 212]. For these, we use the inferred values of  $E_C^S$ ,  $E_C^N$ , and  $E_0$ , and resonator parameters from Ref. [204]. Extracting the lowest-energy states of the system with a capacitance model allows for calculating a theoretical resonator response [64, 182, 191] (Supplemental Sec. 4.7.3). States are labeled with the relative number of electrons in dots  $L$ ,  $M$ , and  $R$ , respectively, with 0 charge on island  $M$  corresponding to an even charge. As expected, transitions separating two charge states show response only from resonators coupled to the involved QDs. The different structure between the two CSDs is controlled by the conditions  $E_C^S < E_0$  (device A) or  $E_C^S > E_0$  (device B). Crucially, in device A, a transition between (020) and (101) can be observed, corresponding to a Cooper pair leaving the SCI while QDL and QDR each gain an electron. Conversely, device B only exhibits transitions involving the exchange of single electrons.

#### 4.4. GATE-INDUCED SINGLE COOPER PAIR SPLITTING

Next, we examine this (020)-(101) transition—only reachable if  $E_C^S < E_0$  as for device A—in more detail in Fig. 4.2. The frequency response of the island  $M$  resonator is measured at each gate voltage then fitted to a complex transmission model [158, 187, 190]. In Fig. 4.2(a), the obtained resonance frequency shifts from the value in Coulomb blockade  $\Delta\omega_0$  and photon decay rates  $\kappa_d$  are shown. The resonator responds strongly for single-electron transitions with  $\Delta\omega_0 > 2\pi \times 2.5$  MHz.

We isolate the (020)-(101) transition by measuring along the arrow labeled  $\zeta$ , defined as  $V_L + V_R$  up to an offset, in Fig. 4.2(a). This is approximately equivalent to changing island  $M$ 's gate voltage in the opposite direction. Figs. 4.2(b) and 4.2(d) show the response across the transition, where a significant dispersive shift  $\Delta\omega_0 > 2\pi \times 1$  MHz is observed. There, the underlying tunneling process is likely CPS dominated by coherent

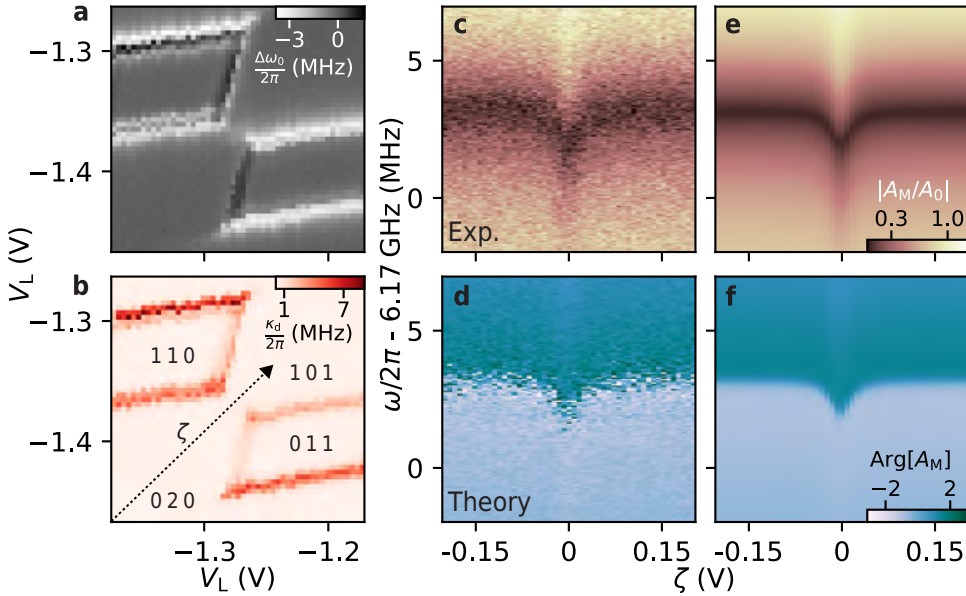


Figure 4.2: Middle resonator response in the floating TQD regime of device A. (a) The resonance frequency shift  $\Delta\omega_0$  and (b) linewidth  $\kappa_d$  of the middle resonator. (c),(d) Phase and amplitude response of resonator M along the  $\zeta$  axis defined in (b). (e),(f) Fits of the response to a low-energy CAR model.

CAR [64], since other processes are suppressed by large energy costs of breaking a Cooper pair  $2E_0$  or by  $E_C^N$ . Additionally, a lesser cost  $E_0 - E_C^S$  suppresses (020)-(101) transitions involving intermediate (110) or (011) states with a quasiparticle on the SCI. Including single-electron tunnel couplings however, these states may be weakly occupied as the least energetically unfavorable states mediating a CPS process, namely CAR [96, 178]. CAR mediated by the Al shell is suppressed by the length of the SCI,  $L = 1.2\mu\text{m}$  over the superconducting coherence length,  $\xi$ , as  $\exp(-L/\pi\xi)$  [213], but can also be mediated by extended bound states in the proximitized InAs [101, 113]. Given a  $\xi$  of 260 nm reported in similar nanowires [60], we conclude CAR-dominated CPS is likely.

To corroborate this conclusion, we use a low-energy Hamiltonian describing CAR mediated by an arbitrary number of degenerate quasiparticle states and fit the resonator response to its corresponding input-output model [111, 112, 119, 134, 182, 204, 214] (Supplemental Sec. 4.7.4). From the fit, we extract the effective electron- and holelike tunnel couplings  $t_{\text{eff},e/h}$  leading to coupling between the (020) and (101) states [215]. Resonator parameters are fixed by fits from Fig. 4.2(a), while the  $\zeta$  lever arm is estimated from Coulomb diamond measurements. This leaves  $t_{\text{eff},e/h}$ , the total dephasing and decay rate  $\gamma$ , and the resonator coupling to the (020)-(101) transition  $g_c$  as free parameters. The fit is plotted in Figs. 4.2(c) and 4.2(e), showing excellent agreement with the data for coherent tunneling amplitudes of  $t_{\text{eff},h} = t_{\text{eff},e}/1.1 = 2\pi \times 24\text{GHz}$ ,  $\gamma/2\pi$  of 1.1 GHz, and  $g_c/2\pi$  of 0.23 GHz. Notably,  $t_{\text{eff},e/h}$  is substantially smaller than the  $2E_0$  or  $E_C^N$  costs of non-CAR-related tunneling processes, and the dephasing rate is more than an order of magnitude smaller than the single-electron tunneling amplitudes. This relation of pa-

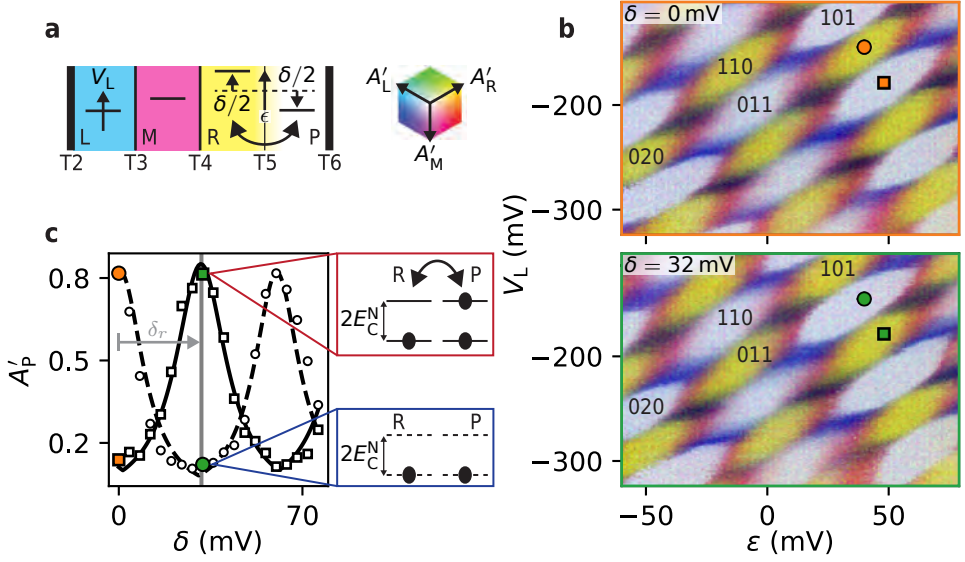


Figure 4.3: Parity measurement using a DQD in Device B. **(a)** Chemical potential schematic of the quadruple dot. **(b)** Multiplexed CSDs in the floating quadruple dot regime at fixed  $\delta = 0$  mV on the top and 32 mV on the bottom, with the color map shown above. Charge plateaus are labeled to represent the relative occupancy of the dots where the rightmost number represents the combined occupation of QDR and QDP. The individual resonator responses are shown in Supplemental Fig. 4.6. **(c)** Linecuts of the resonator  $P$  response as a function of  $\delta$ , measured at voltages indicated by the square and circle markers in **(b)**. The solid and dashed curves show fits to a periodic Lorentzian. At zero detuning between the dots, resonator  $P$  shows a response for one parity value, but is blocked for the other. The insets show cartoons of the sensor DQD levels in both cases.

rameters indicates that the  $(020) - (101)$  transition corresponds to the coherent splitting of a Cooper pair by crossing a single resonant charge transition.

Future experiments may increase the size in gate space of the CPS transition by increasing  $E_0/E_C^S$ , or increase the CAR amplitude by reducing the SCI length relative to  $\xi$ . Concurrently, the presence of this transition requires that  $E_C^S \leq E_0$ , necessitating a large total capacitance of the SCI. These conditions may be simultaneously met using methods presented in Ref. [216] to extend the SCI perpendicular to the nanowire, or to replace it with a grounded superconductor as demonstrated in Ref. [101]. Conversely, a finite  $E_C^S$  or ungrounded superconductor protects the SCI from quasiparticle poisoning [217], reducing the probability of independent quasiparticles entering the QDs instead of a split pair.

#### 4.5. PARITY SENSING IN A QUADRUPLE QUANTUM DOT

Having observed a CPS transition in a floating system, we next demonstrate how a split pair's electrons may be detected without external charge sensors in this experimental geometry. In particular, to detect a single charge tunneling into a QD it suffices to measure changes in the dot's parity, which we show is achievable using a DQD probed with DGS. For an isolated DQD where the total charge is fixed, interdot transitions are spaced

in chemical potential by the sum of the dots' charging energies [64]. An electron tunneling into the DQD flips the charge parity and shifts one QD's chemical potential by  $E_C^N$ , offsetting these transitions by half their spacing and potentially shifting the system from Coulomb blockade to charge degeneracy or vice versa. It has been shown that blockade and charge degeneracy can be distinguished rapidly with DGS [134, 135, 137–141, 159, 160, 174, 195, 196, 203, 204], hence DGS is sensitive to parity changes in a coupled DQD. Furthermore, the readout signal persists for most interdot detunings  $\delta = V_R - V_P$  if the dots are strongly hybridized, illustrated by a sweep of  $\delta$  in Fig. 4.3(c). Notably, if the dot orbitals are also spin polarized, Pauli spin blockade renders this sensing principle a spin measurement via spin-to-charge conversion [131, 206].

We implement this method in a floating quadruple dot configuration in device B, shown in Fig. 4.1(b), since the performance of device A deteriorated after multiple thermal cycles. We stress, however, that the parity sensor signal is independent of the origin of electrons flipping its parity and the properties of the coupled SCI. Hence, this technique is equally applicable to devices with a CPS transition or other Coulomb-blockaded systems. In the quadruple dot regime, we aim to observe parity changes in the DQD formed by QDR and QDP. To reach this configuration, T5 is tuned to a strong tunneling regime such that these dots form a DQD while effectively sharing a single charging energy [191]. Additionally, T2 and T6 are pinched-off to prevent tunneling to the leads, effectively removing one charge degree of freedom. We use as voltage coordinates  $V_L$  together with the detuning between the rightmost two dots  $\delta$  and the voltages' average  $\epsilon = (V_R + V_L)/2$ , both defined up to an offset, see Fig. 4.3(a).

The data acquisition method for this measurement is identical to the procedure outlined for Fig. 4.1(f). Here, three-dimensional CSDs are measured: sweeping  $\delta$ ,  $\epsilon$ , and  $V_L$ . Slices are shown in Fig. 4.3(b) for  $\delta$  values chosen such that the sensor DQD is on charge degeneracy for even or odd parity. The yellow regions signify that an electron is hybridizing between QDR and a QD whose resonator is unrepresented in the color map (cf. Fig. 4.3(c)), which is QDP by exclusion. Notably, the charge plateaus for which resonator  $R$  responds are opposite between the two  $\delta$  values, and opposite whenever the sensor changes parity.

Next, we show in Fig. 4.3(c) the response of resonator P as a function of  $\delta$  measured at the circle and square markers in Fig. 4.3(b). We phenomenologically fit the Coulomb oscillations with a periodic Lorentzian and observe that Coulomb resonance for the solid line occurs exactly when the dashed line shows Coulomb blockade. Fixing the peak spacing, we repeat this fitting procedure for all voltages shown in the CSD. Importantly, the detuning offset  $\delta_r$  of the pattern quantifies the position of charge degeneracy in the window  $-14 \text{ mV} < \delta < 43 \text{ mV}$ , allowing inference of the DQD's relative parity.

To demonstrate this correspondence, we plot  $\delta_r$  in Fig. 4.4. Clear regions corresponding to the two sensor DQD parities are visible, consistent with the histogram of  $\delta_r$  values shown on the right. The stark splitting of  $\delta_r$  values demonstrates that readout of parity changes can be accomplished by fixing  $\delta$  to a value maximizing contrast, such as  $\delta = 0$  in this case. This may be extended to single-shot readout provided electrons reside on the sensor DQD longer than the readout time. Placing one DQD sensor on either side of a superconducting reservoir or island would then enable time-resolved detection of both electrons from a split Cooper pair.

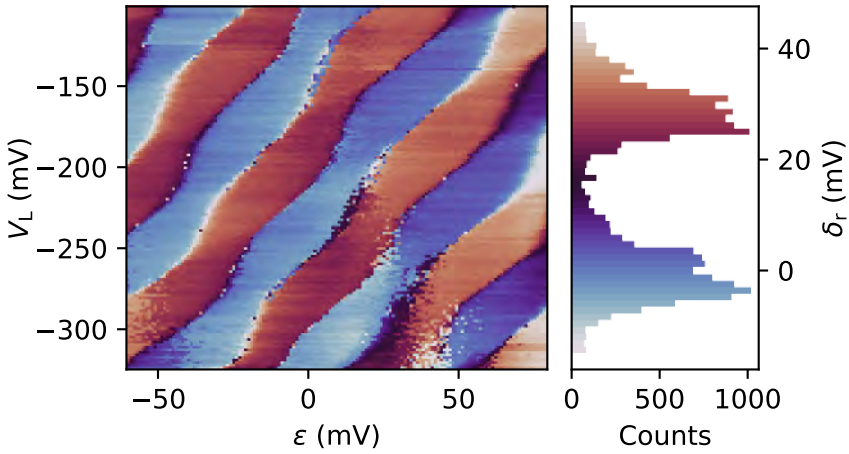


Figure 4.4: Distinguishment of parity in the floating quadruple dot regime for Device B. The detuning for which the sensor DQD is on resonance,  $-14 \text{ mV} < \delta_r < 43 \text{ mV}$ , is shown. On the right, a histogram of  $\delta_r$  value occurrences defines the color map of the stability diagram.

## 4.6. CONCLUSIONS & OUTLOOK

We have realized a normal-superconducting-normal QD system in an InAs nanowire. Multiplexed DGS shows different resonators responding depending on the spatial distribution of tunneling electrons, enabling us to infer the QDs' relative charge states [185, 204]. With DGS we observe a coherent CPS transition, repelling two electrons from the SCI to the surrounding QDs. Crossing this transition splits a single Cooper pair controllably and retains the resulting individual electrons on the outer dots. Importantly, this transition cannot occur concurrently to interdot cotunneling except for the fine-tuned parameters  $E_C^S = E_0$  in a floating TQD, constraining applications to quasiparticle-poisoning-protected Kitaev chains [10, 11, 143]. Furthermore, we have shown that DGS of a DQD is sensitive to its parity and can be used to detect electrons ejected from a neighboring SCI. Lastly, we note the demonstrated sensing method becomes a spin measurement of electrons entering the DQD when its levels are spin-polarized [131, 137, 139–141, 159]. Two such detectors on either side of a superconductor, combined with spin manipulation techniques [218–222], would enable performing a Bell test verifying the spin-singlet entanglement of electrons in Cooper pairs [206–210]. This is possible through comparison with the Clauser-Horne-Shimony-Holt inequality for the two spin qubits formed by the detectors, initialized to entangled states by pulsing gate voltages across the CPS transition [110, 223].

Raw data, analysis code, and scripts for plotting the figures in this chapter are available from Zenodo [224]. We are thankful to P. Krogstrup, D. Bouman and J.D. Mensingh for their contributions to device materials. We also acknowledge valuable technical assistance from N.P. Alberts, O.W.B. Benningshof, R.N. Schouten, M.J. Tiggelman, and R.F.L. Vermeulen, and helpful discussions with J.V. Koski. Lastly, we thank C.-X. Liu and B.M. Varbanov for input regarding the CAR model. This work has been supported by the Netherlands Organization for Scientific Research (NWO) and Microsoft.

## 4.7. SUPPLEMENTAL INFORMATION

### 4.7.1. PROJECTION AND NORMALIZATION OF RESONATOR DATA

Here we describe the process by which the resonator response is normalized in detail. First, in Fig. 4.5 and Fig. 4.6, we show the raw data for the Charge Stability Diagrams (CSDs) shown in Fig. 1 and Fig. 3 of the main text, respectively. The goal of normalizing the resonator response data is to reduce the dimensionality of the data while accentuating the difference between Coulomb blockade and charge degeneracy. First, the complex-valued response is projected onto a line. Then, the data is normalized such that Coulomb blockade is mapped to 0 while charge degeneracy is mapped to 1. By following the same procedure for all CSDs, similar charge transitions show up with the same colors in the different figures.

As an example, we outline the procedure in Fig. 4.7 showing the response of resonator M corresponding to Fig. 4.5(b). To project the complex-valued data onto a line, we first estimate the resonator response  $A_0$  in Coulomb blockade as the most occurring response in the CSD after binning the dataset into a two-dimensional histogram. Secondly, we find the average response,  $A_1$  to estimate the vector along which the resonator responds on average. Both points are marked in Fig. 4.7 and show that the resonator response indeed roughly falls along the vector  $A_1 - A_0$ . The data is subsequently projected onto the line defined by  $A_0$  and  $A_1$  and normalized to range from 0 to 1. This procedure is repeated for every resonator individually before they are combined into the same colormap.

### 4.7.2. DEVICE PROPERTIES

To extract charging energies and lowest lying subgap state energies in device A and B, we first show a Coulomb diamond measurement from which the charging energy of quantum dot (QD) P is inferred in Fig. 4.8. Assuming the other normal QDs have the same charging energy since they have the same gate design and fabrication procedure, this allows us to convert the voltage axes in Fig. 4.5 to energy, and thereby obtain values for  $E_C^S$  and  $E_0$ . Next, as an independent confirmation that device A is superconducting with  $E_0 > E_C^S$ , we show a transition from 2-electron periodic Coulomb resonances to 1-electron periodic resonances in Fig. 4.9 for device A as the in-plane magnetic field increases. We emphasize that the presence or absence of the Cooper pair splitting transition does not depend on the precise values of charging energies, provided that  $E_0 > E_C^S$ . Finally, as noted in the main text,  $E_0$  may vary substantially as the chemical potential in island M is varied. For the measurements of all figures in the main manuscript however, the plunger gate of island M (unlabeled gate in between  $V_L$  and  $V_R$  in Figs. 4.1(a) and 4.1(b)) is fixed to 0 V for Device A and to  $-2.4$  V for Device B.

### 4.7.3. SIMULATION OF CHARGE STABILITY DIAGRAMS

In this section we describe the method by which CSDs, including their corresponding resonator response, were simulated for Fig. 1e. We employ a general formalism for simulating charge stability in multi-quantum-dot and island systems which are floating, that is, without any leads.

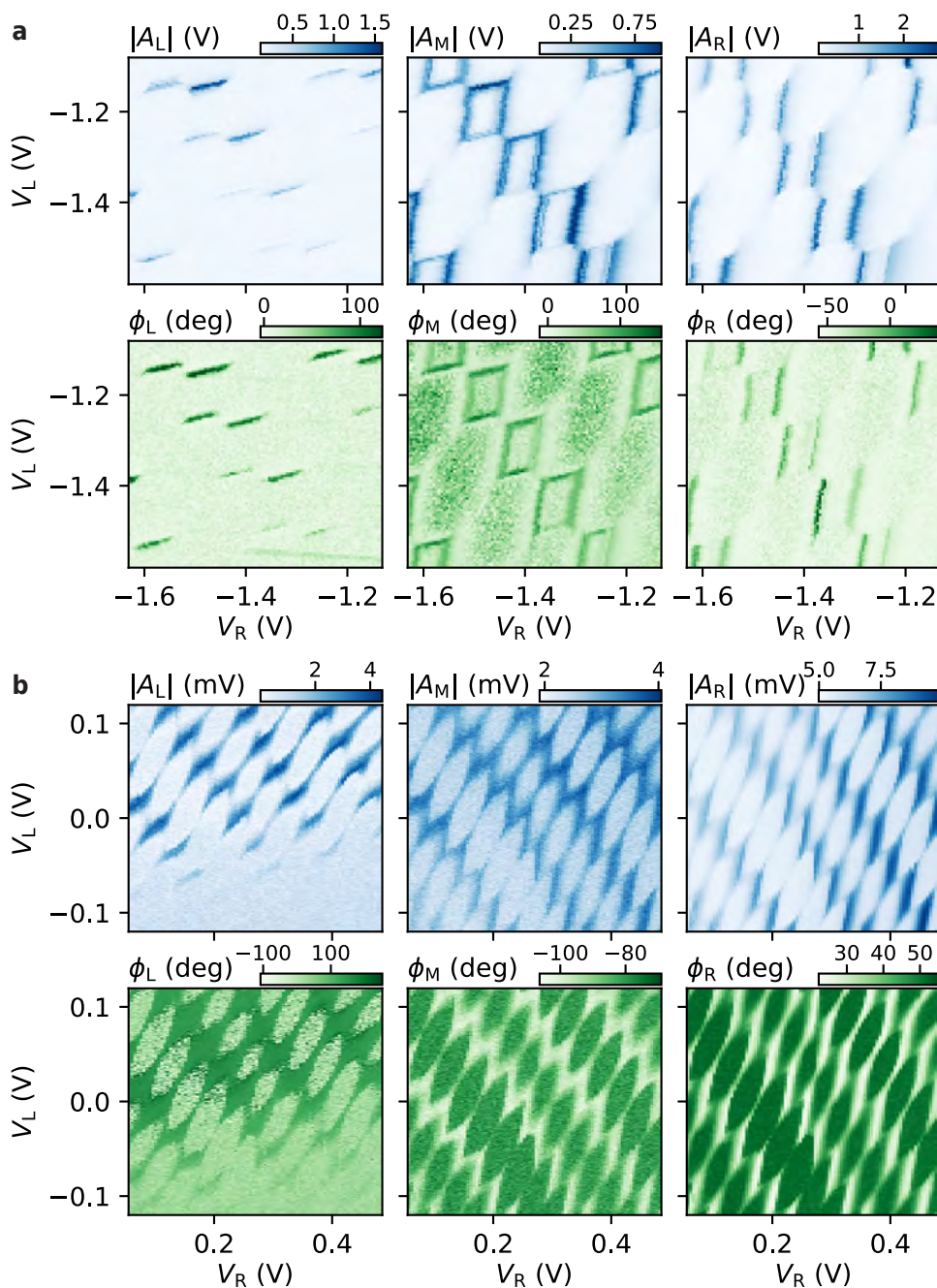


Figure 4.5: The individual resonator responses corresponding to the CSD of (a) device A and (b) device B shown in Fig. 4.1(f). Here,  $|A_i|$  and  $\phi_i = \arg(A_i)$  denote the amplitude and phase response of resonator  $i$  for  $i \in \{L, M, R\}$ .

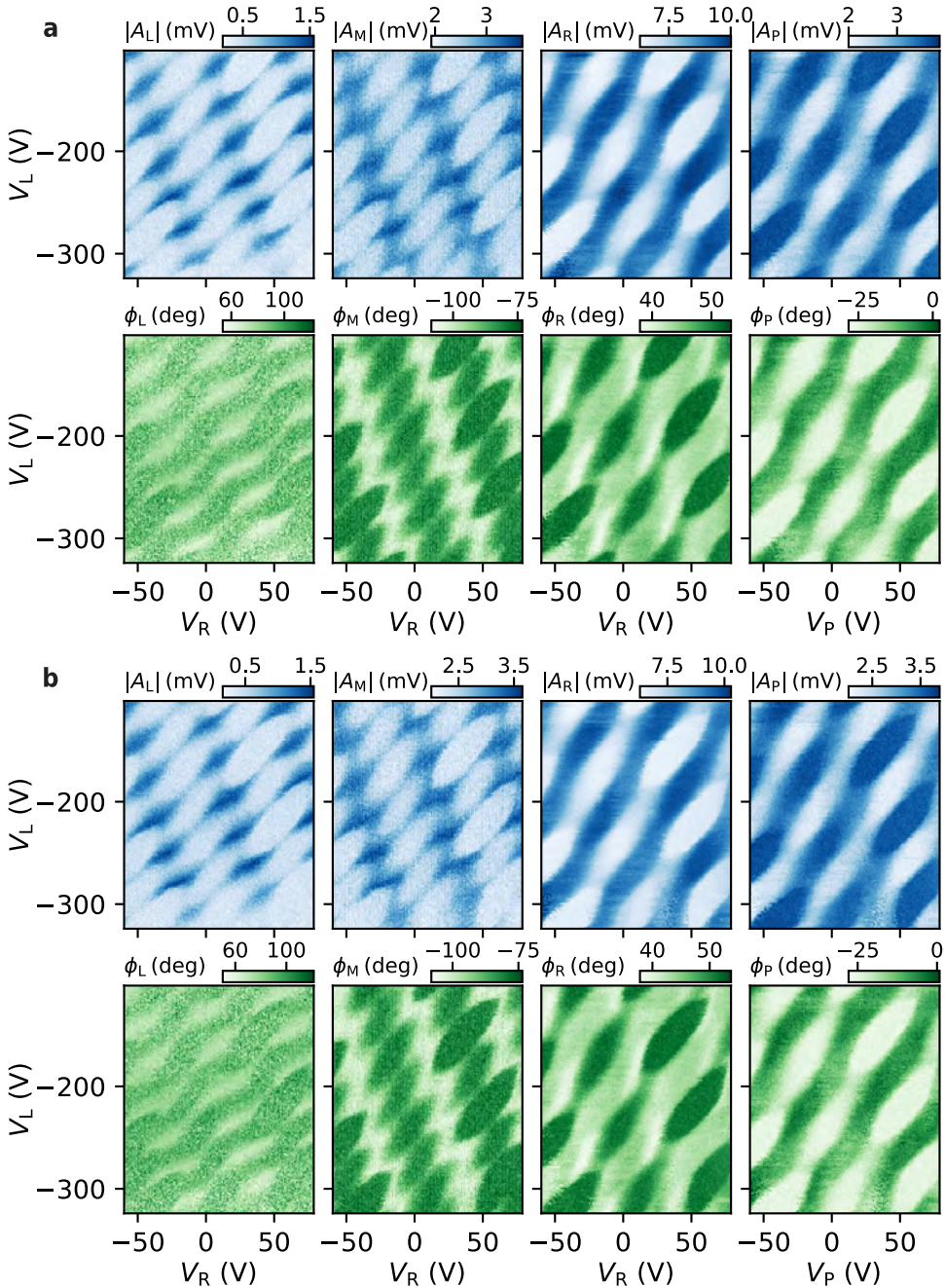


Figure 4.6: The individual resonator responses for device B corresponding to the CSDs shown in Fig. 3b, including slices of the data (a) at  $\delta = 0$  mV and (b) at  $\delta = 32$  mV. Here,  $|A_i|$  and  $\phi_i = \arg(A_i)$  denote the amplitude and phase response of resonator  $i$ . Even though the response of resonator P is not included in the colormap (see Fig. 4.3), it is added here for completeness.

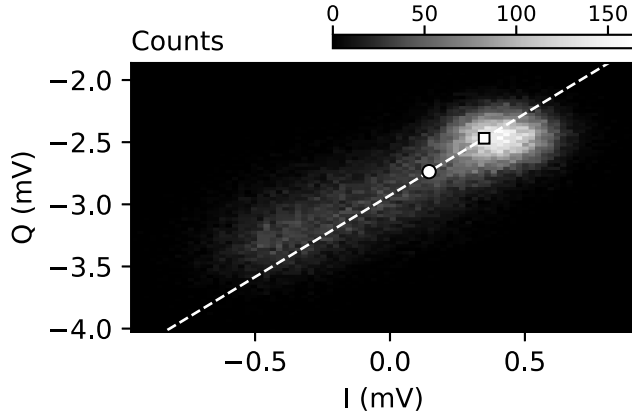


Figure 4.7: Histogram of the IQ response of the middle resonator, corresponding to the middle panel in Fig. 4.5 (b). The square marker denotes the most occurring IQ response  $A_0$  which we associate with Coulomb blockade while the circle marker denotes the average IQ response  $A_1$ . These markers define the dashed line which is used to project the complex-valued data.

The system initially considered is a system of  $N$  quantum dots (QDs) with a corresponding matrix of charging energies  $\mathbf{E}_C$  defined by matrix elements  $\{\mathbf{E}_C\}_{i,j} = e^2/C_{i,j}$  where  $C_{i,i}$  is the total capacitance of dot  $i$ , and  $C_{i,j}$  for  $i \neq j$  is the capacitance between dots  $i$  and  $j$ . Every dot has an energy cost  $E_0^i$  associated with containing an odd number of electrons, where  $E_0^i = 0$  for non-superconducting QDs. Operating in the charge basis  $\{|\mathbf{n}\rangle\}$  where  $\mathbf{n}$  denotes a vector of integers  $n_i$  specifying the charge state of each QD, the ‘on-site’ Hamiltonian  $\hat{H}_0$  of the system in the absence of any inter-dot tunneling is

$$\hat{H}_0 = \sum_{|\mathbf{n}\rangle} \left[ (\mathbf{n} - \mathbf{n}_g)^T \mathbf{E}_C (\mathbf{n} - \mathbf{n}_g) + \sum_i \frac{1 - (-1)^{n_i}}{2} E_0^i \right] |\mathbf{n}\rangle \langle \mathbf{n}| \quad (4.1)$$

where  $\mathbf{n}_g$  is the vector of reduced gate voltages on each quantum dot, including cross-capacitive couplings from all gate voltages [191]. Finally, allowing for quantum mechanical single-electron tunneling amplitudes  $t_{ij}$  between dots, the full Hamiltonian of the multi-dot system is

$$\hat{H} = \hat{H}_0 + \frac{1}{2} \sum_{|\mathbf{n}\rangle} \sum_{i \neq j} (t_{ij} |\mathbf{n} + \mathbf{e}_i\rangle \langle \mathbf{n} - \mathbf{e}_j| + \text{h.c.}) \quad (4.2)$$

where  $\mathbf{e}_i$  is the elementary basis vector on dot site  $i$ . From this Hamiltonian, a suitable range of charge states can be selected and the Hamiltonian can be numerically diagonalized for different  $\mathbf{n}_g$  values to obtain a full CSD. We denote the resulting eigenstates by  $\{|\psi_k\rangle\}_k$ . In this manuscript’s simulations of devices A and B tuned into the floating regime, we use charging energies and  $E_0$  values given in the main text, and for simplicity we neglect cross capacitances between dots. On the other hand, cross-capacitances between gates and other dots are included and chosen to best match with the data. Tunnel couplings are chosen such that every transition appears sharply in the CSD, including a direct tunnel coupling between the outer quantum dots to make the cotunneling transition clearly visible.

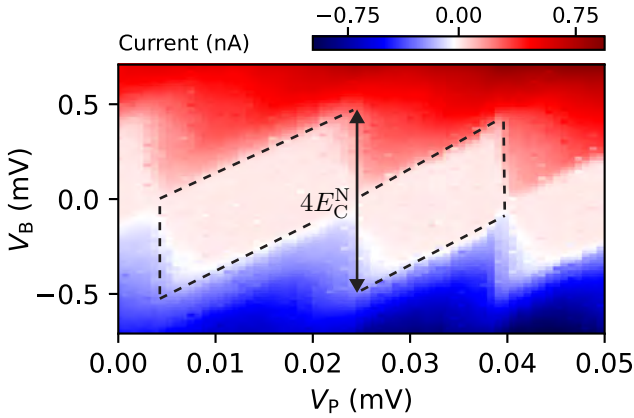


Figure 4.8: Coulomb diamonds measured in current from source to drain for QD P in device B. From the bias axis, we infer  $E_C^N = 250 \mu\text{eV}$ .

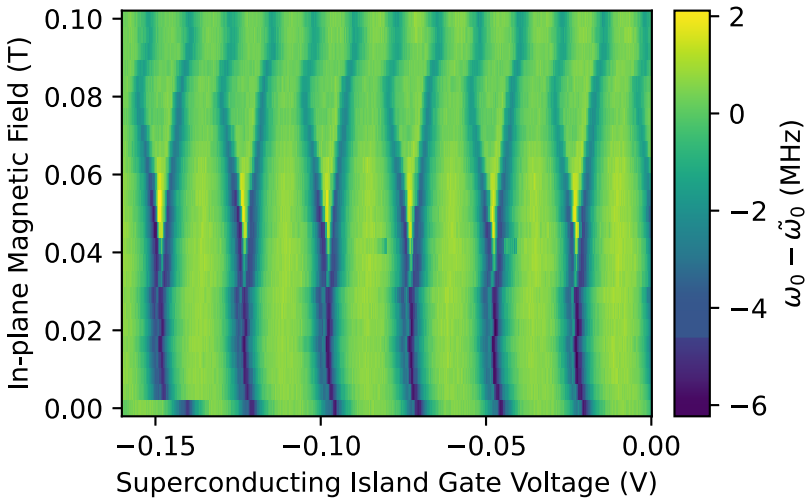


Figure 4.9: Fitted resonance frequency of the superconducting island M's gate resonator in device A as a function of in-plane magnetic field. With increasing field, the transitions split and alternate in separation with a periodicity of two transitions, finally becoming 1-electron periodic at higher fields. The resonance frequency for each magnetic field value is shifted by the median resonance frequency  $\tilde{\omega}_0$  for that particular field such that the shift is with respect to the resonance frequency in Coulomb blockade.

Next, we use an input output theory model to convert the eigenstates and eigenenergies of the charge stability simulations into a predicted resonator signal [119], following the model of Ref. [182, 212] to calculate the electric susceptibility  $\chi_{k,l}$  of each charge transition  $|\psi_k\rangle \rightarrow |\psi_l\rangle$ . Importantly, the electric susceptibilities depend on the matrix

elements  $\langle \psi_k | \hat{H}_c | \psi_l \rangle$  of the Hamiltonian  $\hat{H}_c$  coupling the charge system to the measured resonator. Assuming the resonator capacitively couples only to a single quantum dot with lever arm  $\alpha$ , say dot  $i$  with charge operator  $\hat{n}_i$ , this Hamiltonian is simply  $\hat{H}_c = g_0 \hat{n}_i (\hat{a}^\dagger + \hat{a})$  where  $\hat{a}^\dagger$  is the photon creation operator of the resonator [182]. In calculating the matrix element, we take the average value of  $\hat{a}^\dagger + \hat{a}$ , proportional to the voltage swing in the resonator. We use the same resonator coupling and dephasing as in Ref. [204], since an identical resonator design and nearly identical device design is used here. Finally, the frequency shift  $g_0 \sum_{k,l} \langle \psi_k | \hat{H}_c | \psi_l \rangle \chi_{k,l}$  can be substituted into a complex transmission model for a hanger-type resonator circuit and normalized to find simulated values of  $A'_i$  [158, 204]. To obtain a representative indication of what a gate sensor signal appears as without clouding the results by subtle resonator differences, we use the same resonator parameters from Ref. [204] using a resonance frequency of  $f_0 = 5$  GHz and a probe frequency of 5.005 GHz for all three resonators.

#### 4.7.4. MODEL AND FITS OF THE COOPER PAIR SPLITTING TRANSITION

##### MODEL AND LOW-ENERGY LIMIT

In order to estimate properties of the Cooper Pair Splitting (CPS) discussed in the main text and Fig. 2, we derive an effective three-state model across this transition and fit it to an input-output theory formula. Along the  $\zeta$  axis defined in the main text and near the (0,2,0) to (1,0,1) charge transition, we model the system with the relevant states:

$$\begin{aligned}
 |i\rangle &\equiv |0\rangle \otimes |1\rangle \otimes |0\rangle, & E_i &= E_C^N (n_g^L)^2 + E_C^S (2 - n_g^M)^2 + E_C^N (n_g^R)^2 \\
 |f\rangle &\equiv |1\rangle \otimes |0\rangle \otimes |1\rangle, & E_f &= E_C^N (1 - n_g^L)^2 + E_C^S (n_g^M)^2 + E_C^N (1 - n_g^R)^2 \\
 |v_L^j\rangle &\equiv |1\rangle \otimes \hat{\gamma}_j^\dagger |0\rangle \otimes |0\rangle, & E_L &= E_C^N (1 - n_g^L)^2 + E_C^S (1 - n_g^M)^2 + E_C^N (n_g^R)^2 + E_j \\
 |v_R^j\rangle &\equiv |0\rangle \otimes \hat{\gamma}_j^\dagger |0\rangle \otimes |1\rangle, & E_R &= E_C^N (n_g^L)^2 + E_C^S (1 - n_g^M)^2 + E_C^N (1 - n_g^R)^2 + E_j
 \end{aligned} \tag{4.3}$$

where the left and right kets denote the charge occupation on the outer dots and the central ket denotes the number of Cooper pairs in the superconducting condensate of the central superconducting island, all relative to some arbitrary offset. Additionally,  $n_g^i$  denotes the reduced gate voltage along dot  $i$ . The creation operator  $\hat{\gamma}_j^\dagger$  creates a Bogoliubon in a quasiparticle state in the island with energy  $E_j \geq E_0$ . We index the quasiparticle states by  $j \in \{1, \dots, N\}$  for some  $N$  representing all energetically relevant excitations.

For simplicity, we neglect spin effects, which at zero field are known to suppress quantum capacitance for a given tunnel coupling due to the additional degeneracy [64, 131, 205]. These spin effects manifest at zero field as alternating patterns in the strength of single-electron inter-dot transitions in Fig. 1 depending on the parity of dots involved in the transition, an effect which was not obviously present. Along the  $\zeta$  axis defined in the main text, we have  $n_g^L = n_g^R \equiv n_g$  and choose without loss of generality  $n_g^M = 1$ . Lastly, we note that both for a hard superconducting gap ( $N \gg 1$ ) or for a single discrete sub-gap state ( $N = 1$ ), coupling between  $|i\rangle$  and  $|f\rangle$  mediated by quasiparticle states will be dominated by the lowest energy states. Hence, we set all  $E_j = E_0$ . Shifting all energies by

$(E_i + E_f)/2$ , we may write the Hamiltonian along the  $\zeta$  axis as:

$$\hat{H}_{\text{CPS}} = -\frac{\lambda}{2} |i\rangle \langle i| + \frac{\lambda}{2} |f\rangle \langle f| + \eta \sum_{j,\alpha} |v_\alpha^j\rangle \langle v_\alpha^j| + \sum_{j,\alpha} \left( t_{\alpha,h} |v_\alpha^j\rangle \langle i| + t_{\alpha,e} |v_\alpha^j\rangle \langle f| + \text{h.c.} \right) \quad (4.4)$$

in the basis  $\{|i\rangle, |f\rangle, |v_L\rangle, |v_R\rangle\}$ , where we have included potentially asymmetric tunneling elements  $t_{\alpha\sigma}$  with  $\alpha \in \{L, R\}$  and  $\sigma \in \{e, h\}$  denoting electron-like or hole-like tunneling. This implicitly assumes that all  $\hat{\gamma}_j$  operators have the same electron- and hole-like components. Since charging effects on the superconductor force it to distinguish between gaining a quasiparticle by gaining an electron, or gaining a quasiparticle by losing an electron, the coupling matrix elements are also modulated by electron-like and hole-like coherence factors of the  $\hat{\gamma}_j$  excitations [215]. Because we only wish to demonstrate that these quasiparticle states coherently couple  $|i\rangle$  and  $|f\rangle$ , we model the system with symmetric tunnel barriers, setting all  $t_{\alpha,\sigma} = t_\sigma$  for some  $t_e$  and  $t_h$  to simplify calculations. Allowing asymmetric barriers, however, still leads to a Hamiltonian of the form in Eq. 4.11 provided all  $t_{\alpha,\sigma} \ll \eta$  [111], but suppresses crossed Andreev reflection (CAR) to be limited by whichever tunnel barrier is weaker. We have defined  $\lambda \equiv 2E_C^N(1 - 2n_g)$  as the detuning from the  $E_i = E_f$  degeneracy along  $\zeta$  and  $\eta \equiv E_0 - E_C^S$ .

Immediately, we identify that there are  $2N - 1$  degenerate eigenstates of the form

$$|p_\alpha^j\rangle \equiv \frac{1}{\sqrt{2}} (|v_L^j\rangle - |v_\alpha^j\rangle), \quad E_p = \eta \quad (4.5)$$

for  $\alpha \in \{L, R\}$  and any  $j \in \{1, \dots, N\}$  unless  $\alpha = L$  in which case  $j > 1$ . Second, when  $\lambda = 0$  we observe that the states

$$\begin{aligned} |\phi_e\rangle &\equiv \frac{1}{\sqrt{1 + |t_e/t_h|^2}} \begin{pmatrix} t_e^* \\ t_h^* \end{pmatrix} (|i\rangle - |f\rangle), & E_e = 0 \\ |\phi_\pm\rangle &\equiv \frac{1}{\sqrt{A_\pm}} \left[ \frac{\sqrt{2N}}{E_\pm} (t_h |i\rangle + t_e |f\rangle) + |o\rangle \right], & E_\pm = \frac{\eta}{2} \pm \frac{1}{2} \sqrt{\eta^2 + 8N|t_h|^2 + 8N|t_e|^2} \end{aligned} \quad (4.6)$$

are the remaining three eigenstates of the system, where we defined  $|o\rangle \equiv \frac{1}{\sqrt{2N}} \sum_{j,\alpha} |v_\alpha^j\rangle$ , and  $A_\pm$  are appropriately chosen normalization factors. Importantly, these states are spanned by the basis  $\{|i\rangle, |f\rangle, |o\rangle\}$  and orthogonal to all  $|p_\alpha^j\rangle$  states. The remaining three eigenstates of the full Hamiltonian when  $\lambda \neq 0$  are thus also spanned by this basis. Given the  $2N - 1$  known eigenstates  $|p_\alpha^j\rangle$ , to fully diagonalize  $\hat{H}_{\text{CPS}}$ , we need only diagonalize the  $3 \times 3$  block

$$\hat{H}_{\text{CPS}}^{3 \times 3} \equiv \begin{pmatrix} -\frac{\lambda}{2} & 0 & t_{\text{eff},h} \\ 0 & \frac{\lambda}{2} & t_{\text{eff},e} \\ t_{\text{eff},h}^* & t_{\text{eff},e}^* & \eta \end{pmatrix} \equiv \hat{H}_0 + \hat{V} \quad (4.7)$$

written in the  $\{|i\rangle, |f\rangle, |o\rangle\}$  basis, where  $\hat{H}_0$  is defined to contain the diagonal part of the Hamiltonian and  $\hat{V}$  contains the tunneling matrix elements, and we defined the effective single-electron tunneling amplitudes  $t_{\text{eff},\sigma} \equiv t_{\text{eff},\sigma}$ . Eq. 4.7 is the Hamiltonian we fit to an input-output theory model to extract tunnel couplings and the dephasing rate.

From the results of our input-output theory fit to Eq. 4.7, we extract  $t_\sigma$  of the same order of magnitude as  $\eta$ , rendering any cotunneling approximation  $t_\sigma \ll \eta$  invalid here. Nonetheless, to demonstrate that this Hamiltonian results in CAR – the coherent coupling of  $|i\rangle$  and  $|f\rangle$  via tunneling through quasiparticle states – we consider the limit of  $t_\sigma \ll \eta$  and project the system onto its low-energy subspace following the approach described in Sec. 2.1.5. To proceed, we apply a Schrieffer-Wolff transformation to perturbatively expand the system to second order in  $t_{\text{eff},\sigma}/\eta$  [112]. Hence, we seek a transformation  $e^{\hat{S}} \hat{H}_{\text{CPS}}^{3 \times 3} e^{-\hat{S}}$  which is diagonal to first order in  $t_{\text{eff},\sigma}/\eta$ . By choosing  $\hat{S}$  such that  $[\hat{S}, \hat{H}_0] = -\hat{V}$ , it can be shown that  $e^{\hat{S}} \hat{H}_{\text{CPS}}^{3 \times 3} e^{-\hat{S}} = \hat{H}_0 + [\hat{S}, \hat{V}]/2$  to second order in  $t_{\text{eff},\sigma}/\eta$ . Near the transition, we further assume  $\lambda \ll \eta$ . In this limit it may be verified that

$$\hat{S} = \begin{pmatrix} 0 & 0 & -\frac{t_{\text{eff},h}}{\eta} \\ 0 & 0 & -\frac{t_{\text{eff},e}}{\eta} \\ \frac{t_{\text{eff},h}^*}{\eta} & \frac{t_{\text{eff},e}^*}{\eta} & 0 \end{pmatrix} \quad (4.8)$$

satisfies this condition. This leads to the transformed Hamiltonian

$$e^{\hat{S}} \hat{H}_{\text{CPS}}^{3 \times 3} e^{-\hat{S}} \sim \hat{H}_0 + \frac{1}{2} [\hat{S}, \hat{V}] = \begin{pmatrix} -\frac{\lambda}{2} - \frac{|t_{\text{eff},h}|^2}{\eta} & -\frac{t_{\text{eff},h} t_{\text{eff},e}^*}{\eta} & 0 \\ -\frac{t_{\text{eff},h}^* t_{\text{eff},e}}{\eta} & \frac{\lambda}{2} - \frac{|t_{\text{eff},e}|^2}{\eta} & 0 \\ 0 & 0 & \eta + \frac{|t_{\text{eff},h}|^2 + |t_{\text{eff},e}|^2}{\eta} \end{pmatrix} \quad (4.9)$$

valid to second order in  $t_\sigma/\eta$  and  $\lambda/\eta$ . The transformed Hamiltonian is in the basis of dressed states

$$\begin{aligned} |i'\rangle &\equiv e^{\hat{S}} |i\rangle \sim |i\rangle + \frac{t_{\text{eff},h}^*}{\eta} |o\rangle \\ |f'\rangle &\equiv e^{\hat{S}} |f\rangle \sim |f\rangle + \frac{t_{\text{eff},e}^*}{\eta} |o\rangle \\ |o'\rangle &\equiv e^{\hat{S}} |o\rangle \sim |o\rangle - \frac{1}{\eta} (t_{\text{eff},h} |i\rangle + t_{\text{eff},e} |f\rangle) \end{aligned} \quad (4.10)$$

The eigenstates of the original Hamiltonian  $|p_\alpha^j\rangle$  and the eigenstate  $|o'\rangle$  in the transformed basis have energies of at least  $\eta$  while the  $\{|i'\rangle, |f'\rangle\}$  Hamiltonian block only has elements of order  $\lambda/\eta$  and  $t_\sigma^2/\eta$ . Finally then, at low energies we can neglect all states except  $|i'\rangle$  and  $|f'\rangle$  and are left with the Hamiltonian

$$\hat{H}_{\text{eff}} = \begin{pmatrix} -\frac{\lambda'}{2} & t_{\text{CAR}} \\ t_{\text{CAR}}^* & \frac{\lambda'}{2} \end{pmatrix} \quad (4.11)$$

in this basis. We shifted the Hamiltonian by  $(|t_{\text{eff},h}|^2 + |t_{\text{eff},e}|^2)/2\eta$  and defined  $\lambda' \equiv \lambda + (|t_{\text{eff},h}|^2 - |t_{\text{eff},e}|^2)/\eta$  and  $t_{\text{CAR}} \equiv -t_{\text{eff},h} t_{\text{eff},e}^*/\eta$ . In the following fits we will find that  $t_\sigma$  is comparable in magnitude to  $\eta$ , violating the assumption  $t_\sigma \ll \eta$ . As this is continuously connected to the above  $t_\sigma \ll \eta$  limit by strengthening  $t_\sigma$  and therefore the strength of

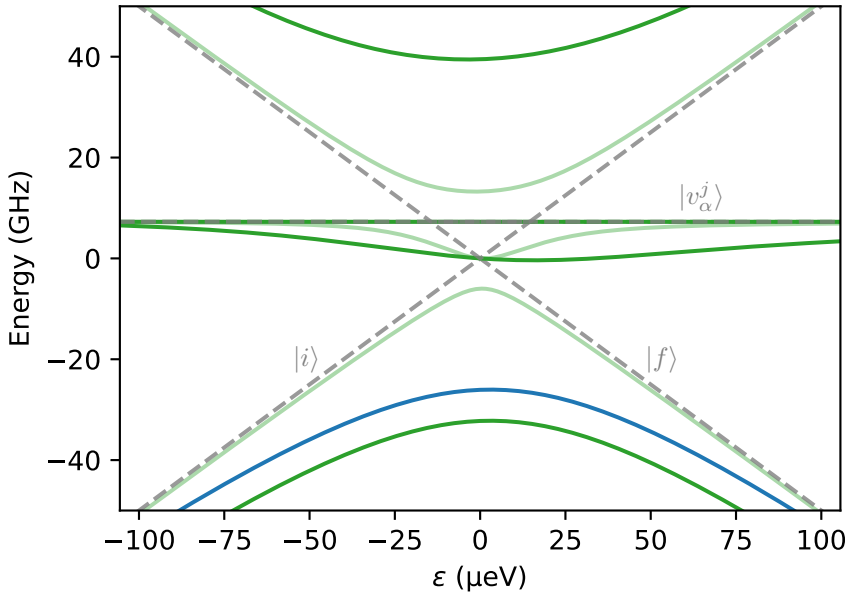


Figure 4.10: The energy spectrum of  $\hat{H}_{\text{CPS}}$  (eq. 4.4) for three values of  $t_e = 1.1 \times t_h$ . We plot the spectrum for the uncoupled system where  $t = 0$  (gray), for the experimentally fit  $t_{\text{eff},h}/2\pi = 24\text{GHz}$  (dark green), and for a much smaller  $t_{\text{eff},h}/2\pi = 6\text{GHz}$  (the light green). From this last case, we see how coupling between even parity states on island M ( $|i\rangle$  and  $|f\rangle$ ) and odd parity states detuned in energy by  $\eta$  opens an effective anticrossing between  $|i\rangle$  and  $|f\rangle$ , mediating CAR. Because for  $N$  degenerate quasiparticles  $\hat{\gamma}_j$  there are  $2N$  degenerate states of energy  $\eta$ , the spectrum appears the same independent of  $N$ , though the effective single-electron tunneling amplitude is scaled by  $\sqrt{N}$ . For this plot, we used the experimentally extracted parameters  $\eta = E_0 - E_C^S = 30\mu\text{eV}$  and  $\lambda/h\zeta = -2\text{THzV}^{-1}$ . In blue, we show the ground state energy shifted up by the resonator M frequency, making it clear that for these  $t_{\text{eff},e/h}$  values, no crossings are expected between the dot states and the resonator cavity states.

CAR, the above argument demonstrates that coherent CAR can occur at a high rate in our floating island system. This model is compared with the more accurate spectrum of  $\hat{H}_{\text{CPS}}$  in Fig. 4.10 by considering fit values of  $t_e$  and  $t_h$  as well as smaller values.

### INPUT-OUTPUT THEORY FITS

We focus on studying the signal measured by the island M resonator, since it exhibits sensitivity to the CPS transition in experiment. This is unsurprising, since dispersive gate sensing measures a coupling of system eigenstates via the charge on dot M [182]. The middle island exchanges two electrons with the outer quantum dots, while the quantum dots each only see a change of one electron in their average charge. Hence, we anticipate that at maximum, a dispersive shift which is twice as large may be imparted on the island M resonator compared to that imparted on the quantum dots' resonators, provided all resonator and coupling parameters are equal.

To study the CPS transition in experiment, we fit the frequency response of resonator M along the  $\zeta$  axis to the input-output model described in Sec. 4.7.3 with the effective Hamiltonian of Eq. 4.7 to extract  $t_h$  and  $t_e$  as well as the dephasing rate. Note that we

need not consider the eigenstates  $|p_\alpha^j\rangle$  of the full  $\hat{H}_{\text{CPS}}$  Hamiltonian since they are orthogonal to any superposition of the  $\{|i\rangle, |f\rangle, |o\rangle\}$  states spanning  $\hat{H}_{\text{CPS}}^{3\times 3}$  and are raised in energy from the system ground state by at least  $\eta$ .

Specifically, we apply the following dispersive shift model for a realistic hanger-style resonator [134, 182, 204]

$$A_M = 1 + \frac{1}{2} \frac{\kappa_{\text{ext}}}{i(\omega - \omega_0) - \frac{\kappa_{\text{ext}} + \kappa_d}{2} - i g_{\text{eff}} \chi} \quad (4.12)$$

which we then multiply by phase and amplitude slopes and offsets to model a realistic resonator [158, 187, 190]. The fitting model and procedure is identical to that in Appendix C but with the addition of the resonator's dispersive shift  $g_{\text{eff}} \chi$  given by

$$g_{\text{eff}} \chi = \sum_k \frac{g_c^2 |\langle \psi_k | \hat{n}_M | \psi_{\text{GS}} \rangle|^2}{\omega + i\gamma_{k, \text{GS}} - (E_k - E_{\text{GS}})}, \quad (4.13)$$

where  $|\psi_{\text{GS}}\rangle$  and  $|\psi_k\rangle$  represent the system's ground and excited states respectively,  $E_{\text{GS}}$  and  $E_k$  are their corresponding energies,  $\gamma_{k, \text{GS}} = \gamma_{\text{deph}} + \gamma_{\text{rel}}/2$  is the sum of the system's dephasing and relaxation rates [182] for the  $|\psi_{\text{GS}}\rangle$  to  $|\psi_k\rangle$  transition, and  $g_c$  is the bare resonator coupling to the system. The bare resonator parameters include the resonator's internal photon dissipation rate  $\kappa_d$ , its resonance frequency  $\omega_0$ , and the photon coupling rate between the resonator and the transmission line  $\kappa_{\text{ext}}$ . This rate is treated as complex to account for asymmetry in the resonator lineshape [158, 187, 190]. The coupling element  $\langle \psi_k | \hat{n}_M | \psi_{\text{GS}} \rangle$  with the charge  $\hat{n}_M$  on island M quantifies the gate dependence of the island-resonator coupling. Above, we assumed that thermal population of excited states is negligible, since they are separated from the ground state by a gap of at least  $\eta$ . Again, because the states  $|p_\alpha^j\rangle$  are orthogonal to  $\{|i\rangle, |f\rangle, |o\rangle\}$  and the ground state is a superposition of these three states, we know that  $\langle p_\alpha^j | \hat{n}_M | \psi_{\text{GS}} \rangle = 0$ . Furthermore, we compared fits including only the transition between the ground state to the first excited state to fits including transitions to the second excited state as well and found negligible difference. This is likely because of an additional energy difference of at least  $\eta$  separating it from  $E_0$ . Hence, to fit the dispersive shift corresponding to the full  $\hat{H}_{\text{CPS}}$  Hamiltonian, it is sufficient to consider only the two lowest energy eigenstates which may be extracted from  $\hat{H}_{\text{CPS}}^{3\times 3}$ . Consequently, our fit model includes only a single dephasing parameter  $\gamma$ .

Before conducting the dispersive fit, all resonator parameters including  $\kappa_{\text{ext}}$ ,  $\kappa_d$ , and  $\omega_0$  are fixed to the same calibrated values used for the fits of Fig. 2a. To convert from our  $\zeta$  voltage axis to  $\lambda$  in units of frequency, we fix a conversion factor equal to  $-2 \text{ THzV}^{-1}$ . We calculate this factor from Coulomb diamond measurements of QDL and QDR, from which we estimated lever arms of  $\alpha_L \approx 0.7\%$  and  $\alpha_R \approx 0.9\%$ . Hence, up to a detuning offset, we have

$$\frac{\lambda}{h} = -\frac{2e/h}{1/\alpha_L + 1/\alpha_R} \zeta + \text{offset} \approx -(2 \text{ THzV}^{-1}) \zeta + \text{offset} \quad (4.14)$$

Our  $\zeta$  axis was chosen such that  $\zeta = 0$  corresponds to the center of the CPS transition, so we fix this detuning offset in the conversion from  $\zeta$  to  $\lambda$  to zero.

Finally, all parameters are fixed except for  $g_c$ ,  $t_{\text{eff}, \sigma}$ , and  $\gamma$ . We summarize tests of the robustness of our fit in Fig. 4.11, where we see that  $g_c$ ,  $\gamma$ , and  $t_e/t_h$  are stable to changes

in  $t_{\text{eff},h}$  and the energy conversion multiplier  $|\lambda'/\zeta|$ . Effectively, we fit  $\gamma$  and electron-hole tunneling asymmetry  $t_e/t_h$  by hand, varying them between different fixed values and observing that a clear minimum fit error occurs at  $\gamma/2\pi = 1.1$  GHz and  $t_e/t_h = 1.1$  (see Fig. 4.11(d)), where we extract  $t_{\text{eff},h} = 24$  GHz and  $g_c/2\pi = 0.23$  GHz. We also observe from Fig. 4.11(e-h) that fixing  $t_{\text{eff},h}$  leads to very poor fits when  $t_{\text{eff},h}/2\pi$  is smaller than the resonator frequency. Also, allowing the  $\zeta$  offset to vary led to a slightly larger optimized  $t_e/t_h$  and smaller absolute  $t_{\text{eff},h}$ , but did not reduce fit error substantially. Hence, fixing this offset to zero is justified to avoid overfitting.

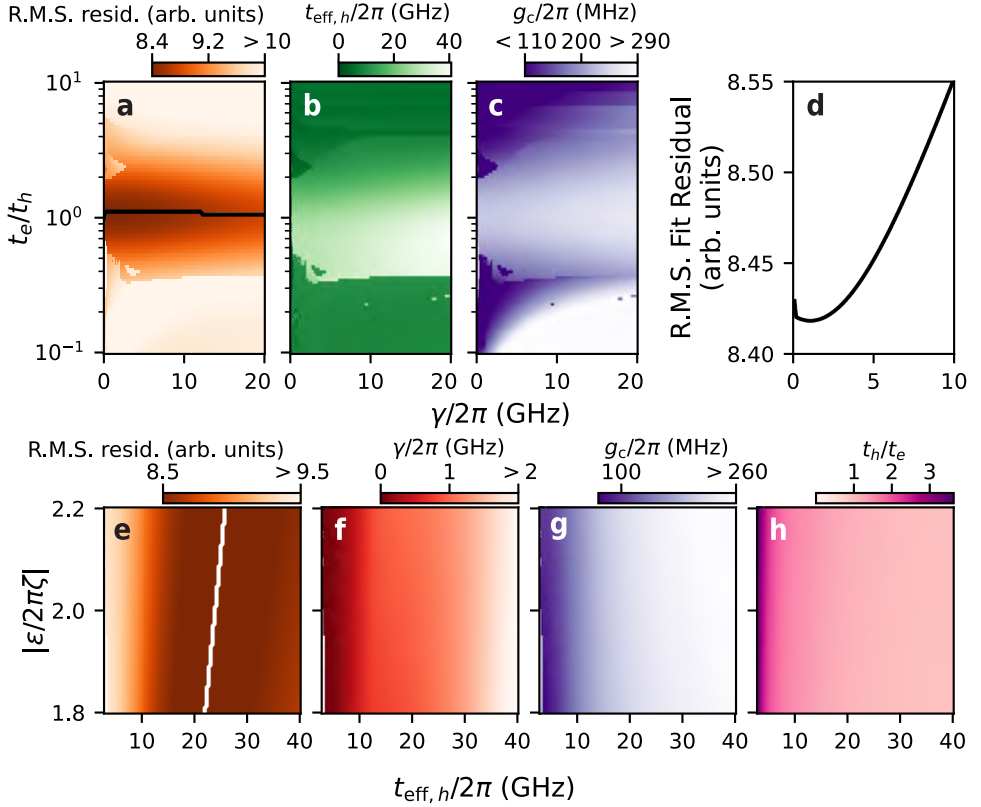


Figure 4.11: **(a)** The root mean square fit residual, **(b)** extracted hole-like tunneling amplitude  $t_{\text{eff},h}$  assuming symmetric tunnel barriers to the left and right QDs, and **(c)** extracted  $g_c$  of the dispersive shift fit of the CPS transition for different fixed electron-hole tunneling asymmetries  $t_e/t_h$  and dephasing rate of the two lowest system states  $\gamma$ . We fix  $|\lambda'/2\pi\zeta| = -2 \text{ THz V}^{-1}$  and all resonator parameters, but allow  $t_{\text{eff},h}$ ,  $g_c$ , and a  $\zeta$  offset to vary. A clear minima in the fit residual is seen at all values of  $t_e/t_h$ , plotted in black in **(a)**. **(d)** Root mean square fit residual at the  $t_e/t_h$  value which minimizes fit residual. A global minimum of fit error occurs at  $t_e/t_h \approx 1.1$  and  $\gamma \approx 1.1 \text{ GHz}$ . Hence, we take these fixed values of  $t_e/t_h$  and  $\gamma$  as their fit values in the main text. **(e)** The root mean square fit residual, **(f)** extracted  $\gamma$ , **(g)** extracted  $g_c$ , and **(h)** extracted tunneling asymmetry  $t_e/t_h$  of the dispersive shift fit of the CPS transition for different fixed  $t_{\text{eff},h}$  and  $\zeta$ -axis energy conversion multipliers  $|\lambda/2\pi\zeta|$ . We consider  $|\lambda/2\pi\zeta|$  fixed within 10% of its experimentally extracted value of  $2 \text{ THz V}^{-1}$ . A clear minima in the fit residual is seen at all values of  $|\lambda/2\pi\zeta|$ , plotted in white in **(e)**. This results in error-minimizing  $t_{\text{eff},h}/2\pi$  between 22.0 GHz and 25.7 GHz across the range of considered  $|\lambda/2\pi\zeta|$  values.

# 5

## FLUX-TUNABLE HYBRIDIZATION IN A DOUBLE QUANTUM DOT INTERFEROMETER

*C. G. Prosko, I. Kulesh, M. Chan, L. Han, D. Xiao, C. Thomas, M. J. Manfra, S. Goswami,  
F. K. Malinowski*

Quantum interference of electron tunneling occurs in any system where multiple tunneling paths connect states. This unavoidably arises in two-dimensional semiconducting qubit arrays, and must be controlled as a prerequisite for the manipulation and readout of hybrid topological and parity qubits. By studying a loop formed by two quantum dots, we demonstrate a magnetic-flux-tunable hybridization between two electronic levels, an irreducibly simple system where quantum interference is expected to occur. Using radio-frequency reflectometry of the dots' gate electrodes we extract an interdot coupling of the double quantum dot exhibiting oscillations with a periodicity of one flux quantum. In different tunneling regimes we benchmark the oscillations' contrast, and find their amplitude varies with the charge state of the quantum dots. These results establish the feasibility and limitations of parity readout of qubits with tunnel couplings tuned by flux.

### 5.1. INTRODUCTION

Magnetic fields impart a phase on electron wave functions, leading to constructive or destructive interference between different electron trajectories. This manifests in commonly observed phenomena such as the Aharonov-Bohm (AB) effect and weak localization [6]. Similarly, confined quantum systems where only a few states are coupled to each other can exhibit interference [225–229], for example due to interference of phases

---

The work in this chapter is under review as an article in an academic journal. Preprint available at arXiv:2303.04144.

imparted by magnetic fields on the couplings [230]. To date however, the phase of tunnel couplings between discrete fermionic levels has never been directly measured. This is particularly relevant for several kinds of semiconductor and hybrid semiconducting-superconducting qubits formed with quantum dots (QDs). QDs are a fundamental component of topological qubits based on Majorana bound states [10, 11, 87, 88, 231] as well as spin qubits [232]. They are also naturally suited for quantum simulation [233]. Since topological qubits are typically composed of multiple QDs connected in a loop, their hybridization is sensitive to the magnetic flux through the loop because it modulates the tunnel couplings' phases, causing interference [230]. This flux-dependent tunneling is a prerequisite for maximizing the readout sensitivity of topological qubits and for tests of Majorana fusion rules [10, 11, 14, 198, 231]. Meanwhile, tunneling may depend on flux in two-dimensional QD arrays for quantum processors [234, 235] or quantum simulation [108, 228, 236], since coherent tunneling can occur across chains of QDs [111]. This highlights the importance of understanding and accounting for this effect. Additionally, it has been proposed that new types of semiconducting qubits could exploit flux-tunable couplings to implement gate operations and noise-protected readout schemes [237–239]. Currently, coupling between dots is typically controlled solely electrostatically with gate voltages [23, 240], and an understanding of how magnetic flux affects tunneling amplitudes is lacking.

Motivated by this, we probe quantum interference in the irreducibly simple case of tunneling between two electronic levels in a loop formed by two QDs. Radio-frequency (RF) gate reflectometry is sensitive to tunnel couplings between QDs [125, 130, 131, 135, 136, 138, 174, 204, 241, 242], and is a candidate for scalable readout of semiconductor and topological qubits [10, 11, 13, 198, 231]. We therefore employ it to quantify the interdot coupling as a function of magnetic flux, and demonstrate a flux-tuned hybridization between electron levels. The specific charge and therefore quantum state of the QD system strongly affects the tunnel coupling and the oscillation amplitude. Importantly for gate reflectometry, the relation between tunnel couplings and measured signal is nonlinear [138]. Therefore, contrary to expectation [198], we find that readout fidelity of qubits with their state information encoded in a flux-tuned tunnel coupling may be optimal for weak coupling between the involved QDs.

This manuscript is organized as follows: In Sec. 5.2, we describe the device fabrication procedure as well as its configurability into an open loop, a quantum ring, or a double quantum dot (DQD). Phase-coherence of electron transport through the device is then established in Sec. 5.3 in two ways. First, we measure the AB effect manifesting in both DC conductance and RF reflectometry of the open loop. Second, we tune the device into a large loop-shaped QD, and measure  $h/e$ -periodic oscillations of its addition energy with flux [243, 244]. This QD exhibits a consistently finite excitation energy despite having an approximate circumference of  $1.4\ \mu\text{m}$ . The main result of the manuscript is then presented in Sec. 5.4, where we demonstrate a flux-tunable tunnel coupling between the levels of two quantum dots arranged in a loop and assess limitations of this tunability in Sec. 5.5. Lastly, in Sec. 5.6 we consider implications of these results for future applications to semiconducting and hybrid superconducting qubits.

## 5.2. DEVICE OVERVIEW

To fabricate a device capable of forming a ring-shaped DQD, we use a  $\text{InSb}_{0.86}\text{As}_{0.14}$  ternary two-dimensional ternary electron gas (2DEG) [245]. The device (Fig. 5.1(a)) consists of three Ti / Pd gate layers patterned on the 2DEG, each separated by 20 nm of deposited  $\text{Al}_2\text{O}_3$  dielectric. Charge is confined to an annular ring geometry by applying voltages to deplete carriers below the outer and inner depletion gates (red). The voltage on the inner depletion gate  $V_C$  also serves to tune the chemical potential of the entire ring. Voltages  $V_{BS}$ ,  $V_{BD}$ ,  $V_{BT}$ , and  $V_{BB}$  on the barrier gates (yellow) define a large curved QD and a smaller QD (denoted QDL and QDR, respectively), while voltages  $V_L$  and  $V_R$  on the plunger gates (blue) control their chemical potentials. Specifically,  $V_{BS}$  and  $V_{BD}$  form tunnel barriers between the QDs and lead reservoirs, while  $V_{BT}$  and  $V_{BD}$  tune the individual interdot couplings between the QDs via each arm of the loop. Two additional unlabeled accumulation gates (gray) control charge density in the exposed 2DEG between the QDs and Al contacts. Additional details of the fabrication may be found in Appendix A.

By appropriately tuning gate voltages, the device can be continuously tuned between an open loop, a loop-shaped QD, or into a DQD (Fig. 5.1(b)). Measurements on the former two configurations enable us to verify that electron transport is phase-coherent over the ring circumference, and that the ring as a whole supports a single extended electron state. The DQD configuration represents a minimal system in which interference of tunneling between two electron states can occur, as we will demonstrate.

Both plunger gates controlling QDL and QDR are bonded to resonators formed by NbTiN spiral inductors with 420 nH and 730 nH inductance and their parasitic capacitances, leading to resonance frequencies of approximately 400 MHz and 315 MHz, respectively [154]. We measure  $V_{RF}^L$  and  $V_{RF}^R$ , the signal reflected from the resonator connected to gate L or R upon applying a voltage excitation near their resonance frequencies. This complex amplitude depends on the capacitance associated with resonant tunneling and losses from dissipative transport. The former results in a frequency shift of the resonator  $\Delta f_0^L$  or  $\Delta f_0^R$ , while the latter reduces its quality factor [13, 125, 131]. The low-power signals reflected by the device are amplified by a high-electron-mobility transistor at 4 K and measured with a vector network analyzer or ultra-high-frequency lock-in amplifier to produce  $V_{RF}^L$  and  $V_{RF}^R$ , see Fig. 5.1(a). Using frequency multiplexing [154], both quantities can be measured simultaneously. Measurements are performed at the approximately 20 mK base temperature of a dilution refrigerator. For more details of the measurement circuit, see Appendix B.2. Additionally, there may be a large cross-capacitance between gates coupled to resonators and the device depletion gates due to their substantial overlap. To prevent this capacitance from lowering the resonator quality factors and frequencies, large resistors were patterned on the depletion gates serving as low-pass filters. See Appendix A.1 for more details.

In each of the three measurement configurations displayed in Fig. 5.1(b), properties of the device are readily measured using RF reflectometry of resonators connected to gates L or R. The reflectometry signal is sensitive to the RF admittance of the device [13]. In the case of an open loop, the resonator on gate R probes the RF conductance of the loop in series with its gate capacitance, depicted in Fig. 5.1(c). The device admittance is dominated by high frequency conductance of electrons traveling around the

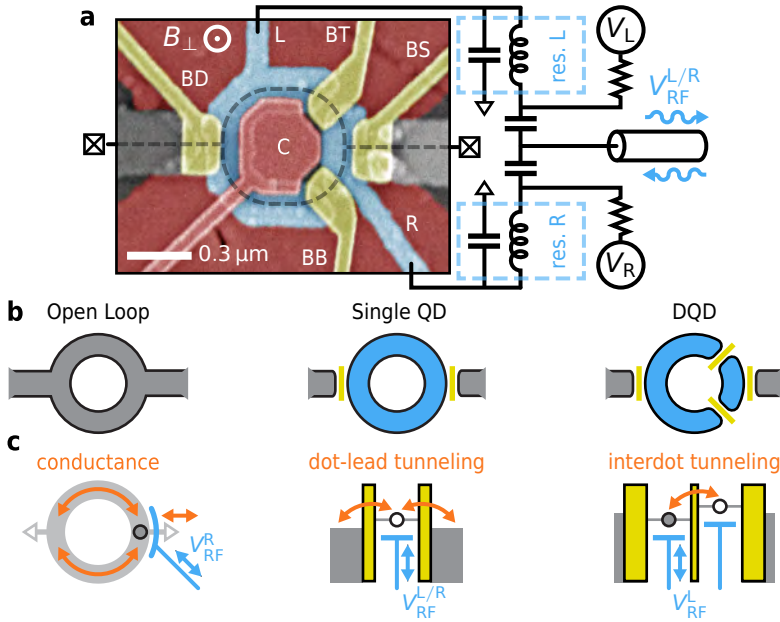


Figure 5.1: Experimental design and device configurations. **(a)** False-color electron micrograph of a nominally equivalent device to the one measured, and a schematic of the resonator circuit. The device may be tuned by depletion (red) and barrier (yellow, labeled) gate electrodes into an open AB loop, a ring-shaped QD, or a DQD with QDL and QDR chemical potentials tuned by plunger gate voltages  $V_L$  and  $V_R$  (blue, labeled), schematized in **(b)**. Outer and inner depletion gates have  $-2\text{V}$  and  $V_C = -3\text{V}$  applied respectively to form a conducting loop unless otherwise specified, illustrated by a dashed line. **(c)** Coupling of the resonator voltages to electron tunneling and transport for the three configurations depicted in **(b)**. The investigated transport mechanisms which couple to the oscillating resonator voltage (blue) are described with orange text and arrows. For the single and double QD configurations, we use a chemical potential illustration to show the oscillating resonator voltage coupling to tunneling events (orange arrows). For the open loop, its RF conductance dominates the resonator signal. For single and double QDs, incoherent tunneling with the leads has capacitive contributions from tunneling capacitance and dissipative contributions from charge relaxation. In addition, interdot tunneling in a DQD quantifiably translates into a quantum capacitance loading the resonator.

loop and into the leads in this case (orange arrows), such that the resonator signal primarily changes due to changes in the resonator's internal quality factor. When tuned into a single loop-shaped QD, both gates L and R tune its chemical potential. Hence, their coupled resonators are sensitive to tunneling effects between the QD ring and the leads. A chemical potential diagram of this coupling is shown in Fig. 5.1(c). Relaxation events in the form of electrons tunneling between the QD and the leads out of phase with the oscillating gate voltage loads the resonator reactively with tunneling capacitance and dissipatively with Sisyphus resistance [13, 128, 129, 142]. Through these signal contributions, Coulomb resonances of the QD are measurable since they lower both the resonator frequency and its quality factor. Finally, when tuned into a loop-shaped DQD, the gate resonators' signals are sensitive to interdot tunneling, depicted in Fig. 5.1(c). In particular, a substantial interdot tunnel coupling manifests in a purely reactive admittance arising from quantum capacitance [13, 125, 130], which can be used to directly measure

the tunnel coupling [138]. Hence, the measurement signal arises almost entirely from a frequency shift of the resonator due to the additional quantum capacitance.

### 5.3. PHASE-COHERENT LOOP AND QUANTUM RING

We begin by verifying the electron phase coherence in our device manifested by the AB effect. To form an open loop without QDs, we set all accumulation, plunger, and barrier gates to positive voltages to remove potential barriers. Fig. 5.2(a) presents the four-terminal conductance  $G$  and response of the right gate R resonator as a function of the out-of-plane field  $B_{\perp}$ . Oscillations of conductance in flux with a periodicity of  $h/ne$  for integer  $n$  are expected, depending on how many times an electron can travel around the loop while maintaining a coherent phase [6]. The resonator is sensitive to dissipative transport in the loop despite being capacitively coupled, manifesting as a reduction of the resonator's quality factor. Matching AB oscillations and higher harmonics are prominent in both  $G$  and the depth of the minimum in the reflection coefficient of the gate R resonator on resonance [246]. We observe a varying  $\phi_0 \equiv h/e$  and  $h/2e$  flux periodicity consistent with the expected bounds on area based on the lithographically defined 180 nm and 360 nm inner and outer radii of the loop. Here,  $h/e$  is the single-electron flux quantum. This suggests a phase coherence length on the order of a micron, based on the inferred circumference of the loop.

To investigate if the entire ring can support an extended electronic state, we continue by tuning the open loop into a large ring-shaped QD. The electron eigenstates of a sufficiently thin ring are angular momentum states with energies quadratic in flux, centered at integer multiples of  $h/e$ . By virtue of the Pauli exclusion principle, the highest unoccupied electron state is expected to exhibit a zig-zag like pattern in energy with an  $h/e$  flux periodicity, illustrated in Fig. 5.2(d). When the quantum ring forms a QD coupled to leads, this results in analogous kinked oscillations of the dot's addition energy—its spacing between Coulomb resonances—as a function of chemical potential [243, 247].

To form such a quantum ring, we lower  $V_{BS}$  and  $V_{BD}$  to form tunnel barriers (Fig. 5.1 (b,c), middle), and tune the QD's chemical potential with  $V_C$ . Both gate L and gate R's resonators are sensitive to tunneling between the dot and surrounding leads, since  $V_L$  and  $V_R$  tune the ring's chemical potential. To project each complex resonator signal into a single real quantity, we calculate the absolute distance of it from the Coulomb blockade signal, denoted  $\tilde{V}_{RF}^L$  or  $\tilde{V}_{RF}^R$  (see Supplemental Sec. 5.7.1). Since both resonators are measured simultaneously in this case, we normalize the resulting magnitudes and sum them for measurements of this QD. In this regime, the large QD exhibits a finite level spacing as demonstrated by the gapped excitation lines visible in Coulomb diamond measurements shown in Fig. 5.2(b). Moreover, we observe  $h/e$ -periodic oscillations of the addition energy as the magnetic flux is swept with zero applied bias in Fig. 5.2(c), consistent with expectations for a quantum ring [243, 244]. Though the oscillations are highly irregular, the peak positions and signal strengths' average Fourier transform shows a clear peak at an  $h/e$  period of 27 mT, shown in the inset. Deviations from a regular zig-zag pattern in the addition energy may arise when the ring is not perfectly one-dimensional, such that radial degrees of freedom contribute to its wave function. Potential irregularities along the ring's perimeter and effects of spin-orbit coupling also can cause the more complex oscillations in its addition energy [248].

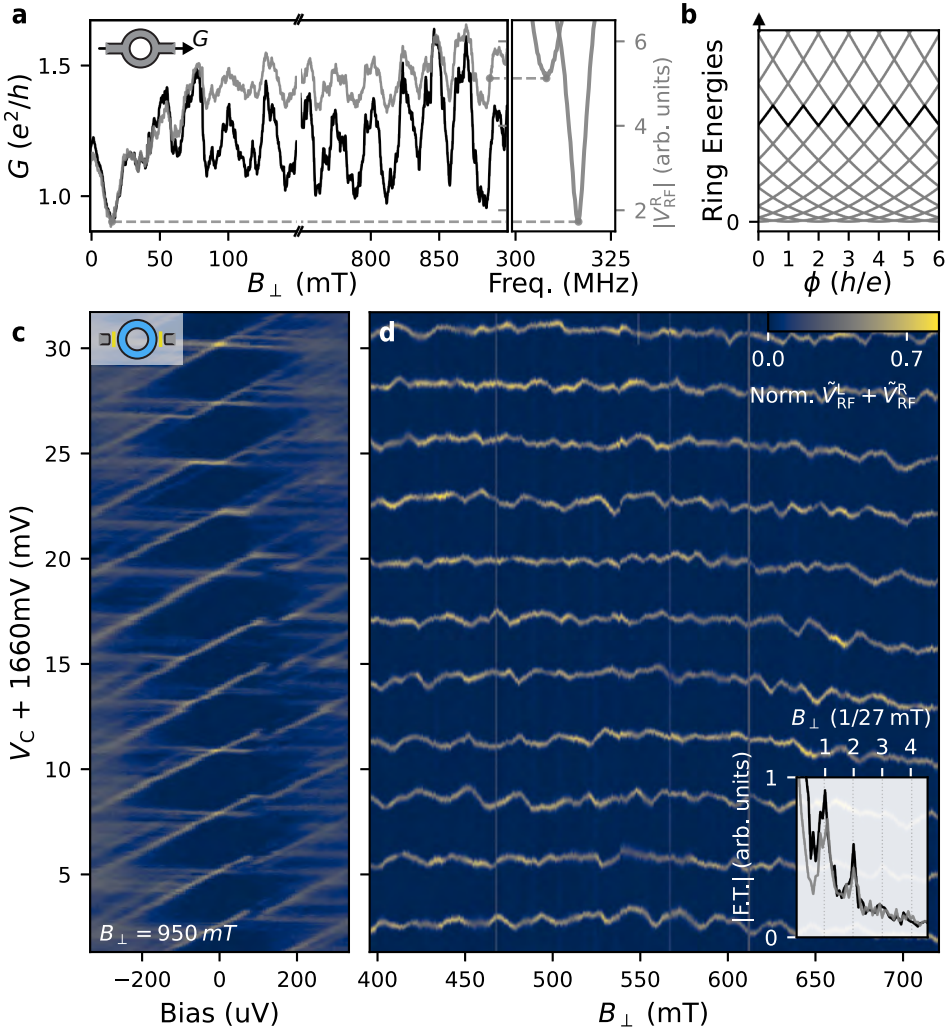


Figure 5.2: Phase-coherent transport and extended electron states. **(a)** AB oscillations in the open loop configuration depicted in the inset. Measurements are at zero bias voltage, of 4-terminal lock-in conductance (black) and of the absolute reflected signal (gray) from the resonator coupled to the  $V_R$  electrode. Here,  $|V_{RF}^R|$  is taken at the field-dependent resonance amplitude minimum (right). On the right, example frequency sweeps from which the minimum signal is calculated are shown.  $h/e$  and  $h/2e$ -periodic oscillations are visible in both the conductance and in the RF signal. **(b)** Single-particle energies for a thin ring  $\propto (e\phi/h + l)^2$  for  $l \in \mathbb{Z}$ . The tenth lowest energy state is highlighted, showing that energies for fixed electron number oscillate in a zig-zag fashion. **(c)** Coulomb diamonds with the device configured into a ring-shaped QD depicted in the inset at  $B_{\perp} = 950 \text{ mT}$ . The sum of normalized signals from both gate resonators is plotted, centered about the signal in Coulomb blockade. A consistently finite excitation energy is visible. **(d)** Zero-bias Coulomb resonances as a function of  $B_{\perp}$ , with measurement frequencies adjusted to be near resonance at each  $B_{\perp}$  value. *Inset:* Normalized absolute Fourier transform of the resonance  $V_C$  position (black) and signal height (gray) averaged across all Coulomb resonances. Both have clear peaks at an  $h/e$  periodicity of 27 mT.

## 5.4. FLUX-TUNABLE INTERDOT COUPLING

Having established phase coherence of the 2DEG loop, we next consider the case of a loop comprising two quantum dots threaded by a magnetic flux, illustrated in Fig. 5.3 (a). For this system, we expect magnetic flux to tune the effective interdot tunnel coupling. This is in contrast to studies embedding QDs into semiconducting rings where one trajectory involving tunneling through a QD could interfere with trajectories involving the other loop arm, potentially containing a second QD [249–258]. Assuming that at each interdot charge transition both QDs are described by a single fermionic level, the DQD can be represented as a two-level system with an effective coupling matrix element  $t_{\text{eff}} \equiv t_{\text{T}} + t_{\text{B}}$ . Here, we define  $t_{\text{T}}$  and  $t_{\text{B}}$  as the interdot coupling due to the top and bottom arms, respectively. Under the Peierls substitution, a magnetic flux  $\phi(B_{\perp})$  imparts a phase on each coupling [230]. Using an appropriate choice of gauge, we then have

$$|t_{\text{eff}}| = \sqrt{|t_{\text{T}}|^2 + |t_{\text{B}}|^2 + 2|t_{\text{T}}t_{\text{B}}| \cos(2\pi\phi/\phi_0)}, \quad (5.1)$$

assuming  $t_{\text{T}}$  and  $t_{\text{B}}$  had equal phases at zero field. Via quantum capacitance,  $t_{\text{eff}}(\phi)$  imparts a frequency shift on QDLs gate resonator with a maximal value in the ground state  $\propto 1/|t_{\text{eff}}|$ . Consequently, we expect the frequency shift to oscillate periodically with  $\phi$ . In Figs. 5.3(b,c), we plot the expected dependence of the resulting frequency shift on flux [125, 130].

Experimentally, we realize this system as a loop-shaped DQD with chemical potentials tuned by voltages  $V_{\text{L}}$  and  $V_{\text{R}}$ . To focus on interdot transitions where the signal contains information about the interdot tunnel coupling  $t_{\text{eff}}$ , we lower  $V_{\text{BS}}$  and  $V_{\text{BD}}$  until tunneling rates to the leads are undetectably small. Meanwhile, we form the DQD by lowering  $V_{\text{BT}}$  and  $V_{\text{BB}}$  into a regime of moderate tunneling, such that interdot transitions exhibit a substantial quantum capacitance signal. The barriers are tuned to be approximately equal based on DC current measurements (Supplemental Sec. 5.7.2). Coulomb diamond measurements demonstrate a varying but finite level spacing above 70  $\mu\text{eV}$  in both QDs (Supplemental Sec. 5.7.3) [20], such that the DQD is well-described by two coupled fermionic levels [33]<sup>1</sup>. Maintaining a finite excitation energy on both QDs despite their large lithographic size is achievable due to the low effective mass of roughly 0.016 $m_{\text{e}}$  in the 2DEG [245], which favors confinement.

Selecting a single interdot transition in this regime, we measure gate and frequency dependent traces of the gate L resonator's response  $V_{\text{RF}}^{\text{L}}$  as a function of  $B_{\perp}$ , aiming to extract  $|t_{\text{eff}}|$ . At each point in the gate space, we fit the results to an asymmetric resonator model to extract the resonance frequency shift  $\Delta f_0^{\text{L}}$  (see Appendix C and Refs. [158, 187, 190]). As no resonator losses were measured over this interdot transition, the resonator response may be described as a quantum capacitance  $C_{\text{q}}$  loading the bare capacitance  $C$  and inductance  $L$  of the resonance frequency as  $f_0 = 1/2\pi\sqrt{L(C + C_{\text{q}})}$ . Accordingly, we fit the  $V_{\text{L}}$  dependence of  $\Delta f_0^{\text{L}}(C_{\text{q}})$  to a thermal quantum capacitance model described by

$$C_{\text{q}} = 2(e\alpha_{\text{L}})^2 \frac{|t_{\text{eff}}|^2}{(\Delta E)^3} \tanh\left(\frac{\Delta E}{2k_{\text{B}}T}\right), \quad (5.2)$$

<sup>1</sup>As we will see in the subsequent section, the specific levels probed in Figs. 5.3 and 5.4 also exhibit signs of spin degeneracy, indicating further that they are fermionic states rather than some other many-body charge level.

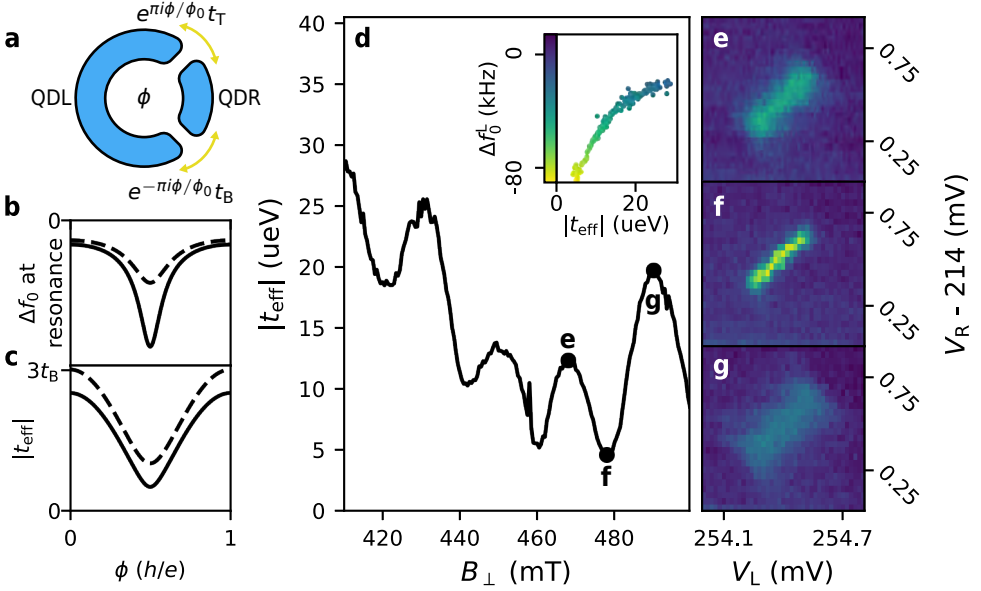


Figure 5.3: Tuning DQD hybridization with flux. **(a)** Diagram of a DQD ring threaded by a magnetic flux  $\phi(B_{\perp})$ . **(b,c)** Schematic mapping of  $|t_{\text{eff}}|$  as a function of magnetic flux  $\phi$  into a final resonator frequency shift  $\Delta f_0(\phi)$  at charge resonance **(b)**, shown for  $t_T = 1.5t_B$  (solid) and  $2t_B$  (dashed). For sizable  $|t_{\text{eff}}|$  the frequency shift is  $\propto 1/|t_{\text{eff}}|$  [125, 130]. **(d)** Fit  $|t_{\text{eff}}|$  values from the frequency response of the gate L resonator as a function of  $B_{\perp}$  for a single interdot transition. The tunnel coupling oscillates periodically with varying contrast and amplitude. The inset defines the charge stability diagram (CSD) color scale and plots the approximately  $\propto 1/|t_{\text{eff}}|$  correspondence between the fit  $|t_{\text{eff}}|$  and maximum observed  $\Delta f_0^L$  for each  $B_{\perp}$  in **(d)**. **(e-g)** Select CSDs at the  $B_{\perp}$  values labeled in **(d)** showing the lineshape of  $\Delta f_0^L$  across the interdot transitions for different tunnel couplings.

to extract  $|t_{\text{eff}}|$ , where

$$\Delta E \equiv \sqrt{\alpha_L^2 (V_L + V_L^{\text{off}})^2 + 4|t_{\text{eff}}|^2} \quad (5.3)$$

is the energy splitting between the two dot levels involved in tunneling [125, 130]. The lever arm  $\alpha_L = 0.18$  and electron temperature  $T = 71$  mK are optimized simultaneously for all field values to produce the minimal fit error (Supplemental Sec. 5.7.4). Subsequently they are fixed, with the only other free parameters being the center offset  $V_L^{\text{off}}$  of the transition and  $f_0$  in the Coulomb blockade.

The resulting values of  $|t_{\text{eff}}|$  are plotted in Fig. 5.3(d), where oscillations of  $|t_{\text{eff}}|$  are clearly visible. In Figs. 5.3(e-g), we show examples of frequency shifts of the gate L resonator for several values of  $B_{\perp}$ , where we see that for smaller tunnel couplings the transition appears to be more narrow, but with a stronger frequency shift. In particular, the tunnel coupling in general does not reach zero at its minima, suggesting that  $t_T$  and  $t_B$  are not precisely equal, as exemplified in Fig. 5.3(c). The average value of  $|t_{\text{eff}}|$  between oscillations also varies unpredictably, indicating that the wave functions of the involved states change over the range of multiple flux periods. Nevertheless, with this measurement we explicitly demonstrate control of the hybridization between two fermionic levels with magnetic flux.

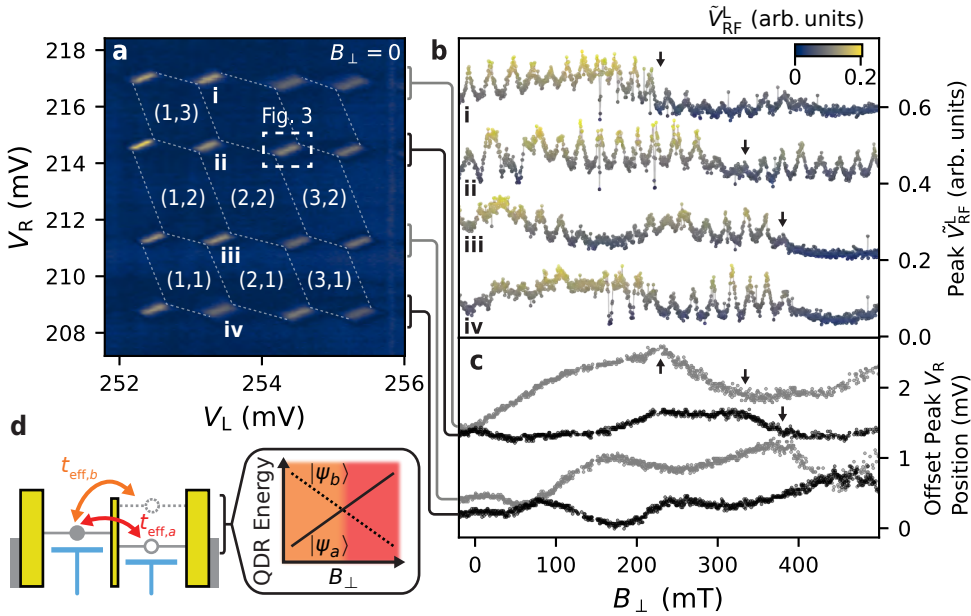


Figure 5.4: Flux-tunable hybridization of the DQD across multiple dot levels. **(a)** CSD with no applied field showing the window of 16 interdot transitions probed over a sweep of  $B_{\perp}$ . Dashed lines show the approximate boundaries of stable charge regions, because weak coupling of the QDs to the leads makes only interdot transitions visible in the gate L resonator's signal. Several charge regions are labeled with their relative charge states up to an offset  $(N_L, N_R)$  for a reference even charge  $N_L$  and  $N_R$  on QDL and QDR, respectively. **(b)** Peak signal deviation from Coulomb blockade  $\tilde{V}_{RF}^L$  of the four numeral-labeled transitions as a function of  $B_{\perp}$ , offset by 0.18 arb. units. **(c)** Peak positions of interdot transitions in  $V_R$  coordinates relative to the lowest peak, averaged across all four columns of transitions shown in **(a)**, and offset by 2.32 mV. The offset voltages vary linearly with the addition energies of QDR, so that anticrossings in the positions correspond to anticrossings between electron states of QDR. The black arrows show example points where a correlation can be observed between the oscillation amplitude of  $\tilde{V}_{RF}^L$  and anticrossings of QDR states. **(d)** Schematic describing the kinks in **(c)** and sudden changes in the  $|t_{eff}|$  oscillations of **(b)**. If a state  $|\psi_b\rangle$  overtakes another state  $|\psi_a\rangle$  as the ground state of QDR, and the former has a different tunnel coupling to the ground state of QDL, then a sudden change in  $|t_{eff}|$  and its oscillation amplitude may occur at this crossing.

## 5.5. LIMITS OF FLUX-TUNED TUNNEL COUPLING READOUT

For applications to topological qubits using QDs potentially containing many electrons, one must choose a particular dot level to optimize tunnel coupling readout. Therefore, in the same DQD regime as in Sec. 5.4, we proceed to study the variance of the oscillation amplitude in a broader field range and for multiple transitions, focusing on the 16 transitions shown in Fig. 5.4(a). There, similar to measurements of the ring-shaped QD, we plot the absolute deviation of the complex reflection signal of QDL's resonator from its average value in Coulomb blockade:  $\tilde{V}_{RF}^L$ . The complex signal is a one-to-one function of the frequency shift of QDL's resonator and is inversely proportional to  $|t_{eff}|$  for substantial  $|t_{eff}|$  [259]. An even-odd alternation in the transition spacing both along the  $V_L$  and  $V_R$  axes suggests that both QDs have spin degenerate levels with a finite level spacing in this window. We sweep  $B_{\perp}$ , measuring new CSDs of the 16 transitions at a single

measurement frequency adjusted to remain close to resonance. From these CSDs, we extract the maximum  $\tilde{V}_{\text{RF}}^L$  signal and the approximate peak position in the gate space for all transitions.

We plot in Fig. 5.4(b) the peak signal height—proportional to  $1/|t_{\text{eff}}|$  except when  $|t_{\text{eff}}|$  is very small—for the column of transitions enumerated in Fig. 5.4(a). For all four transitions,  $h/e$ -periodic oscillations of the peak height are clearly seen in some ranges of  $B_{\perp}$ . There, we identify four distinct features. First, some regions in Fig. 5.4(b) present visible oscillations in an otherwise small signal. One such region is appears at  $B_{\perp} \gtrsim 400$  mT for Transition iii. As schematically depicted in Fig. 5.3(b,c), this corresponds to large average  $|t_{\text{eff}}|$  and asymmetric barriers. Large tunnel couplings lead to a small frequency shift while asymmetry reduces the amplitude of the oscillations. Second, for smaller mean values of  $|t_{\text{eff}}|$  the signal variation with flux is much greater since  $|d\Delta f_0^L/d|t_{\text{eff}}||$  is larger, as seen for transition iv in the range 280 mT to 400 mT. Third, Transition iv at low fields exhibits a substantial peak height, indicating a small tunnel coupling, but a very weak oscillation contrast. This suggests that the tunnel barriers are tuned by  $B_{\perp}$  to be substantially asymmetric in this field range. Finally, a sudden drop of the peak height to near zero appears near the oscillation maximum for some transitions. We expect this to be a result of  $|t_{\text{eff}}|$  being small enough near the maximum peak height that thermal excitations and Landau-Zener transitions populate the excited DQD state, suppressing quantum capacitance (see Sec. 2.2.3 for a more detailed argument) [150, 151]. Importantly, this also suggests that  $t_B \approx t_T$  in those cases.

Differences between these scenarios are known to have consequences when sensing tunnel coupling to manipulate or measure qubits [138, 141, 175]. Probing the tunnel coupling with gate sensing in the regime of very weak tunneling gives a sharp change in the resonator signal for small changes in  $|t_{\text{eff}}|$ , allowing one to couple QDs weakly to the qubit of interest. Conversely, the signal is also sensitive to small changes in flux in this case. Certain topological qubit proposals also rely on a substantial tunneling magnitude for their operation [87].

To better understand Fig. 5.4(b), we now consider the influence of the specific electronic levels involved on the amplitude of the tunnel coupling oscillations. To this end, we plot the relative position  $V_R$  of interdot transitions averaged across all four columns in Fig. 5.4(c) and offset by their charging energy. This position is proportional to the excitation energies of the different QDR levels [22, 32], and we observe that they are nearly spin-degenerate at zero field. Kinks can be seen in the peak positions, indicating (anti)crossings between levels of QDR, depicted schematically in Fig. 5.4(d). At several fields, with examples highlighted by black arrows in Fig. 5.4(b,c), sudden changes in the average peak height and oscillation contrast of a transition appear correlated with anti-crossings of QDR levels. We hypothesize that variation in wavefunction overlap of different levels with field, as well as the particular levels involved, can have a drastic effect on  $t_{T/B}$ . As the cartoon in Fig. 5.4(d) illustrates, it may be the case that two different states of QDR have different wave-function overlaps with the ground state of QDL, and vice-versa. In particular, transitions between states of opposing spin have  $t_{\text{eff}}$  determined by spin-orbit coupling strength [23, 205, 260], while transitions between states of the same spin do not. Given the large out-of-plane  $g$ -factor of these 2DEGs [245], it was difficult to independently study spin and flux effects. Additionally, some changes in the mean peak

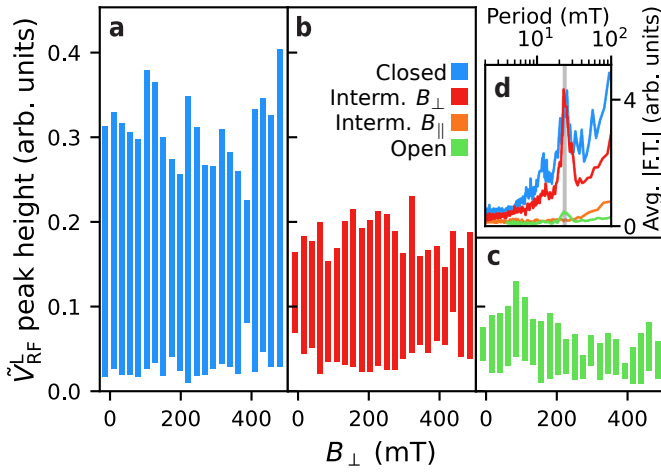


Figure 5.5: Contrast of DQD Tunnel Coupling Variation in Different Regimes. (a-c) Bars showing maximal peak height variation on a single interdot transition spanning the distance between the smallest and largest observed  $\tilde{V}_{\text{RF}}^{\text{L}}$  peak height, binned within one  $h/e$  period of 23.5 mT and plotted for three different regimes of tunnel barrier tuning. Of the 16 interdot transitions tracked in each dataset, only the bar for the transition with the largest signal variation for each period is shown. (a) summarizes a  $B_{\perp}$  sweep in a regime of weak interdot tunneling with more negative barrier voltages, while (c) shows data for strong tunneling and less negative barrier voltages. (b) corresponds to the intermediate tunnel barrier data from Fig. 5.4. The largest contrast in the signal generally occurs within the weak coupling regime. (d) Absolute Fourier transforms in each regime averaged across all 16 transitions. Orange represents a sweep of the in-plane field for the same transitions and tuning as the intermediate regime. A vertical line shows the peak at 23.5 mT.

height and oscillation contrast have no obvious correlation with QDR excitation energies, but we note that changes in the ground state of QDL as a function of field also affect  $t_{\text{eff}}$ . Hence, for any application requiring hybridization readout between QD levels, the specific levels used must be optimized for a given magnetic field range.

Lastly, we compare the differences in tunnel coupling readout contrast for regimes of different  $V_{\text{T/B}}$  and thus average  $t_{\text{T/B}}$  values. From Eq. 5.1 we expect that for nearly equal  $t_{\text{B}}$  and  $t_{\text{T}}$ , large tunnel couplings should produce the best oscillation contrast, since the tunnel coupling ranges from  $|t_{\text{T}}| + |t_{\text{B}}|$  to nearly zero. We therefore conduct measurements analogous to those in the intermediate coupling regime of Fig. 5.4 for other coupling regimes, with results summarized in Fig. 5.5 and shown in more detail in Supplemental Sec. 5.7.5. Namely, we first bin the peak heights for a given regime into windows equal to the  $h/e$  periodicity extracted from their average Fourier transform (Fig. 5.5(d)). Next, we plot bars spanning the minimum  $\tilde{V}_{\text{RF}}^{\text{L}}$  peak height to the maximum for whichever of the 16 transitions maximizes this difference in a given field bin. In addition to the dataset from Fig. 5.4, datasets for more negative (closed) and less negative (open) barrier gate voltages are shown in blue and green, respectively. As a control, in orange we show the data for an in-plane field sweep over the same transitions considered in Fig. 5.4, where no oscillations are seen. Compared to the red ‘intermediate’ coupling regime, the more closed-off regime shows on average a larger variation in peak height across a single  $h/e$  period, due to the increased slope of  $\Delta f_0^{\text{L}}$  with flux as described

above. The open regime shows very weak oscillation contrast despite the tunnel barriers exhibiting similar resistances (Supplemental Sec. 5.7.2), suggesting that larger coupling regimes are more sensitive to slight asymmetries between  $t_T$  and  $t_B$ . If the percent difference between  $|t_T|$  and  $|t_B|$  is non-negligible, then the maximum flux-tuned difference in quantum capacitance signals (proportional to  $1/(|t_T| - |t_B|) - 1/(|t_T| + |t_B|)$ ) becomes smaller for larger average tunnel couplings. Consequently, for flux-tuned qubit readout and manipulation schemes where the state is encoded in the sum or difference of two tunnel couplings [10, 11, 231], the optimal readout fidelity may occur for weak overall couplings.

## 5.6. CONCLUSIONS & OUTLOOK

Herein we measured a tunable hybridization between two electronic levels threaded by a magnetic flux for the first time. Using gate-based RF reflectometry implemented in a phase-coherent  $\text{InSb}_{0.86}\text{As}_{0.14}$  2DEG, we measured  $h/e$ -periodic oscillations of tunnel coupling between the levels of two QDs arranged in a loop. Even for nearly symmetrically tuned interdot tunnel barriers, the coupling was not generically suppressed at its minima, exhibiting a high degree of variability in magnitude and contrast of the tunnel coupling oscillations. We inferred that this variability is in part dependent on the specific QD levels involved. Finally, we found that, given the inherent difficulty of symmetrically tuning two tunnel barriers in parallel, the best signal contrast across an oscillation period occurs for relatively weak average interdot tunnel couplings [138]. On the other hand, tuning a tunnel barrier strength as a function of flux while probing the gate reflectometry signal at an interdot charge resonance serves in itself as a method for tuning  $|t_T|$  and  $|t_B|$  to be equal. In this approach, one would target the barrier strength where Landau-Zener transitions suddenly suppress the signal near its maximum as a function of flux, as described in Sec. 2.2.3. This work establishes a prerequisite for the readout of qubits formed in topological nanowires and Kitaev chains [10, 11, 14, 231, 261]. It also demonstrates a new mechanism by which the effective coupling between localized electronic states can be tuned and illustrates its limitations, applicable to semiconducting spin and charge qubits [237–239]. Even when undesirable, flux-tuned tunnel couplings may arise in two-dimensional QD arrays [228], as direct tunneling or cotunneling between QDs can occur via more than one trajectory in this case.

Raw data, analysis code, and scripts for plotting the figures in this publication are available from Zenodo [262].

The authors are grateful to J.V. Koski, L.P. Kouwenhoven, and F. Borsoi for helpful discussions and input on the manuscript and to L.P. Kouwenhoven for initiating the project. The authors also acknowledge financial support from Microsoft Quantum and the Dutch Research Council (NWO). F.K.M. acknowledges support from NWO under a Veni grant (VI.Veni.202.034).

C.G.P. and I.K. fabricated the device using a 2DEG heterostructure provided by D.X., C.T., and M.J.M.. C.G.P. and M.C. conducted the measurements with input from L.H. and F.K.M. F.K.M. and S.G. supervised the project. C.G.P. analyzed the data and wrote the manuscript with input from all authors.

## 5.7. SUPPLEMENTAL INFORMATION

### 5.7.1. CALCULATING RF SIGNAL DEVIATION FROM COULOMB BLOCKADE

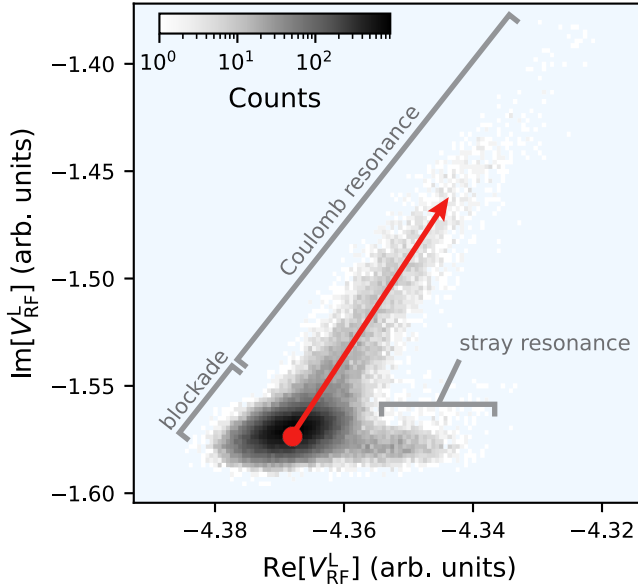


Figure 5.6: Histogram of the measured complex  $V_{\text{RF}}^{\text{L}}$  values from the dataset of Fig. 5.4. The extracted value of  $V_{\text{RF}}^{\text{L0}}$  for this dataset is plotted in red, and is roughly centered over the clustering of points corresponding to the Coulomb blockade signal.  $\tilde{V}_{\text{RF}}^{\text{L}}$  is calculated as the absolute deviation of the signal from this point.

The scattering parameters  $V_{\text{RF}}^{\text{L}}$  and  $V_{\text{RF}}^{\text{R}}$  measured in the reflectometry circuit are complex and at Coulomb resonance the signal information is stored in both their real and imaginary components. To illustrate this, we plot the histogram of measured  $V_{\text{RF}}^{\text{L}}$  values using the dataset of Fig. 5.4(a) in Fig. 5.6. A large concentration of points is centered around the Coulomb blockade signal (denoted  $V_{\text{RF}}^{\text{L0}}$ ) away from  $V_{\text{RF}}^{\text{L}} = 0$ , while an elongated distribution of points corresponds to the signal around a Coulomb resonance. The vector between these two groupings of measured values, illustrated with an arrow for an arbitrary  $V_{\text{RF}}^{\text{L}}$  on Coulomb resonance, contains most of the signal information. Hence, to plot a real quantity representing the RF signal while excluding the minimum possible amount of information, we plot the magnitude of this vector, denoted  $\tilde{V}_{\text{RF}}^{\text{L}} \equiv |V_{\text{RF}}^{\text{L}} - V_{\text{RF}}^{\text{L0}}|$ . We note that a second elongated distribution of points appears in Fig. 5.6 oriented horizontally. This arises from a stray charge resonance unrelated to the QDs but sensed by resonator L [148], appearing as a vertical resonance along the right side of Fig. 5.4(a).

To estimate  $V_{\text{RF}}^{\text{L0}}$ , we use two different methods. For data shown in Fig. 5.2, we take the mean  $V_{\text{RF}}^{\text{L}}$  over a rectangular window observed to correspond to Coulomb blockade from an initial inspection of  $|V_{\text{RF}}^{\text{L}}|$  as  $V_{\text{RF}}^{\text{L0}}$ . This technique is robust provided that charge jumps do not move Coulomb resonances into the window. For the data shown in Figs 5.4, 5.5 and 5.10, however, we use a modified median of the data since it can be

automatically calculated without specifying a window corresponding to Coulomb blockade. Namely, we first extract the lowest 50% of  $V_L$  rows in the dataset in terms of their  $V_{RF}^L$  standard deviation. This is because rows with high standard deviation are expected to contain Coulomb resonances since the signal varies more from its Coulomb blockade value. From this subset of points, we take the median as  $V_{RF}^{LO}$ . To illustrate this, we plot the  $V_{RF}^{LO}$  value extracted with this method in Fig. 5.6 in red. We see that it is roughly centered over the clustering of points corresponding to Coulomb blockade. Note that the same steps are used for  $V_{RF}^R$  data as used in Figs. 5.2(b) and (c). A different Coulomb blockade value is taken at each magnetic field value in the case of a field sweep, since the field affects the resonator's lineshape and resonance frequency.

### 5.7.2. TUNING SYMMETRIC PARALLEL TUNNEL BARRIERS

To tune the bare tunneling strengths  $t_T$  and  $t_B$  to be approximately equal, we select voltages on their corresponding barrier gates such that each admits the same instantaneous conductance when the other barrier is completely closed off. This procedure is summarized in Fig. 5.7. For this method to be valid, we must assume that the barrier gates have a negligible capacitive cross coupling, as evidenced by the approximate rectangular shape of their two-dimensional pinch-off map shown in Fig. 5.7(a).

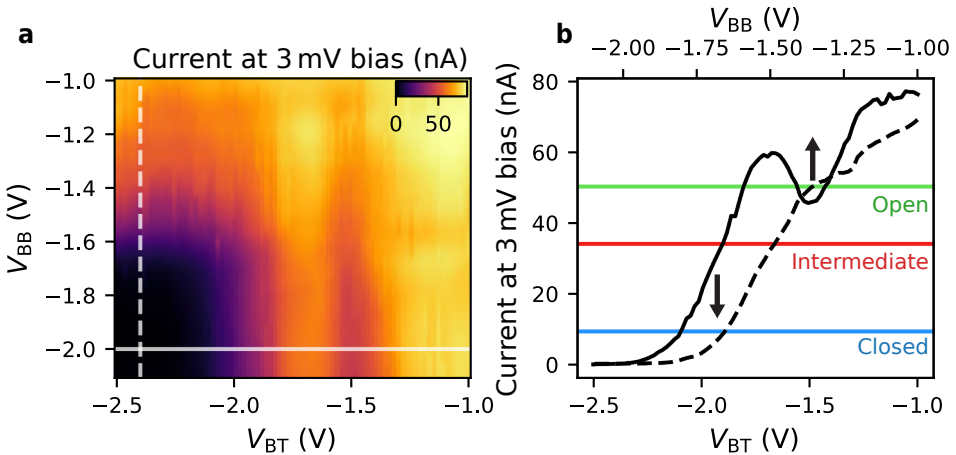


Figure 5.7: Pinch-off scans for approximately symmetric barrier tuning. (a) Current through the device at 3 mV applied bias voltage as a function of  $V_{BT}$  and  $V_{BB}$ , tuned into an otherwise open loop. The roughly rectangular shape of the zero-current region implies a weak cross-coupling between gates BT and BB. Linecuts where BT or BB are closed (white lines) can thus be used to select barrier voltages for roughly equal resistance. (b) Linecuts from the current map of (a). To tune for the intermediate coupling regime of Fig. 5.4 (red), or the more closed off (blue) and open (green) regimes described in Fig. 5.5,  $V_{BT}$  and  $V_{BB}$  voltages are chosen such that when the opposite barrier is pinched off, they both admit roughly the same current. The relatively large bias reduces the influence of QD states under the barriers on the measurement.

### 5.7.3. COULOMB DIAMONDS

Coulomb diamonds of QDL and QDR are shown in Fig. 5.8, from which we observe that both exhibit a consistently finite excitation energy between electronic levels.

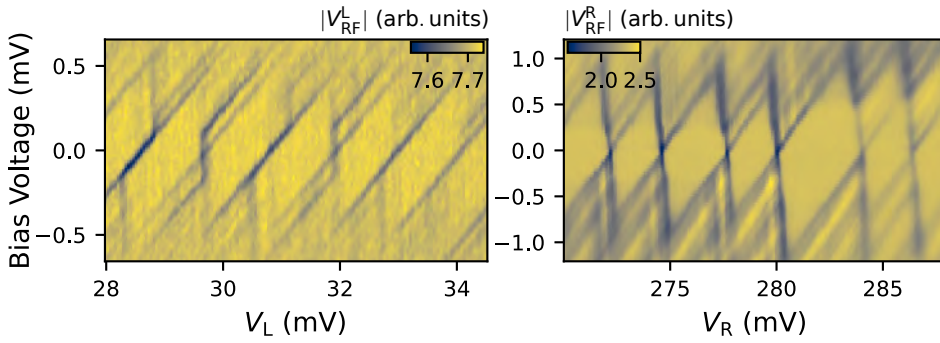


Figure 5.8: Coulomb diamonds of QDL (a) and QDR (b). The single QDs are tuned such that both the relevant lead barrier as well as  $V_{BT}$  and  $V_{BB}$  are in a weak tunneling regime. Magnitude of the reflectometry signal near the resonance frequency of their respective plunger gates' resonators is plotted. A varying but finite level energy spacing is visible for both QDs larger than the linewidth.

#### 5.7.4. FITTING PROCEDURE FOR TUNNEL COUPLING EXTRACTION

Herein we detail the procedure used to extract the effective tunnel coupling magnitude of a DQD ( $|t_{\text{eff}}|$  in the main text), given a CSD spanning an interdot charge transition with a frequency-dependent response measured at each point for a resonator coupled to one of the QD's gates. The parametric capacitance for a gate at voltage  $V_g$  primarily coupled to a single charge island or QD (indexed by  $i$ ) out of multiple potentially coupled islands is

$$C_p = \tilde{\alpha}_i |e| \frac{d\langle \hat{n}_i \rangle}{dV_g}, \quad (5.4)$$

where  $\langle \hat{n}_i \rangle$  is the expectation value of charge on QD  $i$  and  $\tilde{\alpha}_i$  is a lever arm of the gate's coupling to the quantum modified by mutual capacitances of this QD to other charge islands in the system, see Appendix D for further details. In essence, the large interdot capacitance of the system when tuned into the DQD regime (as can be inferred from the interdot transition width in gate space relative to the spacing between transitions in Fig. 5.4(a) [22]) lowers the effective lever arm of the gate to the sensed QD. Consequently, we must fit for  $\tilde{\alpha}_i$  independently, since it is not expected to agree with the lever arms extractable from the Coulomb diamond measurements of Fig. 5.8. This parametric capacitance can be calculated from the fitted resonator frequency  $f_0$  as  $C_p = 1/4\pi^2 L f_0^2 - C$  where  $L$  and  $C$  are the resonator's bare inductance and capacitance, respectively. In practice, we approximate  $L$  at zero magnetic field as its simulated value for the resonator's inductor coil. We calculate  $C$  from the resonance frequency in Coulomb blockade, where  $C_p$  is assumed zero. At each value of the out-of-plane magnetic field  $B_{\perp}$ , we assume that in Coulomb blockade the only shift in the resonator frequency is due to changes in  $L$ , such that from frequency fits at each field we can extract  $L(B_{\perp})$  assuming  $C(B_{\perp})$  is fixed. Thus, the parameters  $L$  and  $C$  are fixed by measurements and not varied in the subsequent fits described below.

As an explicit model for parametric capacitance, we consider the model of Refs. [125, 130] for a DQD coupled to a phonon bath. Near an interdot transition, this model considers two charge states with an excess electron residing either on a discrete fermionic

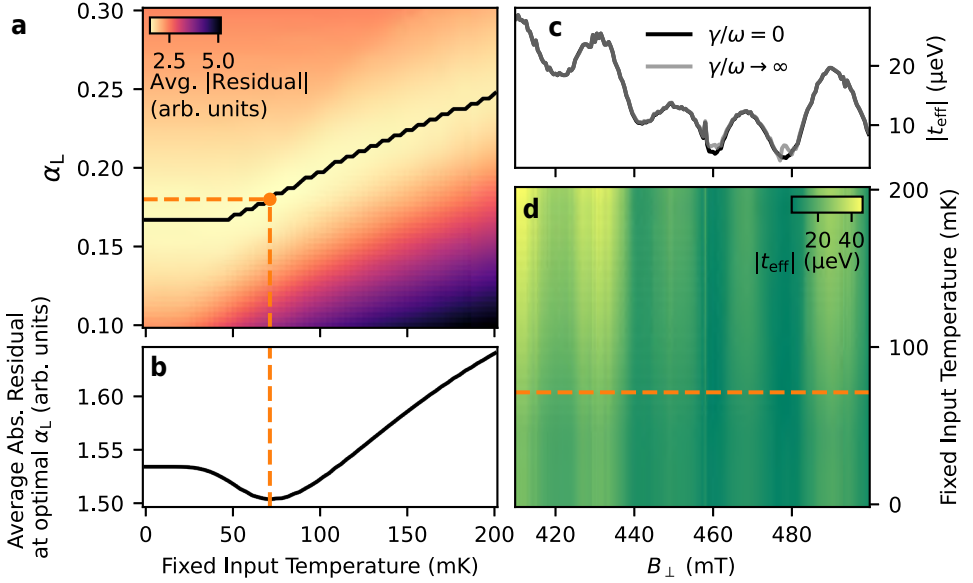


Figure 5.9: Optimization of tunnel coupling fits. **(a)** The mean absolute residual difference between the fit  $C_p$  lineshape of the interdot charge transition as a function of  $V_L$  and the  $C_p$  values extracted from fit frequency shifts of QDL's resonator. The black line shows the fixed  $\alpha_L$  value minimizing the residual error for each fixed  $T$ . **(b)** The mean residual error with  $\alpha_L$  fixed at its optimal value shown in **(a)** for each fixed value of  $T$ . A clear minimum is found at  $T = 71$  mK and  $\alpha_L = 0.18$ . **(c)** The extracted  $|t_{\text{eff}}|$  for zero tunneling capacitance ( $\gamma = 0$ ) and maximal tunneling capacitance, which saturates as  $\gamma \rightarrow \infty$ . The presence of tunneling capacitance has a negligible effect on  $|t_{\text{eff}}|$  except at very small  $|t_{\text{eff}}|$ . **(d)** Fit  $|t_{\text{eff}}|$  with  $\alpha_L$  fixed to the value minimizing fit error for each value of fixed temperature.

mode of the sensed QD, or a mode of a second QD. These two modes are coupled by tunnel coupling  $t_{\text{eff}}$ , and the detuning between their energies is given by  $\varepsilon = \tilde{\alpha}_i (V_g - V_g^{\text{off}})$  where the offset  $V_g^{\text{off}}$  determines the transition position in gate space. In this model, the parametric capacitance is found to be

$$C_p = \underbrace{2(e\tilde{\alpha}_i)^2 \frac{|t_{\text{eff}}|^2}{(\Delta E)^3} \tanh\left(\frac{\Delta E}{2k_B T}\right)}_{\equiv C_q(\varepsilon)} + \frac{(e\tilde{\alpha}_i)^2}{4k_B T} \left(\frac{\varepsilon}{\Delta E}\right)^2 \frac{\gamma^2}{\omega^2 + \gamma^2} \cosh^{-2}\left(\frac{\Delta E}{2k_B T}\right), \quad (5.5)$$

where  $\Delta E \equiv \sqrt{\varepsilon^2 + 4|t_{\text{eff}}|^2}$  is the energy splitting of the charge qubit and  $\omega$  is the angular resonator measurement frequency. The first term above corresponds to quantum capacitance while the second corresponds to so-called tunneling capacitance. The parameter  $\gamma$  quantifies incoherent tunneling due to phonon absorption and emission, and in principle is another parameter we must include in our fit of  $C_p$  to extract  $|t_{\text{eff}}|$ .

A resistive contribution to the effective impedance of the sample known as Sisyphus conductance arises, however, whenever there is substantial tunneling capacitance [125,

130], which would lower the resonator internal quality factor near the transition. In our fits of the frequency-dependent CSDs, the change in resonator quality factor was not discernible at the interdot transition, indicating that Sisyphus resistance and likely tunneling capacitance can be neglected in our fits. This also indicates that all information about interdot tunneling is contained in the frequency shift  $\Delta f_0$ , such that we may solely fit  $\Delta f_0(V_g)$  to extract  $|t_{\text{eff}}|$ , rather than simultaneously fitting the frequency shift and quality factor. Regardless, in Fig. 5.9(c) we show that maximizing the contribution of tunneling capacitance leads to a negligible change to the extracted  $|t_{\text{eff}}|$  except for very small tunnel couplings. Hence, we neglect tunneling capacitance for the fits of Fig. 5.3(d).

Under these constraints, we extract a fitted  $C_p(V_g)$  from fitted  $\Delta f_0^L$  and our knowledge of  $L$  and  $C$  described above, and fit the result to

$$C_p = C_q(\alpha_L(V_g - V_g^{\text{off}})) + C_{\text{off}} \quad (5.6)$$

with  $C_q$  as defined above and where we denoted  $\tilde{\alpha}_i \rightarrow \alpha_L$  as the effective QDL lever arm. In fact, we select five rows of the gate voltage near the center of the transition and fit them simultaneously with the same  $|t_{\text{eff}}|$ ,  $\alpha_L$ , and  $T$ , but allow for a different  $C_{\text{off}}$  and  $V_g^{\text{off}}$  for each row. In other words, we fit multiple traces for values of the other QD's gate voltage near the center of the charge transition in the charge stability diagram. The offset  $C_{\text{off}}$  accounts for errors in converting from  $\Delta f_0$  to  $C_p$ . These parameters are fitted independently for each row.

Since  $T$  and  $\alpha_L$  should be roughly the same at all fields, we sweep different fixed values of these parameters iteratively and choose the values which lead to a minimum total residual across all magnetic field values. We found a global optimum of  $T = 71$  mK and  $\alpha_L = 0.18$  which minimized the mean absolute fit residual error, see Fig. 5.9(a,b). This temperature is larger than the roughly 20 mK temperature of the dilution refrigerator used, which is not unexpected since electron temperature may be raised by connection to higher temperature cables and electronics [20]. Lastly, in Fig. 5.9(d), we observe that the oscillation amplitude of  $|t_{\text{eff}}|$  does vary with increasing temperature used in the fits (with  $\alpha_L$  fixed at the optimum shown in Fig. 5.9(a)), but the oscillations of  $|t_{\text{eff}}|$  are consistently present with a period of one flux quantum.

### 5.7.5. FIELD-DEPENDENCE OF PEAK HEIGHTS IN DIFFERENT COUPLING REGIMES

In this section the full datasets from which Fig. 5.5 was constructed are shown in Fig. 5.10, including the dataset used in Fig. 5.4. The four datasets are measured in three different regimes of interdot barrier gate voltage strengths, denoted the 'closed', 'intermediate', and 'open' regimes ordered from the strongest to the weakest barrier gate voltages separating QDL and QDR. Though not shown in the figure, in the closed regime at fixed field values, some transitions occasionally exhibited a jitter from row to row in  $V_L$ -space. This may be due to very weak coupling from the DQD to the leads resulting in electrons tunneling on to the DQD stochastically as the gate is swept, and may result in unphysical additional suppression of the peak height for some fields. Nonetheless, the prominent peak of the Fourier transform of this data at a periodicity of one flux quantum (shown in Fig. 5.5) indicates that the sharp dips in the data truly correspond to a suppression of the signal periodically as a function of flux.

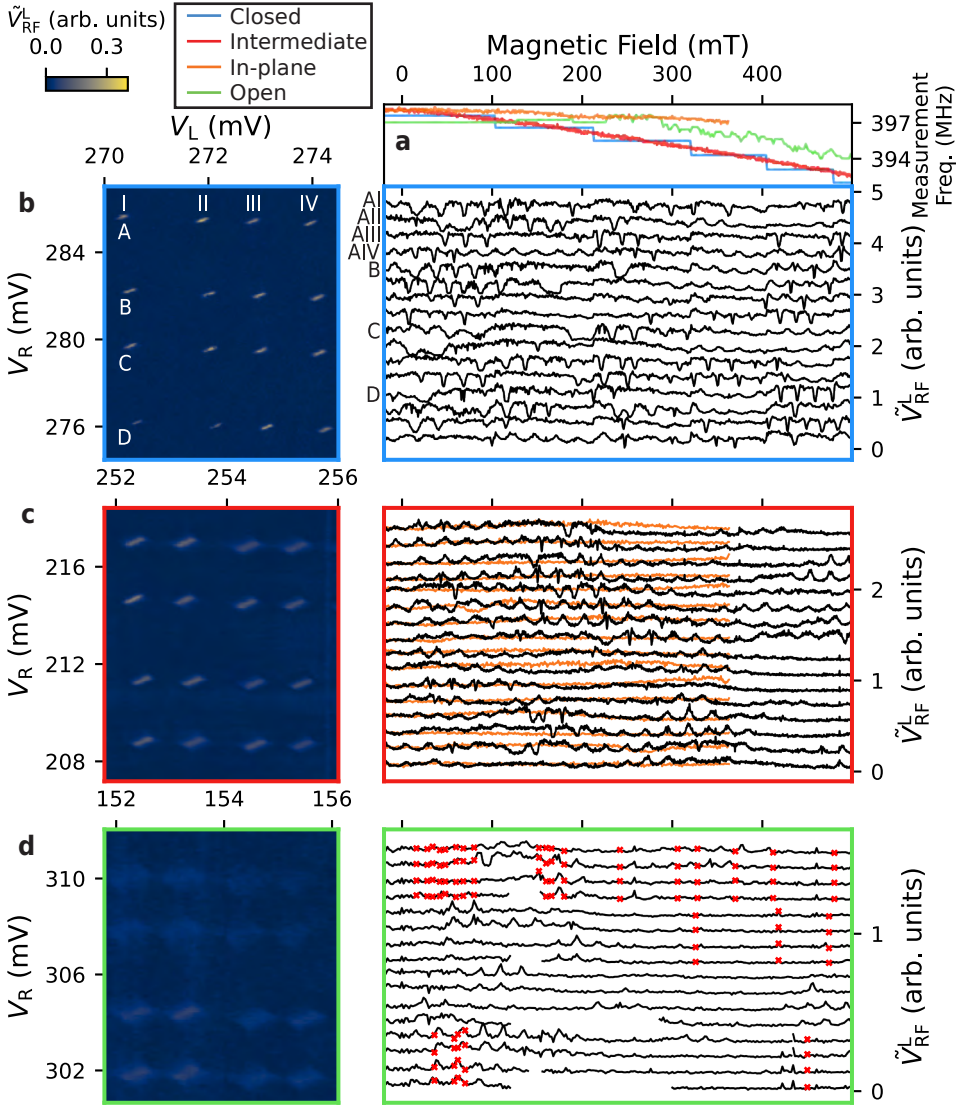


Figure 5.10: Field-dependence of interdot charge transitions in different regimes of tunnel coupling. (a) Measurement frequency used at each out-of-plane field value  $B_{\perp}$  for the three regimes of tunneling strength investigated and for an in-plane field  $B_{\parallel}$  sweep for the same transitions of the intermediate regime. (b-d) Field-dependence data for the closed (b), intermediate (c), and open (d) tunnel coupling regimes. These correspond to voltages  $(V_{BT}, V_{BB}) = (-2.1, -1.65)V$ ,  $(-1.9, -1.49)V$ , and  $(-1.82, -1.34)V$  respectively.  $V_{BS}$  and  $V_{BD}$  were tuned to a very weak tunneling regime of  $V_{BS} = -2.05V$  and  $V_{BD} = -2.75V$ , except in the closed regime where  $V_{BS} = -2.5V$ . *Left*: CSDs measured at zero magnetic field, plotting  $\tilde{V}_{RF}^L$ . *Right*: Field-dependence of the peak deviation from Coulomb blockade for the interdot transitions shown in the CSDs, offset by 0.3 (b), 0.17 (c), and 0.09 arb. units (d). Peak heights in (c) for the  $B_{\parallel}$  sweep are plotted in orange. In (d), a stray resonance appeared which occluded some interdot transitions in a wide window. This resonance interfered with extraction of the peak signal height, and so appears as a gap. Red markers denote points at which charge jumps appeared in the search window used to extract the peak signal height.

# 6

## FLUX-TUNABLE JOSEPHSON EFFECT IN A FOUR-TERMINAL JUNCTION

*C. G. Prosko, W. D. Huisman, I. Kulesh, D. Xiao, C. Thomas, M. J. Manfra, S. Goswami*

We study a phase-tunable four-terminal Josephson junction formed in an InSbAs two-dimensional electron gas proximitized by aluminum. By embedding the two pairs of junction terminals in asymmetric DC SQUIDS we can control the superconducting phase difference across each pair, thereby gaining information about their current-phase relation. Using a current-bias line to locally control the magnetic flux through one SQUID, we measure a nonlocal Josephson effect, whereby the current-phase relation across two terminals in the junction is strongly dependent on the superconducting phase difference across two completely different terminals. In particular, each pair behaves as a  $\phi_0$ -junction with a phase offset tuned by the phase difference across the other junction terminals. Lastly, we demonstrate that the behavior of an array of two-terminal junctions replicates most features of the current-phase relation of different multiterminal junctions. This highlights that these signatures alone are not sufficient evidence of true multiterminal Josephson effects arising from hybridization of Andreev bound states in the junction.

### 6.1. INTRODUCTION

Multiterminal Josephson junctions (JJs) with more than two terminals have current-phase relations (CPRs) determined by the superconducting phases of all terminals [263]. The Andreev bound state (ABS) spectrum of multiterminal junctions can manifest topological phases containing Majorana bound states [264] or protected Weyl nodes in their band structure [15, 265–268], with the superconducting phases of the terminals behaving as momentum degrees of freedom [15]. To form Weyl nodes in the absence of a flux through the junction [269] at least four terminals are required, because an  $n$ -terminal

---

The work in this chapter is under review as an article in an academic journal. Preprint available at arXiv:2311.17158.

junction manifests topology in  $n - 1$  dimensions. Additionally, four-terminal JJs (4TJJs) are expected to exhibit non-trivial CPRs of the supercurrent through the junction [270–274], and can form a superconducting phase qubit bypassing some constraints of conventional flux qubits [275]. In particular, the phase difference across two terminals is expected to induce a phase difference and supercurrent across the other two terminals, giving them applicability as switching elements for superconducting electronics [274].

Previous work on multiterminal JJs observed multiterminal DC and AC Josephson effects [276–284], signatures of supercurrent mediated by Cooper quartets [285–288], and strong diode behavior [284, 289, 290]. Many signatures of quartet supercurrents can also be explained solely with two-terminal junction physics however [291], though tunneling spectroscopy measurements of the multiterminal JJ may reveal spectra of the prerequisite extended ABS [292]. For three-terminal JJs, signatures of Andreev molecules [293, 294] and more complicated subgap state spectra affected by spin-orbit coupling have been observed [295]. Meanwhile, despite numerous experiments on 4TJJs [277–279, 287, 288], the CPR of any four-terminal junction has yet to be probed with control over two or more phase degrees of freedom.

We thus consider a four-terminal JJ (4TJJ) embedded in two asymmetric DC SQUIDS penetrated by independently controllable magnetic fluxes. This allows us to control two phase differences across pairs of terminals in the junction. Accordingly, we can measure SQUID oscillations containing information about the CPR across their corresponding 4TJJ terminals in the form of a current-flux relation (CFR). Furthermore, with four instead of three terminals we are able to measure a Josephson effect which is fully ‘non-local’ in that the CPR between two superconducting terminals is modified by a phase difference across a completely independent pair of terminals [272, 273]. Correspondingly, two terminals of the 4TJJ form a tunable  $\phi_0$ -junction with a phase offset tunable in a range larger than  $0.2\Phi_0$  where  $\Phi_0 = h/2e$  is the superconducting flux quantum [296]. For this experiment and others in three-terminal JJs [297, 298], we model the junction as an array of two-terminal junctions and find that this  $\phi_0$ -junction effect can exist even in the absence of a hybridized ABS spectrum in the junction, necessitating other experimental signatures for ABS hybridization.

## 6.2. DEVICE DESIGN & CHARACTERIZATION

The devices (denoted A and B) are formed in an  $\text{InSb}_{0.86}\text{As}_{0.14}$  two-dimensional electron gas (2DEG) proximitized by epitaxial aluminum. Selective etching of the Al defines the multiterminal DC SQUID [245], see Figs. 6.1(a-c). A schematic depiction of the circuit is given in Fig. 6.1(d). The SQUIDS are designed such that two pairs of terminals in the 4TJJ each form one junction of a DC SQUID (labeled L or R). For each SQUID, the other roughly  $3\text{ }\mu\text{m}$ -wide reference junction (labeled J1L or J1R) is much larger and therefore has a much higher critical current  $I_{c,L}^{\text{ref}}$  or  $I_{c,R}^{\text{ref}}$ . In this DC SQUID configuration with asymmetric critical currents, the CPR of each pair of the 4TJJ terminals can be directly measured if the SQUID loop inductance is negligible [299, 300].

Two Ti/Pd layers of gate electrodes were then patterned, separated by a 20 nm thick  $\text{AlOx}$  dielectric from the 2DEG and from each other. These include top gates over the reference junctions J1L and J1R of each SQUID applying voltages  $V_{L,\text{ref}}$  and  $V_{R,\text{ref}}$  respectively. These allow us to pinch off conductance through these junctions and remove the

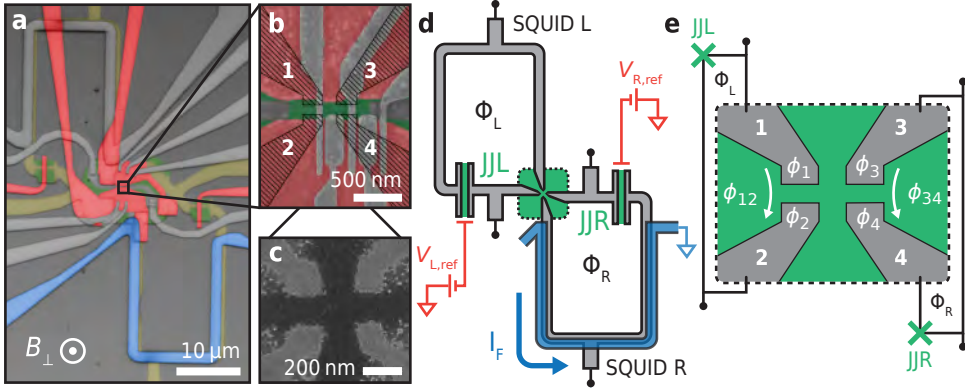


Figure 6.1: Experimental Setup. **(a)** False-color optical image of measured Device A, highlighting the 4TJJ's depletion gate and reference junction gates (red), the flux-bias line (blue), exposed portions of the 2DEG mesa (green), and the Al forming the SQUID circuits (yellow). **(b)** False-color scanning electron micrograph of Device A near its central 4TJJ. Unused misaligned gates in the second layer and unused normal-metal tunnel probe leads are shown in gray, while the designed pattern of the Al 4TJJ is superimposed in black on the image. **(c)** As in **(b)** but before any gates were deposited. Overetching of the Al caused the 4TJJ junction dimensions to be slightly larger than the design shown in **(b)**. Residues are visible surrounding the designed pattern, arising during an Al etching step. **(d)** Schematic of the device consisting of SQUIDs labeled L and R penetrated by fluxes  $\Phi_{L/R}$ . **(e)** Schematic of the 4TJJ itself, with the superconducting terminals numbered, and their wave function phases and phase differences labeled.

corresponding SQUID's flux-dependent behavior. Second, a large depletion gate in the first layer surrounding the 4TJJ (red in Fig. 6.1(b)) allows us to apply a voltage  $V_D$  depleting carriers surrounding it and eventually within the junction itself. This gate is kept grounded for all measurements except those in Supplemental Sec. 6.6.1 where we investigate its behavior. All other gates (gray in Figs. 6.1(a,b)) are kept grounded unless otherwise specified, since an unintentional misalignment with respect to the superconducting terminals limited their functionality<sup>1</sup>. Metallic Ti/Pd probe contacts near the 4TJJ are kept electrically floating or grounded to not interfere with measurements<sup>2</sup>. Lastly, a NbTiN flux bias line (blue in Figs. 6.1(a,d)) was sputtered around SQUID R to locally bias the magnetic flux  $\Phi_R$  penetrating it without significantly tuning the flux  $\Phi_L$  through SQUID L. This line is biased by a current  $I_F$  which generates a magnetic field penetrating SQUID R, and has a critical current of 1.05 mA. Combined with a global magnetic field

<sup>1</sup>The unused gates consisted of three barrier gates alternated with two wider gates. The former, in conjunction with the depletion gate, were intended to confine carriers underneath two two-terminal Josephson junctions formed between terminal pairs (1,2) and (3,4), while the latter could tune the carrier density within each junction. This in principle would enable forming Josephson junctions with transport mediated by a single ABS in each, while the middle barrier voltage could tune the wave-function overlap of the ABSs, thus tuning the four-terminal Josephson effects. The outer barriers would also have enabled using the normal metal leads to perform tunneling spectroscopy separately on each junction. Due to their misalignment, they are kept grounded to simplify interpretation of the experimental results.

<sup>2</sup>The probes are floating for all measurements except those of Figs. 6.2(d), 6.3(c), and 6.5, where one is grounded. As switching current measurements, these measurements are unaffected by the grounded probes, since current favors traveling through the superconducting circuit until the current bias is large enough that the circuit switches into a resistive state.

with an almost fully out-of-plane component  $B_{\perp}$  (calibrated in Supplemental Sec. 6.6.2), this allows for independent control of the magnetic flux through both SQUIDs. For additional fabrication details see Appendix A, and for details of the measurement setup supporting high currents on the flux bias line see Appendix B.4. Measurements are conducted at the 20–70 mK base temperature of a dilution refrigerator.

Before proceeding to measurements, we remark that the supercurrent across any two terminals  $i, j \in \{1, 2, 3, 4\}$  (labeled in Fig. 6.1(e)) of the 4TJJ is a  $\Phi_0$ -periodic function of all phase differences  $\phi_{i'j'} \equiv \phi_{i'} - \phi_{j'}$  of their superconducting wave functions [263]. Because only the relative phase differences determine the junction's behavior, there are only  $n - 1$  phase degrees of freedom for any  $n$ -terminal JJ. As we embed the 4TJJ in two DC SQUIDs, we have control of only  $\phi_{12}$  and  $\phi_{34}$ , meaning that a third independent phase difference (e.g.  $\phi_{13}$ ) is not directly controlled by experimentally tunable parameters.

To probe any uniquely multiterminal Josephson effects in this 4TJJ, we deduce phase shifts in its CPR through SQUID oscillation measurements, that is, measurements of the CFR. For two-terminal JJs, an established technique for measuring their CPR is to embed the JJ in a DC SQUID containing another 'reference' JJ and measure the SQUID's critical current as a function of flux. When the reference JJ's critical current is much higher than that of the probed junction the CFR of the SQUID becomes equivalent to the CPR of the probed junction [299–301]. It is important to note however that in the presence of a small but finite loop inductance, this is not strictly true. Nonetheless, we show that the CFR possesses key properties of the true CPR: its periodicity in flux, and shifts in its phase offset (see Supplemental Sec. 6.6.3).

6

We begin by characterizing each SQUID individually, with results summarized in Fig. 6.2. For these measurements, one SQUID is probed while the other's leads are kept floating, see Fig. 6.2(a). To exclude effects from the opposing SQUID, we set  $V_{L,\text{ref}} = -1\text{V}$  or  $V_{R,\text{ref}} = -1.2\text{V}$  to eliminate conductance through the opposite SQUID's reference junction. This prevents applied fields from tuning the phase across the opposite SQUID's 4TJJ terminals. The junctions in these devices have large enough self-capacitances that they are underdamped, potentially from capacitances to the nearby floating 4TJJ terminals. This is signified by their switching currents  $I_{\text{sw,L}}$  and  $I_{\text{sw,R}}$  varying stochastically between values less than or equal to their critical currents  $I_{C,L/R}$  [19, 302]. Here, we define the switching current as the applied current at which the voltage across the SQUID circuit jumps from zero to a finite value. Voltages  $V_L$  or  $V_R$  across the contacts of SQUID L or R are measured in a current sweep upwards from  $I_L$  or  $I_R = 0\text{A}$  to ensure the switching current and not retrapping current is measured, where  $I_{L/R}$  is the current applied across the SQUID with the other SQUID's contacts floating. An example CFR measurement is in Fig. 6.2(b), where we show switching current oscillations of SQUID L measured with a single current trace upwards from  $I_L = 0$  for each  $B_{\perp}$  value. At several  $B_{\perp}$  values  $I_{\text{sw,L}}$  appears much lower than the overall nearly-sinusoidal trend. We observe that SQUID L exhibits a  $\Phi_0$  periodicity of  $8.4\ \mu\text{T}$  as a function of  $B_{\perp}$ , expected to be roughly the same for SQUID R as they have identical lithographically-defined loop areas. Since  $I_{\text{sw,L/R}} \leq I_{C,L/R}$  and  $I_{\text{sw,L/R}}$  varies randomly between each trace, we focus on the maximum observed  $I_{\text{sw,L/R}}$  across repeated sweeps.

The resulting CFR measurements of SQUIDs L and R as a function of  $I_F$  are plotted in Figs. 6.2(c) and 6.2(d). SQUID R has a periodicity of roughly one flux quantum per  $85\ \mu\text{A}$

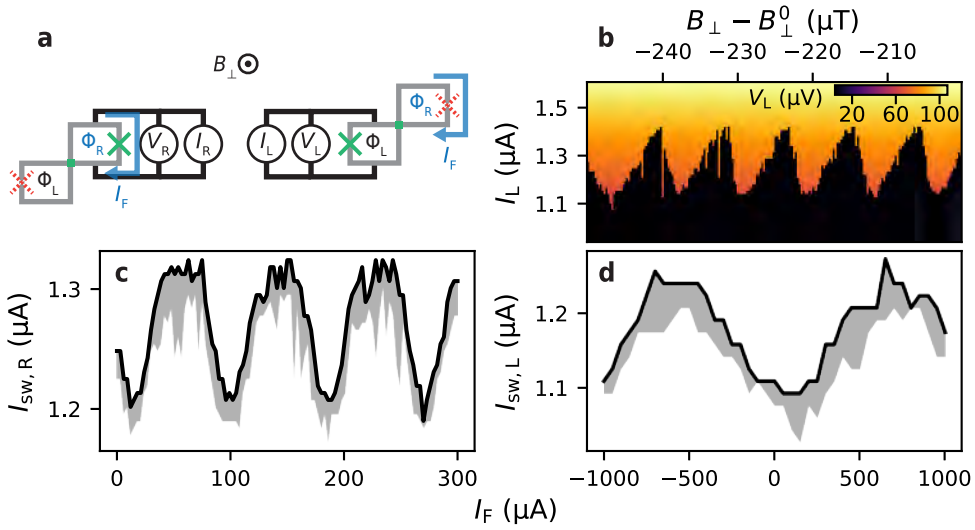


Figure 6.2: Characterization of individual SQUIDs. (a) Measurement circuit configurations for CFR measurements of the individual SQUIDs L (b,c), and R (d), taken with the opposite SQUID's reference junction pinched-off by setting  $V_{L/R,\text{ref}}$  to a strongly negative voltage, and with current applied across one SQUID's leads with the other's floating. (b) A SQUID oscillation measurement with a single current trace per  $B_\perp$  value for SQUID L. Current is swept positively from 0 A. (c) Maximum switching current  $\max[I_{sw,R}]$  (black) extracted as the largest  $I_{sw,R}$  measured across multiple current traces of SQUID R as a function of the flux line current. Variation of the switching current across the repeated traces is shown in gray. (d) Analogous measurements of SQUID L as a function of flux line current, where we observe a very weak cross-coupling of the flux line to this SQUID. All  $B_\perp$  scans are offset by  $B_\perp^0 \equiv -7.5\text{mT}$  determined as the  $B_\perp$  value at which JIL and JIR showed a maximum critical current in Fraunhofer measurements. The field is fixed to  $B_\perp = B_\perp^0$  when not being varied. Switching current offsets between (b) and (d) result from shifts in the effective zero-field point over time due to hysteresis in the system.

change in  $I_F$  while SQUID L has a periodicity of 1.3 mA, indicating that the flux-bias line almost exclusively tunes  $\Phi_R$ .

### 6.3. FLUX-TUNABLE NONLOCAL JOSEPHSON EFFECT

We proceed by conducting measurements involving both SQUIDs, aiming to probe non-local effects of the phase difference across two terminals of the 4TJJ on the CPR through the other two. To do so, we float the leads of SQUID R but keep JIR conducting unless otherwise specified, measuring the voltage  $V_L$  across SQUID L as a function of  $B_\perp$  and  $I_F$ . Recall that  $B_\perp$  roughly equally tunes  $\Phi_L$  and  $\Phi_R$  while  $I_F$  almost exclusively tunes  $\Phi_R$  (see Figs. 6.2(c,d)). This means we can fully navigate the space of phase differences  $\phi_{12}$  and  $\phi_{34}$  by sweeping these two parameters. Our results are summarized in Fig. 6.3.

In Figs. 6.3(a,b) we fix  $I_L = 1.1\mu\text{A}$  to a value near the SQUID L critical current and measure  $V_L$ . The SQUID voltage in its resistive state is a function of its critical current, and so must have the same periodicity and phase offset [19]. Hence, from the positions of extrema in  $V_L$  we can extract the relative value of the  $\phi_0$  offset  $\Delta\phi_{12}$  across terminals 1 and 2. When JIR is closed as in Fig. 6.3(a) so that  $\phi_{34}$  is not tuned by  $B_\perp$  or  $I_F$ , only local

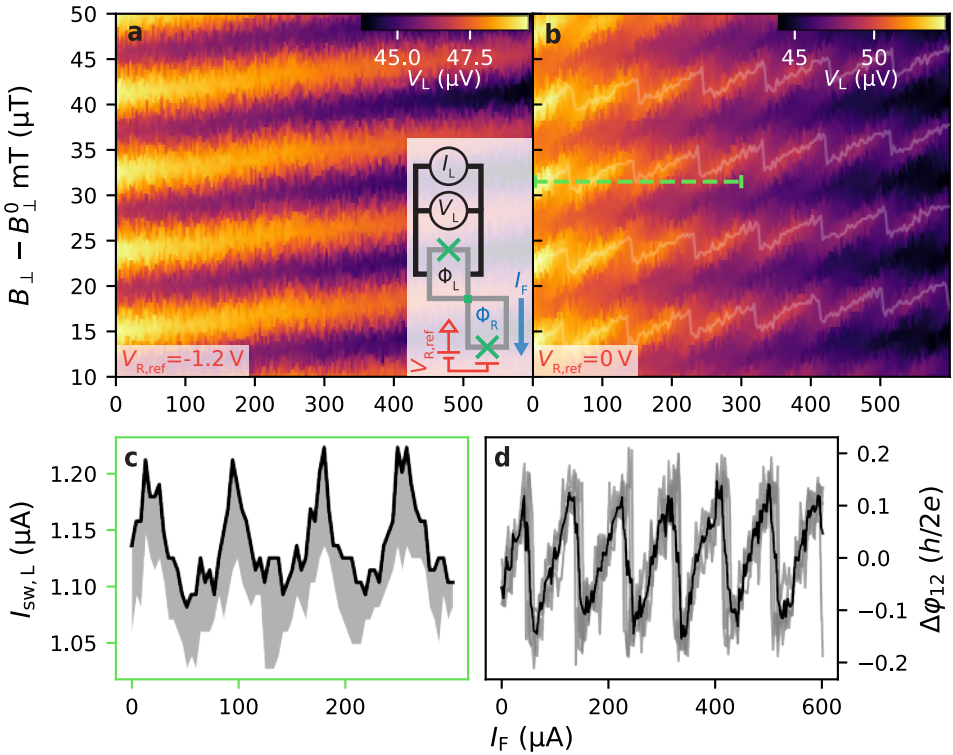


Figure 6.3: Flux-Tunable Josephson effect in Device A SQUID L. (a,b) Voltage measured with the junction in a resistive state after applying a  $I_L = 1.1\mu\text{A}$  current across SQUID L with SQUID R leads floating (inset) and (a) JJR pinched-off or (b) with it at 0V. Extracted  $V_L$  maxima are plotted in faint white, and show a zig-zag like variation with a periodicity equal to SQUID R's  $h/2e$ -periodicity in flux line current. (c) Extracted maximum switching current (black) along the green line in (b), calculated from 10 current traces swept upwards from zero current. Variation across the repeated current traces is shown in gray. Maxima in  $I_{\text{sw},L}$  correspond to maxima in the measured voltage of (b). Cross coupling of the flux-line field to SQUID L is negligible in this flux-current range, so the observed oscillations in the CPR are purely due to the nonlocal superconducting phase difference across terminals 3 and 4. (d) Phase offsets of SQUID L's local CPR (gray) for the four flux periods visible in (b), and their mean (black), calculated from (b) up to a constant offset. We observe a  $\phi_0$  tunability in a range greater than 0.2 flux quanta.

SQUID oscillations as a function of  $B_{\perp}$  are visible, tilted upwards due to the small cross coupling of  $I_F$  into  $\Phi_L$ . Remarkably however, when  $V_{R,\text{ref}} = 0\text{ V}$  as in Fig. 6.3(b), lobes of SQUID oscillation maxima appear in a zig-zag pattern. The lines of maximum  $V_L$  (highlighted in gray) are oriented diagonally along the  $B_{\perp}$  and  $I_F$  axes in a different direction than the maxima lines in Fig. 6.3(a). This feature thus arises due to a variation in  $\Phi_R$  changing  $\phi_{34}$ . In other words, the supercurrent through terminals 1 and 2 of the 4TJJ is tuned by the phase difference across two completely different terminals of the junction, manifesting a flux-tunable  $\phi_0$ -junction. Three-terminal circuits of two JJs sharing a common lead have enabled observations of similar nonlocal Josephson effects [297, 298, 303] as well as one controlled by excess spins in the junction [304]. In these experiments, nonlocal coupling between junctions was claimed to arise due to the direct wave

function overlap of ABSs in either junction. While these experiments have no obvious analog in four-terminal circuits, the effect observed here may be described as the limit of ABS wave functions in two JJs completely merging together [293]. We compare these experiments with theory further in Sec. 6.4.

To make this observation concrete, in Fig. 6.3(c) we measure repeated current traces of SQUID L along the green line highlighted in Fig. 6.3(b). The maximum observed switching current across all traces is shown as a black line while the variation of  $I_{\text{sw,L}}$  is shown in gray. Large  $\gtrsim 0.1 \mu\text{A}$  oscillations in the switching currents are visible as a function of  $I_{\text{F}}$  with the periodicity of SQUID oscillations in SQUID R. Since a change of over 1 mA in  $I_{\text{F}}$  is required to tune  $\Phi_{\text{L}}$  by one flux quantum due to direct cross coupling, these SQUID oscillations are purely due to coupling of  $\phi_{34}$  to the CPR between terminals 1 and 2. Additionally, we quantify the degree to which the  $\phi_0$  offset between terminals 1 and 2 can be tuned in Fig. 6.3(d). From the positions of successive SQUID oscillation maxima plotted in Fig. 6.3(b) in white, we extract the relative change  $\Delta\phi_{12}$  of each peak as a function of  $I_{\text{F}}$ . Since we can only extract the relative apparent  $\phi_{12}$  offset of the junction, we arbitrarily define  $\Delta\phi_{12} = 0$  as the maximum position at  $I_{\text{F}} = 0$ . A linear offset is also subtracted from each maximum to remove the effect of cross coupling between  $I_{\text{F}}$  and  $\Phi_{\text{L}}$ , and the result is converted into units of flux quanta from the  $B_{\perp}$ -periodicity of SQUID L oscillations. The average  $\Delta\phi_{12}$  across all maxima is plotted in black, while individual peak oscillations are in gray. We see that the  $\phi_0$ -junction formed across terminals 1 and 2 can have its phase offset tuned continuously in a range of over  $0.2\Phi_0$ . Behavior consistent with this is observed for analogous measurements of SQUID R, shown in Supplemental Sec. 6.6.4, and similar effects are also seen in measurements of device B which has an identical design in Supplemental Sec. 6.6.5.

Importantly, the  $\Phi_0$ -periodic circulating current in SQUID R could couple trivially to the flux through SQUID L via the loops' mutual inductance in the absence of any four-terminal junction effects. Due to the device design maximizing the spatial separation between SQUID loops however (Fig. 6.1(a)), such a coupling could not cause the observed strength of oscillations in  $\Delta\phi_{12}$ : the magnetic field produced by such loops carrying currents of less than  $2 \mu\text{A}$  produces less than 1 % of a flux quantum in the opposing loop.

## 6.4. MULTITERMINAL JUNCTIONS AS TWO-TERMINAL JUNCTION ARRAYS

In multiterminal JJs and Andreev molecule devices, tunable  $\phi_0$ -junctions are often considered a signature of behavior distinct to hybridized ABSs [305, 306] or of an ABS spectrum distinctly associated with multiterminal JJs [272]. In this section, we demonstrate that modeling these systems with networks of two-terminal JJs produces a tunable  $\phi_0$ -junction behavior which may be difficult to distinguish from the case where bound states in these junctions are truly hybridized into a multiterminal JJ or an Andreev molecule. Namely, while several superconducting terminals connected to a semiconducting region smaller than the superconducting coherence length  $\xi$  is naturally described by a hybridized ABS spectrum [263], similar nontrivial behavior in the CPR is also expected for a network of two-terminal JJs connecting each terminal. Notably, when a network of

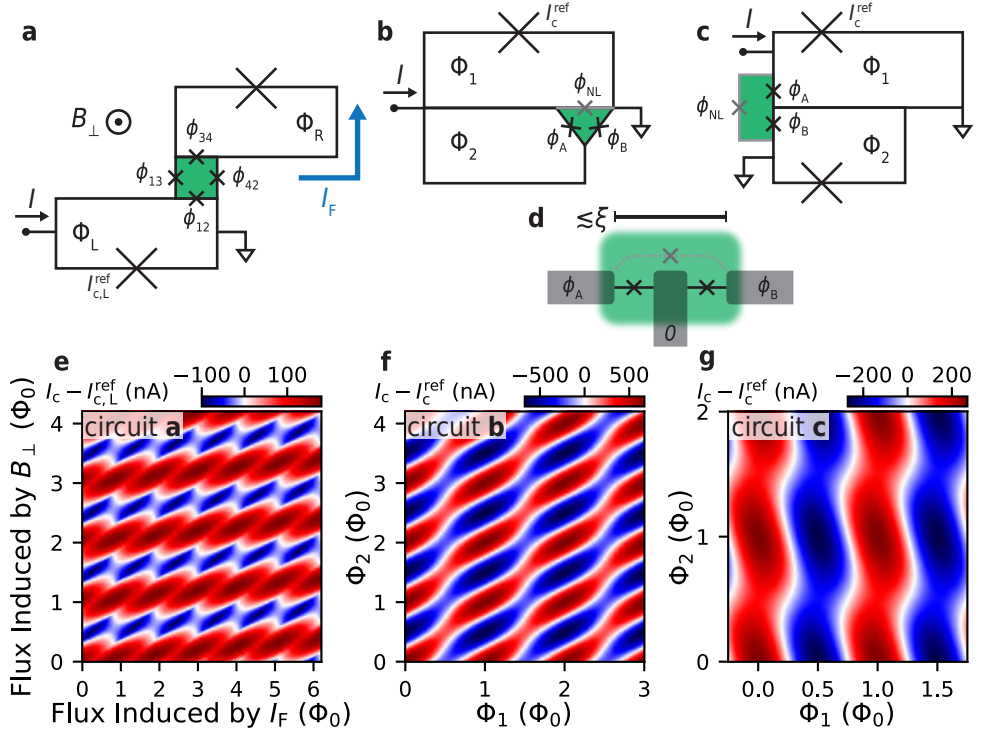


Figure 6.4: Simulations of multiterminal JJs as networks of two-terminal JJs. **(a-c)** Two-terminal JJ models of the 4TJJ in this article **(a)**, and of the Andreev molecule device geometries of Ref. [297] **(b)** and Ref. [298] **(c)**. We model the 4TJJ (green) as four two-terminal JJs between each neighboring terminal. For the Andreev molecule devices we model two nearby JJs (labeled A and B with phase differences  $\phi_A$  and  $\phi_B$ ) as well as an incidental JJ (gray, with phase difference  $\phi_{NL}$ ) shunting the two JJs through the same semiconducting region (green). Large crosses indicate reference JJs with critical currents much larger than those of the JJs in the green regions. **(d)** Close-up schematic of the layout of leads (gray) in the green regions of **(c)** and **(d)** patterned over a semiconducting 2DEG (green). **(e)** Simulated critical current  $I_c$  of SQUID L with SQUID R floating as a function of  $B_{\perp}$  and  $I_F$  in units of flux quanta, modeling the 4TJJ-SQUID circuit with the circuit model in **(a)**. We use  $I_{c,12} = I_{c,34} = 100$  nA and  $I_{c,13} = I_{c,24} = 80$  nA. Critical current maxima qualitatively reproduce the zig-zag pattern observed in Fig. 6.3(b). **(f,g)** Simulated critical current of the circuits in **(b)** and **(c)** as a function of the fluxes  $\Phi_1$  and  $\Phi_2$  threading the loops. We use  $I_{c,A/B} = 450$  nA **(f)** and  $I_{c,A/B} = 200$  nA **(g)** as in Refs. [297] and [298], respectively. Additionally, we choose  $I_{c,NL} = 180$  nA **(e)** and  $I_{c,NL} = 70$  nA. In all plots,  $I_c$  is offset by the reference junction's critical current.

JJs contains multiple loops sharing branches with Josephson junctions, the phase differences across the junctions become interdependent [307]. As a minimal model, we consider circuits of JJs neglecting linear inductances and capacitive effects, and approximate each junction as possessing a sinusoidal CPR. As examples, we consider a two-terminal JJ network designed to emulate the results measured in Fig. 6.3(b) and others to reproduce results of recent experiments observing CPRs consistent with Andreev molecule effects [297, 298].

Beginning with the 4TJJ embedded in two asymmetric DC SQUIDs as in this exper-

iment, we model the 4TJJ as four two-terminal JJs of critical current  $I_{c,ij}$  coupling each neighboring superconducting terminal  $i, j \in \{1, 2, 3, 4\}$ , see Fig. 6.4(a). From switching current measurements of SQUID L with its reference junction pinched off, we estimate the equivalent critical current between terminals 1 and 2 as  $I_{c,12} = I_{c,34} = 100$  nA, approximating the same between terminals 3 and 4 by symmetry in the device design. Since the distance between terminals 1 and 3 or 2 and 4 is larger, we select  $I_{c,13} = I_{c,24} = 80$  nA to approximate the qualitative behavior of the CFR maxima seen in Fig. 6.3(b). By applying Kirchhoff's current law and flux quantization while assuming the flux threading the 4TJJ (green in Fig. 6.4(a)) is negligible, we can calculate the critical current across SQUID L [307]. Results are shown in Fig. 6.4(e). While the functional dependence of  $V_L$  measured at fixed current in the resistive state is not expected to precisely match the CPR, it is expected to have the same periodicity and phase offset [19]. The simulated critical current exhibits a similar zig-zag pattern in the positions of maximum critical current. This indicates that a tunable  $\phi_0$ -junction alone is not unique to multiterminal JJ behavior. Namely, this demonstrates that while the lithographic design of the devices measured here contain a 4TJJ, the  $\phi_0$ -junction could appear even if the ABSs formed between each pair of terminals were not hybridized with any other ABSs.

As further examples, we model devices expected to host ABSs hybridized into Andreev molecules [305, 306]. These devices consist of two two-terminal JJs of critical current  $I_{c,A/B}$  and phase difference  $\phi_{A/B}$  sharing a common superconducting lead and separated by a distance on the order of  $\xi$ , depicted in Fig. 6.4(d). Due to wave function overlap between the ABS in each junction, an Andreev molecular state is expected to form. A stark signature of this state is a phase offset in one junction tunable by the phase difference across the other junction [305, 306]. In practice however, measured CPRs of Andreev molecule devices have formed the two JJs from a common region of semiconducting material [297, 298]. Since their separation is less than  $\xi$ , supercurrent could pass between the outer terminals in the absence of any hybridization of the ABSs in the intended junctions.

We thus model the device geometries of Refs. [297] and [298] with the circuits shown in Figs. 6.4(b) and 6.4(c) respectively. Nonlocal effects are modeled by a JJ directly coupling the outer leads with phase difference  $\phi_{NL}$  and critical current  $I_{c,NL} < I_{c,A/B}$ . Since each pair of leads is expected to support supercurrent in the absence of the remaining lead, this is roughly equivalent to considering the three-terminal junction with hybridization of the ABSs formed in each junction neglected. Specific values of  $I_{c,A/B}$  are extracted directly from Refs. [297, 298], while  $I_{c,NL}$  values are chosen to best match their measurements. The resulting simulations are shown in Figs. 6.4(f) and 6.4(g). They bear remarkable similarity with the measurements, in particular producing similar  $\phi_0$ -junction tunability to these experiments in the absence of any ABS hybridization. For more details of these calculations, see Supplemental Sec. 6.6.6.

As these junctions are defined in a region smaller than  $\xi$ , hybridization between the ABSs within is expected to contribute to the measured CPRs [308]. The above modeling shows, however, that the level of ABS hybridization in existing experiments does not yield CPRs easily distinguishable from the case of a non-interacting three-terminal junction. To exclude this trivial coupling between leads in Andreev molecule devices, measuring similar devices designed with no direct path through the semiconductor between

the outer superconducting leads rules out this shunting effect. For example, each junction could be formed from different semiconducting nanowires [303, 309]. Importantly, tunneling spectroscopy measurements of the semiconducting region could also reveal an ABS spectrum exhibiting anticrossings indicative of hybridization between the ABSs [293, 295, 305].

## 6.5. CONCLUSIONS & OUTLOOK

We have studied a 4TJJ by embedding it in two asymmetric DC SQUIDS, observing non-trivial properties of the CPR of a 4TJJ. Namely, we were able to measure SQUID oscillations of two pairs of terminals forming the junction and independently tune two of the three independent phase differences controlling it. From these measurements, we observed a nonlocal Josephson effect: two terminals of the 4TJJ behaved as a  $\phi_0$ -junction with a phase offset tunable by the nonlocal flux biasing the phase difference across two independent junction terminals. This tunability had a range exceeding  $0.2\Phi_0$ , and allows the 4TJJ to serve as a superconducting current switch [274]. Modeling multiterminal junctions as two-terminal JJ arrays, we also found that  $\phi_0$ -junction effects alone are not sufficient evidence of hybridization between extended ABSs in the junction.

Future devices with a barrier gate separating the lead pairs could demonstrate for the first time tunable direct wave function overlap between phase-tunable ABSs. Coupling between relatively distant ABSs mediated by supercurrents or photons in a macroscopic circuit has been observed [310, 311], but demonstrating a tunable local coupling would enable the formation of Andreev molecule-based quasiparticle charge qubits [305, 312], or densely-spaced conventional Andreev qubits. Andreev molecule devices where ABSs are coupled with a superconducting lead in between have exhibited hybridization effects [293, 294], but their coupling is fixed by the superconducting lead dimensions [305, 308]. A tunable wave function overlap with directly tunnel-coupled ABSs in JJs provides an alternate mechanism for realizing qubits based on ABSs or Kitaev chains [88], allowing for readout via inductive coupling of resonators to the phase-biased loops containing each JJ [313, 314]. Last and most notably, with control over one more phase difference in the 4TJJ, Weyl singularities in this system's subgap state spectrum could be probed [15, 268, 315].

Raw data and scripts for plotting the figures in this publication are available from Zenodo [316].

The authors would like to thank O.W.B. Benningshof and J.D. Mensingh for technical assistance with the cryogenic electronics. We would also like to thank M. Coraiola and F. Nichele for input on the manuscript, and A.R. Akhmerov and K. Vilkelis for invaluable discussions on theoretical modeling. The authors also acknowledge financial support from Microsoft Quantum and the Dutch Research Council (NWO).

The devices were designed by W.D.H., fabricated by W.D.H. and I.K. using a 2DEG heterostructure provided by D.X., C.T., and M.J.M.. Data was measured, analyzed, and modeled by C.G.P. I.K. assisted with designing the measurement setup, and S.G. supervised the project. C.G.P. wrote the manuscript with input from all authors.

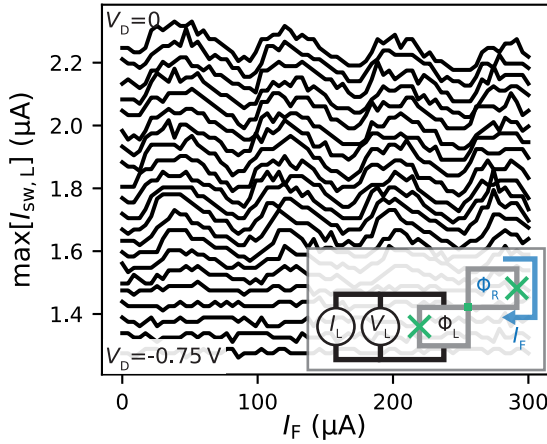


Figure 6.5: Depletion Gate Dependence of nonlocal SQUID L oscillations in Device A. As the depletion gate  $V_D$  is swept, five current traces at each  $I_F$  are measured and used to extract  $\max[I_{sw,L}]$ . Traces are offset from each other by 50 nA for clarity.

## 6.6. SUPPLEMENTAL INFORMATION

### 6.6.1. GATE PERFORMANCE

In Fig. 6.5 we plot a characterization of SQUID L oscillations as a function of the nonlocal flux  $\Phi_R$  tuned by  $I_F$  in Device A as the central device depletion gate voltage (red in Fig. 6.1(b))  $V_D$  is swept down from 0V. Repeating multiple current traces at each  $I_F$  value, we plot the maximum observed switching current as it is closest to the SQUID critical current. As the gate depletes carriers in the 4TJJ, the amplitude of oscillations decreases until none are observed by  $V_D = -0.75$ V. When  $V_D = 0$ , the SQUID oscillations are slightly skewed to the left, and this skewness also appears to reduce, leaving the oscillations more sinusoidal at intermediate  $V_D$  values. A detailed investigation of the influence of patterned gates on the 4TJJ characteristics was made impossible by the misalignment of gates in the second layer (gray in Fig. 6.1). These gates were designed to tune the chemical potential selectively between pairs of terminals, enable tunneling spectroscopy with the normal metal probes, and tunably isolate SQUID L from SQUID R.

### 6.6.2. FIELD DIRECTION CALIBRATION

For all measurements in the main text of this manuscript, the external magnetic field used  $B_x$  (as opposed to the field generated by the flux current  $I_F$ ) was along a three-axis magnet's 'x' direction, mostly out-of-plane of the chip, see Fig. 6.6(a). To calculate the out-of-plane component  $B_\perp$  as labeled in both figures, we calibrate the field direction with measurements on Device B, summarized in Fig. 6.6. Measuring SQUID oscillations of SQUID L in its resistive state, akin to the measurements of Figs. 6.3(a) and 6.3(b), we extract the periodicity of oscillations along each of the magnets three axes. From these measurements, we infer that the angles  $\theta_j$  for  $j \in \{x, y, z\}$  of field  $B_j$  with respect to the out-of-plane vector are  $\theta_x = 8.3^\circ$ ,  $\theta_y = 82^\circ$ , and  $\theta_z = 86^\circ$ . This implies that the  $h/2e$  pe-

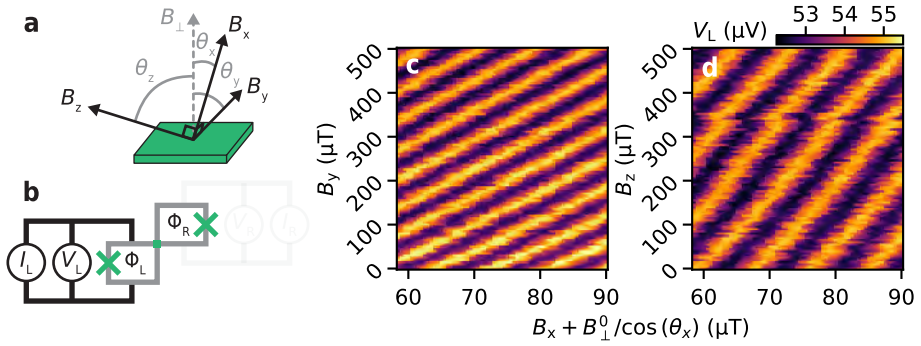


Figure 6.6: Field direction calibration in Device B. (a) Diagram schematically depicting how the applied field in the  $B_x$  direction translates to an out-of-plane component  $B_\perp$  as well as small components  $B_y$  and  $B_z$  in the  $y$ - and  $z$ -directions respectively. The angle  $\theta_x$  is exaggerated for clarity. (b) Measurement configuration for field orientation calibration. (c),(d) SQUID L oscillations as a function of  $B_x$  and  $B_y$  (c) and  $B_z$  (d) with a fixed current  $I_L = I_R = 1.45\mu\text{A}$  applied by independent sources across both SQUIDS, though these measurements are only used to infer the oscillation periodicity of SQUID L in each field direction. For these measurements,  $V_D = -0.15\text{V}$  while each second-layer gate except the rightmost one (gray gates in Fig. 6.1(b)) has  $0.8\text{V}$  applied. From these scans, we infer a mean peak spacing of oscillations along each axis of approximately  $\Delta B_x = 8.5\mu\text{T}$ ,  $\Delta B_y = 64\mu\text{T}$ , and  $\Delta B_z = 0.14\text{mT}$ . Measurements are with respect to an approximate zero-field point along the  $B_x$  direction of  $B_\perp^0 = -7.15\text{mT}$  calculated from Fraunhofer pattern measurements of the reference junctions.

6

riodicity of SQUID L with respect to  $B_\perp$  is approximately  $8.4\mu\text{T}$  in Device B, consistent with the devices' loop areas (see Fig. 6.1(a)).

As Device A may have been loaded in a different direction with respect to the magnet compared to Device B, these angles are not the same for Device A. Despite this, because Device A has the same lithographical design as Device B, its SQUIDS' oscillation periodicities are expected to be the same. Hence, from the  $B_x$  periodicity of SQUID L extracted from the data of Fig. 6.3(a) before converting the  $B_x$  axis to  $B_\perp$ , we infer  $\theta_x = 14^\circ$  for Device A. This enables us to calculate  $B_\perp$  from the applied field.

### 6.6.3. CURRENT-PHASE RELATIONS OF FOUR-TERMINAL JUNCTIONS EMBEDDED IN ASYMMETRIC SQUIDS

On its own, it is impossible to measure the CPR of the 4TJJ because the phase differences  $\phi_{ij}$  across its terminals  $\{1, 2, 3, 4\}$  cannot be controlled. Embedding each pair of terminals (namely  $\{1, 2\}$  and  $\{3, 4\}$ ) from the 4TJJ into a DC SQUID penetrated by magnetic fluxes  $\Phi_L$  and  $\Phi_R$  allows control of  $\phi_{12}$  and  $\phi_{34}$ , respectively, through tuning of these fluxes. Reference junctions J1J2 and J3J4 must also be embedded in each SQUID loop to prevent the SQUID's critical current from being too large to practically measure. In that case, the supercurrent across SQUID L when the other SQUID's leads are floating is

$$I = I_{c,L}^{\text{ref}} f_L(\phi_L) + I_{c,M} f_{12}(\phi_{12}, \phi_{34}, \phi_{13}) \quad (6.1)$$

where  $\phi_{L/R}$  is the phase difference across reference junction L/R with critical current  $I_{c,L/R}^{\text{ref}}$ ,  $I_{c,M}$  is the critical current of the 4TJJ, and  $f_L$  and  $f_{12}$  are some  $\Phi_0$ -periodic functions such that  $|f_L|, |f_{12}| \leq 1$  [317]. In other words,  $I_{c,M} f_{ij}$  is the current phase relation of the 4TJJ between leads  $i$  and  $j$ , which depends on all phase differences across it.

We assume the other SQUID's leads are floating so that current into the 4TJJ is conserved. By flux quantization, we have that

$$\phi_{12} - \phi_L = \frac{2\pi(\Phi_L + L_L J_L)}{\Phi_0} \pmod{2\pi} \quad (6.2)$$

where  $L_{L/R}$  and  $J_{L/R}$  are the self-inductance and the circulating current around SQUID L/R. Note that  $J_{L/R}$  must itself be  $\Phi_0$  periodic in flux. Because we have that  $I_{c,L/R}^{\text{ref}} \gg I_{c,M}$ , the phase difference  $\phi_L$  will adjust itself to whichever value  $\phi_L^{\text{max}}$  maximizes the current flowing through JJL, since this in turn maximizes the SQUID's critical current. As the 4TJJ by comparison has a negligible effect on the SQUID supercurrent, the phase difference  $\phi_{12}$  adjusts to the value allowing the flux quantization condition to be satisfied:  $\phi_{12} = 2\pi(\Phi_L + L_L J_L)/\Phi_0 + \phi_L^{\text{max}}$ . Meanwhile, the opposite SQUID has no current bias applied directly across it, and before the circuit critical current is reached, cannot have more than  $I_{c,M}$  circulating through it. Because  $I_{c,R} \gg I_{c,M}$ , this means  $\phi_R$  must be at a value corresponding to a near zero fraction of its critical current, namely  $\phi_R \approx 0$ . The critical current of the entire SQUID is then:

$$I_{c,L} = I_{c,L}^{\text{ref}} + I_{c,M} f_{12} \left( \frac{2\pi(\Phi_L + L_L J_L)}{\Phi_0} + \phi_L^{\text{max}}, \frac{2\pi(\Phi_R + L_R J_R)}{\Phi_0}, \phi_{13} \right). \quad (6.3)$$

When the loop inductances  $L_{L/R}$  are negligible, note that  $\phi_{12}$  and  $\phi_{34}$  are linear in the applied flux, so we can directly control the phase difference across each pair of the 4TJJ's leads by tuning  $\Phi_{L/R}$ . Hence, the critical current of the SQUID is equal to the CPR of the 4TJJ across two terminals shifted by the critical current of the reference junction and skewed by non-zero loop inductances  $L_L$  and  $L_R$ .

Summarily, we have that  $\phi_{12/34} = 2\pi(\Phi_{L/R} + L_{L/R} J_{L/R})/\Phi_0$  plus a constant offset. Conservatively estimating that the individual SQUIDs have inductances of  $L_{L/R} < 100$  pH and circulating currents bounded by  $J_{L/R} \leq (I_{c,L/R}^{\text{ref}} + I_{c,M})/2 \approx 0.7$   $\mu$ A, circulating currents perturb  $\phi_{12/34}$  by less than 0.09 radians. Without knowing  $L_{L/R}$  precisely, the CFR still possesses key properties of the true CPR due to the periodicity of  $J_{L/R}$ : its periodicity in flux, and shifts in its phase offset.

#### 6.6.4. NONLOCAL FLUX DEPENDENCE IN SQUID R

For comparison with Fig. 6.3, we measure the nonlocal coupling of  $\Phi_L$  into the SQUID R oscillations containing the junction formed across terminals 3 and 4, with results summarized in Fig. 6.7. The manifestation or strength of nonlocal effects is distorted in this case because the parameter tuning the nonlocal flux  $\Phi_L$  is  $B_{\perp}$ , which nearly equally tunes  $\Phi_R$ . Conversely, in this case the parameter  $I_F$  tuning the local flux  $\Phi_R$  has a negligible effect on the nonlocal flux. As in Fig. 6.3(b), we first fix the current  $I_R$  across SQUID R near  $I_{c,R}$  and measure voltage  $V_R$  in Fig. 6.7(a).

Despite  $B_{\perp}$  tuning both  $\Phi_L$  and  $\Phi_R$ , nonlocal features are still visible in Fig. 6.7(a). Namely, in addition to the expected diagonal  $V_R$  oscillations associated with local SQUID R oscillations, the intensity of the voltage oscillations changes periodically with SQUID L's  $B_{\perp}$  periodicity. To emphasize this, we plot the positions of SQUID L oscillation maxima extracted from Fig. 6.3(b) in white, where it aligns with the local maxima in  $V_R$  along the diagonal. Additionally, a minor zig-zag perturbation of the SQUID R oscillations from

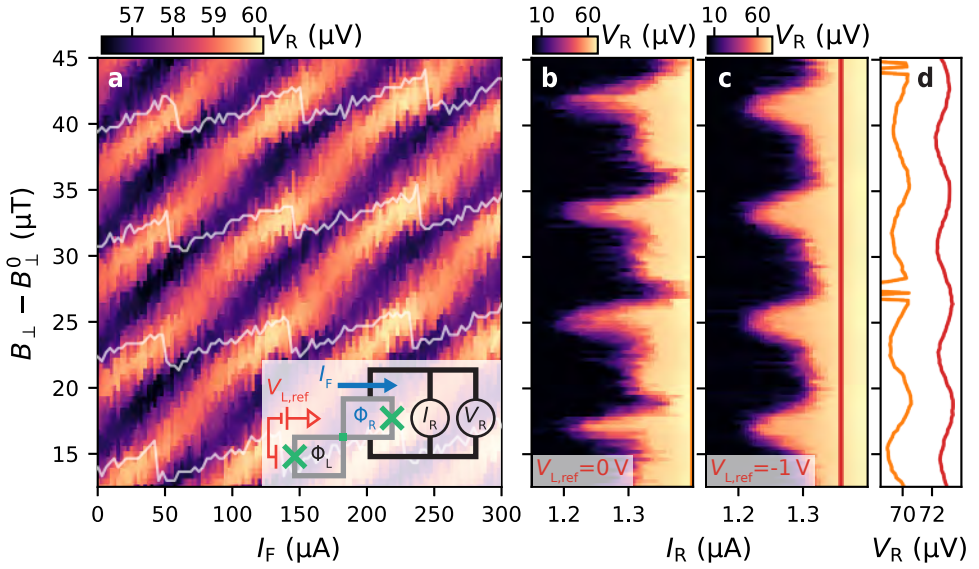


Figure 6.7: Nonlocal Josephson Effect SQUID R on Device A. (a) Voltage  $V_R$  measurements at a fixed current  $I_R = 1.25\mu\text{A}$  across SQUID R with SQUID L leads floating (inset). Because  $B_\perp$  tunes both the nonlocal flux  $\Phi_L$  and local flux  $\Phi_R$ , SQUID L oscillations appear perpendicular to the diagonal. Nonlocal effects from SQUID L perturb the path of local SQUID oscillations in a zig-zag fashion, and cause oscillations along the diagonal of the voltage measured. In white, positions of SQUID L oscillation maxima from Fig. 6.3(b) are plotted to emphasize these correlations. (b) Current-voltage traces of SQUID R oscillations at  $I_F = 0$  with the SQUID L reference junction open, where strongly non-sinusoidal effects are observable, in addition to apparent minima lobes in  $I_{c,R}$  spaced by half the flux periodicity. Each full  $B_\perp$  and current sweep is repeated 25 times and averaged. (c) As in (b), but with the SQUID L reference junction closed off  $V_{L,\text{ref}} = -1\text{ V}$  and averaged 15 times. SQUID oscillations are still highly non-sinusoidal, but distinctly lack the additional lobes present in (b). (d) Averaged linecuts at fixed current taken along the vertical lines in (b) and (c). The positions of maxima and minima in these linecuts align with extrema in the full current sweep measurements, but the resistive voltage lacks the additional  $(\Phi_0/2)$ -periodic oscillation component and appears sinusoidal. As in the main text,  $B_\perp^0 = -7.5\text{ mT}$  for Device A.

6

a simple diagonal path is visible, but because of the strong dependence of  $\Phi_R$  on both  $B_\perp$  and  $I_F$ , it is difficult to quantify the degree to which  $\Phi_L$  tunes this junction into a  $\phi_0$ -junction.

To investigate the degree to which four-terminal Josephson effects are present across terminals 3 and 4, we plot full current traces with JJJ open (Fig. 6.7(b)) and closed off (Fig. 6.7(c)). Each plot is averaged over many  $I_R$  and  $B_\perp$  measurements to alleviate effects from instability of the SQUIDs as a function of  $B_\perp$ . Remarkably, when JJJ has a finite critical current, lobes in the SQUID oscillations are visible spaced by half the SQUID L  $B_\perp$  periodicity. Conversely, when JJJ is closed, these higher harmonic lobes vanish, though the oscillations remain significantly non-sinusoidal. In Fig. 6.7(a) only  $\Phi_0$ -periodic oscillations are visible along both axes, however. Based on existing theories of 4TJJs [272, 273], this behavior is actually expected, and can be thought of as two flux quanta being threaded into the SQUIDs per  $\Phi_0$  period of  $B_\perp$ . For such junctions, there are regions of  $(\phi_{12}, \phi_{34})$ -space where phase slips of the JJ occur due to the appearance of vortex states

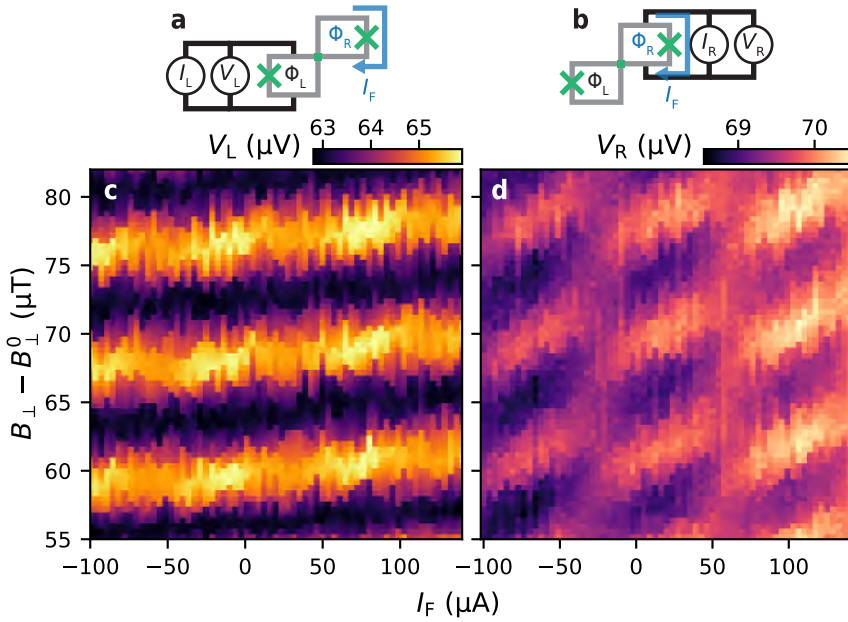


Figure 6.8: Fixed-Current SQUID Oscillations in Device B. (a),(b) SQUID oscillation measurement circuit for (c) and (d), respectively. (c),(d) Fixed-current CPR Measurements in the resistive state of SQUID L (c) with  $I_L = 1.45 \mu\text{A}$  and SQUID R (d) with  $I_R = 1.45 \mu\text{A}$ , with the opposite SQUID's leads floating. The magnetic field was swept near an approximate zero-field point  $B_{\perp}^0 = 7.15 \text{ mT}$  determined from Fraunhofer pattern measurements of the reference Josephson junctions.

inside the junction, producing additional local extrema in the CPR along lines of equal  $\phi_{12}$  and  $\phi_{34}$ .

Interestingly, these additional extrema in the critical current are not reflected in the voltage measured in the resistive state, emphasized by linecuts in Fig. 6.7(d). A nearly sinusoidal resistive-state voltage is observed even when  $V_{L,\text{ref}} = 0$ , indicating that certain features of the CPR are not noticeably reflected in  $V_R$ . From the perspective of a resistively and capacitively shunted junction (RCSJ) model [19], for example, this is possible for an underdamped junction possessing a substantial self-capacitance. Due to the stochastically varying switching current observed in current traces (see the averaged traces of Fig. 6.2 for example), it is clear that the 4TJJ is underdamped. Nonetheless, we emphasize that the periodicity and phase offset of the fixed-current measurements accurately reflect that of the CPR.

### 6.6.5. SUPPORTING DATA ON A SECOND DEVICE

Here we present a second set of nonlocal SQUID oscillation measurements akin to those in Fig. 6.3(b) and Fig. 6.7(a) on another device (Device B), with results shown in Fig. 6.8. This device has an identical design to Device A and was fabricated on the same chip. Measurements for both SQUID L and SQUID R are presented in Figs. 6.8(c) and 6.8(d), respectively. The corresponding measurement circuits are shown in Figs. 6.8(a,b). In

these measurements, with the opposite SQUID's leads floating, we observe  $\Phi_0$ -periodic oscillations in  $V_L$  primarily as a function of  $B_\perp$  and in  $V_R$  both as a function of  $B_\perp$  and  $I_F$ , consistent with the flux-bias line almost exclusively affecting  $\Phi_R$  by design. In addition to the small direct cross coupling of  $I_F$  to  $\Phi_L$  giving the SQUID L oscillations a slight tilt in Fig. 6.8(c), periodic oscillations in the peak height are observed as a function of  $I_F$ . The oscillations also exhibit a slight zig-zag pattern comparable to those of Device A seen in Fig. 6.3, but due to the significant jitter visible in the measurements, extracting a  $\phi_0$  shift of the junction is difficult. The measurements of SQUID R are also qualitatively similar to those of Device A.

### 6.6.6. TWO-TERMINAL ARRAY MODELS OF MULTITERMINAL JUNCTIONS

Herein we derive expressions for the critical current of the four- and three-terminal JJ circuits shown in Fig. 6.4(a-c) by maximizing the supercurrent carried through the terminal labeled with an input current  $I$ . In both cases, we assume that the flux threading the multi-terminal JJ is negligible. We also assume that the reference junction critical currents are much larger than the critical currents of all two-terminal JJs describing the multiterminal JJ. For simplicity we neglect capacitances and linear inductances, and assume all junctions have CPRs of the form  $I_c \sin(\phi)$  where  $\phi$  is the phase difference across the junction.

We begin with the Andreev molecule device of Fig. 6.4(b), which is designed to contain two JJs sharing a common superconducting terminal and separated by a distance on the order of the superconducting coherence length  $\xi$ , see Fig. 6.4(d). To separately control the phase differences  $\phi_{A/B}$  across each junction, the two junctions are embedded in loops threaded by fluxes  $\Phi_1$  and  $\Phi_2$  (in units of  $2\pi/\Phi_0$ ). Lastly, in one of the loops a reference junction of large critical current  $I_{c,1}^{\text{ref}}$  is embedded to measure one of the JJ's CPRs. As these devices in previous experiments have been formed by connecting three superconducting contacts to a continuous region of conducting semiconducting material smaller than the coherence length [297, 298], it is feasible that supercurrent can directly travel between the two outermost terminals even in the absence of a central terminal. Consequently, we model the nonlocal coupling between the two JJs as a third JJ connecting the two outer terminals while bypassing the central one (gray in Fig. 6.4(d)). Notably, this model does not include wave function overlap between ABSs from different individual junctions.

Given the phase differences across the junctions as defined in Fig. 6.4(b), by flux quantization we have that  $\phi_A = \Phi_2$  modulo  $2\pi$  (we consider the modulus as implied for all further mentioned flux quantization conditions) [307]. Next, since the critical current of the reference junction is very large compared to all others, its phase difference will adjust to whichever value maximizes the supercurrent through it, in this case  $\pi/2$ . Finally, by flux quantization we then have that  $\pi/2 - \phi_{\text{NL}} = \Phi_1$  and  $\phi_{\text{NL}} - \phi_B - \phi_A = 0$ . The signs of the phase differences are determined by an arbitrary but consistent definition of the current direction through each circuit branch [307], with fluxes defined as being associated with a clockwise current through a given loop. Accordingly, the critical current of the circuit is

$$I_c = I_{c,1}^{\text{ref}} + I_{c,B} \cos(\Phi_1 + \Phi_2) + I_{c,\text{NL}} \cos(\Phi_1). \quad (6.4)$$

Notably, the decision to approximate the flux  $\Phi_1$  producing a phase difference across

the shunting junction as opposed to directly tuning  $\phi_{A/B}$  was somewhat arbitrary. Modeling the circuit as the shunting junction existing out-of-plane such that  $\Phi_1$  tunes  $\phi_{A/B}$  produces the same result as in eq. 6.4 except shifted by  $\pi$  along the  $\Phi_1$  axis.

Proceeding to the circuit of Fig. 6.4(c) representing the device geometry of Ref. [298], we conduct similar calculations using flux quantization rules. In this case, there are reference junctions of critical currents  $I_{c,1}^{\text{ref}}$  and  $I_{c,2}^{\text{ref}}$  in the  $\Phi_1$ - and  $\Phi_2$ -threaded loops, respectively. With current  $I$  being passed into the top left port and the others grounded, maximizing the supercurrent requires maximizing the current through reference junction 1, since we assume the reference junctions have arbitrarily large critical current. Hence, its phase will tend to  $\pi/2$ . For the other reference junction, it is connected to grounded terminals on both sides and so is not a bottleneck for the device's critical current. We can thus take the limit of infinite critical current such that no phase drop occurs across this junction, and we have  $\phi_B = \Phi_2$ . This is evident from the fact that a large wire containing no Josephson junction, where no phase drop is expected to occur, can equally-well be considered as a Josephson junction with an arbitrarily large critical current.

Other flux quantization loops yield  $\Phi_A = \pi/2 - \Phi_1$  and  $\phi_{NL} = \phi_A - \phi_B = \pi/2 - \Phi_1 - \Phi_2$ . Hence, by calculating the current through each circuit branch connecting to the  $I$  input, we find the device critical current to be

$$I_c = I_{c,1}^{\text{ref}} + I_{c,A} \cos(\Phi_1) + I_{c,NL} \cos(\Phi_1 + \Phi_2). \quad (6.5)$$

Lastly, we consider the 4TJJ circuit of Fig. 6.4(a). Again, there are reference junctions of large critical currents  $I_{c,L}^{\text{ref}}$  and  $I_{c,R}^{\text{ref}}$  in the loops threaded by  $\Phi_L$  and  $\Phi_R$ . The current  $I$  flows through the branches containing reference junction L, the junction between terminals 1 and 2, and the junction between terminals 1 and 3. Since  $I_{c,L}^{\text{ref}}$  is assumed very large, its phase infinitesimally below the critical current by the same reasoning as before is roughly  $\pi/2$ . Again, as in the previous case we can take  $I_{c,R}^{\text{ref}} \rightarrow \infty$  since it is not a bottleneck for the critical current. More precisely, given that all supercurrent passing between the JJs with phase difference  $\phi_{13}$  and  $\phi_{42}$  can either pass through this reference junction or the JJ with phase difference  $\phi_{34}$ , the latter two junctions' phases are only constrained by flux quantization of their loop threaded by  $\Phi_R$ . In the absence of other constraints, the system will tend to a state which minimizes its energy, here given by the Josephson energy of both junctions. This energy is proportional to  $-I_{c,R}^{\text{ref}} \cos(\phi_R) - I_{c,34} \cos(\phi_{34})$  [19], where  $\phi_R$  is the phase difference across reference junction R. Since  $I_{c,R}^{\text{ref}} \gg I_{c,34}$ , this energy is minimized when  $\phi_R \approx 0$ . Whatever current must pass through these parallel arms can pass through the reference junction with only a negligible correction to its phase difference due to its large critical current, while  $\phi_{34}$  can adjust to satisfy flux quantization without substantially increasing the total energy. From flux quantization, we then obtain  $\phi_{12} = \Phi_L + \pi/2$ ,  $\phi_{34} = -\Phi_R$ , and  $\phi_{13} + \phi_{34} + \phi_{42} - \phi_{12} = 0$ . To obtain enough equations to solve for all phases, we note that by Kirchhoff's current law we have  $I_{c,13} \sin(\phi_{13}) = I_{c,42} \sin(\phi_{42})$ . Solving the last flux quantization condition for  $\phi_{42}$  and substituting the result into the current conservation equation, we obtain

$$I_{c,13} \sin(\phi_{13}) = I_{c,42} \cos(\Phi_L + \Phi_R - \phi_{13}). \quad (6.6)$$

This is a transcendental equation and has multiple solutions between  $\phi_{13} \in [0, 2\pi)$ . The

critical current of the circuit is by definition the maximum possible supercurrent it can sustain, so for every  $(\Phi_L, \Phi_R)$  value we choose the  $(\Phi_L, \Phi_R)$ -dependent solution  $\phi_{13}^{\max}$  to eq. 6.6 which maximizes  $I$ . The critical current of the circuit is then the sum of the current through the three paths branching from the input current  $I$ , given as

$$I_c = I_{c,L}^{\text{ref}} + I_{c,12} \cos(\Phi_L) + I_{c,13} \sin(\phi_{13}^{\max}). \quad (6.7)$$

For the calculated results in Fig. 6.4(e), we plot them as a function of the flux generated by  $I_F$  and  $B_\perp$ , considering cross coupling of  $I_F$  into SQUID L determined from the oscillation periodicities of Fig. 6.2. The  $I_F$  axis is converted into units of  $\Phi_0$  by defining  $1 \times \Phi_0$  as a single flux quantum threading SQUID R due to  $I_F$  as well as the resulting cross coupling to SQUID L. For  $B_\perp$ ,  $1 \times \Phi_0$  is defined as a single flux quantum threading both SQUIDS.

# 7

## CONCLUSION & OUTLOOK

*"A picnic. Picture a forest, a country road, a meadow. A car drives off the country road into the meadow, a group of young people get out of the car carrying bottles, baskets of food, transistor radios, and cameras. They light fires, pitch tents, turn on the music. In the morning they leave. The animals, birds, and insects that watched in horror through the long night creep out from their hiding places. And what do they see? Gas and oil spilled on the grass. Old spark plugs and old filters strewn around. Rags, burnt-out bulbs, and a monkey wrench left behind. Oil slicks on the pond. And of course, the usual mess – apple cores, candy wrappers, charred remains of the campfire, cans, bottles, somebody's handkerchief, somebody's penknife, torn newspapers, coins, faded flowers picked in another meadow."  
"I see. A roadside picnic."*

Arkady & Boris Strugatsky, in *Roadside Picnic*

This thesis explored two largely overlapping themes: localized states in hybrid semi-conducting and superconducting systems, and exploiting microwave measurements in such systems over conventional DC measurements. Both topics are motivated by the potential to explore topological systems in condensed matter, or to leverage hybrid systems to form new types of protected qubits. Despite this, no qubits were characterized, and the described experiments didn't seek topological phases. This chapter therefore aims to discuss how these experiments can be built upon to probe bulk properties of hybrid devices with RF measurements (Sec. 7.2), characterize limitations on future hybrid qubits (Sec. 7.3), and to form Kitaev chains and qubits with more complete isolation from the environment (Sec. 7.4). We begin, however, by summarizing the key results of our experiments.

### 7.1. CONCLUSIONS

In Chapter 3 we showed semiconducting quantum devices can be completely characterized using microwave reflectometry without supporting DC measurements, which are

generally much slower. This enables more efficient and complete exploration of parameter space in hybrid devices [189, 318] and allows measurement setups to be optimized with more stringent filtering for microwave-focused measurements. Microwave reflectometry also offers the opportunity to probe device characteristics not easily discernible from DC measurements, which require a finite conductance across the device. For example, in Chapter 3 we utilized the fact that dispersive gate sensing (DGS) is sensitive to the hybridization between charge states in systems of quantum dots (QDs) to resolve electron tunneling with an SNR of 15 in a 1  $\mu$ s measurement. Measurement based topological qubits require such tunneling measurements for the readout and manipulation of their parity states [10, 11, 231]. Meanwhile, in Chapter 5, this sensitivity of DGS to tunneling was exploited to measure a flux-dependent hybridization between two fermionic states for the first time. This flux dependence was granted by forming a loop out of two QDs threaded by magnetic flux, and is required for guaranteeing readout sensitivity in parity and topological qubits.

Another unique application of DGS is as a local probe of tunneling. Though not unique to this dissertation [185], we demonstrated in Chapter 4 that DGS serves as such. Probing each QD in a floating triple or quadruple QD coupled to a superconducting island with their own gate resonator, we uniquely distinguished which pairs of dots were involved in any measured tunneling process. Notably, this allowed us to identify a charge transition corresponding to the coherent resonant splitting and recombination of a single Cooper pair, and characterize the corresponding crossed Andreev reflection (CAR) hybridization strength.

Finally, in Chapter 6 we attempted to measure tunneling between nearby Andreev bound states (ABS): a superconducting analog of QDs [313]. We attempted this by placing the Josephson junctions (JJs) of two DC SQUIDs within the superconducting coherence length of each other. This could be exploited to hybridize superconducting spin qubits [305] or study the evolution from conventional to multiterminal Josephson effects. Unfortunately this original goal was made impossible due to gate electrodes not functioning as designed in the measured devices. Nonetheless, we had the opportunity to explore current-flux relations of a four-terminal junction, with control over two of the three independent superconducting phase differences determining the junction's behavior. Accordingly, we showed that one pair of leads in the junction behaves as a  $\varphi_0$ -junction, with a superconducting phase offset tuned by the phase difference across the other completely independent pair of leads. On the other hand, we also showed that this and other multiterminal junctions can reproduce this behavior if they behave as an array of two-terminal junctions—that is, without any hybridization of the subgap states in the junctions.

## 7.2. NONLOCAL RF MEASUREMENTS OF HYBRID DEVICES

As previously described, RF measurements serve as a fast probe of two-terminal conductance and as local probes of charge tunneling. Nonlocal conductance, however, has become a frequently used tool in experiments on hybrid systems since it encodes information about the bulk state of a hybrid region [320, 321], and not only information about the local density of states near tunnel barriers or gates. It involves applying voltages at one lead in a multiterminal system and measuring current through another lead.

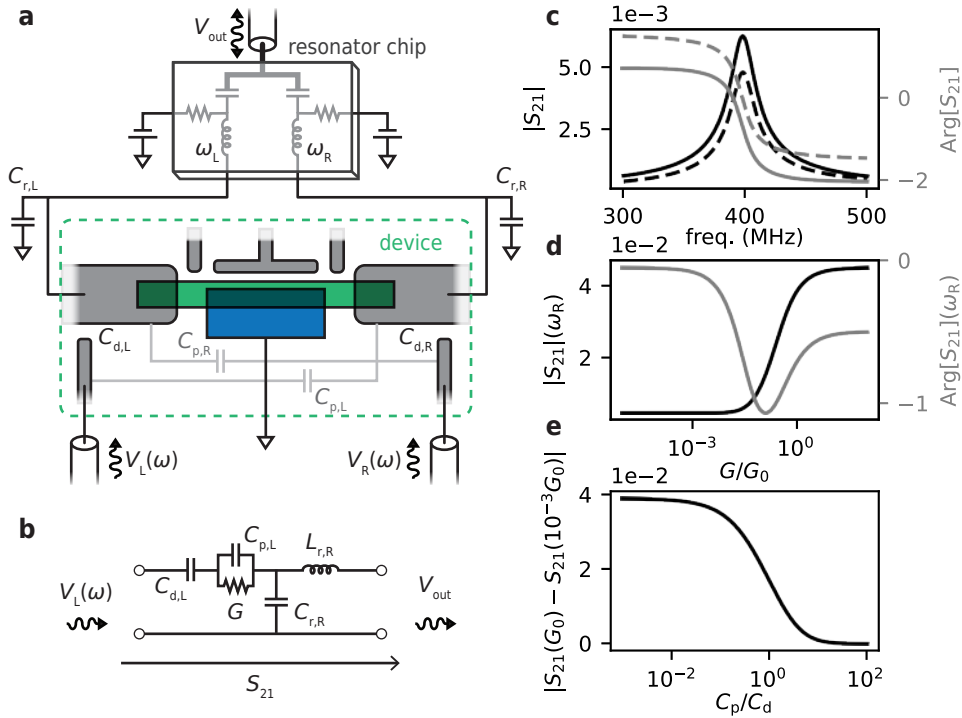


Figure 7.1: Nonlocal RF measurements of a three-terminal hybrid device. **(a)** Schematic of a nonlocal measurement setup. *Bottom:* A three-terminal device consisting of a semiconducting nanowire (green) proximitized by a grounded aluminum shell (blue) is connected to leads on either side, as well as some gates for tuning tunnel barriers and chemical potentials in the wire (gray). Drive lines for nonlocal RF transmission measurements are coupled to their respective leads with capacitances  $C_{d,L/R}$  as well as trivially to ground via unintended parasitic capacitances  $C_{p,L/R}$ . *Top:* A readout resonator chip consisting of two inductors forming angular resonance frequencies  $\omega_L$  and  $\omega_R$  in combination with their parasitic capacitances to ground  $C_{r,L/R}$ . The resonators are coupled to a common reflectometry readout line via coupling capacitors, as well as resistive bias tees for applying DC voltages to the leads they are bonded to. **(b)** Two-port circuit model of nonlocal measurements from lead L to resonator R, assuming that the resonator coupled to the lead being driven completely filters the drive tone, so that it can only travel across the device via parasitic capacitance  $C_p$  or nonlocal conductance  $G$  to the opposite resonator. **(c-e)** Nonlocal transmission response of a resonator using the circuit model of **(b)**. The resonator circuit parameters  $L_r = 420$  nH and  $C_r = 0.38$  pF are extracted from a resonator measured in Chapter 5, giving it a resonance at  $\omega_r/2\pi = 400$  MHz. For the drive line capacitance and parasitic coupling across the device, we use  $C_d = 10$  pF and  $C_p = 1$  pF. We show the frequency response for  $G = 0$  (dashed) and  $G = 0.003 \times G_0$  (solid) in **(c)** based on typical values measured in previous experimental work [319]. In **(d)**, we plot the response for different nonlocal conductances on resonance, and in **(e)** we plot the signal difference between a small and large conductance for different parasitic capacitances.

A schematic of a typical three-terminal hybrid device used to probe proximitized superconducting nanowires is shown in Fig. 7.1(a) [318, 319, 322–324], consisting of a semiconducting nanowire (green) with a grounded superconducting shell (blue), in addition to metallic contacts and gates (gray).

As the name suggests, the reflectometry technique used in this dissertation measures the ratio of reflected to incident radiation on some device impedance, an inherently lo-

cal probe. This is typically accomplished by sending the input radio waves through the used resonator chip and measuring the returning demodulated voltage. It is also possible, however, to send the RF drive in via a separate line and measure whatever comes out of the resonator circuit in a transmission measurement [13]. Unfortunately, while DC voltage sources and multimeters can be reconfigured outside a dilution refrigerator at room temperature, the resonators used for RF measurements are bonded directly to the device under test or are on the same chip and cannot be rewired to different leads of the device in situ. The other obstacle to implementing nonlocal RF measurements is thus that resonators will serve as a filter excluding frequencies away from their resonance frequency. If we could selectively drive one lead of the device with a tone at the frequency of the opposite side's resonator, the output voltage of this resonator would contain information about the device's nonlocal conductance.

In order to overcome these obstacles, we propose employing RF drive lines weakly coupled to the device leads with capacitances  $C_{d,L/R}$ , with an example setup shown in Fig. 7.1(a). In that example, one can apply a drive tone  $V_L$  at the frequency of the right lead's resonator  $\omega_R$  to the left drive line, and read the voltage output from the resonator chip. Because the left resonator filters radio frequencies far from its resonance  $\omega_L$ , the drive tone is routed into the device. Much of the signal will then leak through parasitic capacitances  $C_{p,L/R}$  across the device or to the grounded superconductor, but this merely imposes a constant change to the background of the signal. The remainder of the signal will pass through the nanowire itself and through the right resonator to the reflectometry circuit's output, containing information about the device's nonlocal conductance. Of course, the reverse principle can be used to probe nonlocal conductance from the right to the left. Meanwhile, applying probe tones to the resonator chip allows ordinary local reflectometry of either lead. The reason this can in principle work is as follows: the drive line is only weakly capacitively coupled to the leads, so local reflectometry signals do not substantially leak through it to ground. On the other hand, when one seeks to do nonlocal transmission measurements, one can apply such a powerful drive tone to the drive line that it overcomes this weak capacitance and enters the lead. A constraint on this setup is that the capacitances of the resonators  $C_{r,L/R}$  together with the other capacitances satisfy the constraints:

$$C_{p,L/R} \ll C_{d,L/R} \ll C_{r,L/R} \quad (7.1)$$

If the leftmost constraint isn't satisfied, the drive line will not selectively couple to its lead, but will broadcast the probe tone across the entire device. If the right-hand constraint isn't satisfied, the drive line will drastically lower the resonator frequency and its internal quality factor. Since for off-chip resonators one typically has  $C_{r,L/R} \approx 0.1 - 1$  pF [13], it may be difficult to satisfy the right constraint without violating the other.

To demonstrate this measurement principle's functionality we present in Figs. 7.1(c-e) transmission simulations (say, from lead L to resonator R) of a lumped circuit model shown in Fig. 7.1(b). We assume that resonator L is well-separated in frequency from resonator R such that the left drive line probe tone is perfectly filtered by resonator L. As is particularly visible in Fig. 7.1(c), a very small nonlocal conductance may produce a measurable shift in the transmission measurement, provided a large enough power can be used for the drive without heating or otherwise perturbing the device. For these

simulations, a small drive line capacitance of  $C_d = 10\text{pF}$  was used, which for a square parallel plate capacitor separated by 20 nm of  $\text{Al}_2\text{O}_3$  dielectric would correspond to a side length of roughly 160 nm. Clearly, capacitances in this range or smaller are experimentally achievable, by simply not having the drive line overlap directly with the lead for example. Meanwhile, the parasitic capacitance across the device can be minimized by coupling the drive line to its lead at a position far away from the device's nanowire or superconducting shell. Nonetheless, whether or not this technique can be feasibly implemented in such a way that it still enables measurements faster than conventional DC techniques remains to be seen.

### 7.3. QUASIPARTICLE POISONING OF PARITY QUBITS

Quasiparticle poisoning broadly refers to any instance where quasiparticle tunneling, excitation, or relaxation alters or destroys a coherent quantum state involving a superconductor. Within the realm of superconducting qubits, quasiparticles are known to cause relaxation, dephasing, and excitation to leakage states, depending on the specific type of qubit. Many other mechanisms significantly affect coherence of superconducting qubits, however [2]. For topological and hybrid parity qubits on the other hand, poisoning is one of few mechanisms expected to determine their coherence [85, 231, 325, 326]. As these qubits are formed in hybrid semiconducting-superconducting systems, this has motivated numerous studies of quasiparticle poisoning in hybrid material platforms that are candidates for such qubits [59, 61, 72, 217, 327–329] and in non-hybrid superconducting islands [95, 330].

Given that quasiparticles injected from lead reservoirs may be the dominant source of quasiparticle poisoning for ABSs in open systems and superconducting islands [85], it is worth considering if qubits could be optimized by removing the leads entirely. We explore this possibility further in Sec. 7.4. This principle motivated designs for Majorana-based qubits involving embedding the entire qubit in a Coulomb blockaded island [10, 11], but even in Coulomb blockade quasiparticles may still enter an island from the leads. Moreover, there has yet to be any measurement of poisoning rates in QDs coupled to subgap states, namely Majorana bound states in quantum-dot-based Kitaev chains [231].

To emphasize that quasiparticle poisoning rates are not yet well understood for hybrid systems, we consider measurements of a hybrid triple QD (Device A in Chapter 4). A schematic of the device is shown in Fig. 7.2(a). In the first cooldown of this device, the microwave measurement circuit had not yet been optimized and contained no filtering. It consisted only of an input line with attenuation at each stage of the dilution refrigerator, and an output line with no added attenuation and a high-electron-mobility transistor (HEMT) amplifier at the 4 K stage. Notably, no circulators were present in the circuit, meaning for example that reflections and noise from the 4 K amplifier could reach the device with little attenuation.

Despite this setup being far from optimized to reduce quasiparticle poisoning in the sample, signs of superconductivity were observed in Coulomb diamond measurements of the superconducting island. These measurements are shown in Fig. 7.2(d), where the Coulomb resonances are seen to be spaced by twice the distance in gate voltage  $V_M$  at low bias voltages as they are for higher bias. This is indicative of the island charging

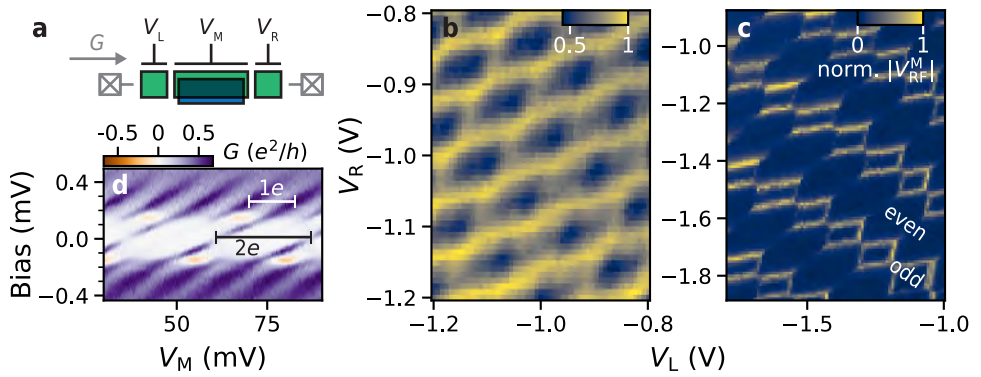


Figure 7.2: Effect of filtering on a floating superconducting island. (a) Diagram of the measured device (Device A from Chapter 4), consisting of a superconducting QD (blue) surrounded by two semiconducting QDs (green), and leads (gray). Each QD can have its chemical potential tuned by plunger gate voltages  $V_L$ ,  $V_M$  and  $V_R$ . (b) A charge stability diagram (CSD) of the device tuned into a floating triple QD with the leads completely cut off such that its total charge is conserved. Measurements are the normalized reflected amplitude  $|V_{RF}^M|$  near the resonance frequency of the gate resonator coupled to the superconducting island. These measurements were taken before filtering was added to the microwave measurement setup in the dilution refrigerator. Stable charge regions are all the same hexagonal shape even though the superconductor alternates between even parity and odd parity, and boundaries between regions are highly broadened. (c) As in (b), but in a later cooldown of the same device after filtering was added to the microwave measurement circuit. As described in Chapter 4, stable charge regions alternate in size between large and small depending on the superconductor's parity, since an odd parity superconductor has an additional free energy cost of  $E_0$ . (d) Coulomb diamonds of the superconducting island before filtering was added to the measurement setup with the semiconducting QDs not tuned up. Conductance is calculated using a Savitzky-Golay filter from measurements of current. Spacing between Coulomb peaks halves for biases larger than  $E_0$ , indicating  $E_0$  is larger than the island's charging energy.

energy being smaller than its lowest quasiparticle excitation energy, such that each resonance corresponds to the transfer of two electrons into the island. Moreover, the absence of even faint additional Coulomb resonances at low bias spaced by half this distance indicates that the island is on average not in a poisoned state, defined here as quasiparticle states being occupied [61]. Curiously, when we tune the system into a floating triple QD with the island surrounded by two semiconducting QDs and the leads completely cut off (as in the measurements of Fig. 4.1(f) and Fig. 4.2), all signs of superconductivity vanish. These measurements are shown in Fig. 7.2(b), where we measure the absolute reflected signal  $|V_{RF}^M|$  near resonance of a resonator coupled to the island gate as a function of the two QDs' gate voltages. In contrast to the measurements of Chapter 4, no alternation in the size of stable charge regions is observable, even though the parity of the superconducting island must be changing as  $V_L$  and  $V_R$  increase. We may therefore infer that the superconducting island has a finite density of quasiparticles on average, such that the system does not distinguish between the island containing an odd number of charges (where there must be a quasiparticle) and an even number (where no quasiparticles exist in the ground state). The refrigerator was then opened to improve the measurement circuit: we added circulators before and after the sample, infrared and low-pass filters, and a parametric amplifier to the circuit. See Appendix B for details. Measuring a floating triple QD in the same device upon cooling it back down to millikelvin temperatures in

Fig. 7.2(c), we then observed signs of superconductivity. There were small stable charge regions where the superconductor has an odd parity and larger regions where it has even parity, indicating that the island on average does not contain quasiparticles when its parity is even.

Several things can be concluded from these measurements. First, the density of quasiparticles in a superconducting island may be completely different when it is coupled to leads compared to when it is floating. Before adding filtering to the setup, this device showed negligible population of quasiparticle states when tuned into an island coupled to leads, but was on average poisoned in the floating triple QD configuration. This is consistent with previous work which observed that normal metal reservoirs and gapless semiconductors serve as quasiparticle traps, lowering the quasiparticle density of coupled superconductors [327, 331, 332]. Second, in the floating regime we hypothesize that coupling of radiation and noise in the microwave measurement lines to the island created a steady-state population of quasiparticles which could not escape to lead reservoirs. These quasiparticles could only be removed through recombination into Cooper pairs. Lastly, measurements using the improved microwave measurement setup indicate that sufficient filtering could take the floating system from having a finite steady-state population of quasiparticles to containing quasiparticles an immeasurably small fraction of the time.

Despite an attempt at indirectly quantifying quasiparticle poisoning in floating islands [95], it remains to be seen how fast Cooper pair breaking and recombination rates are in hybrid floating systems. If quasiparticles were present a substantial fraction of the time in a system like that measured in Fig. 7.2, one would expect a faint signal not only at the ground state positions of Coulomb resonances as in Fig. 7.2(c), but also at the resonances in the poisoned state like those seen in Fig. 7.2(b) [61]. No such resonances were observed in this and similar devices however [333], indicating a negligible average occupation of quasiparticle states. This measurement says little about Cooper pair breaking and recombination rates, however. Recombination rates may be much higher than pair breaking rates [85], in which case poisoning may still be very important despite a low average population of quasiparticle states.

Crucially, neither these experiments nor those referenced above measure the poisoning rate of a specific subgap state in a superconductor. Instead, they probed the overall density of quasiparticles in hybrid superconducting systems, measured the parity lifetime of an entire superconducting island, or indirectly measured bounds for the parity lifetime of a finite energy quasiparticle state [59]. More relevantly, poisoning rates of bound states in Andreev spin and charge qubits have been probed [314, 329, 334], but these states had non-zero energy and were not protected from poisoning by a charging energy. The poisoning rate which limits the lifetime of Majorana-based qubits is the rate at which the joint parity of two Majorana states flips. For example, a quasiparticle tunneling into a Majorana box qubit will not effect the qubit state if it does not relax into a Majorana bound state. Hence, only a direct measurement of the bound state's poisoning rate will give information about the coherence time of a qubit based on an ABS' parity. Additionally, it is expected that the presence of a Majorana bound state in a hybrid system itself alters the density of quasiparticles in the material [85]. In other words, the most pertinent measure of quasiparticle poisoning relevant to Majorana- and ABS-based

qubits is to actually form the qubit and measure its parity.

## 7.4. FLOATING KITAEV CHAINS & HYBRID QUBITS

The competition between superconducting pairing and Coulomb repulsion in hybrid systems offers unique opportunities for quantum computation, from Majorana-based qubits [10, 11, 231] and variations on Andreev spin qubits [335] to fermionic quantum computation [336]. All qubits exploiting partially superconducting systems can have their quantum coherence destroyed by quasiparticle poisoning, however, and there are not yet any proposals for implementing Majorana bound states in Kitaev chains protected by charging energies from quasiparticle poisoning. Scaling up to longer Kitaev chains or systems consisting of multiple topological qubits, it also becomes increasingly difficult to fit Ohmic contacts for each qubit or QD in the system. Hence, we employ a minimal theoretical model to argue that a Kitaev chain can be formed in a charge-conserving system provided it can be coupled to another floating system which can coherently change its parity (such as another floating Kitaev chain). We then briefly summarize proposals for a category of qubits exploiting the competition between charging energies and superconducting pairing: qubits based on Yu-Shiba-Rusinov (YSR) states.

### KITAEV CHAINS IN COULOMB BLOCKADE

Since forming a Kitaev chain in Coulomb blockade requires being able to form one in a system with conserved total charge, for simplicity we consider a floating system without leads here. Accordingly, we demonstrate in this section that a floating QD system can be tuned to have a Hamiltonian equivalent to that of a two-site Kitaev chain [87]. We thus consider a system of two QDs separated by a central hybrid superconducting island isolated from all leads such that the total charge is fixed. ‘Poor man’s Majorana’ sweet spots were found in Ref. [337] in a related system formed in a triple QD, but calculations were done in a formalism not conserving total particle number and requiring coupling to a superconducting lead, making it incompatible with placing the entire system in Coulomb blockade.

To begin, we define the system under consideration. We consider two semiconducting QDs denoted L and R with charging energies  $E_C^L$  and  $E_C^R$  coupled to a central hybrid superconducting island ‘M’ of charging energy  $E_C^M$  and with lowest subgap state excitation energy  $E_0$  and having electron- and hole-like coherence factors  $u$  and  $v$ , depicted in Fig. 7.3(a). The energies  $E_C^{L/R}$  are assumed the largest energy scales of the system. Since the existence of CAR transitions in this system is a prerequisite for the formation of a minimal Kitaev chain [337], we know from the results of Chapter 4 we must restrict ourselves to the regime  $E_C^M < E_0$ . We consider each QD as having a single spinful fermionic mode and an arbitrary manifold of quasiparticle states on island M with excitation energies  $\geq E_0$ . Each QD has a Zeeman splitting  $E_Z^j$  for  $j \in \{L, R\}$  favoring a spin-down state, but we neglect Zeeman splitting in island M as in Ref. [231]. Given a total charge of  $N$  in the system, the QDs have a charging energy of  $E_C^j (\hat{n}_j - n_{gj})^2$  where  $\hat{n}_j$  is the electron number operator on QD  $j \in \{L, R\}$  and  $n_{gj}$  is the reduced gate voltage on the dot [22]. By charge conservation, the charging energy of island M is  $E_C^S (N - \hat{n}_L - \hat{n}_R - n_{gM})^2$  and any state with odd charge on the island has a free energy cost of  $E_0$  at minimum since a

quasiparticle state must be occupied [64].

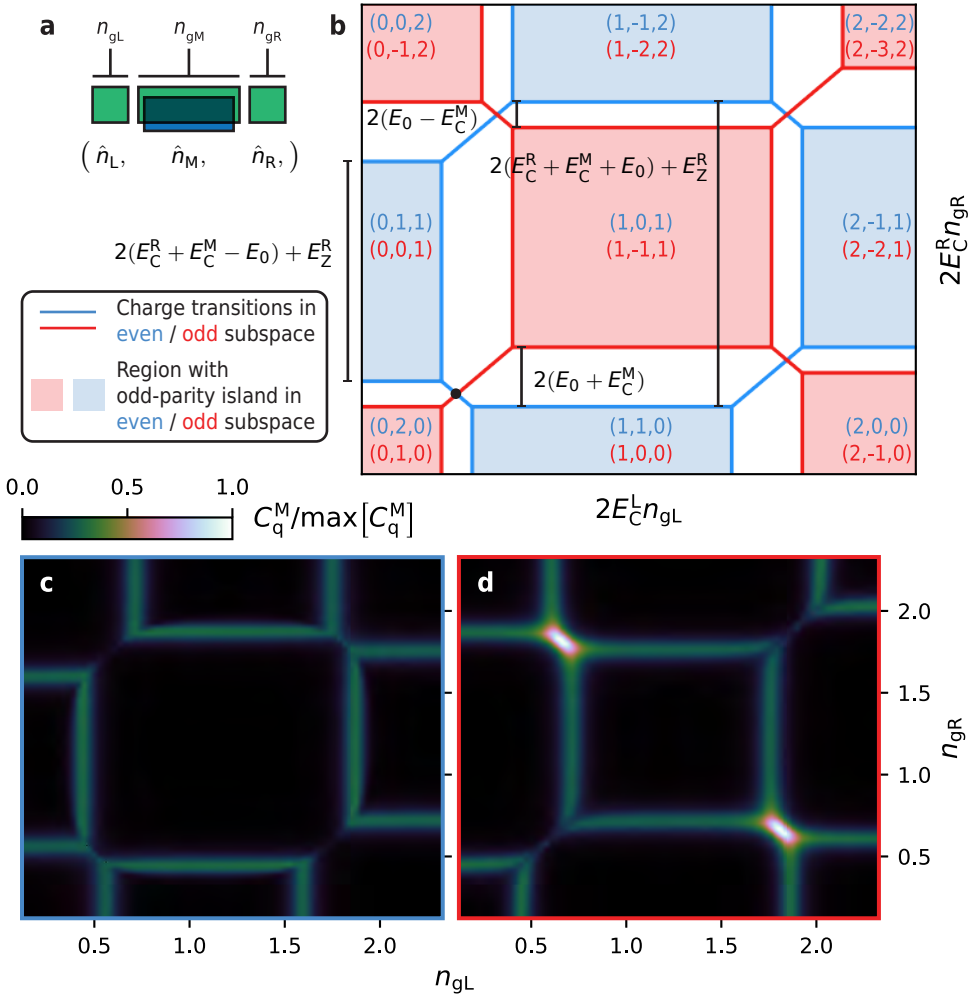


Figure 7.3: Simulations of a two-site Kitaev chain in a floating triple quantum dot. **(a)** Diagram of a triple QD system of two semiconducting dots (green) separated by an island (green) proximitized by a superconducting shell (blue). With normal reservoirs and a ground connection on the superconductor, this becomes a standard QD-based two-site Kitaev chain device [143, 144]. Otherwise, it is a floating triple QD. **(b)** Superimposed CSDs of the floating triple QD neglecting tunneling showing the ground charge state for total fixed charge  $N = 2$  (blue lines and labels) and  $N = 1$  (red). Charge states are labeled as  $(\langle \hat{n}_L \rangle, \langle \hat{n}_M \rangle, \langle \hat{n}_R \rangle)$  up to an arbitrary even offset on the superconducting island. Energy scales determining the sizes of different transitions in parameter space are also labeled. A black dot indicates the position in parameter space described by eq. 7.2. **(c),(d)** Thermally averaged quantum capacitance  $C_q^M$  as would be probed by a resonator connected to the gate of island M for total charge  $N = 2$  **(c)** and  $N = 1$  **(d)**. Parameters used in the simulations were  $E_C^L = E_C^R = 5E_0$ ,  $E_C^M = 0.4E_0$ ,  $E_Z^L = E_Z^R = 1.5E_0$ ,  $E_Z^M = 0$ ,  $t_L = t_R = 0.5E_0$ ,  $t_L^{so} = t_R^{so} = 0.2t_L$ , temperature  $T = E_0/40$ ,  $u = 1/\sqrt{2}$ , and  $v = i/\sqrt{2}$ , except in **(b)** where tunnel couplings were neglected. A phase of  $\pi/2$  was added to  $v$  to prevent accidental cancellations of the effective CAR amplitude. Seven outlier points due to discontinuities at fine-tuned points in the data were excluded from the simulations for clarity.

Finally, with the system defined, we argue that near the parameter regime  $n_{\text{gL/R}}^0 = (1 - E_Z^{\text{L/R}}/E_C^{\text{L/R}})/2$  and  $n_{\text{gM}} = 1$ , the system may form a two-site Kitaev chain across the Hilbert spaces of total charge  $N = 1$  and  $N = 2$ . Near this operating point, the potential ground states are those where the QDs contain zero charge  $|0\rangle$  or a spin-up electron  $|\uparrow\rangle$ , and the states  $\{|-1_j\rangle, |0\rangle, |1_j\rangle, |2\rangle\}$  on island M containing up to a single quasiparticle of energy  $\geq E_0$ . The CSD without tunnel couplings for  $N = 2$  and  $N = 1$  are superimposed in Fig. 7.3(b). There, we see that the center of the CAR transition coupling  $|0, 2, 0\rangle$  to  $|\uparrow, 0, \uparrow\rangle$  exactly coincides with the odd-parity sector's transition between  $|\uparrow, 0, 0\rangle$  and  $|0, 0, \uparrow\rangle$ . For the island states, the integer denotes the island's charge up to some even offset, and the subscript  $j$  denotes the quantum number of the occupied quasiparticle state. In particular, it may be verified that for  $N = 2$ , either  $|0, 2, 0\rangle$  or  $|\uparrow, 0, \uparrow\rangle$  are the ground state while  $|\uparrow, 1_j, 0\rangle$  and  $|0, 1_j, \uparrow\rangle$  are the closest excited states. Meanwhile, for  $N = 1$  the ground state is either  $|\uparrow, 0, 0\rangle$  or  $|0, 0, \uparrow\rangle$  and the nearest excited states are  $|0, 1_j, 0\rangle$  and  $|\uparrow, -1_j, \uparrow\rangle$ . In the  $N = 2$  and  $N = 1$  cases, the two ground states are effectively coupled by second-order tunneling through the closest excited states by an effective CAR amplitude  $t_{\text{CAR}}$  and elastic cotunneling (ECT) amplitude  $t_{\text{ECT}}$ , respectively, as argued in Sec. 2.1.5. Experimental evidence of nonzero  $t_{\text{CAR}}$  and  $t_{\text{ECT}}$  can also be seen in the stability diagrams of Fig. 4.1, indicated by a dispersive shift of the gate resonators probed across cotunneling and Cooper pair splitting transitions. Near the operating point, such that  $n_{\text{gL/R}} = n_{\text{gL/R}}^0 + \delta n_{\text{gL/R}}$  for some  $\delta n_{\text{gL}}, \delta n_{\text{gR}} \ll 1$ , the low energy Hamiltonian can be calculated to be:

$$\hat{H} = \begin{pmatrix} 0 & 0 & 0 & t_{\text{CAR}} \\ 0 & \varepsilon_{\text{L}} & t_{\text{ECT}} & 0 \\ 0 & t_{\text{ECT}}^* & \varepsilon_{\text{R}} & 0 \\ t_{\text{CAR}}^* & 0 & 0 & \varepsilon_{\text{L}} + \varepsilon_{\text{R}} \end{pmatrix} \quad (7.2)$$

up to a constant, in the basis  $\{|0, 2, 0\rangle, |1, 0, 0\rangle, |0, 0, 1\rangle, |1, 0, 1\rangle\}$  dressed by perturbative occupation of states containing a quasiparticle<sup>1</sup>. This small odd occupation is exactly what makes  $t_{\text{CAR}}$  and  $t_{\text{ECT}}$  nonzero (see Sec. 2.1.5). Above, we defined  $\varepsilon_{\text{L/R}} \equiv -2E_C^{\text{L/R}}\delta n_{\text{gL/R}}$ . Ignoring the state of the superconductor, which has a constant state up to a change in the number of Cooper pairs in the superconducting condensate, this is precisely the Hamiltonian of a two-site Kitaev chain, and forms Majorana bound states when  $t_{\text{CAR}} = t_{\text{ECT}}$  [87].

While  $|0, 2, 0\rangle$  and  $|\uparrow, 0, \uparrow\rangle$  are degenerate in the absence of tunneling at this operating point, we should note that charge noise in  $n_{\text{gM}}$  away from 1 breaks this degeneracy. As a floating system, however, decreasing  $n_{\text{gM}}$  is equivalent to increasing  $n_{\text{gL}} = n_{\text{gR}}$  by a proportional amount, except that  $n_{\text{gM}}$  noise is local to the superconducting island. This susceptibility to local noise may be detrimental to the coherence of qubits based on Kitaev chains where the central superconductor has a charging energy. It could be diminished by lowering  $E_C^{\text{M}}$ , which would not increase quasiparticle poisoning rates if it is a truly floating system.

Next, we consider how the state of a floating two-site Kitaev chain might be measured. Either the left or right QD is both sensitive to ECT and CAR and the gate sensor enables measurement of the CSD, though a resonator must couple to both QDs to be sensi-

<sup>1</sup>The same is true for dot-based Kitaev chains in open systems: the charge states coupled by CAR and ECT are dressed by some occupation of the 'virtual' states mediating these couplings.

tive to the Majorana bound state parity [14]. In a grounded Kitaev chain, parity readout could also be accomplished with a resonator coupled to the superconducting lead, since the lead resonantly loses and gains charge in the even parity subspace where CAR occurs. On the other hand, it is relatively insensitive to ECT in the odd-parity subspace because electron wave functions only weakly occupy the superconductor for resonant ECT. The same readout principle applies for a floating Kitaev chain, so we plot quantum capacitance  $C_q^M$  of the superconducting island in Figs. 7.3(c) and 7.3(d), respectively. Quantum capacitances are calculated with thermal averaging according to eq. 2.24, from results of a full fermionic simulation of the system described in Appendix F. Simulation parameters are chosen to be similar to Ref. [337] and are given in the Fig. 7.3 caption, but with a finite charging energy on the island to emphasize how this alters the CSD. As expected, we find that  $C_q^M$  is substantial at charge transitions coupled via CAR, but relatively small at ECT transitions. Additionally, the shape and strength of the CAR and ECT transitions differs between the  $N = 2$  and  $N = 1$  cases. This is because CAR can occur without any spin-flipping processes in the odd-parity case.

Hence, we have found that a two-site Kitaev chain can be implemented in a floating system. Furthermore, we found that a resonator coupled to the floating superconductor can distinguish between the even and odd parity subspaces. This is only one schema by which a floating Kitaev chain could be implemented, however—forming them by coupling superconducting islands directly may be possible [338], rather than coupling QDs via a superconductor.

### QUBITS BASED ON YU-SHIBA-RUSINOV STATES

Outside of topologically protected qubits and qubits formed from Josephson junction ABSs, other hybrid qubit schemes have favorable characteristics such as protection from noise. YSR states can form as subgap states in superconductors coupled with semiconducting QDs, screening the spin and charge of a spinful QD in an effective singlet state. For example, one may tune the TQD system discussed above to a sweet spot where the superconducting island equally favorably wants to screen an unpaired spin on either of the outer dots [79]. At this operating point, any superposition of the two lowest-energy states have equal expected charge on each of the three QDs and are insensitive almost to third-order in charge fluctuations. This suppression of charge dispersion is caused by the superconductor screening any electron-hole asymmetry in the QDs, and makes this system interesting to study as a qubit. Turning the system inside out—it has also been proposed to form a qubit based on YSR states in a TQD system of two superconducting islands separated by a semiconducting QD [25]. In this case, states where a YSR singlet is formed between the left or right superconducting island can hybridize, forming a YSR-analog to a DQD charge qubit [41, 42] with some charge noise protection. Qubits based on a similar principle could also be constructed from a pair of impurities or a DQD coupled to a superconducting reservoir [339, 340].



# A

## FABRICATION DETAILS

### A.1. RF-COMPATIBLE DEVICES IN TWO-DIMENSIONAL ELECTRON GASES

The sensitivity of a resonator to a small capacitance (such as the quantum capacitance of a multi-quantum-dot system) increases as this capacitance becomes a larger fraction of the total resonator capacitance [13]. Such a resonator, be it an off-chip inductor or on-chip resonator, must eventually connect to the device through a gate electrode extending onto the active device region. For a device formed in a two-dimensional electron gas (2DEG) material platform, this means the gate lead must extend over the 2DEG mesa (see Sec. A.2), possibly separated by one or more other layers of gates or dielectric. The InSbAs platform used for Chapters 5 and 6 has a conducting surface 2DEG when no voltage is applied to any coupled gates, so we must pattern depletion gates in order to define a conducting region with the desired shape of the device. Due to limitations in our fabrication recipe the 2DEG mesa can only be coarsely patterned, meaning that this overlap region of the resonator gate lead with gates in other layers and the 2DEG is necessarily substantial. Evidently, this proximity of the lead to other conducting materials contributes a capacitance which must be minimized to optimize the resonator's sensitivity to the capacitance of interest. Moreover, unintended capacitances to a resistive 2DEG or filtered DC lines of the measurement setup introduce losses to the resonator, lowering its internal quality factor. Typical low-pass filter resistances of several  $k\Omega$  can drastically lower the resonator quality factor depending on capacitances to these lines. Ultimately, this can result in a quality factor and resonator frequency too low to be usable for sub-GHz reflectometry measurements.

Two clear options for alleviating this issue are to reduce the capacitance between resonator leads and DC gate leads, or to apply filtering around the resonator's frequency on the latter. The latter works because any unintended capacitance is the same as no capacitance at all if it is in series with a high impedance such as that of a filter. Note that other lines coupled to RF resonators are not as much of a concern provided their resonators have narrow enough linewidth: in this case the resonator itself serves as a band-pass fil-

ter which excludes the frequency of the resonator we are discussing here. We can reduce the unintended capacitances by applying thicker dielectric material between gate layers or between gate layers and the 2DEG, but this would proportionately decrease the capacitor of the resonator lead to the device region of interest. Hence, it is not a viable solution. Some additional reduction of this capacitance can also be attained by simply designing the device such that other gates in the same layer as the resonator gate are separated from it by as large of a distance as possible. For example, it is a good practice to have gate leads 'fan out' from the central device region rather than running close together in parallel. Unfortunately, this does not affect the expected dominant contribution to the stray capacitance: that to the 2DEG or underlying depletion gate layers.

Thus, the remaining option is adding additional filtering to DC lines. This filtering should be on the device chip, such that it is 'seen' by the capacitively-coupled resonator line before the resonator sees the standard DC line filtering. Inductors serve as natural filters, given that they have an impedance increasing linearly with frequency [341]. For a sub-GHz resonator frequency, achieving a filtering impedance much larger than the few-k $\Omega$  DC line resistance would require an inductance on the order of tens or hundreds of  $\mu\text{H}$ ! This requires an infeasibly large footprint for an on-chip geometric or kinetic inductor [154, 342]. Instead, our solution is to use a high-resistance material to pattern resistors on the depletion gate lines of well over 100 k $\Omega$ . Though resistors are lossy, a large enough resistor actually serves to decrease loss in the resonator, as it approaches the limit of this DC line appearing as an open circuit to the resonator. Further details on the fabrication of these resistors are given below, but they are made from Ti/Pd nanowires thin enough and narrow enough to have a very large resistance. These materials were chosen primarily due to their availability in the deposition machines available at the time of device fabrication. Other materials with much larger resistances per square exist, but if the length of the resistor is too short, then there will be a significant capacitance between the two resistor leads allowing RF signals to bypass it.

## A.2. FABRICATION PROCEDURE

Here, we list the fabrication recipes used for fabricating the samples based in InSbAs ternary two-dimensional electron gas heterostructures in Chapters 5 and 6 in Table A.1. Please note that the multi-gate-layer fabrication recipe was developed primarily by Ivan Kulesh as preliminary test devices for Chapter 5 were fabricated, and the final four-terminal junction devices measured in Chapter 6 were fabricated by Wietze D. Huisman. The measured device of Chapter 5 was fabricated by the author. Samples measured in chapters 3 and 4 were fabricated by Damaz de Jong, so details of the corresponding fabrication procedure may be found in Ref. [37].

First, we describe more broadly the design considerations in fabricating the measured device of Chapter 5. For a precise list of the fabrication steps employed, please see Table A.1. below. For the devices measured in Chapter 6, the same fabrication procedure was used but with two instead of three gate layers, and with additional aluminum etching steps to produce the fine Josephson junction structures. A device equivalent in design to the one measured in Chapter 5 from the same chip is shown in Fig. A.1(a). Initially, the chip is covered with a <10 nm epitaxial layer of Al which was selectively etched away everywhere except in a region to the left and right of the pictured device to form leads,

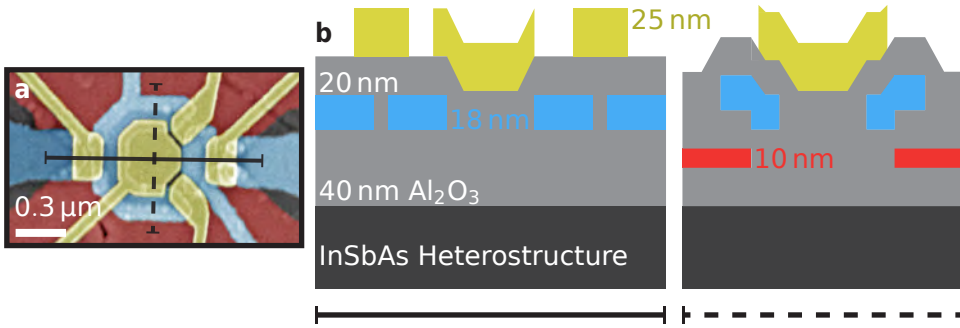


Figure A.1: Device design and layer stack. **(a)** False-color scanning electron micrograph for a device nominally equivalent to the one measured in Chapter 5 from the same chip. The colors are encoded by gate layer, of which there are three, instead of by the gates' purpose as was done in Fig. 1a of the main text. **(b)** Cross-sections approximately depicting the layer stack of the device along the solid and dashed lines shown in **(a)**. Thicknesses of the dielectric and Ti/Pd gate layers are relatively to scale, but the widths are not, and the topography is only schematically depicted.

exposing the  $\text{InSb}_{0.86}\text{As}_{0.14}$  2DEG heterostructure [245]. Next, the 2DEG was etched away except in a region close to the active device and along a roughly  $140\ \mu\text{m}$  path connecting it to the Al leads, forming a mesa. We then alternated between using atomic layer deposition to deposit roughly  $20\ \text{nm}$   $\text{Al}_2\text{O}_3$  dielectric layers then evaporating Ti/Pd gate layers to form three electrically isolated gate layers. Each layer also contains coarse gate leads (not shown), required to facilitate climbing the mesa. The 2DEG mesa on which the device was fabricated conducts, so forming a loop required application of negative voltages both along the outer perimeter of the loop, as well as in the hole in the center. Fabricating a double quantum dot (DQD) in this loop further necessitated plunger gates to tune the chemical potential of the quantum dots (QDs) and gates to form barriers between them and to the contacts. One option to satisfy these requirements is to pattern depletion gates in a layer above the plunger gates needed to tune the QDs, however in this case the leads of the lower layer gates were found in previous devices to screen the depletion gate voltage and prevent forming a stable loop. Hence, it was topologically required to fabricate three gate layers in order to both have an outer depletion gate underneath the plunger and barrier gates, as well as a central depletion gate which can cross over the plunger gates to deplete the center of the loop. The corresponding layer stack is schematized in Fig. A.1(b). A third gate layer had the added advantage that tunnel barriers could be made effectively more narrow, since barrier gates in the third layer may overlap with plunger gates in the second layer.

Step Description	Details	
	DQD Ring Devices (Ch. 5)	4TJJ Devices (Ch. 6)
Chip Cleaning	Strip protective resist layer in room temp. acetone overnight, then rinse in acetone & IPA	
Coarse Al & Mesa Etch	Spin-coat AR300.80 resist adhesion promoter at 4000 rpm. Bake in room temperature vacuum oven at least 1 h.	
	Spin-coat PMMA A4 950 resist at 4000 rpm. Bake in room temperature vacuum oven for at least 2 h.	
	<i>Electron-beam patterning:</i> Expose pattern in shape of desired 2DEG mesa, using no proximity effect correction for coarse features with dose of $790 \mu\text{C cm}^{-2}$ . For finer features (close to where device mesa will be) use proximity effect correction and a dose of $900 \mu\text{C cm}^{-2}$ .	
	Develop resist 50 s in MIBK:IPA mixed in a 1:3 ratio, then 10 s in IPA.	
	Bake resist again for at least 40 min, and clean with oxygen plasma again before or afterwards.	
	Etch in Transene-D at $48.2^\circ\text{C}$ <sup>1</sup> .	
		Strip resist in AR600.71 resist stripper, optionally sonicate, then rinse in acetone followed by IPA.
Fine Alignment Marker Deposition	Etch 2DEG mesa for 70 s using remaining coarse aluminum pattern as a mask, in a solution of 560 mL water, 4 mL phosphoric acid, 5 mL hydrogen peroxide, and 9.6 g citric acid using a stirring bar.	
	Strip resist in AR600.71 resist stripper, optionally sonicate, then rinse in acetone followed by IPA.	Rinse again in IPA.
	Spin-coat PMMA A4 950 resist at 4000 rpm. Bake in room temperature vacuum oven for at least 2 h.	
	<i>Electron-beam patterning:</i> Expose fine marker pattern using proximity error correction and a dose of $900 \mu\text{C cm}^{-2}$ .	
	Develop resist 50 s in MIBK:IPA mixed in a 1:3 ratio, then 10 s in IPA.	

<sup>1</sup>For Al etching with Transene-D, the etching was followed immediately by a brief dip in a water beaker at the same temperature as the Transene-D, another brief dip in a room temperature water beaker, followed by a longer rinse in another room temperature water beaker. The reason for this is to remove the Transene-D as quickly as possible to prevent overetching. The etch time for Transene-D varies from wafer to wafer, and must be precisely calibrated based on the thickness of the aluminum layer. Typical etch times are less than 10 s.

	<i>Deposition:</i> Evaporate 5 nm titanium followed by 60 nm gold.	
	Also deposit 5 nm palladium.	
	Liftoff in AR600.71 resist stripper, sonicate, then rinse in acetone followed by IPA.	
Fine Al Etch #1	Spin-coat AR300.80 resist adhesion promoter at 4000 rpm. Bake in room temperature vacuum oven at least 1 h.	
	Spin-coat PMMA A4 950 resist at 4000 rpm. Bake in room temperature vacuum oven for at least 2 h.	
	<i>(Al contacts)</i>	<i>(Josephson junction outlines)</i>
	<i>Electron-beam patterning:</i> Expose pattern using proximity error correction and a dose of:	
	950 $\mu\text{C cm}^{-2}$	970 $\mu\text{C cm}^{-2}$
	Develop resist 50 s in MIBK:IPA mixed in a 1:3 ratio, then 10 s in IPA.	
		Bake again in vacuum oven overnight.
	Etch Al in Transene-D at 38.2 °C.	
	Strip resist in AR600.71 resist stripper, optionally sonicate, then rinse in acetone followed by IPA.	
Fine Al Etch #2		Procedure is the same for this aluminum etching step as for Fine Al Etch #1, where the thin ‘slits’ dividing Josephson junction terminals are patterned, except that a dose of 900 $\mu\text{C cm}^{-2}$ is used during electron beam exposure.
Bondpad Deposition	Spin resist at 4000 rpm, then bake in room temperature vacuum oven at least 2 h, using resist:	
	PMMA 950 A4	PMMA 950 A6
	<i>Electron-beam patterning:</i> Expose bondpad pattern with a dose of:	
	1400 $\mu\text{C cm}^{-2}$	1200 $\mu\text{C cm}^{-2}$
	Develop resist 50 s in MIBK:IPA mixed in a 1:3 ratio, then 10 s in IPA.	
	<i>Etching &amp; Deposition:</i> Briefly etch with argon plasma, then in-situ sputter a thick layer of MoRe as a bondpad ‘foundation’.	<i>Deposition:</i> Evaporate 50 nm titanium, followed by 50 nm chromium, and finally 5 nm palladium.

	Liftoff in AR600.71 resist stripper, sonicate, then rinse in acetone followed by IPA.	
Metal Contacts (unused in Ch. 6)		Spin-coat PMMA A4 950 resist at 4000 rpm. Bake in room temperature vacuum oven for at least 2 h.
		<i>Electron-beam patterning:</i> Expose metal contact pattern using proximity error correction with a dose of $950 \mu\text{C cm}^{-2}$ .
		Develop resist 50 s in MIBK:IPA mixed in a 1:3 ratio, then 10 s in IPA.
		<i>Etching &amp; Deposition:</i> Mill with argon plasma for 20 s, then in-situ evaporate 3 nm titanium followed by 10 nm palladium.
		Liftoff in AR600.71 resist stripper, sonicate, then rinse in acetone followed by IPA.
Dielectric Layer #1	<i>Deposition:</i> Deposit 20 nm $\text{Al}_2\text{O}_3$ with room-temperature atomic layer deposition (200 cycles) after preconditioning the chamber without the sample for 5-10 cycles.	
Resistor Deposition (see Sec. A.1)		Spin-coat PMMA A4 950 resist at 4000 rpm. Bake in room temperature vacuum oven for at least 2 h.
		<i>Electron-beam patterning:</i> Expose resistor pattern using proximity error correction, a 18 nm beam spot size, and a dose of $1000 \mu\text{C cm}^{-2}$ .
		Develop resist 50 s in MIBK:IPA mixed in a 1:3 ratio, then 10 s in IPA.
		<i>Deposition:</i> Evaporate 12 nm titanium followed by 4 nm palladium.
		Liftoff in AR600.71 resist stripper, sonicate, then rinse in acetone followed by IPA.
Gate Layer #1, Fine Gates	Spin-coat ARP6200.04 resist at 4000 rpm. Bake in $40^\circ\text{C}$ vacuum oven for at least 2 h.	

	<i>Electron-beam patterning:</i> Expose fine gate pattern with a dose of: $320 \mu\text{Ccm}^{-2}$ <span style="float: right;"><math>310 \mu\text{Ccm}^{-2}</math></span>	
	Develop resist 60 s in pentylacetate, then 5 s in Xylene, then 30 s in IPA.	
	<i>Deposition:</i> Evaporate:	
	6 nm titanium followed by 4 nm palladium.	3 nm titanium followed by 11 nm palladium
	Liftoff in AR600.71 resist stripper, sonicate, then rinse in acetone followed by IPA.	
Dielectric Etching #1 (for easier wire-bonding)	Spin-coat AR300.80 resist adhesion promoter at 4000 rpm. Bake in room temperature vacuum oven at least 1 h.	
	Spin-coat ARP6200.04 resist at 4000 rpm. Bake in $40^\circ\text{C}$ vacuum oven for at least 2 h.	
	<i>Electron-beam patterning:</i> Expose region over MoRe bondpads with a dose of $320 \mu\text{Ccm}^{-2}$ .	
	Develop resist 60 s in pentylacetate, then 5 s in Xylene, then 30 s in IPA.	
	<i>Etching:</i> Use chlorine reactive ion etching to remove dielectric in exposed area.	
	Strip resist in AR600.71 resist stripper, optionally sonicate, then rinse in acetone followed by IPA.	
Gate Layer #1, Coarse Gates	Spin resist at 4000 rpm, then bake in room temperature vacuum oven at least 2 h, using resist:	
	PMMA 950 A4	PMMA 495 A6
		Spin-coat PMMA A3 950 resist at 4000 rpm. Bake in room temperature vacuum for at least 2 h.
	<i>Electron-beam patterning:</i> Expose coarse gate pattern with a dose of: $1400 \mu\text{Ccm}^{-2}$ <span style="float: right;"><math>950 \mu\text{Ccm}^{-2}</math> for gate leads and with <math>750 \mu\text{Ccm}^{-2}</math> over bondpads.</span>	
Develop resist 50 s in MIBK:IPA mixed in a 1:3 ratio, then 10 s in IPA.		
<i>Deposition:</i> Evaporate:		

	10 nm, 75 nm gold, then 10 nm palladium.	5 nm titanium, 80 nm gold, then 5 nm palladium.
	Liftoff in AR600.71 resist stripper, sonicate, then rinse in acetone followed by IPA.	
Dielectric Layer #2	Identical to procedure for Dielectric Layer #1.	
Gate Layer #2, Fine Gates	Spin-coat ARP6200.04 resist at 4000 rpm. Bake in 40 °C vacuum oven for at least 2 h.	
	<i>Electron-beam patterning:</i> Expose fine gate pattern with a dose of:	
	350 $\mu\text{C cm}^{-2}$	330 $\mu\text{C cm}^{-2}$
	Develop resist 60 s in pentylacetate, then 5 s in Xylene, then 30 s in IPA.	
	<i>Deposition:</i> Evaporate 3 nm titanium followed by:	
	15 nm palladium	16 nm palladium
	Liftoff in AR600.71 resist stripper, sonicate, then rinse in acetone followed by IPA.	
Dielectric Etching #2 (for easier wire-bonding)		Spin-coat AR300.80 resist adhesion promoter at 4000 rpm. Bake in room temperature vacuum oven at least 1 h.
		Spin-coat ARP6200.04 resist at 4000 rpm. Bake in 40 °C vacuum oven for at least 2 h.
		<i>Electron-beam patterning:</i> Expose the region over bondpads with a dose of 320 $\mu\text{C cm}^{-2}$ .
		Develop resist 60 s in pentylacetate, then 5 s in Xylene, then 30 s in IPA.
		<i>Etching:</i> Use chlorine reactive ion etching to remove dielectric in exposed area. Using roughly double the time as Dielectric Etching #1 to etch through two layers of dielectric.
		Liftoff in AR600.71 resist stripper, sonicate, then rinse in acetone followed by IPA.
Gate Layer #2, Coarse Gates	Identical to Gate Layer #1 Coarse gates, but with thicknesses of 10 nm titanium, 95 nm gold, and 15 nm palladium.	Spin-coat PMMA A6 495 at 4000 rpm. Bake in room temperature vacuum oven for at least 2 h.

		<p>Spin-coat PMMA A3 950 resist at 4000 rpm. Bake in room temperature vacuum for at least 2 h.</p> <p><i>Electron-beam patterning:</i> Expose coarse gate pattern and bondpads with doses of <math>1050 \mu\text{C cm}^{-2}</math> and <math>900 \mu\text{C cm}^{-2}</math>, respectively.</p> <p>Develop resist 50 s in MIBK:IPA mixed in a 1:3 ratio, then 10 s in IPA.</p> <p><i>Deposition:</i> Evaporate 5 nm titanium followed by 100 nm gold.</p> <p>Liftoff in AR600.71 resist stripper, sonicate, then rinse in acetone followed by IPA.</p>
Flux-bias Lines		<p>Spin-coat PMMA A6 495 at 4000 rpm. Bake in room temperature vacuum oven for at least 2 h.</p> <p><i>Electron-beam patterning:</i> Expose flux-bias line pattern with a dose of <math>1350 \mu\text{C cm}^{-2}</math>.</p> <p>Develop resist 50 s in MIBK:IPA mixed in a 1:3 ratio, then 10 s in IPA.</p> <p><i>Deposition:</i> Sputter roughly 100 nm NbTiN.</p>

		Liftoff in AR600.71 resist stripper, sonicate, then rinse in acetone followed by IPA.
Dielectric Layer #3	Identical to procedure for Dielectric Layer #1.	
Gate Layer #3, Fine Gates	Identical to procedure for Gate Layer #2 fine gates but with thicknesses of 3 nm titanium and 22 nm palladium.	
Dielectric Etching #3	Identical to Dielectric Etching #1 but with roughly double the etching time in order to remove two layers of dielectric.	
Gate Layer #3, Coarse Gates	Identical to Gate Layer #1 Coarse gates, but with thicknesses of 10 nm titanium and 105 nm gold with no palladium.	

Table A.1: Fabrication procedure for both types of  $\text{InSb}_{0.86}\text{As}_{0.14}$  devices measured in this dissertation, fabricated on 2DEG heterostructures provided by the research group of Michael J. Manfra [245]. Chips are assumed to already have an epitaxial layer of aluminum coating the entire chip covered in a protective resist layer, and to have coarse alignment markers deposited. While not listed in the table, resist residuals were cleaned from the chips in a gentle oxygen plasma after each resist development step, and chips were generally cleaned in a more aggressive oxygen plasma after each lithography or etching step.

# B

## MEASUREMENT SETUPS

In this appendix we describe the measurement setups used throughout this dissertation (Sections B.1, B.2, and B.4), as well as a new microwave measurement setup designed and built during the course of this thesis research in Sec. B.3. This latter setup was designed to be capable of both sub-GHz reflectometry and circuit quantum electrodynamics experiments at few-GHz frequencies.

As general considerations, we note that connections between the mixing chamber stage and higher stages in the microwave setups had to be via superconducting coaxial cables to prevent a thermal connection. Similarly, connections between higher stages used coaxial cables which, while not superconducting, had low thermal conductance. In general, the RF input line has to have attenuators thermally contacted to each plate of the fridge in order to reduce the effective noise temperature of photons entering the circuit<sup>1</sup>. Attenuators inside dilution refrigerators are especially designed for cryogenic purposes such that their attenuation meets specifications at low temperature and such that they thermalize properly with their connected fridge plates. Photons output from measurement electronics may also be much 'hotter' than room temperature, such that an attenuator is often placed at the output port of electronics as well. Until one reaches limits determined by the maximum power output of measurement electronics, one can always add more attenuation at each temperature stage with diminishing returns on the lowering noise temperature. Hence, this must be balanced with considerations relating to the possible output powers of measurement electronics and the cooling power of each temperature stage. Typically, the largest attenuation is placed at the 4 K stage since it is the closest temperature stage to the mixing chamber with a very large cooling power, but some attenuation should be placed at higher stages as well. Lower temperature stages should also contain some attenuation in order to reach mK level photon noise temperatures.

Other passive components in the measurement setup are often not designed specifically for cryogenic purposes. Directional couplers designed for sub-GHz bandwidths

---

<sup>1</sup>See the blog post by Matthew Sarsby for a guide to the subject at <https://blog.qutech.nl/2020/02/20/cooling-a-hot-photon-wind-part-1/>.

are sometimes designed with magnetic components and do not function at cryogenic temperatures. Couplers, filters, and circulators not designed for cryogenic applications are also often made with a stainless steel casing that has very low thermal conductivity at cryogenic temperatures compared to other materials like copper. The K&L tubular filters used in the setups measured have stainless steel casings, but are used simply because they are known to function properly at mK temperatures. Even worse, stripline directional couplers are often made of aluminum which superconducts at sub-1 K temperatures, making its thermal conductivity even lower. Aside from utilizing cryogenic microwave components (a newly emerging market at the time of this dissertation's writing), all one can do is provide these components with the best possible thermal contact to the refrigerator. Ideally, this is in the form of a rigid bracket made of a high thermal-conductance metal like copper. For round or suspended components like the filters in Fig. B.1, tightly wrapping copper ribbon around the component can be used as a last resort, but this provides less thermal contact.

### B.1. MICROWAVE TRANSMISSION MEASUREMENT SETUP

The experimental setup employed for microwave transmission measurements of coplanar waveguide resonators in Chapters 3 and 4 is schematically shown in Fig. B.1(a). This setup was contained in a Bluefors bottom-loaded dry dilution refrigerator, where most of the microwave electronics are mounted on the fridge plates rather than in the inserted sample probe. On-chip superconducting CPW resonators are fabricated from a 20 nm NbTiN layer using reactive ion etching, similar to Ref. [156] ensuring magnetic field compatibility. Since each resonator is terminated by a device gate or the semiconducting nanowire itself, either of which forms an impedance much larger than the waveguide characteristic impedance, these waveguides form half-wavelength resonances. The resonator design is a hanger-style geometry with each resonator coupled to a central feedline via a coupling capacitor, with further details given in Refs. [155, 204] based on design considerations introduced in Ref. [156]. These capacitors are tuned to be suitable for DGS measurements with an external photon coupling rate around  $\kappa_{\text{ext}} \simeq 10$  MHz. The reflection coefficient of each resonator can be simultaneously probed by measuring transmission through the feedline, since transmitted RF signals contain information about the reflection coefficient of the resonators 'hanging' off of it [187]. To minimize the noise temperature in our measurements we use a traveling-wave parametric amplifier (TWPA) [153] on the base temperature stage of a dilution refrigerator operating at 20 mK. Additionally, a high-electron-mobility transistor amplifier at 4 K is used to further amplify the signal.

One disadvantage of transmission-style setups is that, when measuring transmission through a feedline with hanger-style resonators capacitively coupled to it, half of the signal reflected from the resonator is directed back to the input port [187]. As a result, roughly half of the measurement signal is lost. This can be mitigated by placing a weak capacitor on the input side of the feedline and simply applying more input power to overcome the capacitance [335]. In this case, photons emerging from a resonator will be mostly reflected from the input capacitor's large impedance and directed towards the output port, though we do not implement such a capacitor in our feedline.

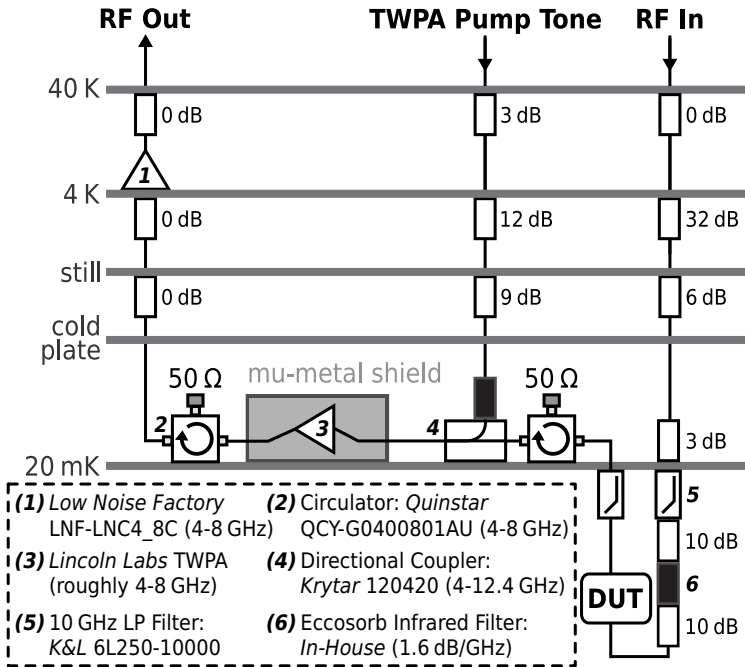


Figure B.1: **RF circuit of the dilution refrigerator used in Chapters 3 and 4.** An RF signal generated by a vector network analyzer, Quantum Machines OPX pulse generator, or custom multiplexing circuit read by an Alazar ADC card is attenuated at each stage of the refrigerator on its way to the device under test (DUT) at base temperature. The signal is amplified on the way out of the fridge first by a TWPA at base temperature, driven by a GHz-frequency pump tone, and then by a 4 to 8 GHz bandwidth high-electron-mobility transistor (HEMT) amplifier at the 4 K plate. The TWPA is enclosed in a mu-metal shield protecting it from applied magnetic fields. In front of and behind the TWPA are circulators and a directional coupler designed to reduce back-action of the TWPA on the DUT and attenuate any noise traveling down the output and pump tone lines. Low pass filters are also present to reduce noise above the measurement bandwidth. Any component not directly connected to a fridge plate was contacted by a copper bracket or ribbon to thermally connect it to the nearest plate. For the measurements of Figs. 7.2(a) and 7.2(b), only the attenuators and 4 K amplifier were present with no filtering, circulators, or parametric amplifier.

## B.2. SUB-GHz REFLECTOMETRY MEASUREMENT SETUP

The microwave measurement setup utilized in Chapter 5 is shown in Fig. B.2(a). We had no involvement in the design of this circuit, and so only briefly summarize the details. This dilution refrigerator is a dry Leiden Cryogenics fridge with a narrow top-loaded probe, which contains all measurement electronics lines and so had to be compactly designed. Stripline directional couplers operating below 1 GHz are not compact enough to fit inside the probe of this dilution refrigerator so a transformer-based coupler had to be used instead. These couplers are compact and the used model is known to operate at mK-temperatures, but generally have an upper frequency limit of 1 to 2 GHz. Consequently, this measurement setup is tailored to sub-GHz reflectometry. Measurements were conducted with a Rohde & Schwarz vector network analyzer or a Zurich Instruments Ultra High Frequency Lock-in Amplifier.

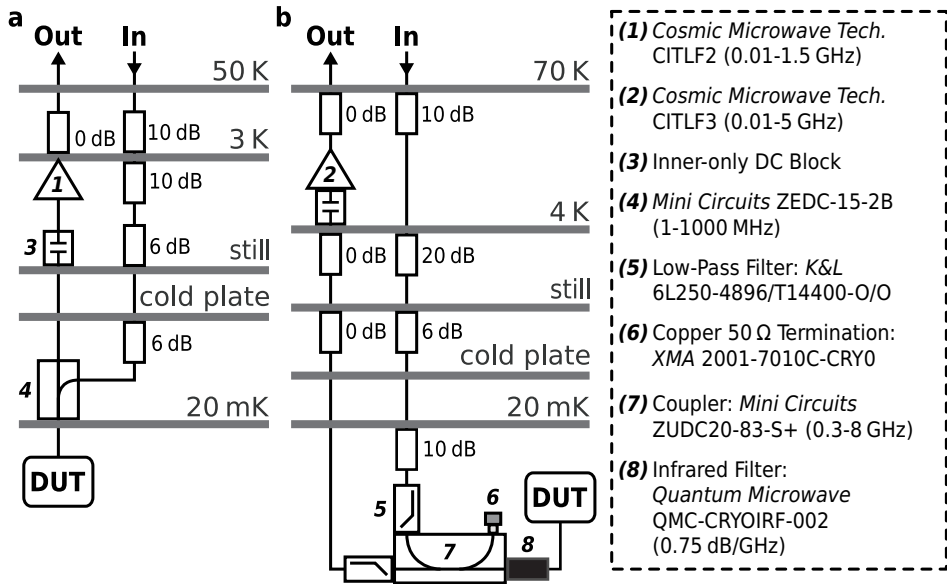


Figure B.2: **Reflectometry measurement circuits.** (a) Sub-GHz reflectometry circuit used for Chapter 5 in a Leiden Cryogenics dry cryostat. (b) Wideband reflectometry circuit designed and assembled in an Oxford Triton cryostat during this dissertation's research, but not measured in any chapter. The amplifier (2) and 50  $\Omega$  termination (6) are connected to the 4 K and mixing chamber plates, respectively, by flexible copper brackets. The directional coupler (7) is rigidly connected by a copper bracket to the mixing chamber plate. All parts shown as touching fridge plates are directly connected to them, and all other suspended components have copper ribbon wrapped around them and connected to the mixing chamber plate.

### B.3. WIDEBAND REFLECTOMETRY SETUP

During the course of this dissertation's research, a microwave measurement setup operable from 0.3 to 5 GHz was designed for and assembled in an Oxford Triton dry dilution refrigerator. Herein we describe the design considerations leading to the final circuit depicted in Fig. B.2(b). The overall goal was to design a measurement circuit capable of reflectometry measurements at sub-GHz frequencies as well as at higher frequencies in the few-GHz range approaching energy scales of quantum systems of interest. This is because the former band is the practical limit for measurements using off-chip inductor coils, possessing resonance frequencies limited to below 1 GHz due to their unavoidable parasitic capacitance to ground defining the resonance [13]. Meanwhile, the latter band is of relevance for faster measurements of qubits or circuit quantum electrodynamics experiments where the measurement frequencies approach the energy scales of the system [5].

The main components preventing the creation of such a wide bandwidth microwave measurement setup are cryogenic amplifiers, directional couplers, and circulators. Most circulators have very narrow bandwidths if they exist at all at low frequencies—the most typical circulators used in cryogenic setups have bandwidths beginning at a few GHz (see e.g. Fig. B.1). Without circulators, there is no obvious method to protect the device from backaction and reflections from the amplifier, but this is unavoidable for low-frequency

reflectometry setups because of the limitation mentioned above. Stripline directional couplers actually are available in fairly wide bandwidths reaching to sub-GHz frequencies, but they are over 10 cm in length, like the 15.2 cm long one used in this setup. Hence, a wide bandwidth coupler can only be employed in larger dilution refrigerators where the electronics are statically mounted on the fridge plates and not on a sample probe. Lastly, the amplifier used here was the cryogenic amplifier which at the time had the highest upper band limit while also reaching down to a few hundred MHz in operating range. This amplifier ultimately sets the upper limit of our bandwidth to 5 GHz.

The cutoff frequency of the low-pass filters used was chosen according to this upper frequency limit. Additionally, infrared filtering (and shielding of the sample) is expected to be important for reducing noise at frequencies well above the bandwidth of the system [343]. We employed the only (at the time) commercially available cryogenic infrared filter, though due to its extremely weak  $0.75 \text{ dB GHz}^{-1}$  attenuation, a more strongly attenuating filter would have been desirable<sup>2</sup>. Only one of each filter is needed if placed at the device side of the directional coupler, but due to spatial constraints we were forced to instead place the two K&L filters at the other ports of the coupler.

Regarding thermalization of the components, attenuators were chosen according to the considerations described at the beginning of this appendix. Different combinations of attenuators were checked to see which did not introduce too much dissipation onto the mixing chamber plate which has less cooling power, while still ensuring that the final expected noise temperature is comparable to the mixing chamber temperature<sup>3</sup>. Wideband directional couplers were only available in superconducting aluminum casings, so to alleviate thermalization issues, a rigid copper bracket was designed which has strong thermal contact across a large surface area of one of the coupler's rectangular faces. When operating the coupler, the power transferred from the RF-input to the device side is attenuated by 20 dB, while the remaining  $\approx 99\%$  of the signal is dissipated in the  $50 \Omega$  terminated port. This power dissipation may drastically heat up the already poorly thermally conducting coupler, so the stock termination was replaced by a copper cryogenic  $50 \Omega$  termination from XMA. This termination was then connected with a copper clamp to copper ribbon thermalized to the mixing chamber plate. Other filters were wrapped tightly with copper ribbon connected to the mixing chamber plate as a makeshift substitute for more rigid clamps.

## B.4. DC SETUP WITH HIGH-CURRENT LINES

For the experiments of Chapter 6, a Leiden Cryogenics wet dilution refrigerator containing only DC lines was used. Conventionally, DC lines in a dilution refrigerator are connected to low-pass filters at a low-temperature stage. In order to control the flux-bias current line in the sample measured in Ch. 6, however, currents on the order of 1 mA had to be passed through it to generate sufficient fields through the nearby SQUID. Typically, for DC lines a stringent RC-style filtering is used, and the associated resistances would lead to too much heat dissipation on low-temperature stages of the fridge relative to its cooling power. In the case of the fridge used for this experiment, the filters were placed

<sup>2</sup>Infrared filters can be made by injecting Eccosorb into a barrel connection or other filter. Infrared filters are also commercially available from XMA now.

<sup>3</sup>See the Python notebook available at [https://github.com/cprosko/photon\\_thermalization](https://github.com/cprosko/photon_thermalization).

at the mixing chamber stage at tens of mK where the cooling power is very small in order to minimize Johnson-Nyquist noise. Passing 1 mA current through such a few-k $\Omega$  line would lead to heat dissipation on the order of milliwatts and the fridge would not be able to stay cold.

**B**

As a result, some of the filtering must be sacrificed for high-current lines. We thus repurposed a DC line to bypass the low-temperature RC filters. Using a low-thermal-conductance wire with less than 50  $\Omega$  room-temperature resistance, we routed a connection from the sample circuit board to an RC filter at the 1 K temperature stage where cooling power was much larger<sup>4</sup>. This filter also had a lower resistance on the order of a few-hundred Ohms. For measurements, the drain of the flux-bias line was then connected to the cold ground of the fridge itself. Notably, this meant that the sample probe could no longer be floating, and the fridge had to be defined as the ground for the entire setup. In this case however, the fridge had additional Ohmic connections, such as one to the helium recovery pipes. This introduced ground loops which may have led to additional noise in the measurements of Ch. 6.

---

<sup>4</sup>This line was designed and built by Ivan Kulesh with assistance from Christian Prosko, Olaf Benningshof and Jason Mensingh.

# C

## RESONATOR RESPONSE FITTING

In this appendix we describe the fitting procedure for resonator responses measured in Chapters 3, 4, and 5. The model used for fitting the transmission  $S_{21}$  through a directional coupler reflectometry circuit, or through a feedline with a ‘hanger-’ or ‘notch-style’ resonator or reflected directly from a resonator is given by [158, 187, 190, 344, 345]

$$S_{21} = e^{i(\theta_0 + \theta_1 \omega)} s_0 \left( 1 + s_1 \frac{\omega - \omega_0}{\omega_0} \right) \left( 1 - \lambda \frac{i \kappa_{\text{ext}}}{i(\text{Re}[\kappa_{\text{ext}}] + \kappa_{\text{d}})/2 - \omega + \omega_0} \right), \quad (\text{C.1})$$

where the probe frequency is denoted by  $\omega$  and the resonator frequency by  $\omega_0$ , and where  $\lambda = 1$  for a reflectometry circuit (as in Chapter 5) and  $1/2$  for a hanger-style transmission circuit (as in Chapters 3 and 4). Intuitively, this factor accounts for the fact that half the reflected signal from a resonator coupled to a feedline is lost to the input of the feedline [37]. To account for the line delay—the time required for photons to propagate through the measurement circuit— $\theta_0$  and  $\theta_1$  add a linear offset in phase. Essentially, the number of wavelengths of light which ‘fit’ in the circuit determine an additional frequency-dependent phase offset photons will have upon reaching readout electronics. Similarly, we account for a linear amplitude offset by  $s_0$  and  $s_1$  caused by frequency-dependent gain or loss in the measurement circuit components. Namely, a value of  $s_0$  other than 1 indicates a net attenuation or gain in the measurement circuit. Meanwhile a nonzero  $s_1$  offset can arise due to other complications in the circuit, like impedance mismatches at amplifier inputs creating resonant cavities in the circuit for example [259], or a frequency-dependent gain response of the amplifier or attenuation response from filters. Photon losses to outside the system are represented by a decay rate  $\kappa_{\text{d}}$ , and the external coupling rate  $\kappa_{\text{ext}}$  describes photon coupling between the resonator and readout circuit. The latter parameter is complex to account for impedance mismatches along the feedline [37, 190, 345] or with the earliest amplification stage [259], or mutual inductance between the resonator and feedline [158]. This complex phase added to  $\kappa_{\text{ext}}$  can substantially change the resonator lineshape, most noticeably giving it an asymmetric amplitude response about its resonance frequency. Impedance mismatches are expected to be the cause of this asymmetry in our experiments, and can be thought of

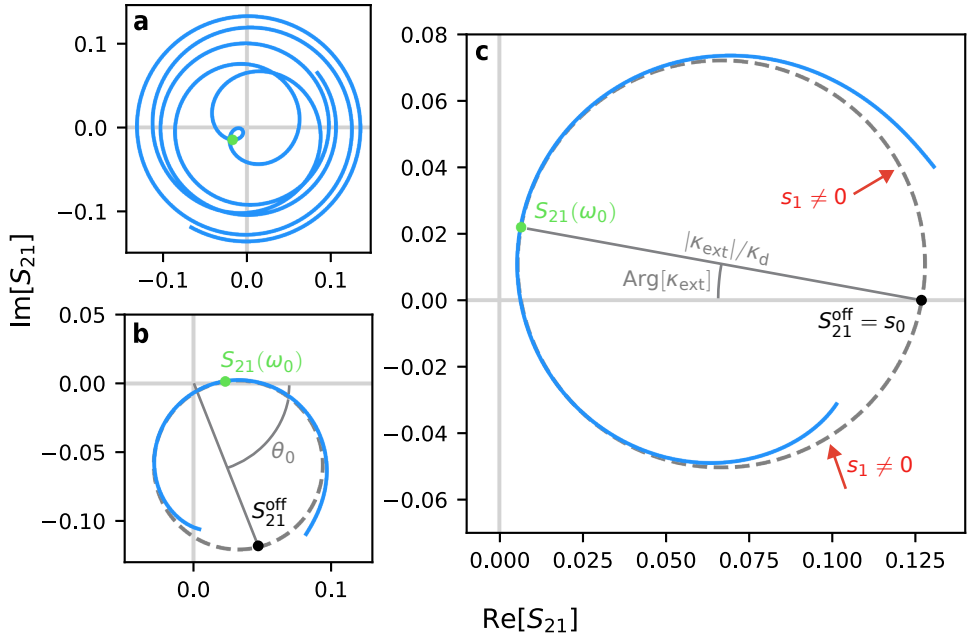


Figure C.1: **Lineshape of  $S_{21}$  for a hanger-style resonator coupled to a feedline.** (a) The raw resonator circuit transmission, which appears highly complicated due to the rotating phase arising from nonzero  $\theta_1$ . (b) Resonator circuit transmission after dividing out  $e^{i\theta_1\omega}$ . The phase offset  $\theta_0$  can be inferred as the angle between the far off resonance  $S_{21}$  value of the resonator lineshape if  $s_1$  were zero (gray dashed circle),  $S_{21}^{\text{off}}$ , and the real axis. (c) Resonator circuit transmission after dividing out  $e^{i(\theta_0+\theta_1\omega)}$ . From this plot, more parameters of the resonator can be estimated as highlighted. For these plots, the parameters for the lead resonator measured in Chapter 3 are used:  $\omega_0/2\pi = 4.298$  GHz,  $\kappa_d = 6.269$  MHz,  $\kappa_{\text{ext}} = (116.926 - 21.104i)$  MHz,  $\theta_0 = -1.228$ ,  $\theta_1 = 92.19$  ns, and  $s_0 = 0.12681$ . One exception is that we have increased  $s_1$  to  $s_1 = 10$  to make its skewing effect on the lineshape more clear.

as causing additional resonant cavities along the measurement circuit. Though one may expect to see  $\kappa_{\text{ext}} + \kappa_d$  in the denominator, we instead have  $\kappa_{\text{ext}} \rightarrow \text{Re}[\kappa_{\text{ext}}]$  since this is equivalent up to a change to an (arguably more correct [158]) definition of  $\omega_0$ . We will see below that this definition leads to a more intuitive geometric correspondence between  $\text{Arg}[\kappa_{\text{ext}}]$ ,  $\omega_0$ , and the lineshape of the resonator. We visually summarize the effect of these resonator parameters on a resonator's response in Fig. C.1.

With eight fitting parameters one might suppose the model is overfitted, allowing one to easily fit any resonator response. In reality, the opposite is often true: real resonators can have even more complexities such as nonlinear amplitude offsets which make it very difficult to automatically fit the resonator response in a single iteration [259]. Hence, it is crucial to provide good initial guesses to the fitting algorithm, and furthermore to fix any parameters which are experimental constants after calibration. Namely, the parameters  $\theta_0$ ,  $\theta_1$ ,  $s_0$ , and  $s_1$  should be constant as long as the experimental setup is not modified, but  $\theta_1$ ,  $s_0$ , and  $s_1$  may vary depending on which resonator is to be fitted. For  $s_0$  and  $s_1$ , this is because the approximation of a linear amplitude offset breaks down in a larger frequency band. Meanwhile,  $\theta_0$ ,  $s_0$ , or  $s_1$  can all be perturbed by

unintended resonant cavities distorting the measurement circuit's phase and amplitude response locally in frequency space. Because automatically fitting resonator lineshapes with so many fit parameters can be difficult, we summarize a systematic procedure for manually fitting the resonator below. In practice, one can follow these steps until enough parameters are fixed that the automatic fitting algorithm produces a good convergent fit result using the manually fit parameters as initial guesses.

### Manual Resonator Response Fitting Guidelines:

1. Fit  $\theta_1$  by fitting  $\text{Arg}[S_{21}]$  over a wide frequency range to a linear slope, or by manually calibrating it out directly in the measurement equipment<sup>1</sup>. This parameter can be subsequently fixed even for the final automatic fitting.
2. Note that the resonator response would fall on a circle if  $s_1$  were zero. Estimating the shape of this circle (gray in Figs. C.1(b) and C.1(c)), take  $S_{21}^{\text{off}}$  (the expected far off-resonance response of the resonator when  $s_1 = 0$  and  $\omega \rightarrow \pm\infty$ ) as the point on this circle diametrically opposed to the on-resonance point  $S_{21}(\omega_0)$ . Adjust  $\theta_0$  until  $S_{21}^{\text{off}}$  falls upon the  $\text{Re}[S_{21}]$  axis. As  $\omega_0$  has not yet been fitted for, one may instead adjust  $\theta_0$  until the 'open ends' of the resonator response are equally spaced about the  $\text{Re}[S_{21}]$  axis. This second technique will be more inaccurate the larger  $|s_1|$  is.
3. Adjust  $s_1$  (using a reasonable estimate for  $\omega_0$  given the center of the resonance dip in  $|S_{21}|$  or position of maximum phase slope in  $\text{Arg}[S_{21}]$ ) until the two open ends of the resonator response fall on the circumference of the idealized circle mentioned in Step 2. When  $s_1$  is set incorrectly, one open end will point away from the mostly-circular resonator lineshape, and one end will point inward within the circle's perimeter, as highlighted by red arrows in Fig. C.1(c).
4. Extrapolating the open ends of the resonator lineshape to see the point  $S_{21}^{\text{off}}$  where the now-circular resonator lineshape would intersect with the  $\text{Re}[S_{21}]$  axis, adjust  $s_0$  until this point is at  $S_{21}^{\text{off}} = 1$ , *i.e.* take  $s_0 = S_{21}^{\text{off}}$ .
5. Given  $S_{21}^{\text{off}}$  as one point on the resonator response circle from the previous step,  $\omega_0$  is the frequency corresponding to the point  $S_{21}(\omega_0)$  which is diametrically opposed to  $S_{21}^{\text{off}}$  on the circle.
6. Estimate  $\text{Arg}[\kappa_{\text{ext}}]$  as the angle between the vector  $S_{21}(\omega_0) - S_{21}^{\text{off}}$  and the negative  $\text{Re}[S_{21}]$  axis [158].
7. The diameter of the resonator circle at the previous step should be  $|\kappa_{\text{ext}}|/\kappa_d$ , while one can get an order-of-magnitude estimation of  $\kappa_d$  from the full-width-at-half-maximum of the resonator's amplitude response. The resulting estimates for  $\kappa_d$  and  $|\kappa_{\text{ext}}|$  will likely be highly inaccurate, and should only serve as initial guesses for a fitting algorithm.

The method of estimating  $\omega_0$  in step 5 is the practical reason for our usage of  $\text{Re}[\kappa_{\text{ext}}]$  in the denominator of eq. C.1: using  $\kappa_{\text{ext}}$  instead would correspond to an  $\omega_0$  definition for which this method cannot be applied. Note also that all of these steps also apply for

<sup>1</sup>For vector network analyzers, this parameter is sometimes called 'electrical delay' or 'phase delay'.

a resonator in a reflectometry circuit ( $\lambda = 1$ ), except that the radius of the circle after step 4 should be 1 instead of  $1/2$  when  $|\kappa_{\text{ext}}| \gg \kappa_{\text{d}}$ .

Lastly, we discuss a substantial weakness of typical resonator fitting methods. Because on the circular resonator lineshape (after calibrating out  $\theta_1$  and  $s_1$ ) we have that  $S_{21} \rightarrow S_{21}^{\text{off}}$  as  $\omega \rightarrow 0$  or  $\omega \rightarrow \infty$ , this means that in a wide sweep of linearly spaced frequency points, the points will be at a higher density the farther from  $\omega_0$  they are. Hence, if we try to fit a resonance in a fairly wide frequency window, there will be many more points far-off-resonance contributing to the fit than there are near-on-resonance points. Accounting for the importance of the handful of points near resonance can be accomplished by adding a fitting weight which is larger near resonance or for points which conform more to the expected circular resonator lineshape [344]. While not employed in this thesis, through experiments with fitting in this way we found it had little obvious advantage over fitting without weighting, except when stray resonances perturb the resonator to be fitted away from the resonance frequency. Given noise in experiment, it may instead be beneficial to measure in an unevenly spaced frequency sweep: taking more points close to the resonator frequency and less farther away. In practice, however, the situations in experiments where resonator response fitting is required are generally situations in which a frequency shift of the resonance is to be measured, in which case the center of this varying points distribution would have to adjust along with the resonance frequency. Regardless, what is always important is to have a high enough sweep resolution to resolve the full depth of the resonator ‘dip’ in amplitude or the slope of the resonator ‘step’ in phase without any aliasing effects.

# D

## QUANTUM CAPACITANCE FORMULA INCLUDING MUTUAL CAPACITANCES

In order to determine the degree to which mutual capacitances between QDs suppress parametric capacitance, we follow the approach of Refs. [125, 130] to derive an expression for parametric capacitance, additionally considering mutual capacitance effects to second order. We consider the case of  $N$  charge islands coupled capacitively to a single gate voltage  $V_g$  via capacitances  $C_{gi}$  for  $i \in \{1, 2, \dots, N\}$ , with mutual capacitances between the islands of  $C_{ij}$  for  $i \neq j$ , and other capacitive couplings to ground encompassed by an environmental capacitance  $C_{ei}$ . The latter includes any capacitances to lead reservoirs, for example. We refer to the total capacitance of each island as  $C_i \equiv C_{gi} + C_{ei} + \sum_{j \neq i} C_{ij}$ . Note that by definition, we have  $C_{ij} = C_{ji}$ . The total differential capacitance  $C_{\text{diff}}$  as seen by  $V_g$  can then be written as the sum over differential capacitance contributions of each island

$$C_{\text{diff}} = \sum_{i=1}^N \frac{d\langle Q_i \rangle}{dV_g} = \frac{d\sum_{i=1}^N \langle Q_i \rangle}{dV_g} \quad (\text{D.1})$$

where  $Q_i$  is the total effective charge on the capacitor  $C_{gi}$  as seen by  $V_g$  and the angular brackets denote the statistical average of the charge. In general, this average must include thermodynamic, quantum mechanical, and driving effects.

To solve this expression, we write  $\langle Q_i \rangle$  in terms of known capacitances and the expectation values  $\langle \hat{n}_i \rangle$  of electron number on each island with charge number operator  $\hat{n}_i$ . First, by definition of the gate capacitances we may write  $\langle Q_i \rangle = C_{gi}(V_g - V_i)$  where  $V_i$  is the electrostatic potential on island  $i$ . On average, we can write the charge expectation value on island  $i$  as a sum over all of the voltage induced charges from each capacitor

$$-|e|\langle \hat{n}_i \rangle = C_{gi}(V_i - V_g) + \sum_{j \neq i} C_{ij}(V_i - V_j) + C_{ei}V_i \quad (\text{D.2})$$

with  $e$  being the electron charge [22]. Solving for  $V_i$  and recalling the definition of  $C_i$ , we find

$$V_i = \frac{1}{C_i} \left( C_{gi}V_g + \sum_{j \neq i} C_{ij}V_j - |e|\langle \hat{n}_i \rangle \right). \quad (\text{D.3})$$

By substituting this result for each  $V_j$  into the original expression for  $V_i$ , we may recursively generate expressions for  $V_i$  to higher and higher orders in the mutual capacitance lever arms  $C_{ij}/C_i$ . Doing so twice, substituting the result into the definition of  $\langle Q_i \rangle$ , and using the resulting expression to calculate  $C_{\text{diff}}$ , we find

$$C_{\text{diff}} = C_{\text{geom}} + C_p + \mathcal{O}(C_{ij}^3/C_i^3) \quad (\text{D.4})$$

with contributions from a constant geometric capacitance

$$C_{\text{geom}} \equiv \sum_{i=1}^N \alpha_i \left[ C_i - C_{gi} - \sum_{j \neq i} \left( \alpha_j C_{ij} + \sum_{k \neq j} \frac{C_{ij} C_{jk}}{C_j} \alpha_k \right) \right] \quad (\text{D.5})$$

and a  $\langle \hat{n}_i \rangle$ -dependent parametric capacitance:

$$C_p \equiv \sum_{i=1}^N \left[ \alpha_i + \sum_{j \neq i} \left( \alpha_j \frac{C_{ij}}{C_j} + \sum_{k \neq j} \alpha_k \frac{C_{ij} C_{jk}}{C_i C_k} \right) \right] |e| \frac{d\langle \hat{n}_i \rangle}{dV_g} \quad (\text{D.6})$$

where we have defined the bare lever arms  $\alpha_i \equiv C_{gi}/C_i$ .

Hence, in addition to large mutual capacitances renormalizing a coupled island's lever arm by increasing  $C_i$ , there is an additional renormalization factor due to mutual capacitances increasing the effective lever arm. The lowest-order of the latter corrections are multiplied by the cross-capacitive lever arms  $\alpha_j \ll 1$ , however. Note additionally that as  $V_g$  tunes the islands near an inter-dot charge transition between islands  $i$  and  $j$ , the transfer of an electron by this tuning implies  $d\langle \hat{n}_i \rangle / dV_g \approx -d\langle \hat{n}_j \rangle / dV_g$  so that cross-capacitances  $C_{gj}$  between the gate voltage and islands other than the island it is designed to sense suppresses the parametric capacitance signal at these transitions [125, 130]. From the slope of successive triple points across multiple inter-dot transitions, these cross capacitances are estimated to be negligible in the measured regimes of this experiment. In this limit, where  $V_g$  primarily couples to a single island  $i$ , but the island itself has relatively larger mutual capacitances to the other islands, we discard terms of the order  $C_{ij}\alpha_j/C_j$  for  $j \neq i$  but preserve terms to second order in  $C_{ij}/C_j$  when multiplied by  $\alpha_i \gg \alpha_j$ , leading to

$$C_p \sim \left( 1 + \sum_{j \neq i} \frac{C_{ij}^2}{C_i^2} \right) \alpha_i |e| \frac{d\langle \hat{n}_i \rangle}{dV_g} = \frac{1 + \sum_{j \neq i} C_{ij}^2 / C_i^2}{C_{ei} + C_{gi} + \sum_{j \neq i} C_{ij}} C_{gi} |e| \frac{d\langle \hat{n}_i \rangle}{dV_g} \quad \begin{array}{l} C_{ij}/C_i, \alpha_j \ll 1 \\ \alpha_j \ll C_{ij}/C_i \end{array} \quad (\text{D.7})$$

for all  $j \neq i$ .

# E

## CAPACITANCE OF A DOT WITH NORMAL AND SUPERCONDUCTING LEADS

Gonzalez-Zalba *et al* showed that a gate resonator coupled to a quantum dot with an electron resonantly tunneling to a normal lead experiences a measurable tunneling capacitance [129]. Since this capacitance depends on the density of states in the reservoir, the signal observed when the normal lead is replaced by a hard-gapped superconducting one is not trivial. Hence, we are motivated to investigate the analogous tunneling capacitance for a dot coupled to a superconducting lead in addition to a normal one, as the resonator signal contains information about the superconductor, particularly its density of states.

### THE MODEL

We follow Ref. [129] in applying a master equation approach to calculate electron tunneling dynamics between a single-orbital quantum dot with one normal and one superconducting contact, neglecting spin physics. The superconducting contact in our case is assumed to have a gap  $\Delta$  softened by a phenomenological Cooper pair breaking rate  $\gamma$  [145]. We further treat the dot-lead tunnel magnitudes as constant with respect to energy.

To calculate tunneling capacitance, we need to know the tunneling rates for electrons from the dot to each lead and vice versa. For weak tunneling amplitude  $t_c$  between individual states the dynamics follow Fermi's Golden Rule, written here as in Ref. [346] for tunneling between two sets of states  $A$  and  $B$ :

$$\Gamma_{A \rightarrow B} = \frac{2\pi}{\hbar} \int_{-\infty}^{+\infty} |t_c|^2 v_A(E - \mu_A) v_B(E - \mu_B) f(E - \mu_A) [1 - f(E - \mu_B)] dE \quad (\text{E.1})$$

where  $v_{A/B}(E)$  and  $\mu_{A/B}$  are the density of states and chemical potentials of state manifolds  $A$  and  $B$ , respectively, while  $f(x) = [1 + e^{x/k_B T}]^{-1}$  is the Fermi-Dirac distribution. The presence of the Fermi distribution implies the subsystem in question is thermally coupled to a reservoir of electrons which can occupy states depending on chemical potential and temperature. For a quantum dot with level spacing much larger than  $k_B T$ ,

we may assume that the level is *always full* when considering tunneling off the dot, and *always empty* for the opposite process. This is justified because in the limit of large level spacings, the only electrons energetically available to fill the dot orbital come from the secondary subsystem for which tunneling rates are being calculated. Hence, we either remove the first or second Fermi factor in eq. E.1 depending on if the dot represents system *A* or *B* respectively<sup>1</sup>.

For the superconducting reservoir's density of states, we use the phenomenologically broadened Dynes formula:

$$v_S(E) = v_S^0 \left| \operatorname{Re} \left[ \frac{E + i\gamma}{\sqrt{(E + i\gamma)^2 - \Delta^2}} \right] \right| \equiv v_S^0 \hat{v}_{SC}(E) \quad (\text{E.2})$$

which includes an imaginary energy scale  $\gamma$  related to pair breaking rates in the superconductor [145]. Not only is this relation more realistic than the ideal BCS density of states (obtained when  $\gamma \rightarrow 0$ ), it is useful for our calculations since it removes the singularity at  $E = \pm\Delta$ . Note also that in the limit  $\Delta \rightarrow 0$  and  $\gamma \rightarrow 0$  this density approaches a constant, as is assumed in Ref. [129]. For a quantum dot with a single (possibly degenerate) orbital of energy  $\epsilon$ , the density of states is simply a  $\delta$ -function:

$$v_D(E) = v_D^0 \delta(E - \epsilon) \quad (\text{E.3})$$

The prefactor  $v_D^0$  accounts for any degeneracy of the dot orbital due to *e.g.* spin. Meanwhile, for the normal contact we assume a constant density of states  $v_N$ . Inserting these expressions into eq. E.1 and removing the Fermi factors for the quantum dot, we find the rates:

$$\Gamma_{SC \rightarrow D} = \Gamma_0 f(\epsilon - \mu_S) \hat{v}_{SC}(\epsilon - \mu_S) \quad (\text{E.4})$$

$$\Gamma_{D \rightarrow SC} = \Gamma_0 [1 - f(\epsilon - \mu_S)] \hat{v}_{SC}(\epsilon - \mu_S) \quad (\text{E.5})$$

$$\Gamma_{N \rightarrow D} = \Gamma_0 \lambda f(\epsilon - \mu_N) \quad (\text{E.6})$$

$$\Gamma_{D \rightarrow N} = \Gamma_0 \lambda [1 - f(\epsilon - \mu_N)] \quad (\text{E.7})$$

Above, we defined the relative tunneling factor  $\lambda \equiv |t_c^N / t_c^S|^2 (v_N^0 / v_S^0)$  for brevity, where  $t_c^N$  ( $t_c^{SC}$ ) is the constant tunneling matrix element between the dot and the normal (superconducting) contact. We also defined the bare superconductor tunneling strength  $\Gamma_0 \equiv 2\pi |t_c^S|^2 v_S^0 v_D^0 / \hbar$ .

Because of the quantum dot's charging energy  $E_C$ , which we assume is much larger than all other energy scales in the system (except perhaps  $\Delta$ ), we can safely consider only a single electron tunneling in and out of the dot orbital. Parametric capacitance of electron tunneling depends on the change of average charge which under this assumption is equal to the change in the topmost orbital's occupation probability  $dP_1 / dV_g$ . The time dependent parametric capacitance is given by [129, 130]:

$$C_t(t) = e\alpha \frac{dP_1}{dV_g(t)} = -(e\alpha)^2 \frac{dP_1}{d\epsilon(t)} = - \left( \frac{(e\alpha)^2}{\epsilon_{\text{RF}} \omega \cos(\omega t)} \right) \dot{P}_1 \quad (\text{E.8})$$

<sup>1</sup>Note that this precise assumption is also used in the analogous calculation in [129].

Above, we have assumed that the dot gate voltage  $V_g$  oscillates at frequency  $\omega$  as  $V_g(t) = V_g^0 + V_g^{\text{RF}} \sin(\omega t)$  such that  $\varepsilon(t) = \varepsilon_0 + \varepsilon_{\text{RF}} \sin(\omega t)$ . We further used the relation  $\varepsilon_{\text{RF}} = -e\alpha V_g^{\text{RF}}$ , valid for small voltage oscillations on a quantum dot.

To calculate  $P_1$ , we use a master equation approach, and solve the phenomenological differential equations:

$$\begin{aligned} \dot{P}_1 &= \Gamma_{SC \rightarrow D}[1 - P_1] - \Gamma_{D \rightarrow SC}P_1 + \Gamma_{N \rightarrow D}[1 - P_1] - \Gamma_{D \rightarrow N}P_1 \\ &= \Gamma_{\text{in}}(t) - \Gamma_{\text{tot}}(t)P_1 \end{aligned} \quad (\text{E.9})$$

where above we applied conservation of probability  $P_0 + P_1 = 1$  and defined

$$\Gamma_{\text{in}} \equiv \Gamma_{SC \rightarrow D} + \Gamma_{N \rightarrow D} = \Gamma_0 [\hat{v}_{SC}(\varepsilon - \mu_S)f(\varepsilon - \mu_S) + \lambda f(\varepsilon - \mu_N)] \quad (\text{E.10})$$

$$\Gamma_{\text{tot}}(t) \equiv \Gamma_{SC \rightarrow D} + \Gamma_{D \rightarrow SC} + \Gamma_{N \rightarrow D} + \Gamma_{D \rightarrow N} = \Gamma_0 [\hat{v}_{SC}(\varepsilon - \mu_S) + \lambda] \quad (\text{E.11})$$

Since we are using a master equation approach, the parametric capacitance will only include contributions from tunneling (and not quantum) capacitance (hence why we labelled it  $C_t$ ), and  $C_t(t)$  will have to be time-averaged to calculate the effective capacitance:  $C_t \equiv \langle C_t(t) \rangle$ .

### EXACT SOLUTION FOR $C_t$

To calculate tunneling capacitance, we must first solve eq. E.9. Motivated by the solution in Ref. [129] where  $\Gamma_{\text{tot}}$  was a constant (as is the case here when  $\Delta, \gamma \rightarrow 0$ ), we seek solutions of the form

$$P_1(t) = f(t)e^{-\int_0^t \Gamma_{\text{tot}} dt'}. \quad (\text{E.12})$$

Substituting this ansatz into eq. E.9 yields  $\dot{f}(t) = \Gamma_{\text{in}}e^{\int_0^t \Gamma_{\text{tot}} dt'}$  which can be directly integrated to obtain the solution

$$P_1(t) = e^{-\int_0^t \Gamma_{\text{tot}}(t_1) dt_1} \int_0^t \Gamma_{\text{in}}(t_2) e^{\int_0^{t_2} \Gamma_{\text{tot}}(t_1) dt_1} dt_2 = \int_0^t \Gamma_{\text{in}}(t_2) e^{-\int_{t_2}^t \Gamma_{\text{tot}}(t_1) dt_1} dt_2, \quad (\text{E.13})$$

neglecting integration constants from initial conditions because they can only lead to transient terms, which we discard in favour of the longer term behaviour.

In order to calculate  $C_t$ , we now aim to simplify  $\dot{P}_1(t)$ . Differentiating the above solution yields

$$\dot{P}_1(t) = \Gamma_{\text{in}}(t) - \Gamma_{\text{tot}}(t) \int_0^t \Gamma_{\text{in}}(t_2) e^{-\int_{t_2}^t \Gamma_{\text{tot}}(t_1) dt_1} dt_2 \quad (\text{E.14})$$

We may now write down an exact form of the tunneling capacitance using eq. E.8 and averaging over one resonator cycle  $2\pi/\omega$ :

$$C_t = \frac{e\alpha}{2\pi V_g^{\text{RF}}} \int_0^{2\pi/\omega} \frac{\Gamma_{\text{in}}(t) - \Gamma_{\text{tot}}(t) \int_0^t \Gamma_{\text{in}}(t_2) e^{-\int_{t_2}^t \Gamma_{\text{tot}}(t_1) dt_1} dt_2}{\cos(\omega t)} dt \quad (\text{E.15})$$

### APPROXIMATE ANALYTICAL SOLUTION

In order to find an analytical solution to eq. E.15, we make the approximation that voltage oscillations are very small: valid at low enough RF powers. This is equivalent to assuming that  $\varepsilon_{\text{RF}}$  is the smallest energy scale of the system. Hence, we will Taylor expand eq. E.13 to first order in  $\varepsilon_{\text{RF}}$ . Firstly, we write expansions of the two main rates in our problem as

$$\Gamma_{\text{in}} \sim \Gamma_{\text{in}}^0 + \Gamma_{\text{in}}^{0'} \varepsilon_{\text{RF}} \sin(\omega t), \quad \Gamma_{\text{tot}} \sim \Gamma_{\text{tot}}^0 + \Gamma_{\text{tot}}^{0'} \varepsilon_{\text{RF}} \sin(\omega t), \quad \varepsilon_{\text{RF}} \sin(\omega t) \ll \Delta, k_B T, \quad (\text{E.16})$$

noting that in fact  $\Gamma_{\text{in}}$  and  $\Gamma_{\text{tot}}$  are only dependent on time through  $\varepsilon(t)$ , and where for brevity we defined  $g^0 \equiv f(x_0)$  and  $g^{0'} \equiv (dg/dx)|_{x=x_0}$  for any function  $g$ . We calculate the derivatives of these rates to be

$$\Gamma_{\text{in}}^{0'} = \Gamma_0 \left\{ -\text{sign}[\hat{v}_{\text{SC}}(\varepsilon - \mu_S)] \Delta^2 \text{Re} \left[ ((\varepsilon_0 - \mu_S + i\gamma)^2 - \Delta^2)^{-3/2} \right] f(\varepsilon_0 - \mu_S) \right. \\ \left. + \hat{v}_{\text{SC}}(\varepsilon_0 - \mu_S) f'(\varepsilon_0 - \mu_S) + \lambda f'(\varepsilon_0 - \mu_N) \right\}, \quad (\text{E.17})$$

$$\Gamma_{\text{tot}}^{0'} = -\text{sign}[\hat{v}_{\text{SC}}(\varepsilon - \mu_S)] \Delta^2 \Gamma_0 \text{Re} \left[ ((\varepsilon_0 - \mu_S + i\gamma)^2 - \Delta^2)^{-3/2} \right], \quad (\text{E.18})$$

where  $f'(E) = -e^{E/k_B T} / [k_B T (1 + e^{E/k_B T})^2]$  is the derivative of the Fermi-Dirac distribution. Substituting this expression into eq. E.13, we find to first order in  $\varepsilon_{\text{RF}}$

$$P_1(t) \sim e^{-\Gamma_{\text{tot}}^0 t} \int_0^t e^{\Gamma_{\text{tot}}^0 t'} \left\{ \Gamma_{\text{in}}^0 \left[ 1 + \frac{\Gamma_{\text{tot}}^{0'} \varepsilon_{\text{RF}}}{\omega} (\cos(\omega t) - \cos(\omega t')) \right] + \Gamma_{\text{in}}^{0'} \varepsilon_{\text{RF}} \sin(\omega t') \right\} dt'. \quad (\text{E.19})$$

The above integrals can be analytically evaluated by writing all trigonometric functions in terms of exponential functions. The result is

$$P_1(t) \sim \frac{(\Gamma_{\text{tot}}^0 \sin(\omega t) - \omega \cos(\omega t)) \Gamma_{\text{in}}^{0'} \varepsilon_{\text{RF}} - (\Gamma_{\text{tot}}^0 \cos(\omega t) + \omega \sin(\omega t)) \Gamma_{\text{in}}^0 \Gamma_{\text{tot}}^{0'} \varepsilon_{\text{RF}} / \omega}{(\Gamma_{\text{tot}}^0)^2 + \omega^2} \\ + \frac{\Gamma_{\text{in}}^0}{\Gamma_{\text{tot}}^0} \left( 1 + \frac{\Gamma_{\text{tot}}^{0'} \varepsilon_{\text{RF}}}{\omega} \cos(\omega t) \right) \quad t \rightarrow \infty. \quad (\text{E.20})$$

Since we only care about long term behaviour independent of initial conditions, we discarded all transient  $e^{-\Gamma_{\text{tot}}^0 t}$  terms. To calculate the time averaged tunneling capacitance from the above result, we insert it into eq. E.8 and average over time. In this calculation we used the fact that the average of any trigonometric function or its reciprocal over one period is zero. Finally, this leads to the result

$$C_t \equiv \langle C_t(t) \rangle = (e\alpha)^2 \frac{\Gamma_{\text{in}}^0 \Gamma_{\text{tot}}^{0'} - \Gamma_{\text{tot}}^0 \Gamma_{\text{in}}^{0'}}{(\Gamma_{\text{tot}}^0)^2 + \omega^2} \quad (\text{E.21})$$

with rates and their derivatives given by eqs. E.10, E.11, E.17, and E.18.

## SISYPHUS RESISTANCE

To obtain an equivalent parallel resistance describing dissipation from the gate into the dot-lead system, we follow the more general theory of Esterli *et al* [125]. As we neglect any cross capacitance between the dot and lead, the current through the gate  $I_g$  may be written as (see equation 3 of [125])

$$I_g = C_{\text{geom}} \frac{dV_g}{dt} - (e\alpha) \frac{dP_1}{dt}, \quad (\text{E.22})$$

where  $C_{\text{geom}}$  represents the classical ‘geometric’ capacitance of the gate. Since we wish to calculate the equivalent impedance of our circuit, we would like to write the right hand side of the above expressions as a sum of terms proportional to  $V_g$  (representing a parallel resistance) and terms proportional to  $dV_g/dt$  (representing a parallel capacitance).

To this end, we begin by differentiating  $P_1(t)$ :

$$\frac{dP_1}{dt} = \left[ \frac{\omega^2 \left( \Gamma_{\text{in}}^{0'} \Gamma_{\text{tot}}^0 - \Gamma_{\text{in}}^0 \Gamma_{\text{tot}}^{0'} \right)}{\Gamma_{\text{tot}}^0 \left( (\Gamma_{\text{tot}}^0)^2 + \omega^2 \right)} \right] \varepsilon_{\text{RF}} \sin(\omega t) + \left[ \frac{\Gamma_{\text{tot}}^0 \Gamma_{\text{in}}^{0'} - \Gamma_{\text{in}}^0 \Gamma_{\text{tot}}^{0'}}{(\Gamma_{\text{tot}}^0)^2 + \omega^2} \right] \omega \varepsilon_{\text{RF}} \cos(\omega t). \quad (\text{E.23})$$

Recalling that for small changes in voltage  $V_g^{\text{RF}}$ , we have  $e\alpha V_g^{\text{RF}} = \varepsilon_{\text{RF}}$ , we can identify the first term above as being proportional to the gate voltage up to a constant since  $\varepsilon_{\text{RF}} \sin(\omega t) \sim e\alpha (V_g(t) - V_g^0)$ . Similarly, we have that  $e\alpha dV_g/dt = \omega \varepsilon_{\text{RF}} \cos(\omega t)$  so

$$I_g = C_{\text{geom}} \frac{dV_g}{dt} + \underbrace{(e\alpha)^2 \left[ \frac{\Gamma_{\text{in}}^0 \Gamma_{\text{tot}}^{0'} - \Gamma_{\text{tot}}^0 \Gamma_{\text{in}}^{0'}}{(\Gamma_{\text{tot}}^0)^2 + \omega^2} \right]}_{C_t} \frac{dV_g}{dt} + \underbrace{(e\alpha)^2 \left[ \frac{\omega^2 \left( \Gamma_{\text{in}}^0 \Gamma_{\text{tot}}^{0'} - \Gamma_{\text{tot}}^0 \Gamma_{\text{in}}^{0'} \right)}{\Gamma_{\text{tot}}^0 \left( (\Gamma_{\text{tot}}^0)^2 + \omega^2 \right)} \right]}_{\equiv 1/R_{\text{sis}}} V_g. \quad (\text{E.24})$$

Hence, we see that our dot’s impedance as seen from the gate contains three contributions in parallel. The classical geometric capacitance  $C_{\text{geom}}$  the semi-classical tunneling capacitance  $C_t$ , and the Sisyphus resistance  $R_{\text{sis}}$

$$R_{\text{sis}} = \frac{\Gamma_{\text{tot}}^0}{(e\alpha\omega)^2} \left( \frac{(\Gamma_{\text{tot}}^0)^2 + \omega^2}{\Gamma_{\text{in}}^0 \Gamma_{\text{tot}}^{0'} - \Gamma_{\text{tot}}^0 \Gamma_{\text{in}}^{0'}} \right). \quad (\text{E.25})$$

Notably,  $1/R_{\text{sis}}$  is simply  $C_t$  multiplied by  $\omega^2/\Gamma_{\text{tot}}^0$ .



# F

## FERMIONIC SIMULATION OF A FLOATING HYBRID TRIPLE QUANTUM DOT

In this appendix, we justify a Hamiltonian employed to describe a floating system of two quantum dots coupled via a central hybrid superconducting island. For simplicity, we consider a single spinful orbital of annihilation operator  $\hat{c}_{\alpha\sigma}$  on each quantum dot and island, labeled with spin  $\sigma \in \{\downarrow, \uparrow\}$  and with  $\alpha \in \{L, M, R\}$  for the left QD, middle island, or right QD respectively, as in Fig. 7.3(a). The hybrid island consists both of a QD level  $\hat{c}_{M\sigma}$  and the floating piece of superconducting material proximitizing it. This superconductor causes the dot level to form an ABS  $\hat{\gamma}$  at energy  $E_0$  such that  $\hat{c}_{M\sigma} = u^* \hat{\gamma}_\sigma + \sigma v \hat{\gamma}_\sigma^\dagger$  for some coherence factors  $u$  and  $v$  such that  $\sqrt{|u|^2 + |v|^2} = 1$  [60]. Here we define  $\sigma = \uparrow \equiv +1$  and similarly  $\sigma = \downarrow \equiv -1$ . Additionally, the superconducting shell's Cooper pairs contribute to the total island charging energy. As the system has conserved charge, the fixed charge constraint on this island may be written as  $\hat{n}_M = N - \hat{n}_L - \hat{n}_R$  where  $N$  is the total system charge and  $\hat{n}_\alpha \equiv \sum_\sigma \hat{n}_{\alpha\sigma} = \sum_\sigma \hat{c}_{\alpha\sigma}^\dagger \hat{c}_{\alpha\sigma}$  are the fermions' charge operators. Notably, this constraint equation for  $\hat{n}_M$  does not involve  $\hat{c}_{M\sigma}$  at all on the right hand side. To fully apply the constraint of fixed total charge, then, we must further project the system onto states for which the ABS' parity matches the overall island parity [73, 74]. We do so by applying the projection operator

$$\hat{P} = \frac{1}{4} \left[ (-1)^{\hat{n}_M} + (-1)^{N - \hat{n}_L - \hat{n}_R} \right]^2 \quad (\text{E.1})$$

to the full system Hamiltonian

$$\begin{aligned} \hat{H} = & \sum_{\alpha=L,R} E_C^\alpha (\hat{n}_\alpha - n_{g\alpha})^2 + E_C^M (N - \hat{n}_L - \hat{n}_R - n_{gM})^2 + E_0 \sum_\sigma \hat{\gamma}_\sigma^\dagger \hat{\gamma}_\sigma \\ & + \sum_\alpha E_Z^\alpha \hat{n}_{\alpha\downarrow} + \sum_{\sigma,\alpha} \left( t_\alpha \hat{c}_{\alpha\sigma}^\dagger \hat{c}_{M\sigma} + \text{h.c.} \right) + \sum_\alpha \left[ t_\alpha^{\text{so}} \left( \hat{c}_{\alpha\downarrow}^\dagger \hat{c}_{M\downarrow} - \hat{c}_{\alpha\downarrow}^\dagger \hat{c}_{M\uparrow} \right) + \text{h.c.} \right]. \end{aligned} \quad (\text{E.2})$$

This Hamiltonian is similar to that of Ref. [337], but with our charge constraint included, and where we presuppose the existence of an ABS with some electron- and hole-like coherence factors [60, 113], rather than modeling the ABS as a QD orbital proximitized by

a pairing potential. Above,  $E_C^\alpha$  are the charging energies of each QD,  $n_{g\alpha}$  are the reduced gate charges [22],  $E_Z^\alpha$  are Zeeman splittings of each level,  $t_\alpha$  is the spin-conserving tunneling amplitude between QD  $\alpha$  and QD M, and  $t_\alpha^{\text{so}}$  is the spin-flipping tunneling arising due to spin-orbit coupling [347].

To numerically diagonalize the Hamiltonian, we write the fermionic operators in matrix form as

$$\hat{c}_{L\sigma}^\dagger = \hat{f}_\sigma^\dagger \otimes \hat{\Lambda} \otimes \hat{\Lambda}, \quad \hat{\gamma}_\sigma^\dagger = \hat{I} \otimes \hat{f}_\sigma^\dagger \otimes \hat{\Lambda}, \quad \hat{c}_{R\sigma}^\dagger = \hat{I} \otimes \hat{I} \otimes \hat{f}_\sigma^\dagger \quad (\text{E.3})$$

where  $\hat{I}$  denotes the identity matrix for a single  $\alpha$  state subspace, and the other matrices are given by

$$\hat{f}_\uparrow^\dagger = \begin{pmatrix} 0 & 0 & 0 & 0 \\ 0 & 0 & 0 & 0 \\ 1 & 0 & 0 & 0 \\ 0 & 1 & 0 & 0 \end{pmatrix}, \quad \hat{f}_\downarrow^\dagger = \begin{pmatrix} 0 & 0 & 0 & 0 \\ 1 & 0 & 0 & 0 \\ 0 & 0 & 0 & 0 \\ 0 & 0 & -1 & 0 \end{pmatrix}, \quad \hat{\Lambda} = \begin{pmatrix} 1 & 0 & 0 & 0 \\ 0 & -1 & 0 & 0 \\ 0 & 0 & -1 & 0 \\ 0 & 0 & 0 & 1 \end{pmatrix} \quad (\text{E.4})$$

in the basis  $\{|0\rangle, \hat{f}_\uparrow^\dagger |0\rangle, \hat{f}_\downarrow^\dagger |0\rangle, \hat{f}_\uparrow^\dagger \hat{f}_\downarrow^\dagger |0\rangle\}$ . The matrix  $\hat{\Lambda}$  and minus signs in the definition of  $\hat{f}_\downarrow^\dagger$  are included to ensure all operators satisfy the fermionic anticommutation relations.

## BIBLIOGRAPHY

1. Nielsen, M. & Chuang, I. *Quantum Computation and Quantum Information: 10th Anniversary Edition* ISBN: 9781139495486. <https://books.google.nl/books?id=-s4DEy7o-a0C> (Cambridge University Press, 2010).
2. Krantz, P., Kjaergaard, M., Yan, F., Orlando, T. P., Gustavsson, S. & Oliver, W. D. A quantum engineer's guide to superconducting qubits. *Applied Physics Reviews* **6**, 021318. ISSN: 1931-9401. doi:[10.1063/1.5089550](https://doi.org/10.1063/1.5089550) (June 2019).
3. Kjaergaard, M., Schwartz, M. E., Braumüller, J., Krantz, P., Wang, J. I.-J., Gustavsson, S. & Oliver, W. D. Superconducting Qubits: Current State of Play. *Annual Review of Condensed Matter Physics* **11**, 369–395. ISSN: 1947-5462. doi:[10.1146/annurev-conmatphys-031119-050605](https://doi.org/10.1146/annurev-conmatphys-031119-050605) (Mar. 2020).
4. Blais, A., Huang, R.-S., Wallraff, A., Girvin, S. M. & Schoelkopf, R. J. Cavity quantum electrodynamics for superconducting electrical circuits: An architecture for quantum computation. *Physical Review A* **69**, 062320. doi:[10.1103/physreva.69.062320](https://doi.org/10.1103/physreva.69.062320) (June 2004).
5. Blais, A., Grimsmo, A. L., Girvin, S. & Wallraff, A. Circuit quantum electrodynamics. *Reviews of Modern Physics* **93**. doi:[10.1103/revmodphys.93.025005](https://doi.org/10.1103/revmodphys.93.025005) (May 2021).
6. Ihn, T. *Semiconductor Nanostructures: Quantum States and Electronic Transport* ISBN: 9780199534432 (Oxford University Press Inc., 2010).
7. Lutchyn, R. M., Sau, J. D. & Sarma, S. D. Majorana Fermions and a Topological Phase Transition in Semiconductor-Superconductor Heterostructures. *Physical Review Letters* **105**, 077001. doi:[10.1103/physrevlett.105.077001](https://doi.org/10.1103/physrevlett.105.077001) (Aug. 2010).
8. Oreg, Y., Refael, G. & von Oppen, F. Helical Liquids and Majorana Bound States in Quantum Wires. *Physical Review Letters* **105**, 177002. doi:[10.1103/physrevlett.105.177002](https://doi.org/10.1103/physrevlett.105.177002) (Oct. 2010).
9. Majorana, E. Teoria simmetrica dell'elettrone e del positrone. *Il Nuovo Cimento* **14**, 171–184. ISSN: 1827-6121. doi:[10.1007/bf02961314](https://doi.org/10.1007/bf02961314) (Apr. 1937).
10. Plugge, S., Rasmussen, A., Egger, R. & Flensberg, K. Majorana box qubits. *New Journal of Physics* **19**, 012001. doi:[10.1088/1367-2630/aa54e1](https://doi.org/10.1088/1367-2630/aa54e1) (Jan. 2017).
11. Karzig, T., Knapp, C., Lutchyn, R. M., Bonderson, P., Hastings, M. B., Nayak, C., Alicea, J., Flensberg, K., Plugge, S., Oreg, Y., Marcus, C. M. & Freedman, M. H. Scalable designs for quasiparticle-poisoning-protected topological quantum computation with Majorana zero modes. *Physical Review B* **95**. doi:[10.1103/physrevb.95.235305](https://doi.org/10.1103/physrevb.95.235305) (June 2017).

12. Schoelkopf, R. J., Wahlgren, P., Kozhevnikov, A. A., Delsing, P. & Prober, D. E. The Radio-Frequency Single-Electron Transistor (RF-SET): A Fast and Ultrasensitive Electrometer. *Science* **280**, 1238–1242. doi:[10.1126/science.280.5367.1238](https://doi.org/10.1126/science.280.5367.1238) (May 1998).
13. Vigneau, F., Fedele, F., Chatterjee, A., Reilly, D., Kuemmeth, F., Gonzalez-Zalba, M. F., Laird, E. & Ares, N. Probing quantum devices with radio-frequency reflectometry. *Applied Physics Reviews* **10**. doi:[10.1063/5.0088229](https://doi.org/10.1063/5.0088229) (Feb. 2023).
14. Liu, C.-X., Pan, H., Setiawan, F., Wimmer, M. & Sau, J. D. Fusion protocol for Majorana modes in coupled quantum dots. *Physical Review B* **108**. ISSN: 2469-9969. doi:[10.1103/physrevb.108.085437](https://doi.org/10.1103/physrevb.108.085437) (Aug. 2023).
15. Riwar, R.-P., Houzet, M., Meyer, J. S. & Nazarov, Y. V. Multi-terminal Josephson junctions as topological matter. *Nature Communications* **7**. doi:[10.1038/ncomms11167](https://doi.org/10.1038/ncomms11167) (Apr. 2016).
16. Christian G. Prosko. *Data repository for Chapters 2 and 7 of “Hybridization of Localized States in Semiconducting and Superconducting Circuits”* 2024. doi:[10.5281/zenodo.10615526](https://doi.org/10.5281/zenodo.10615526).
17. Bachtold, A., Moser, J. & Dykman, M. Mesoscopic physics of nanomechanical systems. *Reviews of Modern Physics* **94**. doi:[10.1103/revmodphys.94.045005](https://doi.org/10.1103/revmodphys.94.045005) (Dec. 2022).
18. Pekola, J. P. Towards quantum thermodynamics in electronic circuits. *Nature Physics* **11**, 118–123. doi:[10.1038/nphys3169](https://doi.org/10.1038/nphys3169) (Feb. 2015).
19. Tinkham, M. *Introduction to superconductivity* 2nd ed. ISBN: 0486435032 (Dover publications, inc., 1996).
20. Kouwenhoven, L. P., Marcus, C. M., McEuen, P. L., Tarucha, S., Westervelt, R. M. & Wingreen, N. S. in *Mesoscopic Electron Transport* 105–214 (Springer Netherlands, 1997). doi:[10.1007/978-94-015-8839-3\\_4](https://doi.org/10.1007/978-94-015-8839-3_4).
21. Kouwenhoven, L. P., Austing, D. G. & Tarucha, S. Few-electron quantum dots. *Reports on Progress in Physics* **64**, 701–736. ISSN: 1361-6633. doi:[10.1088/0034-4885/64/6/201](https://doi.org/10.1088/0034-4885/64/6/201) (May 2001).
22. Van der Wiel, W. G., Franceschi, S. D., Elzerman, J. M., Fujisawa, T., Tarucha, S. & Kouwenhoven, L. P. Electron transport through double quantum dots. *Reviews of Modern Physics* **75**, 1–22. doi:[10.1103/revmodphys.75.1](https://doi.org/10.1103/revmodphys.75.1) (Dec. 2002).
23. Hanson, R., Kouwenhoven, L. P., Petta, J. R., Tarucha, S. & Vandersypen, L. M. K. Spins in few-electron quantum dots. *Reviews of Modern Physics* **79**, 1217–1265. doi:[10.1103/revmodphys.79.1217](https://doi.org/10.1103/revmodphys.79.1217) (Oct. 2007).
24. Koch, J., Yu, T. M., Gambetta, J., Houck, A. A., Schuster, D. I., Majer, J., Blais, A., Devoret, M. H., Girvin, S. M. & Schoelkopf, R. J. Charge-insensitive qubit design derived from the Cooper pair box. *Physical Review A* **76**. doi:[10.1103/physreva.76.042319](https://doi.org/10.1103/physreva.76.042319) (Oct. 2007).
25. Pavešić, L. & Žitko, R. Qubit based on spin-singlet Yu-Shiba-Rusinov states. *Physical Review B* **105**. ISSN: 2469-9969. doi:[10.1103/physrevb.105.075129](https://doi.org/10.1103/physrevb.105.075129) (Feb. 2022).

26. Fulton, T. A. & Dolan, G. J. Observation of single-electron charging effects in small tunnel junctions. *Physical Review Letters* **59**, 109–112. doi:[10 . 1103 / physrevlett.59.109](https://doi.org/10.1103/physrevlett.59.109) (July 1987).
27. Zimmerli, G., Eiles, T. M., Kautz, R. L. & Martinis, J. M. Noise in the Coulomb blockade electrometer. *Applied Physics Letters* **61**, 237–239. ISSN: 1077-3118. doi:[10 . 1063/1.108195](https://doi.org/10.1063/1.108195) (June 1992).
28. Meirav, U & Foxman, E. B. Single-electron phenomena in semiconductors. *Semiconductor Science and Technology* **11**, 255–284. doi:[10 . 1088/0268-1242/11/3/003](https://doi.org/10.1088/0268-1242/11/3/003) (Mar. 1996).
29. McEuen, P. L., Foxman, E. B., Meirav, U., Kastner, M. A., Meir, Y., Wingreen, N. S. & Wind, S. J. Transport spectroscopy of a Coulomb island in the quantum Hall regime. *Physical Review Letters* **66**, 1926–1929. doi:[10 . 1103/physrevlett.66.1926](https://doi.org/10.1103/physrevlett.66.1926) (Apr. 1991).
30. Ashoori, R., Stormer, H., Weiner, J., Pfeiffer, L., Baldwin, K. & West, K. Energy levels of an artificial atom probed with single-electron capacitance spectroscopy. *Surface Science* **305**, 558–565. doi:[10.1016/0039-6028\(94\)90953-9](https://doi.org/10.1016/0039-6028(94)90953-9) (Mar. 1994).
31. Tarucha, S., Austing, D. G., Honda, T., van der Hage, R. J. & Kouwenhoven, L. P. Shell Filling and Spin Effects in a Few Electron Quantum Dot. *Physical Review Letters* **77**, 3613–3616. doi:[10.1103/physrevlett.77.3613](https://doi.org/10.1103/physrevlett.77.3613) (Oct. 1996).
32. Stewart, D. R., Sprinzak, D., Marcus, C. M., Duruöz, C. I. & Harris, J. S. Correlations Between Ground and Excited State Spectra of a Quantum Dot. *Science* **278**, 1784–1788. doi:[10.1126/science.278.5344.1784](https://doi.org/10.1126/science.278.5344.1784) (Dec. 1997).
33. Averin, D. V., Korotkov, A. N. & Likharev, K. K. Theory of single-electron charging of quantum wells and dots. *Physical Review B* **44**, 6199–6211. doi:[10 . 1103/physrevb.44.6199](https://doi.org/10.1103/physrevb.44.6199) (Sept. 1991).
34. Fujisawa, T., Austing, D. G., Tokura, Y., Hirayama, Y. & Tarucha, S. Nonequilibrium Transport through a Vertical Quantum Dot in the Absence of Spin-Flip Energy Relaxation. *Physical Review Letters* **88**. ISSN: 1079-7114. doi:[10 . 1103 / physrevlett.88.236802](https://doi.org/10.1103/physrevlett.88.236802) (May 2002).
35. Gehring, P., Sowa, J. K., Cremers, J., Wu, Q., Sadeghi, H., Sheng, Y., Warner, J. H., Lambert, C. J., Briggs, G. A. D. & Mol, J. A. Distinguishing Lead and Molecule States in Graphene-Based Single-Electron Transistors. *ACS Nano* **11**, 5325–5331. ISSN: 1936-086X. doi:[10.1021/acsnano.7b00570](https://doi.org/10.1021/acs.nano.7b00570) (Apr. 2017).
36. Thomas, F. S., Nilsson, M., Ciaccia, C., Jünger, C., Rossi, F., Zannier, V., Sorba, L., Baumgartner, A. & Schönenberger, C. Spectroscopy of the local density of states in nanowires using integrated quantum dots. *Physical Review B* **104**. ISSN: 2469-9969. doi:[10.1103/physrevb.104.115415](https://doi.org/10.1103/physrevb.104.115415) (Sept. 2021).
37. De Jong, D. *Gate-based readout of hybrid quantum dot systems* PhD thesis (Delft University of Technology, 2021). <https://doi.org/10.4233/uuid:9cd36947-5e27-4436-9bbb-d7fc5daa6047>.

38. Prosko, C. G. *Dispersive Gate Sensing of Hybrid Quantum Dot Systems* MSc Thesis (Delft University of Technology, 2019). <http://resolver.tudelft.nl/uuid:c1219ece-a3e0-4533-a7e0-13dfc79eb25f>.
39. Chan, I. H., Westervelt, R. M., Maranowski, K. D. & Gossard, A. C. Strongly capacitively coupled quantum dots. *Applied Physics Letters* **80**, 1818–1820. ISSN: 1077-3118. doi:[10.1063/1.1456552](https://doi.org/10.1063/1.1456552) (Mar. 2002).
40. Oosterkamp, T. H., Fujisawa, T., van der Wiel, W. G., Ishibashi, K., Hijman, R. V., Tarucha, S. & Kouwenhoven, L. P. Microwave spectroscopy of a quantum-dot molecule. *Nature* **395**, 873–876. ISSN: 1476-4687. doi:[10.1038/27617](https://doi.org/10.1038/27617) (Oct. 1998).
41. Hayashi, T., Fujisawa, T., Cheong, H. D., Jeong, Y. H. & Hirayama, Y. Coherent Manipulation of Electronic States in a Double Quantum Dot. *Physical Review Letters* **91**. ISSN: 1079-7114. doi:[10.1103/physrevlett.91.226804](https://doi.org/10.1103/physrevlett.91.226804) (Nov. 2003).
42. Gorman, J., Hasko, D. G. & Williams, D. A. Charge-Qubit Operation of an Isolated Double Quantum Dot. *Physical Review Letters* **95**. ISSN: 1079-7114. doi:[10.1103/physrevlett.95.090502](https://doi.org/10.1103/physrevlett.95.090502) (Aug. 2005).
43. Petersson, K. D., Petta, J. R., Lu, H. & Gossard, A. C. Quantum Coherence in a One-Electron Semiconductor Charge Qubit. *Physical Review Letters* **105**. ISSN: 1079-7114. doi:[10.1103/physrevlett.105.246804](https://doi.org/10.1103/physrevlett.105.246804) (Dec. 2010).
44. Gaudreau, L., Studenikin, S. A., Sachrajda, A. S., Zawadzki, P., Kam, A., Lapointe, J., Korkusinski, M. & Hawrylak, P. Stability Diagram of a Few-Electron Triple Dot. *Physical Review Letters* **97**. ISSN: 1079-7114. doi:[10.1103/physrevlett.97.036807](https://doi.org/10.1103/physrevlett.97.036807) (June 2006).
45. Bardeen, J., Cooper, L. N. & Schrieffer, J. R. Theory of Superconductivity. *Physical Review* **108**, 1175–1204. doi:[10.1103/physrev.108.1175](https://doi.org/10.1103/physrev.108.1175) (Dec. 1957).
46. Bretheau, L. *Localized Excitations in Superconducting Atomic Contacts: PROBING THE ANDREEV DOUBLET* PhD thesis (École Polytechnique X, 2013). <https://pastel.hal.science/pastel-00862029>.
47. Prada, E., San-Jose, P., de Moor, M. W. A., Geresdi, A., Lee, E. J. H., Klinovaja, J., Loss, D., Nygård, J., Aguado, R. & Kouwenhoven, L. P. From Andreev to Majorana bound states in hybrid superconductor–semiconductor nanowires. *Nature Reviews Physics* **2**, 575–594. doi:[10.1038/s42254-020-0228-y](https://doi.org/10.1038/s42254-020-0228-y) (Sept. 2020).
48. Meng, T., Florens, S. & Simon, P. Self-consistent description of Andreev bound states in Josephson quantum dot devices. *Physical Review B* **79**. doi:[10.1103/physrevb.79.224521](https://doi.org/10.1103/physrevb.79.224521) (June 2009).
49. Balatsky, A. V., Vekhter, I. & Zhu, J.-X. Impurity-induced states in conventional and unconventional superconductors. *Reviews of Modern Physics* **78**, 373–433. ISSN: 1539-0756. doi:[10.1103/revmodphys.78.373](https://doi.org/10.1103/revmodphys.78.373) (May 2006).
50. Luh, Y. Bound state in superconductors with paramagnetic impurities. *Acta Physica Sinica* **21**, 75. ISSN: 1000-3290. doi:[10.7498/aps.21.75](https://doi.org/10.7498/aps.21.75) (1965).
51. Shiba, H. Classical Spins in Superconductors. *Progress of Theoretical Physics* **40**, 435–451. doi:[10.1143/ptp.40.435](https://doi.org/10.1143/ptp.40.435) (Sept. 1968).

52. Rusinov, A. I. On the Theory of Gapless Superconductivity in Alloys Containing Paramagnetic Impurities. *Soviet Journal of Experimental and Theoretical Physics* **29**, 1101 (Jan. 1969).
53. Pillet, J.-D., Quay, C. H. L., Morfin, P., Bena, C., Yeyati, A. L. & Joyez, P. Andreev bound states in supercurrent-carrying carbon nanotubes revealed. *Nature Physics* **6**, 965–969. ISSN: 1745-2481. doi:[10.1038/nphys1811](https://doi.org/10.1038/nphys1811) (Nov. 2010).
54. Jünger, C., Lehmann, S., Dick, K. A., Thelander, C., Schönenberger, C. & Baumgartner, A. Intermediate states in Andreev bound state fusion. *Communications Physics* **6**. doi:[10.1038/s42005-023-01273-2](https://doi.org/10.1038/s42005-023-01273-2) (July 2023).
55. Van Driel, D., Roovers, B., Zatelli, F., Bordin, A., Wang, G., van Loo, N., Wolff, J. C., Mazur, G. P., Gazibegovic, S., Badawy, G., Bakkers, E. P., Kouwenhoven, L. P. & Dvir, T. Charge Sensing the Parity of an Andreev Molecule. *PRX Quantum* **5**. ISSN: 2691-3399. doi:[10.1103/prxquantum.5.020301](https://doi.org/10.1103/prxquantum.5.020301) (Apr. 2024).
56. Lafarge, P., Joyez, P., Esteve, D., Urbina, C. & Devoret, M. H. Two-electron quantization of the charge on a superconductor. *Nature* **365**, 422–424. doi:[10.1038/365422a0](https://doi.org/10.1038/365422a0) (Sept. 1993).
57. Esteve, D., Lafarge, P., Joyez, P., Urbina, C. & Devoret, M. Measurement of the incremental charge of a superconducting island. *Physica B: Condensed Matter* **197**, 500–505. ISSN: 0921-4526. doi:[10.1016/0921-4526\(94\)90249-6](https://doi.org/10.1016/0921-4526(94)90249-6) (Mar. 1994).
58. Hergenrother, J. M., Tuominen, M. T. & Tinkham, M. Charge transport by Andreev reflection through a mesoscopic superconducting island. *Physical Review Letters* **72**, 1742–1745. ISSN: 0031-9007. doi:[10.1103/physrevlett.72.1742](https://doi.org/10.1103/physrevlett.72.1742) (Mar. 1994).
59. Higginbotham, A. P., Albrecht, S. M., Kiršanskas, G., Chang, W., Kuemmeth, F., Krogstrup, P., Jespersen, T. S., Nygård, J., Flensberg, K. & Marcus, C. M. Parity lifetime of bound states in a proximitized semiconductor nanowire. *Nature Phys.* **11**, 1017 (2015).
60. Albrecht, S. M., Higginbotham, A. P., Madsen, M., Kuemmeth, F., Jespersen, T. S., Nygård, J., Krogstrup, P. & Marcus, C. M. Exponential protection of zero modes in Majorana islands. *Nature* **531**, 206–209. doi:[10.1038/nature17162](https://doi.org/10.1038/nature17162) (Mar. 2016).
61. Albrecht, S., Hansen, E., Higginbotham, A., Kuemmeth, F., Jespersen, T., Nygård, J., Krogstrup, P., Danon, J., Flensberg, K. & Marcus, C. Transport Signatures of Quasiparticle Poisoning in a Majorana Island. *Physical Review Letters* **118**. doi:[10.1103/physrevlett.118.137701](https://doi.org/10.1103/physrevlett.118.137701) (Mar. 2017).
62. Shen, J. *et al.* Parity transitions in the superconducting ground state of hybrid InSb-Al Coulomb islands. *Nature Communications* **9**. ISSN: 2041-1723. doi:[10.1038/s41467-018-07279-7](https://doi.org/10.1038/s41467-018-07279-7) (Nov. 2018).
63. Van Veen, J., Proutski, A., Karzig, T., Pikulin, D. I., Lutchyn, R. M., Nygård, J., Krogstrup, P., Geresdi, A., Kouwenhoven, L. P. & Watson, J. D. Magnetic-field-dependent quasiparticle dynamics of nanowire single-Cooper-pair transistors. *Physical Review B* **98**. doi:[10.1103/physrevb.98.174502](https://doi.org/10.1103/physrevb.98.174502) (Nov. 2018).

64. Van Veen, J., de Jong, D., Han, L., Prosko, C., Krogstrup, P., Watson, J. D., Kouwenhoven, L. P. & Pfaff, W. Revealing charge-tunneling processes between a quantum dot and a superconducting island through gate sensing. *Physical Review B* **100**, 174508. doi:[10.1103/physrevb.100.174508](https://doi.org/10.1103/physrevb.100.174508) (Nov. 2019).
65. Whiticar, A. M., Fornieri, A., O'Farrell, E. C. T., Drachmann, A. C. C., Wang, T., Thomas, C., Gronin, S., Kallaher, R., Gardner, G. C., Manfra, M. J., Marcus, C. M. & Nichele, F. Coherent transport through a Majorana island in an Aharonov-Bohm interferometer. *Nature Communications* **11**. ISSN: 2041-1723. doi:[10.1038/s41467-020-16988-x](https://doi.org/10.1038/s41467-020-16988-x) (June 2020).
66. Shen, J. *et al.* Full parity phase diagram of a proximitized nanowire island. *Physical Review B* **104**. ISSN: 2469-9969. doi:[10.1103/physrevb.104.045422](https://doi.org/10.1103/physrevb.104.045422) (July 2021).
67. Malinowski, F. K., Rupesh, R. K., Pavešić, L., Guba, Z., de Jong, D., Han, L., Prosko, C. G., Chan, M., Liu, Y., Krogstrup, P., Pályi, A., Žitko, R. & Koski, J. V. *Quantum capacitance of a superconducting subgap state in an electrostatically floating dot-island* 2022. arXiv: [2210.01519](https://arxiv.org/abs/2210.01519).
68. Estrada Saldaña, J. C., Vekris, A., Pavešić, L., Krogstrup, P., Žitko, R., Grover-Rasmussen, K. & Nygård, J. Excitations in a superconducting Coulombic energy gap. *Nature Communications* **13**. ISSN: 2041-1723. doi:[10.1038/s41467-022-29634-5](https://doi.org/10.1038/s41467-022-29634-5) (Apr. 2022).
69. Vaitiekėnas, S., Souto, R. S., Liu, Y., Krogstrup, P., Flensberg, K., Leijnse, M. & Marcus, C. M. Evidence for spin-polarized bound states in semiconductor-superconductor-ferromagnetic-insulator islands. *Physical Review B* **105**. ISSN: 2469-9969. doi:[10.1103/physrevb.105.1041304](https://doi.org/10.1103/physrevb.105.1041304) (Jan. 2022).
70. Valentini, M., Borovkov, M., Prada, E., Martí-Sánchez, S., Botifoll, M., Hofmann, A., Arbiol, J., Aguado, R., San-Jose, P. & Katsaros, G. Majorana-like Coulomb spectroscopy in the absence of zero-bias peaks. *Nature* **612**, 442–447. ISSN: 1476-4687. doi:[10.1038/s41586-022-05382-w](https://doi.org/10.1038/s41586-022-05382-w) (Dec. 2022).
71. Wang, J.-Y. *et al.* Supercurrent parity meter in a nanowire Cooper pair transistor. *Science Advances* **8**. ISSN: 2375-2548. doi:[10.1126/sciadv.abm9896](https://doi.org/10.1126/sciadv.abm9896) (Apr. 2022).
72. Hinderling, M., ten Kate, S. C., Haxell, D. Z., Coraiola, M., Paredes, S., Cheah, E., Krizek, F., Schott, R., Wegscheider, W., Sabonis, D. & Nichele, F. *Flip-chip-based fast inductive parity readout of a planar superconducting island* 2023. eprint: [2307.06718](https://arxiv.org/abs/2307.06718).
73. Fu, L. Electron Teleportation via Majorana Bound States in a Mesoscopic Superconductor. *Physical Review Letters* **104**. doi:[10.1103/physrevlett.104.056402](https://doi.org/10.1103/physrevlett.104.056402) (Feb. 2010).
74. Van Heck, B., Hassler, F., Akhmerov, A. R. & Beenakker, C. W. J. Coulomb stability of the  $4\pi$ -periodic Josephson effect of Majorana fermions. *Phys. Rev. B* **84**, 180502. doi:[10.1103/PhysRevB.84.180502](https://doi.org/10.1103/PhysRevB.84.180502) (18 Nov. 2011).
75. Béni, B. & Cooper, N. R. Topological Kondo Effect with Majorana Fermions. *Physical Review Letters* **109**. ISSN: 1079-7114. doi:[10.1103/physrevlett.109.156803](https://doi.org/10.1103/physrevlett.109.156803) (Oct. 2012).

76. Van Heck, B., Lutchyn, R. M. & Glazman, L. I. Conductance of a proximitized nanowire in the Coulomb blockade regime. *Physical Review B* **93**, 235431 (2016).
77. Hell, M., Flensberg, K. & Leijnse, M. Distinguishing Majorana bound states from localized Andreev bound states by interferometry. *Physical Review B* **97**. ISSN: 2469-9969. doi:[10.1103/physrevb.97.161401](https://doi.org/10.1103/physrevb.97.161401) (Apr. 2018).
78. Väyrynen, J. I., Feiguin, A. E. & Lutchyn, R. M. Signatures of topological ground state degeneracy in Majorana islands. *Physical Review Research* **2**. ISSN: 2643-1564. doi:[10.1103/physrevresearch.2.043228](https://doi.org/10.1103/physrevresearch.2.043228) (Nov. 2020).
79. Malinowski, F. K. *Two Anderson impurities coupled through a superconducting island: charge stability diagrams and double impurity qubit* 2023. arXiv: [2303.14410](https://arxiv.org/abs/2303.14410).
80. McMillan, W. L. Tunneling Model of the Superconducting Proximity Effect. *Physical Review* **175**, 537–542. doi:[10.1103/physrev.175.537](https://doi.org/10.1103/physrev.175.537) (Nov. 1968).
81. Sau, J. D., Lutchyn, R. M., Tewari, S. & Sarma, S. D. Generic New Platform for Topological Quantum Computation Using Semiconductor Heterostructures. *Physical Review Letters* **104**, 040502. doi:[10.1103/physrevlett.104.040502](https://doi.org/10.1103/physrevlett.104.040502) (Jan. 2010).
82. Alicea, J. Majorana fermions in a tunable semiconductor device. *Physical Review B* **81**. ISSN: 1550-235X. doi:[10.1103/physrevb.81.125318](https://doi.org/10.1103/physrevb.81.125318) (Mar. 2010).
83. Antipov, A. E., Bargerbos, A., Winkler, G. W., Bauer, B., Rossi, E. & Lutchyn, R. M. Effects of Gate-Induced Electric Fields on Semiconductor Majorana Nanowires. *Physical Review X* **8**. ISSN: 2160-3308. doi:[10.1103/physrevx.8.031041](https://doi.org/10.1103/physrevx.8.031041) (Aug. 2018).
84. Kitaev, A. Y. Unpaired Majorana fermions in quantum wires. *Physics-Uspekhi* **44**, 131–136. ISSN: 1468-4780. doi:[10.1070/1063-7869/44/10s/s29](https://doi.org/10.1070/1063-7869/44/10s/s29) (Oct. 2001).
85. Karzig, T., Cole, W. S. & Pikulin, D. I. Quasiparticle Poisoning of Majorana Qubits. *Physical Review Letters* **126**, 057702. doi:[10.1103/physrevlett.126.057702](https://doi.org/10.1103/physrevlett.126.057702) (Feb. 2021).
86. Sau, J. D. & Sarma, S. D. Realizing a robust practical Majorana chain in a quantum-dot-superconductor linear array. *Nature Communications* **3**. doi:[10.1038/ncomms1966](https://doi.org/10.1038/ncomms1966) (July 2012).
87. Leijnse, M. & Flensberg, K. Parity qubits and poor man's Majorana bound states in double quantum dots. *Phys. Rev. B* **86**, 134528. doi:[10.1103/PhysRevB.86.134528](https://doi.org/10.1103/PhysRevB.86.134528) (13 Oct. 2012).
88. Fulga, I. C., Haim, A., Akhmerov, A. R. & Oreg, Y. Adaptive tuning of Majorana fermions in a quantum dot chain. *New Journal of Physics* **15**, 045020. doi:[10.1088/1367-2630/15/4/045020](https://doi.org/10.1088/1367-2630/15/4/045020) (Apr. 2013).
89. Averin, D. V. & Nazarov, Y. V. Single-electron charging of a superconducting island. *Physical review letters* **69**, 1993 (1992).
90. Pavešić, L., Bauernfeind, D. & Žitko, R. Subgap states in superconducting islands. *Physical Review B* **104**. ISSN: 2469-9969. doi:[10.1103/physrevb.104.1241409](https://doi.org/10.1103/physrevb.104.1241409) (Dec. 2021).

91. Anderson, P. Theory of dirty superconductors. *Journal of Physics and Chemistry of Solids* **11**, 26–30. doi:[10.1016/0022-3697\(59\)90036-8](https://doi.org/10.1016/0022-3697(59)90036-8) (Sept. 1959).
92. Vlaic, S., Pons, S., Zhang, T., Assouline, A., Zimmers, A., David, C., Rodary, G., Girard, J.-C., Roditchev, D. & Aubin, H. Superconducting parity effect across the Anderson limit. *Nature Communications* **8**. doi:[10.1038/ncomms14549](https://doi.org/10.1038/ncomms14549) (Feb. 2017).
93. Nazarov, Y. V. & Blanter, Y. M. *Quantum Transport* doi:[10.1017/cbo9780511626906](https://doi.org/10.1017/cbo9780511626906) (Cambridge University Press, May 2009).
94. Averin, D. V., Korotkov, A. N., Manninen, A. J. & Pekola, J. P. Resonant Tunneling through a Macroscopic Charge State in a Superconducting Single Electron Transistor. *Physical Review Letters* **78**, 4821–4824. ISSN: 1079-7114. doi:[10.1103/physrevlett.78.4821](https://doi.org/10.1103/physrevlett.78.4821) (June 1997).
95. Esmail, A. A., Ferguson, A. J. & Lambert, N. J. Cooper pair tunnelling and quasi-particle poisoning in a galvanically isolated superconducting double dot. *Applied Physics Letters* **111**, 252602. doi:[10.1063/1.5009079](https://doi.org/10.1063/1.5009079) (2017).
96. Recher, P., Sukhorukov, E. V. & Loss, D. Andreev tunneling, Coulomb blockade, and resonant transport of nonlocal spin-entangled electrons. *Physical Review B* **63**, 165314. doi:[10.1103/physrevb.63.165314](https://doi.org/10.1103/physrevb.63.165314) (Apr. 2001).
97. Hofstetter, L., Csonka, S., Nygård, J. & Schönberger, C. Cooper pair splitter realized in a two-quantum-dot Y-junction. *Nature* **461**, 960–963. ISSN: 1476-4687. doi:[10.1038/nature08432](https://doi.org/10.1038/nature08432) (Oct. 2009).
98. Das, A., Ronen, Y., Heiblum, M., Mahalu, D., Kretinin, A. V. & Shtrikman, H. High-efficiency Cooper pair splitting demonstrated by two-particle conductance resonance and positive noise cross-correlation. *Nature Communications* **3**, 1165. doi:[10.1038/ncomms2169](https://doi.org/10.1038/ncomms2169) (Jan. 2012).
99. Baba, S, Jünger, C, Matsuo, S, Baumgartner, A, Sato, Y, Kamata, H, Li, K, Jeppesen, S, Samuelson, L, Xu, H. Q., Schönberger, C & Tarucha, S. Cooper-pair splitting in two parallel InAs nanowires. *New Journal of Physics* **20**, 063021. doi:[10.1088/1367-2630/aac74e](https://doi.org/10.1088/1367-2630/aac74e) (June 2018).
100. Bordoloi, A., Zannier, V., Sorba, L., Schönberger, C. & Baumgartner, A. Spin cross-correlation experiments in an electron entangler. *Nature* **612**, 454–458. doi:[10.1038/s41586-022-05436-z](https://doi.org/10.1038/s41586-022-05436-z) (Nov. 2022).
101. Wang, G., Dvir, T., Mazur, G. P., Liu, C.-X., van Loo, N., ten Haaf, S. L. D., Bordin, A., Gazibegovic, S., Badawy, G., Bakkers, E. P. A. M., Wimmer, M. & Kouwenhoven, L. P. Singlet and triplet Cooper pair splitting in hybrid superconducting nanowires. *Nature* **612**, 448–453. doi:[10.1038/s41586-022-05352-2](https://doi.org/10.1038/s41586-022-05352-2) (Nov. 2022).
102. Herrmann, L. G., Portier, F., Roche, P., Levy Yeyati, A., Kontos, T. & Strunk, C. Carbon nanotubes as Cooper-pair beam splitters. *Physical review letters* **104**, 026801 (2010).
103. Schindele, J., Baumgartner, A. & Schönberger, C. Near-Unity Cooper Pair Splitting Efficiency. *Physical Review Letters* **109**, 157002. doi:[10.1103/physrevlett.109.157002](https://doi.org/10.1103/physrevlett.109.157002) (Oct. 2012).

104. Kürtössy, O., Scherübl, Z., Fülöp, G., Lukács, I. E., Kanne, T., Nygård, J., Makk, P. & Csonka, S. Parallel InAs nanowires for Cooper pair splitters with Coulomb repulsion. *npj Quantum Materials* **7**. doi:[10.1038/s41535-022-00497-9](https://doi.org/10.1038/s41535-022-00497-9) (Sept. 2022).
105. Tan, Z., Cox, D., Nieminen, T., Lähteenmäki, P., Golubev, D., Lesovik, G. & Hakonen, P. Cooper Pair Splitting by Means of Graphene Quantum Dots. *Physical Review Letters* **114**, 096602. doi:[10.1103/physrevlett.114.096602](https://doi.org/10.1103/physrevlett.114.096602) (Mar. 2015).
106. Borzenets, I. V., Shimazaki, Y., Jones, G. F., Craciun, M. F., Russo, S., Yamamoto, M. & Tarucha, S. High Efficiency CVD Graphene-lead (Pb) Cooper Pair Splitter. *Scientific Reports* **6**, 23051. doi:[10.1038/srep23051](https://doi.org/10.1038/srep23051) (Mar. 2016).
107. Pandey, P., Danneau, R. & Beckmann, D. Ballistic Graphene Cooper Pair Splitter. *Phys. Rev. Lett.* **126**, 147701. doi:[10.1103/PhysRevLett.126.147701](https://doi.org/10.1103/PhysRevLett.126.147701) (14 Apr. 2021).
108. Wang, Q., ten Haaf, S. L. D., Kulesh, I., Xiao, D., Thomas, C., Manfra, M. J. & Goswami, S. Triplet correlations in Cooper pair splitters realized in a two-dimensional electron gas. *Nature Communications* **14**. ISSN: 2041-1723. doi:[10.1038/s41467-023-40551-z](https://doi.org/10.1038/s41467-023-40551-z) (Aug. 2023).
109. Deacon, R. S., Oiwa, A., Sailer, J., Baba, S., Kanai, Y., Shibata, K., Hirakawa, K. & Tarucha, S. Cooper pair splitting in parallel quantum dot Josephson junctions. *Nature communications* **6**, 7446. <https://www.nature.com/articles/ncomms8446> (2015).
110. Dehollain, Juan P. and Simmons, Stephanie and Muhonen, Juha T. and Kalra, Rachpon and Laucht, Arne and Hudson, Fay and Itoh, Kohei M. and Jamieson, David N. and McCallum, Jeffrey C. and Dzurak, Andrew S. and Morello, Andrea. Bell's inequality violation with spins in silicon. *Nature Nanotechnology* **11**, 242–246. ISSN: 1748-3395. doi:[10.1038/nnano.2015.262](https://doi.org/10.1038/nnano.2015.262) (Mar. 2016).
111. Braakman, F. R., Barthelemy, P., Reichl, C., Wegscheider, W. & Vandersypen, L. M. K. Long-distance coherent coupling in a quantum dot array. *Nature Nanotechnology* **8**, 432–437. doi:[10.1038/nnano.2013.67](https://doi.org/10.1038/nnano.2013.67) (Apr. 2013).
112. Schrieffer, J. R. & Wolff, P. A. Relation between the Anderson and Kondo Hamiltonians. *Physical Review* **149**, 491–492. doi:[10.1103/physrev.149.491](https://doi.org/10.1103/physrev.149.491) (Sept. 1966).
113. Liu, C.-X., Wang, G., Dvir, T. & Wimmer, M. Tunable Superconducting Coupling of Quantum Dots via Andreev Bound States in Semiconductor-Superconductor Nanowires. *Physical Review Letters* **129**. doi:[10.1103/physrevlett.129.267701](https://doi.org/10.1103/physrevlett.129.267701) (Dec. 2022).
114. Bordin, A., Wang, G., Liu, C.-X., ten Haaf, S. L., van Loo, N., Mazur, G. P., Xu, D., van Driel, D., Zatelli, F., Gazibegovic, S., Badawy, G., Bakkers, E. P., Wimmer, M., Kouwenhoven, L. P. & Dvir, T. Tunable Crossed Andreev Reflection and Elastic Co-tunneling in Hybrid Nanowires. *Physical Review X* **13**. ISSN: 2160-3308. doi:[10.1103/physrevx.13.031031](https://doi.org/10.1103/physrevx.13.031031) (Sept. 2023).

115. Liu, C.-X., Bozkurt, A. M., Zatelli, E., ten Haaf, S. L. D., Dvir, T. & Wimmer, M. *Enhancing the excitation gap of a quantum-dot-based Kitaev chain* 2023. arXiv: [2310.09106](https://arxiv.org/abs/2310.09106).
116. Pozar, D. *Microwave Engineering, 4th Edition* ISBN: 9781118213636. <https://books.google.nl/books?id=JegbAAAAQBAJ> (Wiley, Hoboken, NJ, 2011).
117. Ahmed, I., Haigh, J. A., Schaal, S., Barraud, S., Zhu, Y., Lee, C., Amado, M., Robinson, J. W. A., Rossi, A., Morton, J. J. L. & Gonzalez-Zalba, M. F. Radio-Frequency Capacitive Gate-Based Sensing. *Physical Review Applied* **10**, 014018. doi:[10.1103/physrevapplied.10.014018](https://doi.org/10.1103/physrevapplied.10.014018) (July 2018).
118. Horowitz, P. & Hill, W. *The Art of Electronics* ISBN: 9780521809269 (Cambridge University Press, 2015).
119. Collett, M. J. & Gardiner, C. W. Squeezing of intracavity and traveling-wave light fields produced in parametric amplification. *Physical Review A* **30**, 1386–1391. doi:[10.1103/physreva.30.1386](https://doi.org/10.1103/physreva.30.1386) (Sept. 1984).
120. Gardiner, C. W. & Collett, M. J. Input and output in damped quantum systems: Quantum stochastic differential equations and the master equation. *Physical Review A* **31**, 3761–3774. doi:[10.1103/physreva.31.3761](https://doi.org/10.1103/physreva.31.3761) (June 1985).
121. Schuster, D. I., Wallraff, A., Blais, A., Frunzio, L., Huang, R.-S., Majer, J., Girvin, S. M. & Schoelkopf, R. J. ac Stark Shift and Dephasing of a Superconducting Qubit Strongly Coupled to a Cavity Field. *Physical Review Letters* **94**. doi:[10.1103/physrevlett.94.123602](https://doi.org/10.1103/physrevlett.94.123602) (Mar. 2005).
122. Burkard, G., Gullans, M. J., Mi, X. & Petta, J. R. Superconductor–semiconductor hybrid-circuit quantum electrodynamics. *Nature Reviews Physics* **2**, 129–140. doi:[10.1038/s42254-019-0135-2](https://doi.org/10.1038/s42254-019-0135-2) (Jan. 2020).
123. Park, S., Metzger, C., Tosi, L., Goffman, M., Urbina, C., Pothier, H. & Yeyati, A. L. From Adiabatic to Dispersive Readout of Quantum Circuits. *Physical Review Letters* **125**. doi:[10.1103/physrevlett.125.077701](https://doi.org/10.1103/physrevlett.125.077701) (Aug. 2020).
124. Peri, L., Benito, M., Ford, C. J. B. & Gonzalez-Zalba, M. F. *Unified linear response theory of quantum dot circuits* 2023. arXiv: [2310.17399](https://arxiv.org/abs/2310.17399).
125. Esterli, M., Otxoa, R. M. & Gonzalez-Zalba, M. F. Small-signal equivalent circuit for double quantum dots at low-frequencies. *Applied Physics Letters* **114**, 253505. doi:[10.1063/1.5098889](https://doi.org/10.1063/1.5098889) (June 2019).
126. Manzano, D. A short introduction to the Lindblad master equation. *AIP Advances* **10**. doi:[10.1063/1.5115323](https://doi.org/10.1063/1.5115323) (Feb. 2020).
127. Nazarov, Y. & Danon, J. *Advanced Quantum Mechanics: A Practical Guide* ISBN: 9781139619028. <https://books.google.nl/books?id=w20gAwAAQBAJ> (Cambridge University Press, 2013).
128. Ciccarelli, C & Ferguson, A. J. Impedance of the single-electron transistor at radio-frequencies. *New Journal of Physics* **13**, 093015. doi:[10.1088/1367-2630/13/9/093015](https://doi.org/10.1088/1367-2630/13/9/093015) (Sept. 2011).

129. Gonzalez-Zalba, M. F., Barraud, S., Ferguson, A. J. & Betz, A. C. Probing the limits of gate-based charge sensing. *Nature communications* **6**, 6084 (2015).
130. Mizuta, R., Otxoa, R. M., Betz, A. C. & Gonzalez-Zalba, M. F. Quantum and tunneling capacitance in charge and spin qubits. *Physical Review B* **95**. doi:[10.1103/physrevb.95.045414](https://doi.org/10.1103/physrevb.95.045414) (Jan. 2017).
131. Cottet, A., Mora, C. & Kontos, T. Mesoscopic admittance of a double quantum dot. *Physical Review B* **83**. doi:[10.1103/physrevb.83.121311](https://doi.org/10.1103/physrevb.83.121311) (Mar. 2011).
132. Sillanpää, M. A., Lehtinen, T., Paila, A., Makhlin, Y., Roschier, L. & Hakonen, P. J. Direct Observation of Josephson Capacitance. *Physical Review Letters* **95**. ISSN: 1079-7114. doi:[10.1103/physrevlett.95.206806](https://doi.org/10.1103/physrevlett.95.206806) (Nov. 2005).
133. Duty, T., Johansson, G., Bladh, K., Gunnarsson, D., Wilson, C. & Delsing, P. Observation of Quantum Capacitance in the Cooper-Pair Transistor. *Physical Review Letters* **95**, 206807. doi:[10.1103/physrevlett.95.206807](https://doi.org/10.1103/physrevlett.95.206807) (Nov. 2005).
134. Petersson, K. D., Smith, C. G., Anderson, D., Atkinson, P., Jones, G. A. C. & Ritchie, D. A. Charge and Spin State Readout of a Double Quantum Dot Coupled to a Resonator. *Nano Letters* **10**, 2789–2793. doi:[10.1021/nl100663w](https://doi.org/10.1021/nl100663w) (Aug. 2010).
135. Colless, J. I., Mahoney, A. C., Hornibrook, J. M., Doherty, A. C., Lu, H., Gossard, A. C. & Reilly, D. J. Dispersive Readout of a Few-Electron Double Quantum Dot with Fast rf Gate Sensors. *Physical Review Letters* **110**, 046805. doi:[10.1103/physrevlett.110.046805](https://doi.org/10.1103/physrevlett.110.046805) (Jan. 2013).
136. Urdampilleta, M., Chatterjee, A., Lo, C. C., Kobayashi, T., Mansir, J., Barraud, S., Betz, A. C., Rogge, S., Gonzalez-Zalba, M. F. & Morton, J. J. Charge Dynamics and Spin Blockade in a Hybrid Double Quantum Dot in Silicon. *Physical Review X* **5**. doi:[10.1103/physrevx.5.031024](https://doi.org/10.1103/physrevx.5.031024) (Aug. 2015).
137. Pakkiam, P., Timofeev, A. V., House, M. G., Hogg, M. R., Kobayashi, T., Koch, M., Rogge, S. & Simmons, M. Y. Single-Shot Single-Gate rf Spin Readout in Silicon. *Physical Review X* **8**, 041032. doi:[10.1103/physrevx.8.041032](https://doi.org/10.1103/physrevx.8.041032) (Nov. 2018).
138. De Jong, D., van Veen, J., Binci, L., Singh, A., Krogstrup, P., Kouwenhoven, L. P., Pfaff, W. & Watson, J. D. Rapid Detection of Coherent Tunneling in an InAs Nanowire Quantum Dot through Dispersive Gate Sensing. *Physical Review Applied* **11**, 044061. doi:[10.1103/physrevapplied.11.044061](https://doi.org/10.1103/physrevapplied.11.044061) (Apr. 2019).
139. Urdampilleta, M. *et al.* Gate-based high fidelity spin readout in a CMOS device. *Nature Nanotechnology* **14**, 737–741. doi:[10.1038/s41565-019-0443-9](https://doi.org/10.1038/s41565-019-0443-9) (May 2019).
140. West, A., Hensen, B., Jouan, A., Tanttu, T., Yang, C.-H., Rossi, A., Gonzalez-Zalba, M. F., Hudson, F., Morello, A., Reilly, D. J. & Dzurak, A. S. Gate-based single-shot readout of spins in silicon. *Nature Nanotechnology* **14**, 437–441. doi:[10.1038/s41565-019-0400-7](https://doi.org/10.1038/s41565-019-0400-7) (Mar. 2019).
141. Zheng, G., Samkharadze, N., Noordam, M. L., Kalhor, N., Brousse, D., Sammak, A., Scappucci, G. & Vandersypen, L. M. K. Rapid gate-based spin read-out in silicon using an on-chip resonator. *Nature Nanotechnology* **14**, 742–746. doi:[10.1038/s41565-019-0488-9](https://doi.org/10.1038/s41565-019-0488-9) (July 2019).

142. Persson, F., Wilson, C. M., Sandberg, M., Johansson, G. & Delsing, P. Excess Dissipation in a Single-Electron Box: The Sisyphus Resistance. *Nano Letters* **10**. PMID: 20155965, 953–957. doi:[10.1021/nl903887x](https://doi.org/10.1021/nl903887x) (2010).
143. Dvir, T. *et al.* Realization of a minimal Kitaev chain in coupled quantum dots. *Nature* **614**, 445–450. doi:[10.1038/s41586-022-05585-1](https://doi.org/10.1038/s41586-022-05585-1) (Feb. 2023).
144. Ten Haaf, S. L. D., Wang, Q., Bozkurt, A. M., Liu, C.-X., Kulesh, I., Kim, P., Xiao, D., Thomas, C., Manfra, M. J., Dvir, T., Wimmer, M. & Goswami, S. *Engineering Majorana bound states in coupled quantum dots in a two-dimensional electron gas* 2023. arXiv: [2311.03208](https://arxiv.org/abs/2311.03208) [[cond-mat.mes-hall](https://arxiv.org/archive/cond-mat)].
145. Herman, F. & Hlubina, R. Microscopic interpretation of the Dynes formula for the tunneling density of states. *Physical Review B* **94**. ISSN: 2469-9969. doi:[10.1103/physrevb.94.144508](https://doi.org/10.1103/physrevb.94.144508) (Oct. 2016).
146. Sillanpää, M. A., Park, J. I. & Simmonds, R. W. Coherent quantum state storage and transfer between two phase qubits via a resonant cavity. *Nature* **449**, 438–442. doi:[10.1038/nature06124](https://doi.org/10.1038/nature06124) (Sept. 2007).
147. House, M. G., Kobayashi, T., Weber, B., Hile, S. J., Watson, T. F., van der Heijden, J., Rogge, S. & Simmons, M. Y. Radio frequency measurements of tunnel couplings and singlet-triplet spin states in Si:P quantum dots. *Nature Communications* **6**. ISSN: 2041-1723. doi:[10.1038/ncomms9848](https://doi.org/10.1038/ncomms9848) (Nov. 2015).
148. Croot, X., Pauka, S., Jarratt, M., Lu, H., Gossard, A., Watson, J., Gardner, G., Fallahi, S., Manfra, M. & Reilly, D. Gate-Sensing Charge Pockets in the Semiconductor-Qubit Environment. *Physical Review Applied* **11**. ISSN: 2331-7019. doi:[10.1103/physrevapplied.11.064027](https://doi.org/10.1103/physrevapplied.11.064027) (June 2019).
149. *The SQUID Handbook* (eds Clarke, J. & Braginski, A. I.) doi:[10.1002/9783527609956](https://doi.org/10.1002/9783527609956) (Wiley, Aug. 2006).
150. Ivakhnenko, O. V., Shevchenko, S. N. & Nori, F. Nonadiabatic Landau–Zener–Stückelberg–Majorana transitions, dynamics, and interference. *Physics Reports* **995**, 1–89. doi:[10.1016/j.physrep.2022.10.002](https://doi.org/10.1016/j.physrep.2022.10.002) (Jan. 2023).
151. Gonzalez-Zalba, M. F., Shevchenko, S. N., Barraud, S., Johansson, J. R., Ferguson, A. J., Nori, F. & Betz, A. C. Gate-Sensing Coherent Charge Oscillations in a Silicon Field-Effect Transistor. *Nano Letters* **16**, 1614–1619. doi:[10.1021/acs.nanolett.5b04356](https://doi.org/10.1021/acs.nanolett.5b04356) (Feb. 2016).
152. Didier, N., Bourassa, J. & Blais, A. Fast Quantum Nondemolition Readout by Parametric Modulation of Longitudinal Qubit-Oscillator Interaction. *Physical Review Letters* **115**. doi:[10.1103/physrevlett.115.203601](https://doi.org/10.1103/physrevlett.115.203601) (Nov. 2015).
153. Macklin, C., O’Brien, K., Hover, D., Schwartz, M. E., Bolkhovskiy, V., Zhang, X., Oliver, W. D. & Siddiqi, I. A near-quantum-limited Josephson traveling-wave parametric amplifier. *Science* **350**, 307–310. doi:[10.1126/science.aaa8525](https://doi.org/10.1126/science.aaa8525) (Oct. 2015).
154. Hornibrook, J. M., Colless, J. I., Mahoney, A. C., Croot, X. G., Blanvillain, S., Lu, H., Gossard, A. C. & Reilly, D. J. Frequency multiplexing for readout of spin qubits. *Applied Physics Letters* **104**, 103108. doi:[10.1063/1.4868107](https://doi.org/10.1063/1.4868107) (Mar. 2014).

155. Waardenburg, D. *On-chip circuit design for capacitive gate based readout* MSc Thesis (Delft University of Technology, 2019).
156. Kroll, J., Borsoi, F., van der Enden, K., Uilhoorn, W., de Jong, D., Quintero-Pérez, M., van Woerkom, D., Bruno, A., Plissard, S., Car, D., Bakkers, E., Cassidy, M. & Kouwenhoven, L. Magnetic-Field-Resilient Superconducting Coplanar-Waveguide Resonators for Hybrid Circuit Quantum Electrodynamics Experiments. *Physical Review Applied* **11**, 064053. doi:[10.1103/physrevapplied.11.064053](https://doi.org/10.1103/physrevapplied.11.064053) (June 2019).
157. Göppl, M., Fragner, A., Baur, M., Bianchetti, R., Filipp, S., Fink, J. M., Leek, P. J., Puebla, G., Steffen, L. & Wallraff, A. Coplanar waveguide resonators for circuit quantum electrodynamics. *Journal of Applied Physics* **104**, 113904. doi:[10.1063/1.3010859](https://doi.org/10.1063/1.3010859) (Dec. 2008).
158. Khalil, M. S., Stoutimore, M. J. A., Wellstood, F. C. & Osborn, K. D. An analysis method for asymmetric resonator transmission applied to superconducting devices. *Journal of Applied Physics* **111**, 054510. doi:[10.1063/1.3692073](https://doi.org/10.1063/1.3692073) (Mar. 2012).
159. Crippa, A., Ezzouch, R., Aprá, A., Amisse, A., Laviéville, R., Hutin, L., Bertrand, B., Vinet, M., Urdampilleta, M., Meunier, T., Sanquer, M., Jehl, X., Maurand, R. & Franceschi, S. D. Gate-reflectometry dispersive readout and coherent control of a spin qubit in silicon. *Nature Communications* **10**, 2776. doi:[10.1038/s41467-019-10848-z](https://doi.org/10.1038/s41467-019-10848-z) (July 2019).
160. Ibberson, D. J., Lundberg, T., Haigh, J. A., Hutin, L., Bertrand, B., Barraud, S., Lee, C.-M., Stelmashenko, N. A., Oakes, G. A., Cochrane, L., Robinson, J. W., Vinet, M., Gonzalez-Zalba, M. F. & Ibberson, L. A. Large Dispersive Interaction between a CMOS Double Quantum Dot and Microwave Photons. *PRX Quantum* **2**, 020315. doi:[10.1103/prxquantum.2.020315](https://doi.org/10.1103/prxquantum.2.020315) (May 2021).
161. Wallraff, A., Schuster, D. I., Blais, A., Frunzio, L., Majer, J., Devoret, M. H., Girvin, S. M. & Schoelkopf, R. J. Approaching Unit Visibility for Control of a Superconducting Qubit with Dispersive Readout. *Physical Review Letters* **95**, 060501. doi:[10.1103/physrevlett.95.060501](https://doi.org/10.1103/physrevlett.95.060501) (Aug. 2005).
162. Vijay, R., Slichter, D. H. & Siddiqi, I. Observation of Quantum Jumps in a Superconducting Artificial Atom. *Physical Review Letters* **106**, 110502. doi:[10.1103/physrevlett.106.110502](https://doi.org/10.1103/physrevlett.106.110502) (Mar. 2011).
163. Walter, T., Kurpiers, P., Gasparinetti, S., Magnard, P., Potočnik, A., Salathé, Y., Pechal, M., Mondal, M., Oppliger, M., Eichler, C. & Wallraff, A. Rapid High-Fidelity Single-Shot Dispersive Readout of Superconducting Qubits. *Physical Review Applied* **7**, 054020. doi:[10.1103/physrevapplied.7.054020](https://doi.org/10.1103/physrevapplied.7.054020) (May 2017).
164. Majer, J., Chow, J. M., Gambetta, J. M., Koch, J., Johnson, B. R., Schreier, J. A., Frunzio, L., Schuster, D. I., Houck, A. A., Wallraff, A., Blais, A., Devoret, M. H., Girvin, S. M. & Schoelkopf, R. J. Coupling superconducting qubits via a cavity bus. *Nature* **449**, 443–447. doi:[10.1038/nature06184](https://doi.org/10.1038/nature06184) (Sept. 2007).

165. Scarlino, P., van Woerkom, D. J., Mendes, U. C., Koski, J. V., Landig, A. J., Andersen, C. K., Gasparinetti, S., Reichl, C., Wegscheider, W., Ensslin, K., Ihn, T., Blais, A. & Wallraff, A. Coherent microwave-photon-mediated coupling between a semiconductor and a superconducting qubit. *Nature Communications* **10**, 3011. doi:[10.1038/s41467-019-10798-6](https://doi.org/10.1038/s41467-019-10798-6) (July 2019).
166. Borjans, F., Croot, X. G., Mi, X., Gullans, M. J. & Petta, J. R. Resonant microwave-mediated interactions between distant electron spins. *Nature* **577**, 195–198. doi:[10.1038/s41586-019-1867-y](https://doi.org/10.1038/s41586-019-1867-y) (Dec. 2019).
167. Jerger, M., Poletto, S., Macha, P., Hübner, U., Il'ichev, E. & Ustinov, A. V. Frequency division multiplexing readout and simultaneous manipulation of an array of flux qubits. *Applied Physics Letters* **101**, 042604. doi:[10.1063/1.4739454](https://doi.org/10.1063/1.4739454) (July 2012).
168. Jeffrey, E. *et al.* Fast Accurate State Measurement with Superconducting Qubits. *Physical Review Letters* **112**, 190504. doi:[10.1103/physrevlett.112.190504](https://doi.org/10.1103/physrevlett.112.190504) (May 2014).
169. Delbecq, M. R., Schmitt, V., Parmentier, F. D., Roch, N., Viennot, J. J., Fève, G., Huard, B., Mora, C., Cottet, A. & Kontos, T. Coupling a Quantum Dot, Fermionic Leads, and a Microwave Cavity on a Chip. *Physical Review Letters* **107**, 256804. doi:[10.1103/physrevlett.107.256804](https://doi.org/10.1103/physrevlett.107.256804) (Dec. 2011).
170. Puebla-Hellmann, G. & Wallraff, A. Realization of gigahertz-frequency impedance matching circuits for nano-scale devices. *Applied Physics Letters* **101**, 053108. doi:[10.1063/1.4739451](https://doi.org/10.1063/1.4739451) (July 2012).
171. Hasler, T., Jung, M., Ranjan, V., Puebla-Hellmann, G., Wallraff, A. & Schönenberger, C. Shot Noise of a Quantum Dot Measured with Gigahertz Impedance Matching. *Physical Review Applied* **4**, 054002. doi:[10.1103/physrevapplied.4.054002](https://doi.org/10.1103/physrevapplied.4.054002) (Nov. 2015).
172. Stehlik, J., Liu, Y.-Y., Quintana, C. M., Eichler, C., Hartke, T. R. & Petta, J. R. Fast Charge Sensing of a Cavity-Coupled Double Quantum Dot Using a Josephson Parametric Amplifier. *Physical Review Applied* **4**, 014018. doi:[10.1103/physrevapplied.4.014018](https://doi.org/10.1103/physrevapplied.4.014018) (July 2015).
173. Ranjan, V., Puebla-Hellmann, G., Jung, M., Hasler, T., Nunnenkamp, A., Muoth, M., Hierold, C., Wallraff, A. & Schönenberger, C. Clean carbon nanotubes coupled to superconducting impedance-matching circuits. *Nature Communications* **6**, 7165. doi:[10.1038/ncomms8165](https://doi.org/10.1038/ncomms8165) (May 2015).
174. Frey, T., Leek, P. J., Beck, M., Blais, A., Ihn, T., Ensslin, K. & Wallraff, A. Dipole Coupling of a Double Quantum Dot to a Microwave Resonator. *Physical Review Letters* **108**, 046807. doi:[10.1103/physrevlett.108.046807](https://doi.org/10.1103/physrevlett.108.046807) (Jan. 2012).
175. Petersson, K. D., McFaul, L. W., Schroer, M. D., Jung, M., Taylor, J. M., Houck, A. A. & Petta, J. R. Circuit quantum electrodynamics with a spin qubit. *Nature* **490**, 380–383. doi:[10.1038/nature11559](https://doi.org/10.1038/nature11559) (Oct. 2012).
176. Mi, X., Cady, J. V., Zajac, D. M., Deelman, P. W. & Petta, J. R. Strong coupling of a single electron in silicon to a microwave photon. *Science* **355**, 156–158. doi:[10.1126/science.aal2469](https://doi.org/10.1126/science.aal2469) (Dec. 2016).

177. Stockklauser, A., Scarlino, P., Koski, J., Gasparinetti, S., Andersen, C., Reichl, C., Wegscheider, W., Ihn, T., Ensslin, K. & Wallraff, A. Strong Coupling Cavity QED with Gate-Defined Double Quantum Dots Enabled by a High Impedance Resonator. *Physical Review X* **7**, 011030. doi:[10.1103/physrevx.7.011030](https://doi.org/10.1103/physrevx.7.011030) (Mar. 2017).
178. Bruhat, L. E, Cubaynes, T., Viennot, J. J., Dartiailh, M. C., Desjardins, M. M., Cottet, A. & Kontos, T. Circuit QED with a quantum-dot charge qubit dressed by Cooper pairs. *Physical Review B* **98**. doi:[10.1103/physrevb.98.155313](https://doi.org/10.1103/physrevb.98.155313) (Oct. 2018).
179. Landig, A. J., Koski, J. V., Scarlino, P., Mendes, U. C., Blais, A., Reichl, C., Wegscheider, W., Wallraff, A., Ensslin, K. & Ihn, T. Coherent spin-photon coupling using a resonant exchange qubit. *Nature* **560**, 179–184. doi:[10.1038/s41586-018-0365-y](https://doi.org/10.1038/s41586-018-0365-y) (July 2018).
180. Mi, X., Benito, M., Putz, S., Zajac, D. M., Taylor, J. M., Burkard, G. & Petta, J. R. A coherent spin-photon interface in silicon. *Nature* **555**, 599–603. doi:[10.1038/nature25769](https://doi.org/10.1038/nature25769) (Feb. 2018).
181. Samkharadze, N., Zheng, G., Kalhor, N., Brousse, D., Sammak, A., Mendes, U. C., Blais, A., Scappucci, G. & Vandersypen, L. M. K. Strong spin-photon coupling in silicon. *Science* **359**, 1123–1127. doi:[10.1126/science.aar4054](https://doi.org/10.1126/science.aar4054) (Jan. 2018).
182. Koski, J. V., Landig, A. J., Russ, M., Abadillo-Uriel, J. C., Scarlino, P., Kratochwil, B., Reichl, C., Wegscheider, W., Burkard, G., Friesen, M., Coppersmith, S. N., Wallraff, A., Ensslin, K. & Ihn, T. Strong photon coupling to the quadrupole moment of an electron in a solid-state qubit. *Nature Physics* **16**, 642–646. doi:[10.1038/s41567-020-0862-4](https://doi.org/10.1038/s41567-020-0862-4) (May 2020).
183. Harabula, M.-C., Hasler, T., Fülöp, G., Jung, M., Ranjan, V. & Schönenberger, C. Measuring a Quantum Dot with an Impedance-Matching On-Chip Superconducting LC Resonator at Gigahertz Frequencies. *Physical Review Applied* **8**, 054006. doi:[10.1103/physrevapplied.8.054006](https://doi.org/10.1103/physrevapplied.8.054006) (Nov. 2017).
184. Holman, N., Rosenberg, D., Yost, D., Yoder, J. L., Das, R., Oliver, W. D., McDermott, R. & Eriksson, M. A. Dispersive measurement of a semiconductor double quantum dot via 3D integration of a high-impedance TiN resonator. *arXiv preprint*. arXiv: [2011.08759](https://arxiv.org/abs/2011.08759) [[cond-mat.mes-hall](https://arxiv.org/abs/2011.08759)] (2020).
185. Ruffino, A., Yang, T.-Y., Michniewicz, J., Peng, Y., Charbon, E. & Gonzalez-Zalba, M. F. A cryo-CMOS chip that integrates silicon quantum dots and multiplexed dispersive readout electronics. *Nature Electronics* **5**, 53–59. doi:[10.1038/s41928-021-00687-6](https://doi.org/10.1038/s41928-021-00687-6) (Dec. 2021).
186. Maman, V. D., Gonzalez-Zalba, M. & Pályi, A. Charge Noise and Overdrive Errors in Dispersive Readout of Charge, Spin, and Majorana Qubits. *Physical Review Applied* **14**. doi:[10.1103/physrevapplied.14.064024](https://doi.org/10.1103/physrevapplied.14.064024) (Dec. 2020).
187. Probst, S., Song, F. B., Bushev, P. A., Ustinov, A. V. & Weides, M. Efficient and robust analysis of complex scattering data under noise in microwave resonators. *Review of Scientific Instruments* **86**, 024706. doi:[10.1063/1.4907935](https://doi.org/10.1063/1.4907935) (Feb. 2015).

188. Chorley, S. J., Wabnig, J., Penfold-Fitch, Z. V., Petersson, K. D., Frake, J., Smith, C. G. & Buitelaar, M. R. Measuring the Complex Admittance of a Carbon Nanotube Double Quantum Dot. *Physical Review Letters* **108**, 036802. doi:[10.1103/physrevlett.108.036802](https://doi.org/10.1103/physrevlett.108.036802) (Jan. 2012).
189. Razmadze, D., Sabonis, D., Malinowski, F. K., Ménard, G. C., Pauka, S., Nguyen, H., van Zanten, D. M., O'Farrell, E. C., Suter, J., Krogstrup, P., Kuemmeth, F. & Marcus, C. M. Radio-Frequency Methods for Majorana-Based Quantum Devices: Fast Charge Sensing and Phase-Diagram Mapping. *Physical Review Applied* **11**, 064011. doi:[10.1103/physrevapplied.11.064011](https://doi.org/10.1103/physrevapplied.11.064011) (June 2019).
190. Guan, H, Dai, M, He, Q, Hu, J, Ouyang, P, Wang, Y, Wei, L. F & Gao, J. Network modeling of non-ideal superconducting resonator circuits. *Superconductor Science and Technology* **33**, 075004. doi:[10.1088/1361-6668/ab89eb](https://doi.org/10.1088/1361-6668/ab89eb) (May 2020).
191. Van der Wiel, W. G., De Franceschi, S., Elzerman, J. M., Fujisawa, T., Tarucha, S. & Kouwenhoven, L. P. Electron transport through double quantum dots. *Reviews of Modern Physics* **75**, 1–22. doi:[10.1103/revmodphys.75.1](https://doi.org/10.1103/revmodphys.75.1) (Dec. 2002).
192. Gabelli, J., Fève, G., Berroir, J.-M., Plaçais, B., Cavanna, A., Etienne, B., Jin, Y. & Glattli, D. C. Violation of Kirchhoff's Laws for a Coherent RC Circuit. *Science* **313**, 499–502. ISSN: 0036-8075. doi:[10.1126/science.1126940](https://doi.org/10.1126/science.1126940) (2006).
193. Jung, M., Schroer, M. D., Petersson, K. D. & Petta, J. R. Radio frequency charge sensing in InAs nanowire double quantum dots. *Applied Physics Letters* **100**, 253508. doi:[10.1063/1.4729469](https://doi.org/10.1063/1.4729469) (June 2012).
194. Ares, N., Schupp, F., Mavalankar, A., Rogers, G., Griffiths, J., Jones, G., Farrer, I., Ritchie, D., Smith, C., Cottet, A., Briggs, G. & Laird, E. Sensitive Radio-Frequency Measurements of a Quantum Dot by Tuning to Perfect Impedance Matching. *Physical Review Applied* **5**, 034011. doi:[10.1103/physrevapplied.5.034011](https://doi.org/10.1103/physrevapplied.5.034011) (Mar. 2016).
195. Betz, A. C., Wacquez, R., Vinet, M., Jehl, X., Saraiva, A. L., Sanquer, M., Ferguson, A. J. & Gonzalez-Zalba, M. F. Dispersively Detected Pauli Spin-Blockade in a Silicon Nanowire Field-Effect Transistor. *Nano Letters* **15**, 4622–4627. doi:[10.1021/acs.nanolett.5b01306](https://doi.org/10.1021/acs.nanolett.5b01306) (June 2015).
196. Sabonis, D., O'Farrell, E. C. T., Razmadze, D., van Zanten, D. M. T., Suter, J., Krogstrup, P. & Marcus, C. M. Dispersive sensing in hybrid InAs/Al nanowires. *Applied Physics Letters* **115**, 102601. doi:[10.1063/1.5116377](https://doi.org/10.1063/1.5116377) (Sept. 2019).
197. Schupp, F. J., Vigneau, E., Wen, Y., Mavalankar, A., Griffiths, J., Jones, G. A. C., Farrer, I., Ritchie, D. A., Smith, C. G., Camenzind, L. C., Yu, L., Zumbühl, D. M., Briggs, G. A. D., Ares, N. & Laird, E. A. Sensitive radiofrequency readout of quantum dots using an ultra-low-noise SQUID amplifier. *Journal of Applied Physics* **127**, 244503. doi:[10.1063/5.0005886](https://doi.org/10.1063/5.0005886) (June 2020).
198. Smith, T. B., Cassidy, M. C., Reilly, D. J., Bartlett, S. D. & Grimsmo, A. L. Dispersive Readout of Majorana Qubits. *PRX Quantum* **1**. doi:[10.1103/prxquantum.1.020313](https://doi.org/10.1103/prxquantum.1.020313) (Nov. 2020).

199. Ménard, G., Anselmetti, G., Martinez, E., Puglia, D., Malinowski, F., Lee, J., Choi, S., Pendharkar, M., Palmstrøm, C., Flensberg, K., Marcus, C., Casparis, L. & Higginbotham, A. Conductance-Matrix Symmetries of a Three-Terminal Hybrid Device. *Physical Review Letters* **124**, 036802. doi:[10 . 1103 / physrevlett . 124 . 036802](https://doi.org/10.1103/physrevlett.124.036802) (Jan. 2020).
200. De Jong, D., Prosko, C., Waardenburg, D. M. A., Han, L., Malinowski, F. K., Krogstrup, P., Kouwenhoven, L. P., Koski, J. V. & Pfaff, W. *Data repository accompanying "Rapid microwave-only characterization and readout of quantum dots using multiplexed gigahertz-frequency resonators"* 2021. doi:[10 . 5281 / zenodo . 5036156](https://doi.org/10.5281/zenodo.5036156).
201. Lesovik, G., Martin, T. & Blatter, G. Electronic entanglement in the vicinity of a superconductor. *The European Physical Journal B* **24**, 287–290. doi:[10 . 1007 / s10051-001-8675-4](https://doi.org/10.1007/s10051-001-8675-4) (Dec. 2001).
202. Ranni, A., Brange, E., Mannila, E. T., Flindt, C. & Maisi, V. F. Real-time observation of Cooper pair splitting showing strong non-local correlations. *Nature Communications* **12**, 6358. ISSN: 2041-1723. doi:[10 . 1038 / s41467-021-26627-8](https://doi.org/10.1038/s41467-021-26627-8) (Nov. 2021).
203. Lambert, N. J., Esmail, A. A., Edwards, M., Pollock, F. A., Lovett, B. W. & Ferguson, A. J. Quantum capacitance and charge sensing of a superconducting double dot. *Applied Physics Letters* **109**, 112603. doi:[10 . 1063 / 1 . 4962811](https://doi.org/10.1063/1.4962811) (Sept. 2016).
204. De Jong, D., Prosko, C. G., Waardenburg, D. M. A., Han, L., Malinowski, F. K., Krogstrup, P., Kouwenhoven, L. P., Koski, J. V. & Pfaff, W. Rapid Microwave-Only Characterization and Readout of Quantum Dots Using Multiplexed Gigahertz-Frequency Resonators. *Physical Review Applied* **16**, 014007. doi:[10 . 1103 / physrevapplied . 16 . 014007](https://doi.org/10.1103/physrevapplied.16.014007) (July 2021).
205. Han, L., Chan, M., de Jong, D., Prosko, C., Badawy, G., Gazibegovic, S., Bakkers, E. P., Kouwenhoven, L. P., Malinowski, F. K. & Pfaff, W. Variable and Orbital-Dependent Spin-Orbit Field Orientations in an InSb Double Quantum Dot Characterized via Dispersive Gate Sensing. *Physical Review Applied* **19**. doi:[10 . 1103 / physrevapplied . 19 . 014063](https://doi.org/10.1103/physrevapplied.19.014063) (Jan. 2023).
206. Scherübl, Z., Pályi, A. & Csonka, S. Probing individual split Cooper pairs using the spin qubit toolkit. *Physical Review B* **89**, 205439. doi:[10 . 1103 / physrevb . 89 . 205439](https://doi.org/10.1103/physrevb.89.205439) (May 2014).
207. Einstein, A., Podolsky, B. & Rosen, N. Can Quantum-Mechanical Description of Physical Reality Be Considered Complete? *Physical Review* **47**, 777–780. doi:[10 . 1103 / physrev . 47 . 777](https://doi.org/10.1103/physrev.47.777) (May 1935).
208. Bell, J. S. On the Einstein Podolsky Rosen paradox. *Physics Physique Fizika* **1**, 195–200. doi:[10 . 1103 / PhysicsPhysiqueFizika . 1 . 195](https://doi.org/10.1103/PhysicsPhysiqueFizika.1.195) (3 Nov. 1964).
209. Chtchelkatchev, N. M., Blatter, G., Lesovik, G. B. & Martin, T. Bell inequalities and entanglement in solid-state devices. *Physical Review B* **66**, 161320. doi:[10 . 1103 / physrevb . 66 . 161320](https://doi.org/10.1103/physrevb.66.161320) (Oct. 2002).

210. Samuelsson, P., Sukhorukov, E. V. & Büttiker, M. Orbital Entanglement and Violation of Bell Inequalities in Mesoscopic Conductors. *Physical Review Letters* **91**, 157002. doi:[10.1103/physrevlett.91.157002](https://doi.org/10.1103/physrevlett.91.157002) (Oct. 2003).
211. Averin, D. V. & Nazarov, Y. V. in *Single Charge Tunneling: Coulomb Blockade Phenomena in Nanostructures* (eds Grabert, H. & Devoret, M. H.) 217–247 (Plenum Press and NATO Scientific Affairs Division, New York/London, 1992). doi:[10.1007/978-1-4757-2166-9\\_6](https://doi.org/10.1007/978-1-4757-2166-9_6).
212. Burkard, G. & Petta, J. R. Dispersive readout of valley splittings in cavity-coupled silicon quantum dots. *Phys. Rev. B* **94**, 195305. doi:[10.1103/PhysRevB.94.195305](https://doi.org/10.1103/PhysRevB.94.195305) (19 Nov. 2016).
213. Leijnse, M. & Flensberg, K. Coupling spin qubits via superconductors. *Physical review letters* **111**, 060501 (2013).
214. Eldridge, J., Pala, M. G., Governale, M. & König, J. Superconducting proximity effect in interacting double-dot systems. *Physical Review B* **82**. doi:[10.1103/physrevb.82.184507](https://doi.org/10.1103/physrevb.82.184507) (Nov. 2010).
215. Esben Bork Hansen and Jeroen Danon and Karsten Flensberg. Probing electron-hole components of subgap states in Coulomb blockaded Majorana islands. *Physical Review B* **97**. doi:[10.1103/physrevb.97.041411](https://doi.org/10.1103/physrevb.97.041411) (Jan. 2018).
216. Heedt, S. *et al.* Shadow-wall lithography of ballistic superconductor–semiconductor quantum devices. *Nature Communications* **12**, 4914. doi:[10.1038/s41467-021-25100-w](https://doi.org/10.1038/s41467-021-25100-w) (Aug. 2021).
217. Nguyen, H. Q., Sabonis, D., Razmadze, D., Mannila, E. T., Maisi, V. F., van Zanten, D. M. T., O'Farrell, E. C. T., Krogstrup, P., Kuemmeth, F., Pekola, J. P. & Marcus, C. M. Electrostatic control of quasiparticle poisoning in a hybrid semiconductor-superconductor island. *Physical Review B* **108**. doi:[10.1103/physrevb.108.1041302](https://doi.org/10.1103/physrevb.108.1041302) (July 2023).
218. Golovach, V. N., Borhani, M. & Loss, D. Electric-dipole-induced spin resonance in quantum dots. *Physical Review B* **74**, 165319. doi:[10.1103/physrevb.74.165319](https://doi.org/10.1103/physrevb.74.165319) (Oct. 2006).
219. Flindt, C., Sørensen, A. S. & Flensberg, K. Spin-Orbit Mediated Control of Spin Qubits. *Physical Review Letters* **97**, 240501. doi:[10.1103/physrevlett.97.240501](https://doi.org/10.1103/physrevlett.97.240501) (Dec. 2006).
220. Nowack, K. C., Koppens, F. H. L., Nazarov, Y. V. & Vandersypen, L. M. K. Coherent Control of a Single Electron Spin with Electric Fields. *Science* **318**, 1430–1433. doi:[10.1126/science.1148092](https://doi.org/10.1126/science.1148092) (Nov. 2007).
221. Nadj-Perge, S., Frolov, S. M., Bakkers, E. P. A. M. & Kouwenhoven, L. P. Spin-orbit qubit in a semiconductor nanowire. *Nature* **468**, 1084–1087. doi:[10.1038/nature09682](https://doi.org/10.1038/nature09682) (Dec. 2010).
222. Schroer, M. D., Petersson, K. D., Jung, M. & Petta, J. R. Field Tuning the g Factor in InAs Nanowire Double Quantum Dots. *Physical Review Letters* **107**, 176811. doi:[10.1103/physrevlett.107.176811](https://doi.org/10.1103/physrevlett.107.176811) (Oct. 2011).

223. John F. Clauser and Michael A. Horne and Abner Shimony and Richard A. Holt. Proposed Experiment to Test Local Hidden Variable Theories. *Physical Review Letters* **24**, 549–549. doi:[10.1103/physrevlett.24.549](https://doi.org/10.1103/physrevlett.24.549) (Mar. 1970).
224. Damaz de Jong and Christian G. Prosko and Lin Han and Filip K. Malinowski and Yu Liu and Leo P. Kouwenhoven and Wolfgang Pfaff. *Data repository accompanying “Controllable single Cooper pair splitting in hybrid quantum dot systems”* 2023. doi:[10.5281/zenodo.7842384](https://doi.org/10.5281/zenodo.7842384).
225. Gustavsson, S., Leturcq, R., Studer, M., Ihn, T., Ensslin, K., Driscoll, D. C. & Gosard, A. C. Time-Resolved Detection of Single-Electron Interference. *Nano Letters* **8**, 2547–2550. doi:[10.1021/nl801689t](https://doi.org/10.1021/nl801689t) (July 2008).
226. Noguchi, A., Shikano, Y., Toyoda, K. & Urabe, S. Aharonov–Bohm effect in the tunnelling of a quantum rotor in a linear Paul trap. *Nature Communications* **5**. doi:[10.1038/ncomms4868](https://doi.org/10.1038/ncomms4868) (May 2014).
227. Parto, M., Lopez-Aviles, H., Antonio-Lopez, J. E., Khajavikhan, M., Amezcua-Correa, R. & Christodoulides, D. N. Observation of twist-induced geometric phases and inhibition of optical tunneling via Aharonov-Bohm effects. *Science Advances* **5**. doi:[10.1126/sciadv.aau8135](https://doi.org/10.1126/sciadv.aau8135) (Jan. 2019).
228. Dehollain, J. P., Mukhopadhyay, U., Michal, V. P., Wang, Y., Wunsch, B., Reichl, C., Wegscheider, W., Rudner, M. S., Demler, E. & Vandersypen, L. M. K. Nagaoka ferromagnetism observed in a quantum dot plaquette. *Nature* **579**, 528–533. doi:[10.1038/s41586-020-2051-0](https://doi.org/10.1038/s41586-020-2051-0) (Mar. 2020).
229. Venkatraman, J., Cortinas, R. G., Frattini, N. E., Xiao, X. & Devoret, M. H. A driven quantum superconducting circuit with multiple tunable degeneracies. *arXiv e-prints*. arXiv: [2211.04605](https://arxiv.org/abs/2211.04605) (2022).
230. Hofstadter, D. R. Energy levels and wave functions of Bloch electrons in rational and irrational magnetic fields. *Physical Review B* **14**, 2239–2249. doi:[10.1103/physrevb.14.2239](https://doi.org/10.1103/physrevb.14.2239) (Sept. 1976).
231. Tsintzis, A., Souto, R. S., Flensberg, K., Danon, J. & Leijnse, M. Majorana Qubits and Non-Abelian Physics in Quantum Dot–Based Minimal Kitaev Chains. *PRX Quantum* **5**. ISSN: 2691-3399. doi:[10.1103/prxquantum.5.010323](https://doi.org/10.1103/prxquantum.5.010323) (Feb. 2024).
232. Burkard, G., Ladd, T. D., Pan, A., Nichol, J. M. & Petta, J. R. Semiconductor spin qubits. *Reviews of Modern Physics* **95**. doi:[10.1103/revmodphys.95.025003](https://doi.org/10.1103/revmodphys.95.025003) (June 2023).
233. Barthelemy, P. & Vandersypen, L. M. K. Quantum Dot Systems: a versatile platform for quantum simulations. *Annalen der Physik* **525**, 808–826. ISSN: 1521-3889. doi:[10.1002/andp.201300124](https://doi.org/10.1002/andp.201300124) (Sept. 2013).
234. Li, R., Petit, L., Franke, D. P., Dehollain, J. P., Helsen, J., Steudtner, M., Thomas, N. K., Yoscovits, Z. R., Singh, K. J., Wehner, S., Vandersypen, L. M. K., Clarke, J. S. & Veldhorst, M. A crossbar network for silicon quantum dot qubits. *Science Advances* **4**. doi:[10.1126/sciadv.aar3960](https://doi.org/10.1126/sciadv.aar3960) (July 2018).

235. Borsoi, F., Hendrickx, N. W., John, V., Meyer, M., Motz, S., van Riggelen, F., Sammak, A., de Snoo, S. L., Scappucci, G. & Veldhorst, M. Shared control of a 16 semiconductor quantum dot crossbar array. *Nature Nanotechnology* **19**, 21–27. ISSN: 1748-3395. doi:[10.1038/s41565-023-01491-3](https://doi.org/10.1038/s41565-023-01491-3) (Aug. 2023).
236. Hsiao, T.-K., Cova Fariña, P., Oosterhout, S. D., Jirovec, D., Zhang, X., van Diepen, C. J., Lawrie, W. I. L., Wang, C.-A., Sammak, A., Scappucci, G., Veldhorst, M., Demler, E. & Vandersypen, L. M. K. Exciton Transport in a Germanium Quantum Dot Ladder. *Physical Review X* **14**. ISSN: 2160-3308. doi:[10.1103/physrevx.14.011048](https://doi.org/10.1103/physrevx.14.011048) (Mar. 2024).
237. Weichselbaum, A. & Ulloa, S. Aharonov-Bohm phase as quantum gate in two-electron charge qubits. *Physical Review B* **70**. doi:[10.1103/physrevb.70.195332](https://doi.org/10.1103/physrevb.70.195332) (Nov. 2004).
238. Wang, Y., Yang, N. & Zhu, J.-L. Aharonov-Bohm phase operations on a double-barrier nanoring charge qubit. *Physical Review B* **74**. doi:[10.1103/physrevb.74.035432](https://doi.org/10.1103/physrevb.74.035432) (July 2006).
239. Shim, Y.-P. Pauli spin blockade in a resonant triple quantum dot molecule. *Journal of Applied Physics* **132**, 064402. doi:[10.1063/5.0098716](https://doi.org/10.1063/5.0098716) (Aug. 2022).
240. Petta, J. R., Johnson, A. C., Taylor, J. M., Laird, E. A., Yacoby, A., Lukin, M. D., Marcus, C. M., Hanson, M. P. & Gossard, A. C. Coherent Manipulation of Coupled Electron Spins in Semiconductor Quantum Dots. *Science* **309**, 2180–2184. ISSN: 1095-9203. doi:[10.1126/science.1116955](https://doi.org/10.1126/science.1116955) (Sept. 2005).
241. Talbo, V., Lavagna, M., Duong, T. Q. & Crépieux, A. Charge susceptibility and conductances of a double quantum dot. *AIP Advances* **8**, 101333. doi:[10.1063/1.5043108](https://doi.org/10.1063/1.5043108) (Oct. 2018).
242. Ezzouch, R., Zihlmann, S., Michal, V. P., Li, J., Aprá, A., Bertrand, B., Hutin, L., Vinet, M., Urdampilleta, M., Meunier, T., Jehl, X., Niquet, Y.-M., Sanquer, M., Franceschi, S. D. & Maurand, R. Dispersively Probed Microwave Spectroscopy of a Silicon Hole Double Quantum Dot. *Physical Review Applied* **16**. doi:[10.1103/physrevapplied.16.034031](https://doi.org/10.1103/physrevapplied.16.034031) (Sept. 2021).
243. Fuhrer, A., Lüscher, S., Ihn, T., Heinzl, T., Ensslin, K., Wegscheider, W. & Bichler, M. Energy spectra of quantum rings. *Nature* **413**, 822–825. doi:[10.1038/35101552](https://doi.org/10.1038/35101552) (Oct. 2001).
244. Keyser, U. F., Fühner, C., Borck, S., Haug, R. J., Bichler, M., Abstreiter, G. & Wegscheider, W. Kondo Effect in a Few-Electron Quantum Ring. *Physical Review Letters* **90**. doi:[10.1103/physrevlett.90.196601](https://doi.org/10.1103/physrevlett.90.196601) (May 2003).
245. Moehle, C. M., Ke, C. T., Wang, Q., Thomas, C., Xiao, D., Karwal, S., Lodari, M., van de Kerkhof, V., Termaat, R., Gardner, G. C., Scappucci, G., Manfra, M. J. & Goswami, S. InSbAs Two-Dimensional Electron Gases as a Platform for Topological Superconductivity. *Nano Letters* **21**, 9990–9996. doi:[10.1021/acs.nanolett.1c03520](https://doi.org/10.1021/acs.nanolett.1c03520) (Nov. 2021).

246. Pieper, J. B. & Price, J. C. Frequency dependence of  $h/e$  conductance oscillations in mesoscopic Ag rings. *Physical Review Letters* **72**, 3586–3589. doi:[10.1103/physrevlett.72.3586](https://doi.org/10.1103/physrevlett.72.3586) (May 1994).
247. Büttiker, M. & Y. Imry and R. Landauer. Josephson behavior in small normal one-dimensional rings. *Physics Letters A* **96**, 365–367. doi:[10.1016/0375-9601\(83\)90011-7](https://doi.org/10.1016/0375-9601(83)90011-7) (July 1983).
248. Ortix, C. in *Physics of Quantum Rings* 327–346 (Springer International Publishing, 2018). doi:[10.1007/978-3-319-95159-1\\_12](https://doi.org/10.1007/978-3-319-95159-1_12).
249. Yacoby, A., Heiblum, M., Mahalu, D. & Shtrikman, H. Coherence and Phase Sensitive Measurements in a Quantum Dot. *Physical Review Letters* **74**, 4047–4050. doi:[10.1103/physrevlett.74.4047](https://doi.org/10.1103/physrevlett.74.4047) (May 1995).
250. Schuster, R., Buks, E., Heiblum, M., Mahalu, D., Umansky, V. & Shtrikman, H. Phase measurement in a quantum dot via a double-slit interference experiment. *Nature* **385**, 417–420. doi:[10.1038/385417a0](https://doi.org/10.1038/385417a0) (Jan. 1997).
251. Holleitner, A. W., Decker, C. R., Qin, H., Eberl, K. & Blick, R. H. Coherent Coupling of Two Quantum Dots Embedded in an Aharonov-Bohm Interferometer. *Physical Review Letters* **87**. doi:[10.1103/physrevlett.87.256802](https://doi.org/10.1103/physrevlett.87.256802) (Nov. 2001).
252. Sigrist, M., Fuhrer, A., Ihn, T., Ensslin, K., Ulloa, S. E., Wegscheider, W. & Bichler, M. Magnetic-Field-Dependent Transmission Phase of a Double-Dot System in a Quantum Ring. *Physical Review Letters* **93**. doi:[10.1103/physrevlett.93.066802](https://doi.org/10.1103/physrevlett.93.066802) (Aug. 2004).
253. Sigrist, M., Ihn, T., Ensslin, K., Loss, D., Reinwald, M. & Wegscheider, W. Phase Coherence in the Inelastic Cotunneling Regime. *Physical Review Letters* **96**. doi:[10.1103/physrevlett.96.036804](https://doi.org/10.1103/physrevlett.96.036804) (Jan. 2006).
254. Sigrist, M., Ihn, T., Ensslin, K., Reinwald, M. & Wegscheider, W. Is inelastic cotunneling phase coherent? *Journal of Applied Physics* **101**. doi:[10.1063/1.2722725](https://doi.org/10.1063/1.2722725) (Apr. 2007).
255. Avinun-Kalish, M., Heiblum, M., Zarchin, O., Mahalu, D. & Umansky, V. Crossover from ‘mesoscopic’ to ‘universal’ phase for electron transmission in quantum dots. *Nature* **436**, 529–533. doi:[10.1038/nature03899](https://doi.org/10.1038/nature03899) (July 2005).
256. Hatano, T., Kubo, T., Tokura, Y., Amaha, S., Teraoka, S. & Tarucha, S. Aharonov-Bohm Oscillations Changed by Indirect Interdot Tunneling via Electrodes in Parallel-Coupled Vertical Double Quantum Dots. *Physical Review Letters* **106**. doi:[10.1103/physrevlett.106.076801](https://doi.org/10.1103/physrevlett.106.076801) (Feb. 2011).
257. Edlbauer, H., Takada, S., Roussely, G., Yamamoto, M., Tarucha, S., Ludwig, A., Wieck, A. D., Meunier, T. & Bäuerle, C. Non-universal transmission phase behaviour of a large quantum dot. *Nature Communications* **8**. doi:[10.1038/s41467-017-01685-z](https://doi.org/10.1038/s41467-017-01685-z) (Nov. 2017).
258. Borsoi, F., Zuo, K., Gazibegovic, S., het Veld, R. L. M. O., Bakkers, E. P. A. M., Kouwenhoven, L. P. & Heedt, S. Transmission phase read-out of a large quantum dot in a nanowire interferometer. *Nature Communications* **11**. doi:[10.1038/s41467-020-17461-5](https://doi.org/10.1038/s41467-020-17461-5) (July 2020).

259. Malinowski, F. K., Han, L., de Jong, D., Wang, J.-Y., Prosko, C. G., Badawy, G., Gazibegovic, S., Liu, Y., Krogstrup, P., Bakkers, E. P., Kouwenhoven, L. P. & Koski, J. V. Radio-Frequency C-V Measurements with Subattofarad Sensitivity. *Physical Review Applied* **18**. doi:[10.1103/physrevapplied.18.024032](https://doi.org/10.1103/physrevapplied.18.024032) (Aug. 2022).
260. Nadj-Perge, S., Pribiag, V. S., van den Berg, J. W. G., Zuo, K., Plissard, S. R., Bakkers, E. P. A. M., Frolov, S. M. & Kouwenhoven, L. P. Spectroscopy of Spin-Orbit Quantum Bits in Indium Antimonide Nanowires. *Physical Review Letters* **108**. doi:[10.1103/physrevlett.108.166801](https://doi.org/10.1103/physrevlett.108.166801) (Apr. 2012).
261. Széchenyi, G. & Pályi, A. Parity-to-charge conversion for readout of topological Majorana qubits. *Physical Review B* **101**. doi:[10.1103/physrevb.101.235441](https://doi.org/10.1103/physrevb.101.235441) (June 2020).
262. Christian G. Prosko and Ivan Kulesh and Michael Chan and Lin Han and Di Xiao and Candice Thomas and Michael J. Manfra and Srijit Goswami and Filip K. Malinowski. *Data repository accompanying "Flux-Tunable Hybridization in a Double Quantum Dot Interferometer"* 2023. doi:[10.5281/zenodo.7702118](https://doi.org/10.5281/zenodo.7702118).
263. Beenakker, C. W. J. Universal limit of critical-current fluctuations in mesoscopic Josephson junctions. *Physical Review Letters* **67**, 3836–3839. doi:[10.1103/physrevlett.67.3836](https://doi.org/10.1103/physrevlett.67.3836) (Dec. 1991).
264. Van Heck, B., Mi, S. & Akhmerov, A. R. Single fermion manipulation via superconducting phase differences in multiterminal Josephson junctions. *Physical Review B* **90**. doi:[10.1103/physrevb.90.155450](https://doi.org/10.1103/physrevb.90.155450) (Oct. 2014).
265. Xie, H.-Y., Vavilov, M. G. & Levchenko, A. Topological Andreev bands in three-terminal Josephson junctions. *Physical Review B* **96**. doi:[10.1103/physrevb.96.161406](https://doi.org/10.1103/physrevb.96.161406) (Oct. 2017).
266. Houzet, M. & Meyer, J. S. Majorana-Weyl crossings in topological multiterminal junctions. *Physical Review B* **100**. doi:[10.1103/physrevb.100.014521](https://doi.org/10.1103/physrevb.100.014521) (July 2019).
267. Fatemi, V., Akhmerov, A. R. & Bretheau, L. Weyl Josephson circuits. *Physical Review Research* **3**. doi:[10.1103/physrevresearch.3.013288](https://doi.org/10.1103/physrevresearch.3.013288) (Mar. 2021).
268. Barakov, H. & Nazarov, Y. V. Abundance of Weyl points in semiclassical multiterminal superconducting nanostructures. *Physical Review B* **107**. doi:[10.1103/physrevb.107.014507](https://doi.org/10.1103/physrevb.107.014507) (Jan. 2023).
269. Meyer, J. S. & Houzet, M. Nontrivial Chern Numbers in Three-Terminal Josephson Junctions. *Physical Review Letters* **119**. doi:[10.1103/physrevlett.119.136807](https://doi.org/10.1103/physrevlett.119.136807) (Sept. 2017).
270. De Bruyn Ouboter, R., Omelyanchouk, A. & Vol, E. Multi-terminal SQUID controlled by the transport current. *Physica B: Condensed Matter* **205**, 153–162. doi:[10.1016/0921-4526\(94\)00299-b](https://doi.org/10.1016/0921-4526(94)00299-b) (Feb. 1995).
271. Zareyan, M. & Omelyanchuk, A. N. Coherent current states in a mesoscopic four-terminal Josephson junction. *Low Temperature Physics* **25**, 175–181. doi:[10.1063/1.593723](https://doi.org/10.1063/1.593723) (Mar. 1999).

272. Omelyanchouk, A. & Zareyan, M. Ballistic four-terminal Josephson junction: bistable states and magnetic flux transfer. *Physica B: Condensed Matter* **291**, 81–88. doi:[10.1016/s0921-4526\(99\)00760-7](https://doi.org/10.1016/s0921-4526(99)00760-7) (Aug. 2000).
273. Amin, M. H. S., Omelyanchouk, A. N. & Zagoskin, A. M. Mesoscopic multiterminal Josephson structures. I. Effects of nonlocal weak coupling. *Low Temperature Physics* **27**, 616–623. doi:[10.1063/1.1399198](https://doi.org/10.1063/1.1399198) (Aug. 2001).
274. Alidoust, M., Sewell, G. & Linder, J. Superconducting phase transistor in diffusive four-terminal ferromagnetic Josephson junctions. *Physical Review B* **85**. doi:[10.1103/physrevb.85.144520](https://doi.org/10.1103/physrevb.85.144520) (Apr. 2012).
275. Amin, M., Omelyanchouk, A., Blais, A., van den Brink, A. M., Rose, G., Duty, T. & Zagoskin, A. Multi-terminal superconducting phase qubit. *Physica C: Superconductivity* **368**, 310–314. doi:[10.1016/s0921-4534\(01\)01187-x](https://doi.org/10.1016/s0921-4534(01)01187-x) (Mar. 2002).
276. Vleeming, B., Zakarian, A., Omelyanchouk, A. & de Bruyn Ouboter, R. Macroscopic quantum interference phenomena in a 4-terminal SQUID. *Physica B: Condensed Matter* **226**, 253–258. doi:[10.1016/0921-4526\(96\)00485-1](https://doi.org/10.1016/0921-4526(96)00485-1) (Aug. 1996).
277. Vleeming, B., van Bemmelen, F., Berends, M., Ouboter, R. B. & Omelyanchouk, A. Measurements of the flux, embraced by the ring of a four-terminal SQUID, as a function of the external magnetic flux and the applied transport current. *Physica B: Condensed Matter* **262**, 296–305. doi:[10.1016/s0921-4526\(98\)01122-3](https://doi.org/10.1016/s0921-4526(98)01122-3) (Apr. 1999).
278. Draelos, A. W., Wei, M.-T., Seredinski, A., Li, H., Mehta, Y., Watanabe, K., Taniguchi, T., Borzenets, I. V., Amet, F. & Finkelstein, G. Supercurrent Flow in Multiterminal Graphene Josephson Junctions. *Nano Letters* **19**, 1039–1043. doi:[10.1021/acs.nanolett.8b04330](https://doi.org/10.1021/acs.nanolett.8b04330) (Jan. 2019).
279. Pankratova, N., Lee, H., Kuzmin, R., Wickramasinghe, K., Mayer, W., Yuan, J., Vavilov, M. G., Shabani, J. & Manucharyan, V. E. Multiterminal Josephson Effect. *Physical Review X* **10**. doi:[10.1103/physrevx.10.031051](https://doi.org/10.1103/physrevx.10.031051) (Sept. 2020).
280. Graziano, G. V., Lee, J. S., Pendharkar, M., Palmstrøm, C. J. & Pribiag, V. S. Transport studies in a gate-tunable three-terminal Josephson junction. *Physical Review B* **101**. doi:[10.1103/physrevb.101.054510](https://doi.org/10.1103/physrevb.101.054510) (Feb. 2020).
281. Arnault, E. G., Larson, T. F. Q., Seredinski, A., Zhao, L., Idris, S., McConnell, A., Watanabe, K., Taniguchi, T., Borzenets, I., Amet, F. & Finkelstein, G. Multiterminal Inverse AC Josephson Effect. *Nano Letters* **21**, 9668–9674. doi:[10.1021/acs.nanolett.1c03474](https://doi.org/10.1021/acs.nanolett.1c03474) (Nov. 2021).
282. Graziano, G. V., Gupta, M., Pendharkar, M., Dong, J. T., Dempsey, C. P., Palmstrøm, C. & Pribiag, V. S. Selective control of conductance modes in multi-terminal Josephson junctions. *Nature Communications* **13**. doi:[10.1038/s41467-022-33682-2](https://doi.org/10.1038/s41467-022-33682-2) (Oct. 2022).
283. Lee, H. *Supercurrent and Andreev bound states in multi-terminal Josephson junctions* PhD thesis (University of Maryland, 2022).

284. Chiles, J., Arnault, E. G., Chen, C.-C., Larson, T. F. Q., Zhao, L., Watanabe, K., Taniguchi, T., Amet, F. & Finkelstein, G. Nonreciprocal Supercurrents in a Field-Free Graphene Josephson Triode. *Nano Letters* **23**, 5257–5263. doi:[10.1021/acs.nanolett.3c01276](https://doi.org/10.1021/acs.nanolett.3c01276) (May 2023).
285. Pfeffer, A. H., Duvauchelle, J. E., Courtois, H., Mélin, R., Feinberg, D. & Lefloch, F. Subgap structure in the conductance of a three-terminal Josephson junction. *Physical Review B* **90**. doi:[10.1103/physrevb.90.075401](https://doi.org/10.1103/physrevb.90.075401) (Aug. 2014).
286. Cohen, Y., Ronen, Y., Kang, J.-H., Heiblum, M., Feinberg, D., Mélin, R. & Shtrikman, H. Nonlocal supercurrent of quartets in a three-terminal Josephson junction. *Proceedings of the National Academy of Sciences* **115**, 6991–6994. doi:[10.1073/pnas.1800044115](https://doi.org/10.1073/pnas.1800044115) (June 2018).
287. Huang, K.-F., Ronen, Y., Mélin, R., Feinberg, D., Watanabe, K., Taniguchi, T. & Kim, P. Evidence for  $4e$  charge of Cooper quartets in a biased multi-terminal graphene-based Josephson junction. *Nature Communications* **13**. doi:[10.1038/s41467-022-30732-7](https://doi.org/10.1038/s41467-022-30732-7) (May 2022).
288. Zhang, F., Rashid, A. S., Ahari, M. T., Zhang, W., Ananthanarayanan, K. M., Xiao, R., de Coster, G. J., Gilbert, M. J., Samarth, N. & Kayyalha, M. Andreev processes in mesoscopic multiterminal graphene Josephson junctions. *Physical Review B* **107**. doi:[10.1103/physrevb.107.1140503](https://doi.org/10.1103/physrevb.107.1140503) (Apr. 2023).
289. Gupta, M., Graziano, G. V., Pendharkar, M., Dong, J. T., Dempsey, C. P., Palmström, C. & Pribiag, V. S. Gate-tunable superconducting diode effect in a three-terminal Josephson device. *Nature Communications* **14**. doi:[10.1038/s41467-023-38856-0](https://doi.org/10.1038/s41467-023-38856-0) (May 2023).
290. Coraiola, M., Svetogorov, A. E., Haxell, D. Z., Sabonis, D., Hinderling, M., ten Kate, S. C., Cheah, E., Krizek, F., Schott, R., Wegscheider, W., Cuevas, J. C., Belzig, W. & Nichele, F. Flux-Tunable Josephson Diode Effect in a Hybrid Four-Terminal Josephson Junction. *ACS Nano* **18**, 9221–9231. ISSN: 1936-086X. doi:[10.1021/acsnano.4c01642](https://doi.org/10.1021/acsnano.4c01642) (Mar. 2024).
291. Melo, A., Fatemi, V. & Aikhmerov, A. Multiplet supercurrent in Josephson tunneling circuits. *SciPost Physics* **12**. ISSN: 2542-4653. doi:[10.21468/scipostphys.12.1.017](https://doi.org/10.21468/scipostphys.12.1.017) (Jan. 2022).
292. Ohnmacht, D. C., Coraiola, M., García-Esteban, J. J., Sabonis, D., Nichele, F., Belzig, W. & Cuevas, J. C. *Quartet Tomography in Multiterminal Josephson Junctions* 2023. arXiv: [2311.18544](https://arxiv.org/abs/2311.18544) [cond-mat.supr-con].
293. Coraiola, M., Haxell, D. Z., Sabonis, D., Weisbrich, H., Svetogorov, A. E., Hinderling, M., ten Kate, S. C., Cheah, E., Krizek, F., Schott, R., Wegscheider, W., Cuevas, J. C., Belzig, W. & Nichele, F. Phase-engineering the Andreev band structure of a three-terminal Josephson junction. *Nature Communications* **14**. ISSN: 2041-1723. doi:[10.1038/s41467-023-42356-6](https://doi.org/10.1038/s41467-023-42356-6) (Oct. 2023).

294. Matsuo, S., Imoto, T., Yokoyama, T., Sato, Y., Lindemann, T., Gronin, S., Gardner, G. C., Nakosai, S., Tanaka, Y., Manfra, M. J. & Tarucha, S. Phase-dependent Andreev molecules and superconducting gap closing in coherently-coupled Josephson junctions. *Nature Communications* **14**. ISSN: 2041-1723. doi:[10 . 1038 / s41467-023-44111-3](https://doi.org/10.1038/s41467-023-44111-3) (Dec. 2023).
295. Coraiola, M., Haxell, D. Z., Sabonis, D., Hinderling, M., ten Kate, S. C., Cheah, E., Krizek, F., Schott, R., Wegscheider, W. & Nichele, F. *Spin-degeneracy breaking and parity transitions in three-terminal Josephson junctions* 2023. arXiv: [2307 . 06715 \[cond-mat.mes-hall\]](https://arxiv.org/abs/2307.06715).
296. Buzdin, A. Direct Coupling Between Magnetism and Superconducting Current in the Josephson  $\varphi_0$  Junction. *Phys. Rev. Lett.* **101**, 107005. doi:[10 . 1103 / PhysRevLett. 101 . 107005](https://doi.org/10.1103/PhysRevLett.101.107005) (10 Sept. 2008).
297. Haxell, D. Z., Coraiola, M., Hinderling, M., ten Kate, S. C., Sabonis, D., Svetogorov, A. E., Belzig, W., Cheah, E., Krizek, F., Schott, R., Wegscheider, W. & Nichele, F. Demonstration of the Nonlocal Josephson Effect in Andreev Molecules. *Nano Letters* **23**, 7532–7538. doi:[10.1021/acs.nanolett.3c02066](https://doi.org/10.1021/acs.nanolett.3c02066) (Aug. 2023).
298. Matsuo, S., Imoto, T., Yokoyama, T., Sato, Y., Lindemann, T., Gronin, S., Gardner, G. C., Manfra, M. J. & Tarucha, S. Phase engineering of anomalous Josephson effect derived from Andreev molecules. *Science Advances* **9**. ISSN: 2375-2548. doi:[10.1126/sciadv.adj3698](https://doi.org/10.1126/sciadv.adj3698) (Dec. 2023).
299. Miyazaki, H., Kanda, A. & Ootuka, Y. Current-phase relation of a superconducting quantum point contact. *Physica C: Superconductivity and its Applications* **437-438**, 217–219. doi:[10.1016/j.physc.2005.12.051](https://doi.org/10.1016/j.physc.2005.12.051) (May 2006).
300. Rocca, M. L. D., Chauvin, M., Huard, B., Pothier, H., Esteve, D. & Urbina, C. Measurement of the Current-Phase Relation of Superconducting Atomic Contacts. *Physical Review Letters* **99**. doi:[10.1103/physrevlett.99.127005](https://doi.org/10.1103/physrevlett.99.127005) (Sept. 2007).
301. Nanda, G., Aguilera-Servin, J. L., Rakyta, P., Kormányos, A., Kleiner, R., Koelle, D., Watanabe, K., Taniguchi, T., Vandersypen, L. M. K. & Goswami, S. Current-Phase Relation of Ballistic Graphene Josephson Junctions. *Nano Letters* **17**, 3396–3401. doi:[10.1021/acs.nanolett.7b00097](https://doi.org/10.1021/acs.nanolett.7b00097) (May 2017).
302. Haxell, D., Cheah, E., Křížek, F., Schott, R., Ritter, M., Hinderling, M., Belzig, W., Bruder, C., Wegscheider, W., Riel, H. & Nichele, F. Measurements of Phase Dynamics in Planar Josephson Junctions and SQUIDS. *Physical Review Letters* **130**. doi:[10.1103/physrevlett.130.087002](https://doi.org/10.1103/physrevlett.130.087002) (Feb. 2023).
303. Matsuo, S., Lee, J. S., Chang, C.-Y., Sato, Y., Ueda, K., Palmstrøm, C. J. & Tarucha, S. Observation of nonlocal Josephson effect on double InAs nanowires. *Communications Physics* **5**. doi:[10.1038/s42005-022-00994-0](https://doi.org/10.1038/s42005-022-00994-0) (Sept. 2022).
304. Strambini, E., Iorio, A., Durante, O., Citro, R., Sanz-Fernández, C., Guarcello, C., Tokatly, I. V., Braggio, A., Rocci, M., Ligato, N., Zannier, V., Sorba, L., Bergeret, F. S. & Giazotto, F. A Josephson phase battery. *Nature Nanotechnology* **15**, 656–660. doi:[10.1038/s41565-020-0712-7](https://doi.org/10.1038/s41565-020-0712-7) (June 2020).

305. Pillet, J.-D., Benzoni, V., Griesmar, J., Smirr, J.-L. & Girit, Ç. Ö. Nonlocal Josephson Effect in Andreev Molecules. *Nano Letters* **19**, 7138–7143. doi:[10.1021/acs.nanolett.9b02686](https://doi.org/10.1021/acs.nanolett.9b02686) (Aug. 2019).
306. Mátyás Kocsis and Zoltán Scherübl and Gergő Fülöp and Péter Makk and Szabolcs Csonka. Strong nonlocal tuning of the current-phase relation of a quantum dot based Andreev molecule. *arXiv preprint*. arXiv: [2303.14842](https://arxiv.org/abs/2303.14842) [[cond-mat.mes-hall](https://arxiv.org/abs/2303.14842)] (2023).
307. Rasmussen, S., Christensen, K., Pedersen, S., Kristensen, L., Bækkegaard, T., Loft, N. & Zinner, N. Superconducting Circuit Companion—an Introduction with Worked Examples. *PRX Quantum* **2**. doi:[10.1103/prxquantum.2.040204](https://doi.org/10.1103/prxquantum.2.040204) (Dec. 2021).
308. Kornich, V., Barakov, H. S. & Nazarov, Y. V. Overlapping Andreev states in semi-conducting nanowires: Competition of one-dimensional and three-dimensional propagation. *Physical Review B* **101**. doi:[10.1103/physrevb.101.195430](https://doi.org/10.1103/physrevb.101.195430) (May 2020).
309. Kürtössy, O., Scherübl, Z., Fülöp, G., Lukács, I. E., Kanne, T., Nygård, J., Makk, P. & Csonka, S. Andreev Molecule in Parallel InAs Nanowires. *Nano Letters* **21**, 7929–7937. doi:[10.1021/acs.nanolett.1c01956](https://doi.org/10.1021/acs.nanolett.1c01956) (Sept. 2021).
310. Pita-Vidal, M., Wesdorp, J. J., Splitthoff, L. J., Bargerbos, A., Liu, Y., Kouwenhoven, L. P. & Andersen, C. K. Strong tunable coupling between two distant superconducting spin qubits. *Nature Physics*. ISSN: 1745-2481. doi:[10.1038/s41567-024-02497-x](https://doi.org/10.1038/s41567-024-02497-x) (May 2024).
311. Cheung, L. Y., Haller, R., Kononov, A., Ciaccia, C., Ungerer, J. H., Kanne, T., Nygård, J., Winkel, P., Reisinger, T., Pop, I. M., Baumgartner, A. & Schönenberger, C. *Photon-mediated long range coupling of two Andreev level qubits* 2023. eprint: [2310.15995](https://arxiv.org/abs/2310.15995).
312. Geier, M., Souto, R. S., Schulenburg, J., Asaad, S., Leijnse, M. & Flensberg, K. *A fermion-parity qubit in a proximitized double quantum dot* 2023. eprint: [2307.05678](https://arxiv.org/abs/2307.05678).
313. Zazunov, A., Shumeiko, V. S., Bratus', E. N., Lantz, J. & Wendin, G. Andreev Level Qubit. *Physical Review Letters* **90**. doi:[10.1103/physrevlett.90.087003](https://doi.org/10.1103/physrevlett.90.087003) (Feb. 2003).
314. Janvier, C., Tosi, L., Bretheau, L., Girit, Ç. O., Stern, M., Bertet, P., Joyez, P., Vion, D., Esteve, D., Goffman, M. F., Pothier, H. & Urbina, C. Coherent manipulation of Andreev states in superconducting atomic contacts. *Science* **349**, 1199–1202. doi:[10.1126/science.aab2179](https://doi.org/10.1126/science.aab2179) (Sept. 2015).
315. Xie, H.-Y., Vavilov, M. G. & Levchenko, A. Weyl nodes in Andreev spectra of multi-terminal Josephson junctions: Chern numbers, conductances, and supercurrents. *Physical Review B* **97**. doi:[10.1103/physrevb.97.035443](https://doi.org/10.1103/physrevb.97.035443) (Jan. 2018).

316. Christian G. Prosko and Wietze D. Huisman and Ivan Kuleshand Di Xiao and Candice Thomas and Michael J. Manfra and Srijit Goswami. *Data repository accompanying "Flux-tunable Josephson Effect in a Four-Terminal Junction"* 2023. doi:[10.5281/zenodo.10212998](https://doi.org/10.5281/zenodo.10212998).
317. Golubov, A. A., Kupriyanov, M. Y. & Il'ichev, E. The current-phase relation in Josephson junctions. *Reviews of Modern Physics* **76**, 411–469. doi:[10.1103/revmodphys.76.411](https://doi.org/10.1103/revmodphys.76.411) (Apr. 2004).
318. Wang, J.-Y., van Loo, N., Mazur, G. P., Levajac, V., Malinowski, F. K., Lemang, M., Borsoi, F., Badawy, G., Gazibegovic, S., Bakkers, E. P. A. M., Quintero-Pérez, M., Heedt, S. & Kouwenhoven, L. P. Parametric exploration of zero-energy modes in three-terminal InSb-Al nanowire devices. *Physical Review B* **106**. doi:[10.1103/physrevb.106.075306](https://doi.org/10.1103/physrevb.106.075306) (Aug. 2022).
319. Aghaee, M. *et al.* InAs-Al hybrid devices passing the topological gap protocol. *Physical Review B* **107**, 245423. doi:[10.1103/PhysRevB.107.245423](https://doi.org/10.1103/PhysRevB.107.245423) (24 June 2023).
320. Rosdahl, T. O., Vuik, A., Kjaergaard, M. & Akhmerov, A. R. Andreev rectifier: A non-local conductance signature of topological phase transitions. *Physical Review B* **97**, 045421. doi:[10.1103/physrevb.97.045421](https://doi.org/10.1103/physrevb.97.045421) (Jan. 2018).
321. Pan, H., Sau, J. D. & Sarma, S. D. Three-terminal nonlocal conductance in Majorana nanowires: Distinguishing topological and trivial in realistic systems with disorder and inhomogeneous potential. *Physical Review B* **103**, 014513. doi:[10.1103/physrevb.103.014513](https://doi.org/10.1103/physrevb.103.014513) (Jan. 2021).
322. Puglia, D., Martinez, E. A., Ménard, G. C., Pöschl, A., Gronin, S., Gardner, G. C., Kallaher, R., Manfra, M. J., Marcus, C. M., Higginbotham, A. P. & Casparis, L. Closing of the induced gap in a hybrid superconductor-semiconductor nanowire. *Physical Review B* **103**. doi:[10.1103/physrevb.103.235201](https://doi.org/10.1103/physrevb.103.235201) (June 2021).
323. Pöschl, A., Danilenko, A., Sabonis, D., Kristjuhan, K., Lindemann, T., Thomas, C., Manfra, M. J. & Marcus, C. M. Nonlocal conductance spectroscopy of Andreev bound states in gate-defined InAs/Al nanowires. *Physical Review B* **106**. doi:[10.1103/physrevb.106.1241301](https://doi.org/10.1103/physrevb.106.1241301) (Dec. 2022).
324. Van Loo, N., Mazur, G. P., Dvir, T., Wang, G., Dekker, R. C., Wang, J.-Y., Lemang, M., Sfiligoj, C., Bordin, A., van Driel, D., Badawy, G., Gazibegovic, S., Bakkers, E. P. A. M. & Kouwenhoven, L. P. Electrostatic control of the proximity effect in the bulk of semiconductor-superconductor hybrids. *Nature Communications* **14**. doi:[10.1038/s41467-023-39044-w](https://doi.org/10.1038/s41467-023-39044-w) (June 2023).
325. Rainis, D. & Loss, D. Majorana qubit decoherence by quasiparticle poisoning. *Physical Review B* **85**. doi:[10.1103/physrevb.85.174533](https://doi.org/10.1103/physrevb.85.174533) (May 2012).
326. Knapp, C., Karzig, T., Lutchyn, R. M. & Nayak, C. Dephasing of Majorana-based qubits. *Physical Review B* **97**, 125404. doi:[10.1103/physrevb.97.125404](https://doi.org/10.1103/physrevb.97.125404) (Mar. 2018).

327. Ménard, G. C., Malinowski, F. K., Puglia, D., Pikulin, D. I., Karzig, T., Bauer, B., Krogstrup, P. & Marcus, C. M. Suppressing quasiparticle poisoning with a voltage-controlled filter. *Physical Review B* **100**. doi:[10.1103/physrevb.100.165307](https://doi.org/10.1103/physrevb.100.165307) (Oct. 2019).
328. Vekris, A., Saldaña, J. C. E., Kanne, T., Hvid-Olsen, T., Marnauza, M., Olsteins, D., Wauters, M. M., Burrello, M., Nygård, J. & Grove-Rasmussen, K. Electronic Transport in Double-Nanowire Superconducting Islands with Multiple Terminals. *Nano Letters* **22**, 5765–5772. doi:[10.1021/acs.nanolett.2c01161](https://doi.org/10.1021/acs.nanolett.2c01161) (July 2022).
329. Wesdorp, J., Grünhaupt, L., Vaartjes, A., Pita-Vidal, M., Bargerbos, A., Splitthoff, L., Krogstrup, P., van Heck, B. & de Lange, G. Dynamical Polarization of the Fermion Parity in a Nanowire Josephson Junction. *Physical Review Letters* **131**. doi:[10.1103/physrevlett.131.117001](https://doi.org/10.1103/physrevlett.131.117001) (Sept. 2023).
330. Van Woerkom, D. J., Geresdi, A. & Kouwenhoven, L. P. One minute parity lifetime of a NbTiN Cooper-pair transistor. *Nature Physics* **11**, 547–550. doi:[10.1038/nphys3342](https://doi.org/10.1038/nphys3342) (May 2015).
331. Court, N. A., Ferguson, A. J., Lutchyn, R. & Clark, R. G. Quantitative study of quasiparticle traps using the single-Cooper-pair transistor. *Physical Review B* **77**. doi:[10.1103/physrevb.77.100501](https://doi.org/10.1103/physrevb.77.100501) (Mar. 2008).
332. Riwar, R.-P., Hosseinkhani, A., Burkhart, L. D., Gao, Y. Y., Schoelkopf, R. J., Glazman, L. I. & Catelani, G. Normal-metal quasiparticle traps for superconducting qubits. *Physical Review B* **94**. doi:[10.1103/physrevb.94.104516](https://doi.org/10.1103/physrevb.94.104516) (Sept. 2016).
333. Blaznik, N. *Investigating Quasiparticle Poisoning in Floating Hybrid Double Dot Devices Using Gate-Based Sensing* MSc Thesis (Utrecht University, 2020). <https://studenttheses.uu.nl/handle/20.500.12932/37745>.
334. Hays, M., de Lange, G., Serniak, K., van Woerkom, D. J., Bouman, D., Krogstrup, P., Nygård, J., Geresdi, A. & Devoret, M. H. Direct microwave measurement of Andreev-bound-state dynamics in a semiconductor-nanowire Josephson junction. *Physical review letters* **121**, 047001 (2018).
335. Pita-Vidal, M., Bargerbos, A., Žitko, R., Splitthoff, L. J., Grünhaupt, L., Wesdorp, J. J., Liu, Y., Kouwenhoven, L. P., Aguado, R., van Heck, B., Kou, A. & Andersen, C. K. Direct manipulation of a superconducting spin qubit strongly coupled to a transmon qubit. *Nature Physics* **19**, 1110–1115. doi:[10.1038/s41567-023-02071-x](https://doi.org/10.1038/s41567-023-02071-x) (May 2023).
336. Vilkelis, K., Manesco, A., Luna, J. D. T., Miles, S., Wimmer, M. & Akhmerov, A. *Fermionic quantum computation with Cooper pair splitters* 2023. arXiv: [2309.00447](https://arxiv.org/abs/2309.00447) [[cond-mat.mes-hall](https://arxiv.org/abs/2309.00447)].
337. Tsintzis, A., Souto, R. S. & Leijnse, M. Creating and detecting poor man's Majorana bound states in interacting quantum dots. *Physical Review B* **106**. doi:[10.1103/physrevb.106.1201404](https://doi.org/10.1103/physrevb.106.1201404) (Nov. 2022).
338. Samuelson, W., Svensson, V. & Leijnse, M. Minimal quantum dot based Kitaev chain with only local superconducting proximity effect. *Physical Review B* **109**. ISSN: 2469-9969. doi:[10.1103/physrevb.109.035415](https://doi.org/10.1103/physrevb.109.035415) (Jan. 2024).

339. Estrada Saldaña, J. C., Vekris, A., Žitko, R., Steffensen, G., Krogstrup, P., Paaske, J., Grove-Rasmussen, K. & Nygård, J. Two-impurity Yu-Shiba-Rusinov states in coupled quantum dots. *Physical Review B* **102**. ISSN: 2469-9969. doi:[10.1103/physrevb.102.195143](https://doi.org/10.1103/physrevb.102.195143) (Nov. 2020).
340. Mishra, A., Simon, P., Hyart, T. & Trif, M. Yu-Shiba-Rusinov Qubit. *PRX Quantum* **2**. ISSN: 2691-3399. doi:[10.1103/prxquantum.2.040347](https://doi.org/10.1103/prxquantum.2.040347) (Dec. 2021).
341. Harvey-Collard, P., Zheng, G., Dijkema, J., Samkharadze, N., Sammak, A., Scappucci, G. & Vandersypen, L. M. K. On-Chip Microwave Filters for High-Impedance Resonators with Gate-Defined Quantum Dots. *Physical Review Applied* **14**. ISSN: 2331-7019. doi:[10.1103/physrevapplied.14.034025](https://doi.org/10.1103/physrevapplied.14.034025) (Sept. 2020).
342. Pita-Vidal, M. *Realizing superconducting spin qubits* English. Dissertation (TU Delft) (Delft University of Technology, 2023). ISBN: 978-90-8593-584-1. doi:[10.4233/uuid:1314fbd5-794a-47d7-8bc6-ed73a84d8a6d](https://doi.org/10.4233/uuid:1314fbd5-794a-47d7-8bc6-ed73a84d8a6d).
343. Liu, Y., Li, M., Lan, D., Xue, G., Tan, X., Yu, H. & Yu, Y. Increasing energy relaxation time of superconducting qubits with nonmagnetic infrared filter and shield. *Chinese Physics B* **25**, 058501. doi:[10.1088/1674-1056/25/5/058501](https://doi.org/10.1088/1674-1056/25/5/058501) (May 2016).
344. Petersan, P. J. & Anlage, S. M. Measurement of resonant frequency and quality factor of microwave resonators: Comparison of methods. *Journal of Applied Physics* **84**, 3392–3402. ISSN: 1089-7550. doi:[10.1063/1.368498](https://doi.org/10.1063/1.368498) (Sept. 1998).
345. Deng, C., Otto, M. & Lupascu, A. An analysis method for transmission measurements of superconducting resonators with applications to quantum-regime dielectric-loss measurements. *Journal of Applied Physics* **114**, 054504. doi:[10.1063/1.4817512](https://doi.org/10.1063/1.4817512) (Aug. 2013).
346. Whan, C. B. & Orlando, T. P. Transport properties of a quantum dot with superconducting leads. *Physical Review B* **54**, R5255–R5258. ISSN: 1095-3795. doi:[10.1103/physrevb.54.r5255](https://doi.org/10.1103/physrevb.54.r5255) (Aug. 1996).
347. Stepanenko, D., Rudner, M., Halperin, B. I. & Loss, D. Singlet-triplet splitting in double quantum dots due to spin-orbit and hyperfine interactions. *Physical Review B* **85**. ISSN: 1550-235X. doi:[10.1103/physrevb.85.075416](https://doi.org/10.1103/physrevb.85.075416) (Feb. 2012).



# ACKNOWLEDGEMENTS

*Families is where our nation finds hope, where wings take dream.*

George W. Bush

For the last six or so years as I went through masters and then doctoral studies, so many people not only made this research a reality but also gave me happy memories and helped me improve as a person. **Srijit**, thank you for welcoming me unexpectedly to your group. You've fostered an excellent group culture of camaraderie and passion for physics, and gave detailed input on and support to all the research going on within it. I would also like to thank **Leo**, you established a world-class laboratory always on the cutting edge of exciting physics and I'm grateful for the opportunity to have been a part of it. **Damaz** and **Ivan**, as my closest collaborators you've taught me nanofabrication, most of what I know about cryogenics and measurement equipment, and countless other things, moreover picking up my slack more times than I'd care to admit. It was a pleasure working with you as teammates and friends.

Many others contributed directly to my doctoral research. Though our collaboration during my doctoral research was brief, I'm grateful to **Wolfgang** for initiating me into our research field with great memories and educational discussions. Through the mess of trying to continue research during a pandemic and turmoil in the lab, thank you so much **Jonne** for mentoring and supervising me even when it was not really in your job description to do so. Of course, thank you **Filip** for holding the CQ team together with loads of ideas and with your excellent input on our research. To the **CQ Team**: It's been lots of fun working with you **Damaz, Filip, Jasper, Lin, Michael, and Wolfgang**. Our shared passion for seeing how easily we could shake electrons really fast has led to a great research collaboration. The **2D Topo** group has also been a joy to work with, with everyone regularly sharing experiences, lending a hand, or having physics debates. A part of me wishes I could stay doing research with you all forever! I couldn't proceed without thanking you **Wietze** for making the absolute most out of a somewhat ridiculous experiment I proposed to you, and with your hard work and talent enabling interesting results to come of it. So much of my facade of understanding radio-frequency measurements and theory piggybacks on the deeper understanding **Lukas, Marta**, and the rest of the **cQED Team** were kind enough to share with me, so thank you. Though we worked a little less closely together, I've also had many fruitful discussions and a lot of help from present and past members of the **Kitaev team** for which I'm very grateful. Thank you to **Anton** and the **Quantum Tinkerers** for always being open to discuss my silly ideas and provide insight on them. Thank you to **Jason, Olaf, Raymond S., Raymond V.**, and the rest of TU Delft's research support staff. Your work relentlessly teaching students like me and improving experimental setups forms the backbone of QuTech. I also have to

thank **Csilla** and **Jenny** for your help with the organizational side of research that I am so useless at figuring out myself.

While they weren't so involved in my research, I think it's safe to say my family and friends are what made the last six years (and the rest) of my life so wonderful to live. To **Mom** and **Dad**, aside from literally bringing me to where I am today through your loving parenting, encouragement of my passion for science (and spoiling me with support towards this!), I am lucky to have you and **Ellen** as a family going through the adventure of life together even when we're separated by distance. To my sister **Ellen**, thank you for being a lifelong friend who I always feel at home hanging out with. À **Antonella, Laurent, Camille, et Laurence**, merci de m'avoir accueilli dans votre famille, et d'avoir partagé des aventures inoubliables avec moi au cours des six dernières années. Since moving to the Netherlands I've also made so many good friends. I'll look back nostalgically on all the good times hanging out with **Alina, Boris, Eugenio, Hugo, Ivan, Kostas, Marta, Mattias, Rasa, and Santi**, and hope that there are more to come! **Ivan**, you're one of the strongest people I've met and I know I can always rely on you for friendship, a reasoned opinion, or an adventurous night exploring Dutch cityscapes on bicycles. **Boris**, I'm grateful to have you as a friend who I feel I can talk about anything for hours with, whether in earnest benefitting from you being a considerate listener, or with a dash of your great sense of humor. To **Hugo**, I think I can summarize why I'm thankful for your goodhearted friendship by simply saying you're the only person other than Hélène who couldn't care less about hockey but still asks me how the Oilers are doing! Next, commiserating about research difficulties and chatting about life all the while enjoying a nice long run with my friends **Lukas** and **Qing** is something I'll sorely miss regularly doing. To **Beth, Charlotte, Ian, Johnny, and Luke**: It's hard to think of better gifts I've received than you coming all the way here for Hélène's and my wedding, and I will always be grateful that I can call you my friends in spite of me running off to Europe. The same goes for **Brody, Connor, Danny, Dan, Dylan, Felicia, Jordan, Josh, Kaitlin, Mike M., Nicole, Rob, Shane**, and so many other Canadian friends.

Lastly, it would be hard to list all the things I should thank my loving wife **Hélène** for. I feel I moved to Delft so that I could meet you, and was lucky to coincidentally do some fun research along the way. I have always leaned on your support of my personal growth, my wellbeing, my passions, and (I digress) my research.

Christian Glenn Prosko

# CURRICULUM VITÆ

## Christian Glenn PROSKO

- 22-04-1994      Born in Edmonton, Alberta, Canada.
- 2010–2012      Secondary School  
Bellerose Composite High School, Saint Albert, Alberta, Canada
- 2012–2017      Bachelor of Science with Honors in Mathematical Physics (First Class Honors)  
University of Alberta, Edmonton, Alberta, Canada  
*Thesis:*        Evaporative Cooling of  $^{87}\text{Rb}$  with Microwave Radiation  
*Supervisor:* Prof. Lindsay J. LeBlanc
- 2017–2019      Master of Science in Applied Physics (Cum Laude)  
Delft University of Technology, Delft, The Netherlands  
*Programme:* Quantum Nanoscience  
*Thesis:*        Dispersive Gate Sensing of Hybrid Quantum Dot Systems  
*Supervisors:* Prof. Wolfgang Pfaff  
                    Prof. dr. ir. L. P. Kouwenhoven
- 2018             Industrial internship  
ParaPy B.V., Delft, The Netherlands  
*Supervisor:* Reinier van Dijk
- 2019–2023      PhD research  
Delft University of Technology, Delft, the Netherlands  
*Thesis:*        Hybridization of Localized States in Semiconducting and Superconducting Circuits  
*Promotor:*    Prof. dr. ir. L. P. Kouwenhoven  
*Copromoter:* Dr. S. Goswami



# LIST OF PUBLICATIONS

11.  *Flux-Tunable Josephson effect in a four-terminal junction*  
**C. G. Prosko**, W. D. Huisman, I. Kulesh, D. Xiao, C. Thomas, M. J. Manfra, S. Goswami  
In review.
10. *RF compressibility measurements in Germanium*  
M. Chan, **C. G. Prosko**, L. Han, S. Oosterhout, A. Sammak, G. Scappucci, M. Veldhorst, F. K. Malinowski  
In preparation.
9.  *Flux-Tunable Hybridization in a Double Quantum Dot Interferometer*  
**C. G. Prosko**, I. Kulesh, M. Chan, L. Han, D. Xiao, C. Thomas, M. J. Manfra, S. Goswami, F. K. Malinowski  
In review. [arXiv:2303.04144](https://arxiv.org/abs/2303.04144)
8.  *Controllable single Cooper pair splitting in hybrid quantum dot systems*  
D. de Jong<sup>†</sup>, **C. G. Prosko**<sup>†</sup>, L. Han, F. K. Malinowski, Y. Liu, P. Krogstrup, L. P. Kouwenhoven, and W. Pfaff  
[Physical Review Letters](https://doi.org/10.1103/PhysRevLett.131.157001) **131**, 157001 (2023). [arXiv:2208.05154](https://arxiv.org/abs/2208.05154)
7. *Variable and orbital-dependent spin-orbit field orientations in a InSb double quantum dot characterized via dispersive gate sensing*  
L. Han, M. Chan, D. de Jong, **C. Prosko**, G. Badawy, S. Gazibegovic, E. P. A. M. Bakkers, L. P. Kouwenhoven, F. K. Malinowski and W. Pfaff  
[Physical Review Applied](https://doi.org/10.1103/PhysRevApplied.19.014063) **19**, 014063 (2023). [arXiv:2203.06047](https://arxiv.org/abs/2203.06047)
6. *Quantum capacitance of a superconducting subgap state in an electrostatically floating dot-island*  
F. K. Malinowski, R. K. Rupesh, L. Pavešić, Z. Guba, D. de Jong, L. Han, **C. G. Prosko**, M. Chan, Y. Liu, P. Krogstrup, A. Pályi, R. Žitko, J. V. Koski  
[arXiv:2210.01519](https://arxiv.org/abs/2210.01519)
5. *Radio-frequency C-V measurements with sub-attofarad sensitivity*  
F. K. Malinowski, L. Han, D. de Jong, J.-Y. Wang, **C. G. Prosko**, G. Badawy, S. Gazibegovic, Y. Liu, P. Krogstrup, E. P. A. M. Bakkers, L. P. Kouwenhoven and J. V. Koski  
[Physical Review Applied](https://doi.org/10.1103/PhysRevApplied.18.024032) **18**, 024032 (2022). [arXiv:2110.03257](https://arxiv.org/abs/2110.03257)
4.  *Rapid microwave-only characterization and readout of quantum dots using multiplexed gigahertz-frequency resonators*  
D. de Jong, **C. G. Prosko**, D. M. A. Waardenburg, L. Han, F. K. Malinowski, P. Krogstrup, L. P. Kouwenhoven, J. V. Koski, and W. Pfaff  
[Physical Review Applied](https://doi.org/10.1103/PhysRevApplied.16.014007) **16**, 014007 (2021). [arXiv:2103.03659](https://arxiv.org/abs/2103.03659)

---

Appears to some degree in this thesis.

<sup>†</sup>These authors contributed equally to this work.

3. *Revealing charge-tunneling processes between a quantum dot and a superconducting island through gate sensing*  
J. van Veen, D. de Jong, L. Han, **C. Prosko**, P. Krogstrup, J. D. Watson, L. P. Kouwenhoven, and W. Pfaff  
[Physical Review B \*\*100\*\*, 174508 \(2019\)](#). [arXiv:1903.09066](#)
2. *Simple  $\mathbb{Z}_2$  lattice gauge theories at finite fermion density*  
**C. Prosko**, S.-P. Lee, J. Maciejko  
[Physical Review B \*\*96\*\* \(2017\)](#). [arXiv:1708.08507](#)
1. *The Effect of Next-Nearest Neighbour Hopping in the One, Two, and Three Dimensional Holstein Model*  
C. Chandler, **C. Prosko**, F. Marsiglio  
[Scientific Reports \*\*6\*\*, 32591 \(2016\)](#). [arXiv:1603.04921](#)